Dissertation
submitted to the
Combined Faculties for the Natural Sciences and for Mathematics
of the Ruperto-Carola University of Heidelberg, Germany
for the degree of
Doctor of Natural Sciences

presented by

Diplom-Physicist Andrea Stolte

born in Duisburg

Oral examination 25$^{\text{th}}$ June 2003

Mass Functions and Mass Segregation

in Young Starburst Clusters

Referees: **Prof. Dr. Hans-Walter Rix**

Prof. Dr. Immo Appenzeller

Thesis Abstract

The Milky Way starburst clusters Arches in the Galactic Center region and NGC 3603 in the Carina spiral arm are studied with the aim to gain deeper insight into the stellar mass distribution in starburst clusters. The dense stellar population in both clusters is resolved in unprecedented detail with high angular resolution, near-infrared instruments. In the case of the Arches cluster, diffraction-limited, adaptive optics observations are analysed, and the achievements and limitations of ground-based vs. space-based diffraction-limited imaging are revealed by comparison with HST/NICMOS data. In the case of NGC 3603, seeing-limited $JHKL$ photometry is used to derive colour-excess fractions, and is complemented by space-based Hα data, both serving as tracers for circumstellar disks. Disk survival in starburst clusters is discussed. The present-day mass function (MF) of both clusters is deduced from colour-magnitude diagrams. Radial variations in the MFs reveal a heavily mass-segregated core in both starburst clusters. Dynamical timescales are estimated and interpreted with respect to primordial and dynamical segregation. The implications for massive star and cluster formation scenarios are discussed. Evidence for a low-mass cut-off is observed in the Arches MF, but not in NGC 3603, indicating a reduced formation efficiency for $M \leq 10\,M_{\odot}$ stars in the Galactic Center. This environmental difference has strong implications for the formation of stellar populations in galactic nuclei and starburst galaxies.

Übersicht der Dissertationsinhalte

Die Galaktischen Starburst Sternhaufen Arches im Galaktischen Zentrum und NGC 3603 im Carina Spiralarm wurden mit dem Ziel untersucht, ein tieferes Verständnis für die stellar Massenverteilung in Starburst Haufen zu gewinnen. Die dichte, stellare Population in beiden Sternhaufen konnte mithilfe hochauflösender nah-infrarot Instrumente in einzigartigem Detail aufgelöst werden. Im Falle des Arches Sternhaufens wurden beugungsbegrenzte, mit adaptiver Optik gewonnene Beobachtungen im Hinblick auf die Möglichkeiten bodengebundener, beugungsbegrenzter Aufnahmen analysiert, und technische Grenzen im Vergleich zu Weltraumbeobachtungen mit HST/NICMOS aufgezeigt. Im Falle von NGC 3603 wurden Infrarot-Farbexzesse aus $JHKL$ Aufnahmen bestimmt, und gemeinsam mit beugungsbegrenzten HST Hα Daten verwendet um die Existenz und Überlebensrate von zirkumstellaren Scheiben in Starburst Haufen nachzuweisen. Die aktuelle Massenfunktion (MF) der Starburst Haufen wurde aus Farb-Helligkeits-Diagrammen hergeleitet. Dynamische Zeitskalen wurden abgeschätzt, die Effekte primordialer oder dynamischer Massensegregation werden diskutiert, und die Folgen für Entstehungsmodelle massereicher Sterne und Sternhaufen werden angesprochen. Evidenz für einen Abbruch der MF unterhalb von $M \leq 10\,M_{\odot}$ wird im Arches Sternhaufen beobachtet, jedoch nicht in NGC 3603, was auf eine reduzierte Entstehungsrate von Sternen niedriger Masse nahe des Galaktischen Zentrums hindeutet. Dieser Einfluß der Sternentstehungsumgebung auf die MF hat signifikante Bedeutung für Sternentstehung in Galaxienzentren und Starburst Galaxien.

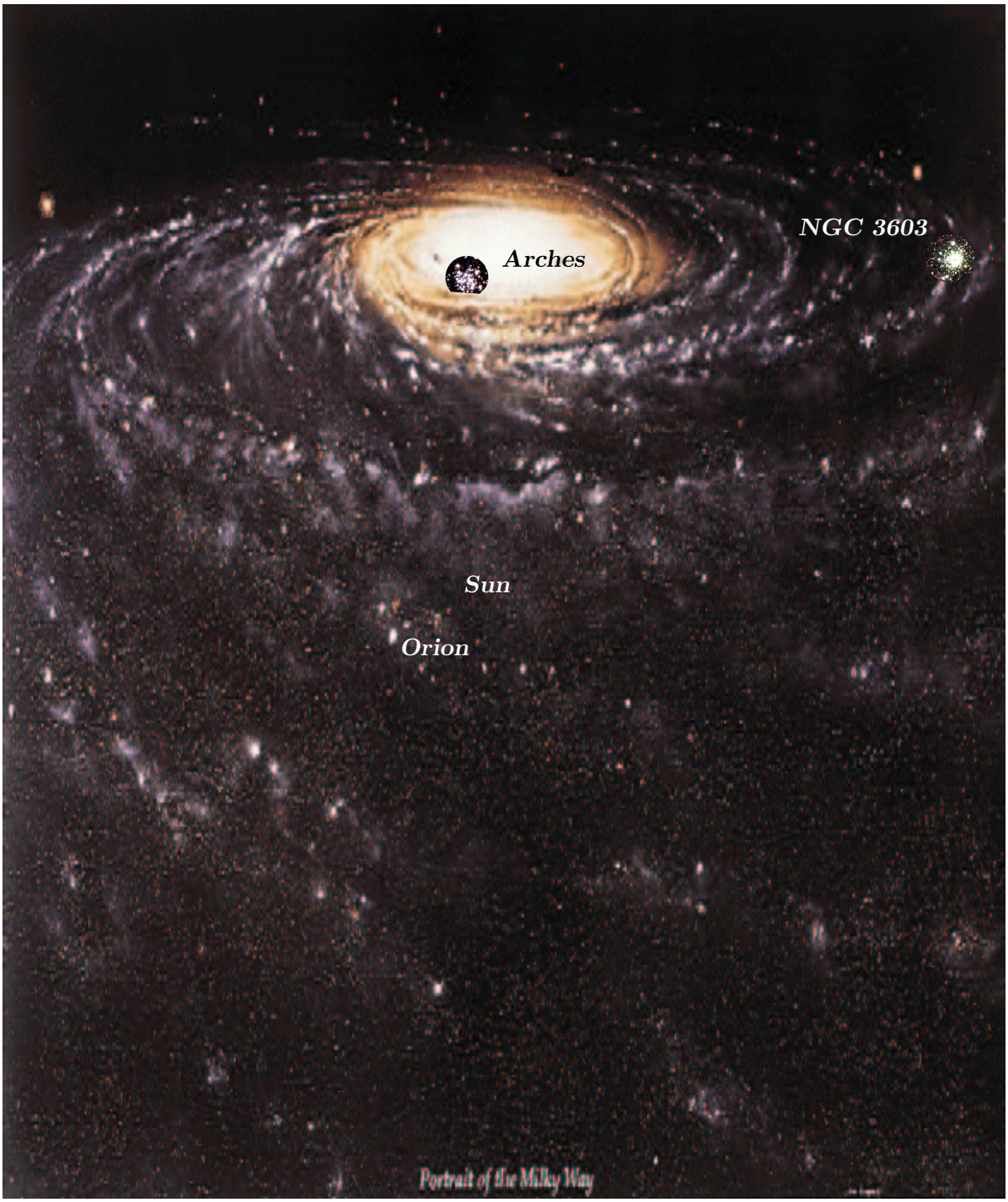

Portrait of the Milky Way - Painting by Jon Lomberg

Astronomical star and cluster data were used to obtain this view of the Milky Way's spiral structure. The position of the Sun and the Orion star-forming region are indicated. The Arches cluster close to the Galactic Center and NGC 3603 in the tangent point of the Carina spiral arm are shown as inserts (not to scale).

dedicated to Rai Weiss

Astronomy is like leaf counting

Rai Weiss

Although the work was often as laborious and painstaking as leaf-counting,
I hope that even a hard-core physicist as Rai Weiss
can find his interesting bits and pieces in this thesis.

Contents

Abbreviations

AO	Adaptive Optics
CF	Cumulative Function
CMD	Colour-Magnitude Diagram
GC	Galactic Center
GMC	Giant Molecular Cloud
IMF	Initial Mass Function
MC	Molecular Cloud
MF	Mass Function
NACO	NAOS/CONICA
TCD	Two-Colour Diagram

We had the sky, up there, all speckled with stars,
and we used to lay on our backs and look up at them,
and discuss whether they was made,
or only just happened.

Jim allowed they was made,
but I allowed they happened;
I judged it would have took too long to MAKE so many.....

Huckleberry Finn by Mark Twain

Chapter 1

Introduction

Star-forming regions come in a wide variety of appearances - from sparse associations such as the low density Taurus region to dispersed OB associations, from small clustered agglomerations with up to a few hundred stars to massive, rich clusters such as the Orion nuclear cluster with more than 2000 members. While these are the dominant modes of star formation in our Galaxy, they are far from giving us a complete notion of star formation in the Universe. Giant HII regions such as the 30 Doradus region in the Large Magellanic Cloud (LMC) produce young star clusters with masses comparable to the lower tail of the Milky Way globular cluster mass scale. At the high-mass end, very compact massive clusters condense in the extreme conditions in the tidal tails of merging galaxies, where tidal shear forces concentrate interstellar material. In the Antennae galaxies, young clusters span a mass range from 10^4 to $10^6\,M_\odot$ (Whitmore et al. 1999), a similar scale as found in globular clusters. Even more extreme star-forming environments are found in the nuclei of starburst galaxies and distant quasars, representing star-formation during an early stage of the Universe.

Most of these massive sources are at large distances, and can consequently not be resolved into individual stars. Numerous assumptions have to be made to understand their observed integrated properties. The underlying stellar population has to be modelled using population synthesis techniques. The basic model assumptions needed to reproduce a stellar population from integrated quantities are the age or age range, the metallicity and the stellar mass distribution, the so-called mass function. While the age and metallicity might be deduced from integrated spectra, there is no means to derive the mass function from integrated quantities alone. At the same time, the mass is the crucial parameter determining the evolution of a star, and thus the evolution of a stellar population. As this evolution is dominated by the core and shell burning processes, with the duration and time of occurance of each phase depending mainly on the star's mass for a given metallicity, the inherent physical processes are fairly well understood, allowing detailed stellar evolution modelling. If the age and metallicity are known, the stellar mass distribution is the remaining uncertainty on the way to understand a stellar population. Therefore, it is particularly important to understand the distribution of stellar masses at the instance of birth, the *initial* mass function.

The observation that most nearby, resolved star-forming regions display a very similar power-law mass spectrum with a small range in exponents led to the concept of a "standard" or "universal" initial mass function. As stars form from fragmentation of molecular clouds, the final mass of a star was long thought to be determined by the Jeans-mass, $M_J \sim T^{3/2}\rho^{-1/2}$, defined as the mass where a spherical cloud fragment becomes gravitationally unstable and collapses. As molecular clouds display a diversity of densities, temperatures and turbulent structure profiles, this scenario suggests a strong dependence of the emergent mass distribution on the molecular environment. Typical Jeans masses range from $1 - 100\,M_\odot$, in the right mass range to form the observed population of stars. This concept, however, faces two severe limitations. First of all, the collapse of a massive star occurs so rapidly that radiation pressure after hydrogen ignition inverts the infall as soon as a mass of $15-20\,M_\odot$ is accumulated. Secondly, if the environmental properties are the crucial parameters determining the

emergent mass spectrum, this spectrum should display strong variations in dependence of the star-forming environment, which, at least in nearby star-forming regions, contradicts the observation of a common mass function.

When infrared observatios allowed to penetrate the dust in the youngest star-forming regions, young stars with ages of a few Myr were observed to host circumstellar disks. This extended the theory of star formation to the concept of disk accretion leading to the gravitational collapse and subsequent disk accretion model, which is now extensively confirmed by observations of proto-stars in their collapse phase and direct detections of disks around young stars, e.g., in the Orion region (O'Dell et al. 1993). The concept of disk accretion, however, does not free us from the dependence of the emergent mass distribution on the star-forming environment. Young stellar disks contain a large fraction of dust re-emitting stellar radiation at long wavelengths. Stars with optically thick disks are thus prominent in the near-infrared regime, such that the disk fraction in a stellar population may be estimated from infrared colour excesses. Disk fractions derived for different environments suggest disks in a low-density star-forming region such as Taurus to survive longer, while dense, massive regions implying the proximity of high-mass O- and B-type stars cause the rapid photo-evaporation of remnant circumstellar material (see, e.g., Haisch et al. 2001). Again, the proto-planetary disks in the Orion region, exhibiting large evaporation cocoons, are an excellent example for this scenario. If accretion has a significant influence on the final mass of a star, the disk lifetime in a certain environment should be a critical parameter for the emergent mass distribution.

In addition, the radiation-pressure problem during the formation of high-mass stars mentioned above is also circumvented by models suggesting a strong dependence of the star's final mass on its immediate surroundings. Enhanced accretion rates and collisional interactions allow stars to be formed with up to $\sim 100\,M_{\odot}$ in such models, as in the observed mass distribution, which is prohibited in the standard fragmentation and gravitational collapse scenario. The essential ingredient to all these high-mass star formation theories is a high-density environment.

In summary, a high-density environment has the capability to form high-mass stars, but limits the survival of disks around low-mass stars as a consequence of the formation of these massive objects. As in the pure Jeans-fragmentation theory, a strong dependence of the emergent stellar mass spectrum on the environment is predicted.

The fact that high-mass stars, i.e. essentially all stars with masses in excess of $20\,M_{\odot}$, require a high-density environment to form, restricts the formation of these objects to the centers of massive molecular clumps evolving into massive star clusters. The involved physical processes are not yet well understood, such that a deeper understanding of young, massive star clusters still hosting the short-lived O-stars is needed to constrain the formation scenarios for high-mass stars further.

In addition to the prediction of such a "primordial segregation" of the high-mass stars due to their spatially restricted formation locus in the cluster center, the dynamical evolution of a star cluster also tends to segregate the massive stars into the center of the gravitational well, the core, while low-mass stars are re-distributed into a wider halo. Such a distribution arises naturally during the relaxation process after the repulsion of remnant gas. In dependence of the compactness of a young cluster, these dynamical segregation processes can alter the appearance of the cluster and spatial distribution of stellar masses significantly, thereby adding to the uncertainty in an unresolved stellar population.

These considerations make the mass function the most uncertain ingredient to stellar population synthesis models, where a wide range of environments has to be covered. While we have no nearby starburst galaxy or (fortunately) quasar at hand, and only a very limited number of nearby galaxies with tidally induced star formation, there are a few dense, massive young star clusters in the Milky Way allowing a detailed analysis of their mass spectrum. These - for Milky Way standards - unusually compact and rich clusters are denoted "starburst clusters" or "mini starbursts". Only four clusters massive enough to be assigned this label are currently known in the Galaxy, although there is evidence from infrared observations that comparably massive objects exist still deeply embedded in their native cloud.

Of these four Milky Way starburst clusters, only two are young enough to be still in their early compact phase, mainly unaffected by stellar and dynamical evolution. As we will see in the course of the analysis, the latter assumption is not quite true for the dense cluster centers even in these very young objects with ages of less than 2 Myr. These two starburst clusters are the Arches cluster in the Galactic Center region and the central cluster HD 97950 in the giant HII region NGC 3603 in the Carina spiral arm. The differences in the environment between Arches and HD 97950 allow to address some of the above questions with respect to star-forming scenarios. This study is supplemented by the comparison with the well-studied Orion nuclear cluster and R 136 in the giant HII region 30 Doradus in the Large Magellanic Cloud. Taken together, these four regions span a wide range in environments and cluster masses ($10^3 < M < 2 \cdot 10^4\,M_\odot$).

With these questions and prospectives for the formation and evolution of nearby and distant massive star clusters in a diversity of environments in mind, the Arches and NGC 3603 starburst clusters are studied. Near-infrared observations with high spatial resolution are used to resolve the dense cluster centers. The near-infrared regime is chosen to minimise the effects of extinction along the line of sight. The mass functions for both clusters are derived, and spatial variations in the emergent mass distribution are analysed with particular focus on mass segregation effects.

A general introduction into massive star forming regions and starburst clusters, as well as the Arches and NGC 3603 clusters, is given in Chapter 2. As Arches was observed with the non-standard adaptive optics technique, the adaptive optics concept is introduced and a detailed technical analysis of the available data sets is presented in Chapter 3 aiming at a deeper understanding of the observations prior to scientific interpretation. In Chapter 4, the scientific analysis of the Arches cluster photometry is performed, including extinction variations over the cluster field, and the mass function is derived in Chapter 5. We will move on to NGC 3603 in Chapter 6, presenting the photometric results from colour-magnitude and colour-colour diagrams including long wavelength L-band and narrow-band Hα observations. The mass function of the central starburst cluster HD 97950 is derived from colour-magnitude diagrams in Chapter 7, and spatial variations in the mass function are discussed. In Chapter 8, a detailed comparison of NGC 3603, Arches, the Orion Nuclear Cluster and R 136 in 30 Doradus reveals similarities and individual characteristics of young, massive star clusters emerging from different environments. The results are summarised in Chapter 9.

Chapter 2

From Massive Star Forming Regions to Mass Functions

A scientific introduction into the physical properties and importance of massive star forming regions and young, massive star clusters for our understanding of star formation processes is given below. In this context, an overview about existing knowledge of the Arches and NGC 3603 starburst clusters studied in this thesis, as well as their native environment, the Galactic Center and the Carina spiral arm, will be given. Unsolved questions concerning massive star formation in general, and the interaction processes between high- and low-mass stars are introduced, as well as their possible consequences for mass functions. Special emphasis will be placed on the suggested influence of the star forming environment on the resultant stellar mass distribution. The concept of mass functions shall be introduced, and outstanding results from prior mass function derivations are presented to allow later comparison with the results obtained in this work for the two starburst clusters.

2.1 Massive Star Forming Regions

The fact that a large fraction of all young (few Myr) stars are observed in groups or clusters, led to the assumption that most if not all stars form in stellar aggregates (see Lada & Lada 2002 for a recent review). Since near-infrared detectors allowed the systematic study of embedded star forming regions, evidence has increased that the youngest stellar populations known indeed form in groups of several ten to hundred members (Lada & Lada 2002). These groups are often loosely bound and with time dissolve, thereby fuelling the field star population. At the time they emerge from the native molecular cloud and become optically visible (within a few Myr after birth), small systems are already dynamically evolved, and the stars are found in a more dispersed state than during formation. From the core mass function in molecular clouds, $dN/dM_{core} \sim M_{core}^{-1.7}$, Lada & Lada argue that a large fraction of the mass of a giant molecular cloud is condensed in the few, very massive dense cores, such that a large fraction of stars is expected to form in massive clusters out of these cloud cores.

Larson (1982) showed that the mass of the most massive star increases with increasing mass of the molecular cloud within which the star formed. In addition, he argues that massive stars, observed to form only in massive clouds and not in isolated sites of star formation, require a dense environment to accumulate sufficient mass. It is interesting to note that Larson also suggested high-mass stars to form in the densest regions of molecular cloud cores, where gas is gravitationally condensed, and that some mechanism enhancing the accretion rate may additionally support massive star formation. As will be discussed in more detail later-on, these models still form the basis for the current theories of massive star formation (Behrend & Maeder 2001, Bonnell et al. 1998, see Sec. 2.2).

From these considerations, the most massive clusters as well as the most massive stars found in the Galaxy are expected to form in the most massive molecular clouds. These regions are particularly

important when the mass function, and especially the initial mass function, shall be derived. First of all, observations of massive star clusters allow to study the MF from the highest to the lowest masses at a single metallicity. In the case of a single star formation burst on a very short timescale ($\Delta\tau < 10^5$ yr), the age of a cluster can also be considered constant as far as evolutionary models are concerned. Both age and metallicity may then be determined from spectroscopy of the brightest cluster members, thus allowing to use a single evolutionary model isochrone to derive the cluster mass function. In the case of very young clusters, with ages younger than a few Myr, stellar and dynamical evolution effects are negligible, thus allowing to trace the initial mass function directly, without need to correct for uncertain evolutionary effects. More precisely, the birth locations of massive vs. low-mass stars can be compared, and possible primordial mass segregation revealed, thus constraining star formation scenarios at the high-mass end as well as in the low-mass regime, as will be discussed in more detail below.

As the youngest clusters are naturally most embedded in their molecular material, a study of the MF down to the lowest masses requires infrared observations in most star forming regions. Near-infrared observations have proved very successful during the past two decades in penetrating the huge amounts of dust present in molecular clouds in order to reveal the embedded stellar populations. A classical example in this context is the intensely studied Orion star forming complex. Originally, Cohen & Kuhi (1979) found the Orion nuclear region to be depleted in low-mass stars from optical data, while recent mass function derivations nicely display a continuous mass distribution down to the lowest masses ($\sim 0.3\,M_\odot$), beyond which a turnover is observed in basically all star forming regions studied in this detail to date (Muench et al. 2002).

Of course, in reality the picture is never this simple. Variable extinction along the line of sight to young star clusters due to changing dust column densities in the molecular material, uncertain distance determinations, as well as significant age spreads observed in extended star forming complexes such as, e.g. Orion or the NGC 3603 giant molecular cloud, complicate the understanding of the stellar population. Such effects have to be taken into account when studying young regions, and will be discussed in detail in the context of MF derivations.

At the massive end of the cluster mass scale are young starburst clusters, being the densest, most concentrated ("compact") and massive young star clusters in the Milky Way. As such, starburst clusters serve as templates for extragalactic starbursts on all scales, as only these nearby objects can be resolved into individual stars. With the determination of spectral types, individual ages and masses of the member stars may be derived, allowing to understand the underlying stellar population in great detail. Given the range in masses observed in a single massive cluster, $0.1 < M < 100\,M_\odot$, its constant metallicity and small range in ages, these objects are ideally suited to probe stellar evolution models. Such models are used in turn to derive physical properties of extragalactic star forming regions by population synthesis (e.g., Charlot & Bruzual 1991). A detailed comparison of resolved local massive star forming regions in the Milky Way and the Magellanic Clouds aids our understanding of giant HII regions in star forming galaxies starting at our close neighbours M33 and M82, to the compact starburst clusters observed in tidal interaction zones of Galaxy mergers such as the Antennae (Whitmore et al. 1999), and eventually even out to the centers of starburst galaxies.

In this work, two of the most massive and compact starburst clusters known in the Milky Way are analysed with respect to their mass functions, and possible dynamical or primordial mass segregation. With the exception of the massive starburst clusters in the LMC and SMC, which yield low-metallicity templates for extragalactic star forming regions, these are the only nearby, spatially resolvable starburst clusters at hand.

As the analysis focusses on the high-mass end of the stellar mass distribution observed in starburst clusters, the theories and problems in the formation of high-mass stars and the concept of the mass function shall be discussed in the following sections, before the Arches and NGC 3603 starburst clusters are introduced.

2.2 Massive Star Formation

The formation of high-mass stars in itself poses serious problems to the standard core collapse and subsequent accretion model, as radiation pressure from the growing star is capable of reversing the gas infall as soon as a mass of $10\,M_\odot$ is reached (Yorke & Krügel 1977). Assuming disk accretion instead of spherical infall, the limiting mass may be increased to $15\,M_\odot$ (Behrend & Maeder 2001), still far below the mass observed in O-type stars. Various scenarios are suggested to circumvent this problem. Simulations with enhanced accretion rates and collision probabilities in dense cluster centers (Bonnell et al. 1998), as well as growing accretion rates depending on the mass of the accreting protostar (Behrend & Maeder 2001), allow stars of up to $100\,M_\odot$ to form in the densest regions of a rich star cluster. In case of the GC environment, a higher gas density may lead to a higher accretion rate and/or longer accretion process in the protostellar phase. As long as the gravitational potential is strongly influenced by the amount of gas associated with the cluster, gas infall causes a decrease in cluster radius and subsequent increase in the collision rate, reinforcing the formation of high-mass stars. Physical processes such as gravitational collapse or cloud collisions scale with the square root of the local density, $\sqrt{\rho}$ (Elmegreen 1999, 2001), causing an enhanced star formation rate (SFR) in high density environments. Elmegreen (2001) shows that the total mass as well as the maximum stellar mass in a cluster strongly depends on the SFR and local density. This is confirmed by observations of high-mass stars found predominantly in the largest star forming clouds (Larson 1982).

Both the growing accretion and the collision scenario predict the high-mass stars to form in the densest central region of a cluster, leading to primordial mass segregation, which may be evidenced in a flat mass function in the dense cluster center. As a high gas and stellar density is the crucial prerequisit for high-mass stars to form, stars with masses $M > 15\,M_\odot$ are expected to be found predominantly in the densest star forming regions. The mass of the most massive star in a young star cluster is directly proportional to the mass of the native molecular cloud (Larson 1982). Together with the fact that models suggest primordial mass segregation to be essential for the formation of massive stars, a relation between the density of the environment and the initial mass function is expected. An overproduction of massive stars in a dense star forming region, or at least in the densest center of a massive star cluster, would cause the IMF to be flattened with respect to more moderate sites of star formation. These scenarios will be discussed in the context of the spatial variations observed in the Arches and NGC 3603 mass functions.

As an additional physical constraint, both scenarios require the low-mass stars to form first, and the high-mass stars latest in the cluster evolution process, leading to significant age spreads. As the strong UV-radiation field after hydrogen ignition in the first generation of high-mass stars expells the remaining gas from the cluster center, the accretion process should be halted immediately after high-mass star formation. While age spreads of up to 10 Myr are observed in massive SF regions with lower stellar density, such as the Orion region (Hillenbrand 1997), starburst clusters apparently formed their entire stellar population in a single, instantaneous burst (e.g., Figer et al. 2002).

The short dynamical timescales of compact clusters are, however, influencing the spatial distribution of stellar masses as well. On the one hand, high-mass stars are dragged into the cluster center due to the gravitational potential of the young cluster. On the other hand, low-mass stars may easily be flung out of the cluster due to interaction processes, especially given star densities as high as in the Arches or the central NGC 3603 cluster. The result of these processes would also be a flat mass function in the cluster center, steepening as one progresses outwards due to dynamical mass segregation. Dynamical segregation is predicted to occur within one relaxation time (Bonnell & Davies 1998), which for compact clusters is only one to a few Myr, and should thus be well observable in the form of a spatially varying mass function in the Arches and NGC 3603 starburst clusters.

In addition to the internal segregation process, the Galactic Center Arches cluster is also subject to the external GC tidal field, which exerts shear forces tearing apart the cluster entity. N-body simulations by Kim et al. (2000) yield tidal disruption timescales as short as 10 to 20 Myr in the GC

tidal field. If mass segregation is already present in a young star cluster due to internal processes, a strong tidal field will strip off the outer halo of low-mass stars first. Depending on the cluster age and the timescales involved, the present-day mass function will appear unusually flat not only in the densest parts of the cluster, but the integrated mass function might be dominated by massive and intermediate mass stars, too. These effects are hard or even impossible to disentangle without a detailed knowledge of the velocity distribution, and we expect to find a mixture of all these effects especially in the Arches cluster.

2.3 The Stellar Mass Function - a short history

In the previous sections, the various massive star formation scenarios suggested a varying stellar mass spectrum in dependence of the physical properties of the star-forming environment. In observational astronomy, the mass spectrum is usually described in the form of a stellar mass function, representing the number of stars within a certain mass intervall.

The concept of mass functions was first introduced by Salpeter in 1955. He defined the mass function (MF), ξ, as the number of stars per unit mass intervall, and found from solar-neighbourhood stars that the number of stars decreases with increasing mass as a power-law. In a logarithmic representation, the exponent of the power-law is given by the slope of the (logarithmic) mass function.

$$\mathrm{d}\,\xi(\log m) \sim m^{\Gamma} \qquad \Leftrightarrow \qquad \mathrm{d}\,\log\xi/\mathrm{d}\,\log m = \Gamma \tag{2.1}$$

This slope is independent of the absolute scaling and thus allows to compare relative fractions of low- to high-mass stars in populations with varying absolute numbers of stars. This scaling independence caused the slope of the MF as defined above to be widely used as a comparison value between stellar mass distributions.

In his initial study, Salpeter finds a slope of $\Gamma = -1.35$ for solar neighbourhood stars after correcting for stellar evolution, thus defining the *initial* mass function (IMF) of stars at the time of birth. Despite assuming an age of only 5 Gyr for the Milky Way and the large uncertainties in stellar evolution models at that time, this slope is still referred to as the "standard" slope in MF comparisons. This is due to the remarkable constancy of derived values for Γ in a diversity of environments over time.

Miller & Scalo (1979) and Scalo (1986) re-investigate the solar neighbourhood population and find a log-normal distribution, $\mathrm{d}\log\xi/\mathrm{d}\log m = -(1+\log m)$[1], which yields, when forced into power-laws, slopes of $\Gamma = -0.4$ for $0.1 < M < 1\,M_\odot$, $\Gamma = -1.5$ for $1 < M < 10\,M_\odot$, $\Gamma = -2.3$ for $M > 10\,M_\odot$. From a literature compilation including a diversity of populations, Kroupa (2001) concludes that the IMF is universal with $\Gamma = -0.3 \pm 0.5$ for $0.08 < M < 0.5\,M_\odot$, and $\Gamma = -1.3 \pm 0.5$ for $M > 0.5\,M_\odot$ (very close to Salpeter's initial value), implying a mean mass of $\langle m_* \rangle = 0.36\,M_\odot$.

Many studies are performed on young star-forming regions in order to avoid stellar evolution effects and trace the IMF directly, as in the study presented in this work. Massey et al. (1995a, 1995b) report slopes between -0.7 and -1.7 with a weighted mean of -1.1 ± 0.1 for $M > 7\,M_\odot$ in 13 star-forming regions in the Milky Way, and $-1.1 < \Gamma < -1.6$ with a mean of -1.3 ± 0.1 for $M > 15\,M_\odot$ in 5 regions in the Large and Small Magellanic Clouds. In the well-studied Trapezium cluster, Muench et al. (2002) obtain $\Gamma = -1.21 \pm 0.2$ for $M > 0.6\,M_\odot$, and $\Gamma = -0.15 \pm 0.15$ in the subsolar mass regime. In the starburst cluster R 136 in the 30 Doradus region in the Milky Way, the most massive local young star cluster, Massey & Hunter (1998) derive $\Gamma = -1.3 \pm 0.1$ covering the entire intermediate- to high-mass regime from 2.8 to $100\,M_\odot$. As a consequence of this remarkable similarity observed in the initial mass function over space and time, metallicity and a wide range in masses from $100\,M_\odot$ down to the subsolar regime, the stellar mass distribution at birth has frequently been suggested to be universal.

[1] This mass function was later-on rejected by Scalo 1998, who extensively discusses the uncertainties inherent to MF slope derivations.

2.4 Milky Way Starburst Clusters

"Luminous clusters of hot stars found within the Local Group are the bridge between nearby individually resolved objects and the distant, more luminous starburst galaxies." (Conti 1999)

In the Milky Way, only very few dense, compact young clusters are known. These clusters are the Arches and Quintuplet clusters located in the Galactic Center region, the Galactic Center cluster itself, and the NGC 3603 central cluster HD 97950 located in the giant HII region NGC 3603 in the Carina spiral arm.

As most young clusters are dispersed quickly in contrast to the bound globular clusters, young clusters are generally referred to as "open clusters". Despite their high central density of $\sim 10^5\,M_\odot\,\mathrm{pc}^{-3}$ indicating that they are bound entities, starburst clusters are frequently classified as "open clusters" to distinguish them from the old cluster population. The dynamical analysis shows indeed a significant difference to globular clusters - starbursts are dynamically instable and will not survive for a Hubble time. Internal interaction processes dissolve the cluster with time. In this respect, the classification as open clusters is justified. The dynamical behaviour and survival timescales of Arches and NGC 3603 will be derived from the mass function and discussed in Secs. 5.2.6 and 7.6.3.

In the following sections, the star forming environment of the two starburst clusters studied here - Arches and HD 97950 in NGC 3603 - will be described, and the basic cluster properties will be outlined.

2.4.1 Arches

2.4.1.1 The Galactic Center environment

The Galactic Center (GC) is the most extreme star-forming environment within the Milky Way. High stellar and gas densities, turbulent motion, tidal torques exerted by the strong gravitational potential, magnetic fields and an intense radiation field determine the physical environment of star formation in the GC. It is surprising that in such a turbulent environment star formation seems to be most efficient. While the gravitational and radiation fields exert disruptive forces on the condensing matter, the concentration of large amounts of gas and dust within a small spatial region allows massive sheets, filaments and dense cores to form. From the densest cores, massive star clusters such as the Arches eventually emerge. In fact, the formation of high mass stars and massive clusters is more successful than in any other region in the Milky Way.

A detailed study of star formation processes and the stellar content of the GC region has until recently been limited to the very brightest and most massive stars due to the huge extinction ($A_V \sim 30$ mag) along the line of sight. Additional constraints are given by the spatial resolution at the GC distance of ~ 8 kpc ($DM = 14.47 \pm 0.08$ mag, e.g. McNamara et al. 2000), much farther than nearby star forming regions such as the Orion or ρ Ophiuchi star forming complexes studied in detail to date. Only with the advent of deep, high resolution near-infrared instruments, the analysis of populations and young star clusters near the GC has become feasible.

During the past few years, it has become evident that three of the four starburst clusters known in the Milky Way are located in the GC region - namely, the Arches and Quintuplet clusters, and the Galactic Center cluster itself. Although rich in young stars, the Galactic Center Cluster is not strictly speaking a starburst cluster, as it is comprised of a mixture of stars of various ages and metallicities that most probably migrated dynamically into the Galactic Center. Krabbe et al. (1991, 1995), however, detect a cluster of young (a few Myr) emission-line stars counter-rotating with respect to the disk very close to the GC, and argue that these stars originated in a single starburst event either in situ or at larger GC distance implying subsequent inward migration. This young cluster is a good example of the difficulties faced when analysing the GC stellar population, as tidal forces cause fast dynamical mixing of stars close to the GC and hamper the determination of their origin.

With a cluster age of only a few Myr for Arches and Quintuplet, the question arises how many

clusters do actually form in the densest environment of the Milky Way. The 2MASS database yielded new insights into the estimated number of star clusters hidden in the dense stellar background. Dutra & Bica (2000, 2001) detect 60 new cluster candidates of various ages located in the innermost 4° (560 pc at a distance of $d = 8$ kpc) of the Galaxy from stellar density enhancements in 2MASS observations. Numerical simulations by Portegies Zwart et al. (2001) suggest that clusters with properties similar to the massive Arches and Quintuplet and ages of a few 10 Myr can easily be concealed in the large stellar densities of the innermost 200 pc. Under the assumption that molecular clouds in the GC region survive ~ 5 Myr, Dutra & Bica (2001) estimate the formation rate of massive clusters to be as high as 2 clusters/Myr. According to the simulations by Portegies Zwart et al. (2001), these clusters are dispersed rapidly (< 20 Myr) to densities indistinguishable from the dense stellar background. As dynamical evolution timescales are short due to the strong tidal field in the GC region (Kim et al. 1999), young star clusters are disrupted quickly after formation, contributing to the Galactic bulge population. Thus, only the youngest clusters remain intact for the study of star formation in this extraordinary environment.

2.4.1.2 The Arches Cluster

The Arches cluster, at a projected distance of only 25 pc ($d = 8$ kpc) from the GC, is one of the most massive young clusters known in the Milky Way. Located near the radio arc region (Yusef-Zadeh et al. 1984), where extended filamentary structure, believed to be collimated by magnetic fields (e.g., Lang, Goss, & Morris 2001), is found, it lives within an environment dominated by a mixture of diverse physical processes. Polarisation along filaments and velocity gradients observed in the radio data by Lang et al. (2001), and gas and dust lanes influenced by the radiation field of high mass stars, are only a few characteristics of this star forming locus.

With an estimated mass of about $10^4\,M_\odot$ and a central density of $3 \cdot 10^5\,M_\odot\,\mathrm{pc}^{-3}$, Arches is the densest Galactic young star cluster (YC) known (Figer et al. 1999). From physical properties of Wolf-Rayet stars, the age of the cluster is estimated to be 2 to 4.5 Myr (Blum et al. 2001). The most recent age estimate is 2.5 ± 0.5 Myr determined from spectroscopy of Wolf-Rayet stars (Figer et al. 2002). Throughout the thesis, stellar evolution models of 2 Myr will be used to transform Arches stellar magnitudes into masses. As will be discussed in Sec. 5.1, these models are most consistent with the observed Arches colour-magnitude diagram and known stellar properties.

Due to the high foreground extinction of $A_V \sim 30$ mag, the first detection of the Arches cluster occured only recently in a near-infrared survey of the Galactic Center region by Nagata et al. (1995). Narrowband properties suggested their "Object #17" to be a cluster of emission-line objects with properties of Wolf-Rayet type stars. The cluster population has subsequently been resolved into the brightest stars by Cotera et al. (1996) and Serabyn et al. (1998), all of which report the "discovery" of a new star cluster unusually rich in emission-line stars. From the location close to the thermal arched filaments ("thermal arches", Timmermann et al. 1996) the name "Arches" was derived.

The first deep study of the stellar content of Arches was carried out by Figer et al. (1999) using HST/NICMOS data. They used NICMOS2 JHK data to derive a shallow initial mass function in the range $10 < M < 125$ $\mathrm{M}_\odot$ with a slope of $\Gamma = -0.7 \pm 0.1$, but with significant flattening observed in the innermost part of the cluster ($\Gamma = -0.1 \pm 0.2$ for $R < 4\farcs5$ or 0.2 pc).

Most young star clusters and associations in the Milky Way display a mass function close to a Salpeter (1955) power law with a slope of $\Gamma = -1.35$, as discussed in Sec. 2.3. Several such star forming regions were studied by Massey et al. (1995a), yielding slopes in the range $-0.7 < \Gamma < -1.7$ with an average of -1.1 ± 0.1, which leads these authors to conclude that within the statistical uncertainties no deviation from a Salpeter slope is observed. A flat mass function as observed particularly in the Arches cluster center implies an overpopulation of high-mass stars as compared to "normal" clusters. The special physical conditions in the GC region, especially the high gas and dust densities, have been suggested to enhance the formation of massive stars, yielding a possible explanation for a flattened

mass function (Morris 1993).

The Arches cluster was observed during commissioning of the Gemini AO system Hokupa'a and the VLT AO system NAOS-CONICA. In Chapter 3, the ground-based AO data shall be technically analysed and compared in detail to the space-based HST/NICMOS data presented in Figer et al. (1999). The mass function of the Arches cluster will be derived from the colour-magnitude distribution of all available data sets, and compared to previous results obtained with HST/NICMOS by Figer et al. (1999).

2.4.2 NGC 3603

2.4.2.1 The Carina spiral arm

The Carina spiral arm is depicted in the spatial distribution of 43 molecular clouds detected in CO spanning a range in longitude from $270° < l < 330°$ (Grabelsky et al. 1987, 1988). This survey yields strong evidence that the Carina arm lines up with the Sagittarius arm to form the largest known spiral structure in the Milky Way, the 40 kpc extended Carina-Sagittarius arm. This structure winds around the Galactic Center spanning 2/3 of the Galaxy at GC distances of $3 - 13$ kpc. The giant molecular clouds traced in the CO data out to heliocentric distances of $d = 22$ kpc all have gas masses $M_{gas} \geq 10^5\ M_\odot$, thus being candidate sites for massive star formation.

The most massive star forming complex in the Carina arm is the region around the massive luminous blue variable star η Car, the CarOBI complex. This region alone includes 5-7 young open clusters, from the Tr 16 cluster hosting η Car with an age of ~ 2 Myr to the 10 Myr old IC 2518 probably associated with the same molecular cloud (MC). The estimated gas mass in this MC is $7 \cdot 10^5\ M_\odot$, at the high mass end of Galactic star forming clouds. The total mass in molecular clouds in the Carina arm is estimated to be on the order of $6 \cdot 10^7\ M_\odot$.

With comparable gas mass, the CarOBI complex is followed by the two giant HII regions NGC 3576 ($M_{gas} \sim 7 \cdot 10^5\ M_\odot$, $d \sim 2 - 3$ kpc) and NGC 3603 ($M_{gas} \sim 4 \cdot 10^5\ M_\odot$, $d \sim 7$ kpc). All these three massive star forming complexes have been studied in some detail, and intense star formation activity with indications of sequential or continuous star formation with stellar ages ranging from $1 - 20$ Myr is found.

When comparing giant molecular clouds (GMCs) in the Carina arm, NGC 3603 has two exceptional characteristics: First, it hosts the only starburst cluster observed in the Milky Way to date outside the Galactic Center region. Secondly, NGC 3603 is the only optically visible giant HII region in the Milky Way.

The fact that its virial mass exceeds the mass derived from CO observations (Grabelsky et al. 1988) indicates that the molecular cloud might not be in virial equilibrium, possibly due to stellar disruption by the winds and radiation from young, massive stars. This is indeed evidenced by the interaction of the starburst cluster with the surrounding medium (DePree et al. 1999, Nürnberger & Stanke 2003).

The low foreground extinction along the line of sight to the Carina spiral arm allowed to trace large portions of the arm early-on in open clusters and HII regions as optical tracers for spiral structure. For the same reason, observations of the exceptional star forming region NGC 3603 including the central starburst cluster are facilitated as compared to the "normal" deeply embedded young stellar populations, permitting to study star formation in NGC 3603 over the entire wavelength range in great detail.

Clearly, the giant molecular clouds in the Carina spiral arm are sites of intense massive star formation, but star formation scenarios may differ significantly from the processes determining massive star formation in the Galactic Center region as discussed above. The star formation process in a giant molecular cloud such as NGC 3603 is locally determined from the physical properties of the local cloud and not influenced by mixing effects and tidal torques as in the case of the Arches cluster.

The environment inside a molecular cloud has long been suggested to influence the star forming process. As a consequence of large differences in gas density, turbulence and dynamic structure, magnetic fields etc., fragmentation and accretion processes may differ among star forming regions as discussed in the introduction. The influence of the environment on the emergent stellar population should be imprinted into the resultant stellar mass distribution. As the mass of a star is the dominant factor determining its evolution, the mass spectrum characterises a stellar population. Environmental differences altering the local fragmentation or accretion rate should be reflected in the emergent mass spectrum. Although the maximum mass found in a young population is proportional to the gas mass in the native molecular cloud, this does not necessarily imply an altered mass function. If the mass function is universal, as frequently argued (see e.g., Kroupa 2001 for a recent review), a massive cloud could simply form a larger number of stars (Larson 1982).

Another important property of the emergent stellar population is the imprinted velocity distribution. The dynamical structure of a young star cluster determines whether or not it will form a bound system during the relaxation process, or whether it will disperse into the surrounding field. In this sense, the dynamical properties determine a young star cluster's ultimate fate.

The Galactic Center and the Carina spiral arm probe very different star forming environments, with the former possibly corresponding more to the dense cores of starburst galaxies, while the latter represents a template for a more regular spiral arm (or other density enhanced) environment in distant galaxies. These two environments shall be compared by analysis of the mass distributions within their youngest and most massive emergent star clusters.

2.4.2.2 NGC 3603

In contrast to Arches, which was long hidden behind the veil of foreground extinction in the direction of the Galactic Center, NGC 3603, being the only optically visible giant HII region in the Milky Way, was intensely studied since its discovery by John Herschel in 1834 (Sher 1965). NGC 3603 is one of the most massive HII regions in the Milky Way (Goss & Radhakrishnan 1969). With an integrated Hα flux of $L(\mathrm{H}\alpha) \sim 2 \cdot 10^{39}$ erg s^{-1} (Kennicut 1984) and a total gas mass of $4 \cdot 10^5\ M_\odot$ (Garebalsky et al. 1988) it qualifies as a giant HII region, with a mass comparable to extragalactic giant HII regions ($M_{gas} \sim 10^4 - 10^7\ M_\odot$, $M_{stars} \sim 10^3 - 10^5\ M_\odot$, $L(\mathrm{H}\alpha) \sim 10^{37} - 10^{40}$erg s^{-1}, Kennicutt 1984). The total luminosity is estimated to $\sim 10^7\ L_\odot$, about 100 times the luminosity of the Orion star forming region and 0.1 times the total luminosity of the giant star forming complex 30 Doradus in the Large Magellanic Cloud.

In its center, NGC 3603 hosts the massive starburst cluster HD 97950 with 3 Wolf-Rayet stars, 6 O3 and at least 30 later O-type stars (Moffat et al. 1994). The intense UV radiation field from the most massive stars located in the cluster center has evaporated the molecular material from which the star cluster formed. Drissen et al. (1995) derive sufficient Lyman continuum flux for the 21 brightest stars in the cluster to account for the Hα luminosity and thus ionisation observed in NGC 3603. The strong Wolf-Rayet (WR) star winds ($v \sim 2000$ km/s, Drissen et al. 1995) continue to blow out remnant gas and dust from the cluster center. Aided by the low line of sight extinction to NGC 3603 from Galactic interstellar material ($A_V \sim 4-5$ mag), these processes reveal the starburst cluster to our view. Due to the hostile environment to molecular material, the extinction in the cluster center is even lower (albeit variable) than in the immediate surrounding, facilitating analysis of the young stellar population in HD 97950.

As a consequence of the UV radiation field of the high-mass cluster stars, bright ionisation fronts are seen to the South of the central cluster, visualising the strong impact of the starburst cluster on its environment. While the lower density material of the molecular cloud is evaporated rapidly, high-density condensations survive as large elephant trunk structures with puffed-up heads and bright ionised rims facing the cluster. These regions of dense molecular material contain strong infrared excess sources, frequently associated with mid-infrared point-sources and maser emission, comprising

the next generation of recently formed stars still embedded in their native material. In the wider field of NGC 3603, 4 ionisation clumps are found (Brandner et al. 2000, Mücke 2002), resembling closely in appearance the Orion protoplanetary disks ("proplyds", O'Dell 1993). The sizes of these objects in NGC 3603 are about 20-30 times larger ($\sim$ 10000 AU) than their Orion counterparts. Therefore, if they are indeed hosting large-scale star-disk systems, these huge disks would argue for a large number of smaller disks to be found in the surrounding of HD 97950. Such a finding would indicate that disks are able to survive the intense radiation field of the massive cluster stars for at least 1 Myr, the minimum cluster age. Until now, only one of the proplyds has a spatially associated NIR point source (Brandner et al. 2000) and none have MIR counterparts (Nürnberger & Stanke 2003). The discovery of strong NIR excess sources within these proplyds and in the vicinity of the cluster would enhance evidence for disk survival in NGC 3603.

From the early 1980's on, multi-wavelength, high-resolution approaches tried to disentangle the star formation history of this - for Milky Way standards - extreme region. The physical properties of gas and dust in NGC 3603, as well as its stellar content and star formation history have been studied in great detail in the past three decades.

Early radio, MIR and NIR maps displayed several knots of enhanced density in the area surrounding the central starburst cluster, leading to a sequential star formation scenario for the NGC 3603 GMC. From the spatial distribution of dense gas and dust from molecular line studies, several individual knots of star formation are found spread out over the entire area of $\sim 20' \times 20'$. Early 2μm maps revealed the existence of dense star-forming cores still heavily embedded in molecular material in NGC 3603 in the immediate vicinity of HD 97950 (Persi et al. 1985). More recently, radio data at 3.4 cm wavelength, tracing the H109α and H113β recombination lines, were used as tracers for turbulent material, outlining sites of recent or future star formation (DePree et al. 1999). These data show strong radio emission predominantly to the South of the starburst cluster, while the cluster itself appears empty of detectable molecular gas, in agreement with a wind-driven bubble with radius ~ 0.6 pc found by Balick et al. (1980), probably caused by the cluster WR stars (Drissen et al. 1995). The strong correlation of radio emission from ionised gas with infrared point-sources as signposts of ongoing star formation supports the sequential star formation scenario for NGC 3603.

According to the spatial distribution of embedded infrared sources to the South of the starburst cluster vs. supergiants to the North (Tapia et al. 2001), sequential star formation was suggested to propagate from the North to the South within NGC 3603 (DePree et al. 1999). Recently, new mid IR data presented by Nürnberger & Stanke (2003) show dense cores associated with a molecular clump as far as 11 pc to the North of HD 97950. Along with embedded mid IR sources detected to the South, these possible proto-stars paint a picture where the starburst cluster is located rather centrally in between star forming events in various stages.

The analysis of the stellar population associated with NGC 3603 supported a sequential star formation scenario. Optical spectroscopy reveals a number of red and blue supergiants in the immediate vicinity of HD 97950 (Frogel et al. 1987), among those the exceptional blue supergiant Sher 25 believed to resemble the progenitor of supernova SN1987a (Brandner et al. 1997). With ages of 10-20 Myr, these giants constitute the oldest part of the stellar population in NGC 3603. On the other hand, the spectral classification of the central Wolf-Rayet stars to type WN6 limits the age of the massive cluster stars to $\tau \lesssim 3$ Myr. With deeper photometry, the pre-main sequence turn-off in HD 97950 suggested ages as young as 0.3-1 Myr for PMS stars (Eisenhauer et al. 1998, Brandl et al. 1999), when compared to stellar evolution models.

Although the entire NGC 3603 region displays fascinating sites of star formation, the central starburst cluster, one of the most recent star forming events, is clearly the most outstanding object. In all studies of the stellar cluster population, the spatial resolution in the cluster center was the most limiting factor. As the integrated optical spectrum of the nucleus of HD 97950 (Walborn 1973) already showed Wolf-Rayet (WR) characteristics, early attempts have been made to resolve the bright central stars into individual objects (e.g., Moffat et al. 1983). Spectra of the 3 brightest stars in the cluster

center confirmed these to be hydrogen-rich WNL6 objects from their emission-line properties (Moffat 1983, Moffat & Niemela 1983, Drissen et al. 1995). Speckle interferometry with a resolution of $< 0\farcs1$ by Baier et al. (1985) and Hofmann & Weigelt (1986) revealed the 4 brightest stars in the innermost $1''$ of the cluster on the first resolved images of the cluster core. Hofmann et al. (1995) obtained speckle images of a $6'' \times 6''$ field of view, yielding photometry of the 28 brightest stars. After the first attempts to resolve the cluster center with speckle techniques, the stellar population of HD 97950 was observed with increasing resolution and photometric sensitivity at optical wavelength. Melnick et al. (1989) presented photometry of 50 cluster members (as determined from their reddened colours) within a radius of $R < 60''$ around the cluster center, followed by Moffat et al. 1994, who exploited the high resolution of the HST/PC camera to derive photometry for 77 stars within the $40''$ FOV of the PC chip.

With the goal to avoid the limitations imposed by the Earth's atmosphere, space-based broad- and narrow-band photometry with the WFPC2 high-resolution optical camera as well as spectroscopy with the HST/FOS spectrograph were obtained (Moffat et al. 1994 and Drissen et al. 1995, respectively). These data allowed spectral classification of the central WR and O stars, and led to the determination of the cluster's stellar density profile, as well as the estimate of the mass function at the high-mass end ($\Gamma = -1.4$). Given the derived profile and parameters, these authors perform a detailed comparison with the 30 Doradus GMC in the Large Magellanic Cloud (LMC), suggesting that both regions are very similar, harbouring starburst clusters with several WR stars in their centers (the massive R136 cluster in the case of 30 Dor) and showing strong signs of sequential star formation. Indeed, the density profiles within the innermost 1 pc of both central clusters resemble each other closely. Contrary to the slightly higher central density estimated for HD 97950 ($\rho_{(HD\,97950)} \sim 3 \cdot 10^5\,M_\odot\,\mathrm{pc}^{-3}$ vs. $\rho_{(R136)} \sim 1 \cdot 10^5\,M_\odot\,\mathrm{pc}^{-3}$), the mass of R136 exceeds the mass of HD 97950 by a factor of 3 ($2 \cdot 10^4\,M_\odot$ vs. $7000\,M_\odot$). The higher cluster mass scales with the estimated total luminosity of the HII regions in which both clusters form, which is estimated to be a factor of 10 larger in 30 Dor. From these physical properties, NGC 3603 has often been called a "scaled down version" of 30 Doradus. The only conspicuous difference observed between the two regions is the spatial distribution of stars surrounding the starburst cluster. While R136 posesses an extended stellar halo including bright WR and OB stars comparable to the cluster center, displaying a density profile joining smoothly into the 30 Dor stellar density distribution out to 100 pc from the cluster center, such a halo appears to be entirely missing in the case of HD 97950. Recently, a cluster extent significantly larger than previously assumed is found from a K_s-band survey of HD 97950 by Nürnberger & Petr-Gotzens (2002), where careful field star estimates led to a cluster radius of $150''$ (5 pc) for HD 97950, while prior estimates from the brighter cluster stars restricted the cluster to $R < 60''$ (e.g., Moffat et al. 1994). This extent is still orders of magnitude below the halo observed around R136. Clearly, the true cluster extent remains a matter of debate as the field star contamination is non-negligible in particular at the faint end. The uncertainty in the true cluster extent and the surrounding field population complicates the derivation of statistical properties such as mass functions of the entire cluster population, and makes HD 97950 a particularly challenging scientific target.

Eisenhauer et al. (1998) first used the ADONIS adaptive optics system at the ESO 3.6 m telescope for a detailed analysis of the cluster center at a resolution below $0\farcs2$. Following up on the earlier speckle techniques, which were limited to a very small field of view and moderate sensitivity, the AO study intended to penetrate into the innermost cluster region. The use of adaptive optics techniques allows to enhance the resolution in ground-based observations to the diffraction limit of optical telescopes. The concentration of flux into a small pixel-area on the detector allows for a large dynamic range and photometric depth, and thus to proceed towards the lower mass stellar population. The advantages and limitations of AO will be discussed in detail in Chap. 3. As a good correction can be achieved only at longer wavelengths, $\lambda \gtrsim 1\,\mu m$, with reasonable technical effort, AO based observations are currently carried out in the NIR regime. This is particularly useful in young star-forming regions such as NGC 3603. NIR observations are less affected by extinction as light at longer wavelengths penetrates

the dust in the molecular cloud, thus allowing to overcome possible selection effects produced by the moderate, but - due to spatial variability - non-negligible extinction in NGC 3603.

Even with this high-resolution technique, however, the heavily crowded cluster center remains more incomplete than the surrounding field distribution. Thus, Eisenhauer et al. were able to observe the pre-main sequence of the starburst cluster with masses $1 < M < 4\,M_{\odot}$, deriving an age of 0.3-1 Myr for the PMS population from comparison with PMS stellar evolution models (Palla & Stahler 1999, hereafter PS99). This age range is also indicated from ISAAC data presented in Brandl et al. (1999). With an age of ~ 3 Myr estimated for the Wolf-Rayet stars, these findings indicate a significant age spread within the cluster of 0.3-3 Myr, with the massive stars being more evolved than the intermediate mass ($1 - 4\,M_{\odot}$) PMS stars. Such an evolution, if confirmed, strongly contradicts star and cluster formation scenarios, where the onset of hydrogen burning in massive stars terminates nearby low-mass star formation. One has to keep in mind, however, that the models for Wolf-Rayet star evolution strongly depend on the mass-loss rate and wind parameters assumed (e.g., Crowther et al. 2002), while the pre-main sequence models in the youngest stages also contain large uncertainties (Baraffe et al. 2002). The age of HD 97950 will be discussed in more detail in the context of the mass function derivation in Sec. 7.1.3.

Despite this age uncertainty, several attempts were made to derive the cluster's mass function from isochrone fitting. In all cases, a single-age isochrone with $\tau = 3$ Myr was used to derive the mass distribution on the main sequence. From optical photometry, Moffat et al. (1994) obtain a MF slope of $\Gamma = -1.4 \pm 0.6$ for $30 < M < 60\,M_{\odot}$, i.e., the 77 brightest stars. Hofmann et al. (1995) derive $\Gamma = -1.6$ in the mass range $15 < M < 50\,M_{\odot}$ from only 28 central stars resolved with speckle interferometry. While these slopes are consistent with a Salpeter MF, only the massive stellar population is traced. The limitations in resolution additionally constrain these results mostly to the outer cluster regions (except for the speckle data, where statistics are very poor). Eisenhauer et al. (1998) derive a mass function with a slope of $\Gamma = -0.73$ for $1 < M < 85\,M_{\odot}$ in the innermost $13''$ of the cluster center from their high-resolution adaptive optics photometry. In this study, crowding effects were taken into account via spatially varying incompleteness ratios, and the presumed age spread on the PMS was considered by calculating a median age of the young, intermediate mass population of 0.7 Myr from individual positions of PMS stars in the colour-magnitude diagram (with respect to PMS isochrones between 0.3 and 1 Myr (PS99)). Although these authors give strong arguments for a younger main-sequence cluster age of only 1-2 Myr, they use a 3 Myr Geneva isochrone to derive the MF at the high-mass end. Most recently, Sagar et al. (2001) confirm this slope with $\Gamma = -0.84$, however from ill-resolved $UBVRI$ data (FWHM between $1''$ and $2''$), such that, again, the innermost cluster region could not be traced. Despite these uncertainties in previous studies, high-resolution VRI HST/PC data (FWHM $< 0\farcs1$) yield a similarly flat slope of $\Gamma = -0.7 \pm 0.1$ using a compound isochrone for the MS and PMS population of age 1 Myr (Grebel et al., in prep.).

We will use the current best estimate on the physical cluster parameters such as age, metallicity and distance, to derive mass functions and possible radial variations in the MF from VLT/ISAAC near-infrared data (see also Brandl et al. 1999) obtained under excellent seeing conditions (FWHM $< 0\farcs4$). Although seeing-limited, these data allow us to penetrate down to $R \sim 7''$ into the cluster center. The crowding losses unavoidable at the low-mass end will be estimated with thorough incompleteness testing, and radially varying incompleteness fractions will be taken into account. This data set contains the deepest currently available photometry of HD 97950, allowing to observe cluster members down to masses of $\sim 0.1\,M_{\odot}$, well into the subsolar regime.

Chapter 3

Adaptive Optics Observations and Technical Analysis

In this chapter, the adaptive optics data obtained with the Gemini North AO system Hokupa'a and the VLT AO system NAOS/CONICA will be introduced. A detailed technical analysis has been performed on both data sets to evaluate the achievements and limitations of ground-based, diffraction limited observations on crowding-limited stellar fields. For this evaluation a thorough comparison is carried out between these ground-based observations and HST/NICMOS space-based observations of the Arches cluster.

First, the Gemini/Hokupa'a observations along with the performed technical analysis will be presented in Sec. 3.2. Afterwards, the more recent NAOS/CONICA data set with significantly better AO performance is compared to the Hokupa'a as well as the NICMOS data, showing the accomplishments of AO with new intermediate-order correcting systems.

A brief introduction to adaptive optics observations and the essential parameters determining the resultant performance will be given prior to the analysis.

The analysis of the Gemini/Hokupa'a data, including the comparison with HST/NICMOS, photometric results and the mass function derivation are published in Stolte et al. (2002). The results of the NAOS/CONICA crowded field study can be found in ESO Report Doc. No. VLT-TRE-ESO-14200-2971.

3.1 Introduction to Adaptive Optics

3.1.1 Characterisation of atmospheric perturbations

Each ground-based observation at a large telescope suffers from the turbulence in the Earth's atmosphere. Depending on the size of the primary mirror, a point-source image will be blurred either by diffraction or by atmospheric fluctuations, usually described as seeing. The resolution, determined as the distance from the central maximum of an Airy pattern to the first minimum in the diffraction-limited case, and as the FWHM of the point-spread function (PSF) in the seeing-limited case, is given by

$$\beta = 1.22\ \lambda/D \qquad \text{diffraction-limited} \tag{3.1}$$

$$\beta\ \approx\ \lambda/r_0 \qquad \text{seeing-limited} \tag{3.2}$$

where λ is the observing wavelength, D the diameter of the primary mirror, and r_0 the scale of the dominating atmospheric turbulence at a given wavelength λ, called the Fried parameter. The

diffraction limit of a single VLT 8m mirror is 39 milliarcseconds (mas) (0.″04) at J-band wavelengths, 55 mas (0.″05) in H, and 69 mas in K (0.″07). With typical seeing values of $\beta \approx 0.''5 - 1''$, one order of magnitude larger than the diffraction limit, the resolution of an 8m class telescope is entirely dominated by atmospheric turbulence. Although the larger collecting area of increasingly larger telescopes allows to enhance the signal-to-noise ratio and thus the detectability of faint targets, the true resolving power cannot be exploited in the presence of turbulence.

In order to overcome this severe limitation, adaptive optics systems have been built to compensate the wave-front fluctuations in real time. An adaptive optics (AO) system consists of a wavefront sensor (WFS), which traces the slopes on the incoming wavefront of a reference source, and, operating in closed-loop, feeds back the measured distortions to a deformable mirror in real time. The deformable mirror is attached to a system of equally spaced correction elements or piezoelectric actuators. The individual movements of these actuators correspond to the measured wavefront distortions and shape the deformable mirror in order to counteract the perturbations in the incoming wavefront. Ideally, a clean wavefront finally reaches the detector surface.

In practice, the performance of an AO system is limited by the number of wavefront measurements provided by the wavefront sensor, the number and spacing of actuators on the deformable mirror available to correct the wavefront, the feedback time of the wavefront sensor limiting the frequency up to which corrections are possible, and the photon noise depending on the brightness of the reference source. In the case of NAOS-CONICA, a Shack-Hartmann wavefront sensor is used. The Shack-Hartmann device consists of a lenslet array projecting the image of the reference source into multiple images on the WFS detector. Due to the atmospheric perturbations of the wavefront, each image will be slightly distorted and shifted within its sub-pupil. From these shifts, the wavefront may either be corrected independently in each sub-aperture, in this case corresponding to one actuator (zonal correction), or the combined measurements in all sub-pupils are used to reconstruct the wavefront (modal correction). In the latter case, the wavefront perturbations are represented in the form of sinusoidal polynomials (e.g., Zernike polynomials), as in standard optics. The first modes of the Zernike polynomials correspond to defocus, tip and tilt, i.e. the defocussing of the image on the image plane, and its vertical and horizontal motion. Higher order modes are known as coma, astigmatism or spherical aberration in optical systems. Ideally, the number of modes that have to be corrected to reach a residual wavefront error below 1 radian, which allows to achieve diffraction-limited resolution, is approximately given by (Roddier 1999, Tokovinin 2001[1])

$$J \approx 0.24 \left(\frac{D}{r_0}\right)^{1.92} \tag{3.3}$$

For $D = 8$ m, $r_0 \approx 0.5$ m at $\lambda = 1.75\,\mu$m and $r_0 \approx 0.1$ m at $\lambda = 0.5\,\mu$m, this would result in $J \approx 60$ modes ideally corrected at K-band wavelength, and $J \approx 1000$ modes in the visual! As the number of actuators is limited by the size of the DM, and the mathematical solution of the system of polynomials by the number of sub-apertures used to trace the wavefront, this is not possible in current systems. In practice, on the order of 15 modes can be corrected in intermediate order systems such as NAOS-CONICA (185 actuators). For higher spatial frequencies, the error of the derived wavefront solution due to the limited number of actuators, response time, etc., becomes larger than the residual wavefront error.

Atmospheric turbulence can be described using a few characteristic parameters, which influence the performance of the AO system and cause the image distortions. The characteristic scale is given by the scale length of the turbulence, r_0, and the timescale within which turbulence profiles change, τ_0. When a wavefront passes through turbulent layers with alternating temperature and density, the wavefront phase will be perturbed, while the optical path length is close to achromatic due to the low dispersion power of air. The phase variations imposed on a wavefront are given by the atmospheric

[1] Andrei Tokovinin's AO tutorial can be found at http://www.ctio.noao.edu/ãtokovin/tutorial/

structure function,

$$D_\phi(\vec{r}) = \langle(\phi(\vec{x}+\vec{r}) - \phi(\vec{x}))^2\rangle = \sigma^2_{turb} \tag{3.4}$$

where $\phi(\vec{x}) = \frac{2\pi}{\lambda} l(\vec{x})$ is the wavefront phase and $l(\vec{x})$ the optical path length. One simple model to describe the phase variation due to atmospheric turbulence is the Kolmogorov model, where the structure function writes

$$D_\phi(\vec{r}) = 6.88 \left(\frac{r}{r_0}\right)^{5/3} \tag{3.5}$$

The characteristic parameter r_0, the Fried parameter or coherence radius, sets the scale for wavefront perturbations projected to the ground layer, $h = 0$. With $D_\phi \sim \phi^2 \sim 1/\lambda^2$, we obtain the wavelength dependence of the coherence length, $r_0 \sim \lambda^{6/5}$. For adaptive optics, this relation is critical as it sets the spatial scale over which variations have to be corrected. Analysis of the theoretical prescription of the point-spread function allows to relate r_0 to the FWHM of the PSF (Roddier 1999), the classical seeing β, as $\beta = 0.98\lambda/r_0 \approx \lambda/r_0$, where the projected scale length r_0 at $h = 0$ replaces the telescope aperture for a Gaussian PSF instead of an Airy function, as given in eq. 3.2. The dependence of r_0 on λ implies that the seeing varies with wavelength as $\beta \sim \lambda/\lambda^{6/5} \sim \lambda^{-1/5}$. The wavelength dependencies of both r_0 and β have to be taken into account when wavefront distortion effects are estimated.

At a seeing of $0\farcs8$ in the visual typical for Paranal observatory, the dominating ground-layer variation scale length at visual wavelength $\lambda = 0.5\mu$m is $r_0 = 0.13$ m, while at infrared wavelength, e.g. K-band, $\lambda = 2.2\mu$m $r_0 = 0.77$ m. At a given wavelength, the structure function will saturate at scales much larger than r_0, while at scales much smaller than r_0, the distortions are small compared to the wavelength of the observation. Consequently, r_0 sets the scale for the corrections that have to be applied to the wavefront. The actuator spacing on the DM has to be chosen such that the spacing is on the order of r_0 when projected onto the primary mirror area (remember that r_0 represents the scale length on the ground layer). This immediately shows the problems faced when correcting at short wavelengths: The smaller the dominant spatial scale of the perturbation, the finer the grid required to measure and correct for wavefront distortions. In practice, this determines the number of actuators on the deformable mirror required in an AO system, and their spatial density when projected onto the primary mirror. At maximum performance, NACO operates with 144 sensing elements or lenslets to measure the wavefront, and 185 equally spaced actuators at projected spatial distances of $d = 0.57$ m with respect to the primary mirror. This actuator spacing matches the H-band coherence length of 0.58 m for typical Paranal conditions ($\beta(V) = 0\farcs8$, $\beta(HK) \approx 0\farcs6$). With this setup, the wavefront can be corrected efficiently for H and K observations, while at shorter wavelength the performance of the system degrades. To achieve the same performance with visual observations would require to cover the VLT 8m pupil with a spacing smaller than 0.13 m or 3000 actuators. Currently, the size of the DM limits the number of actuators. To avoid this limitation, deformable secondary mirrors such as the MMT secondary are developed.

3.1.2 Characterisation of AO images

The scientific image delivered by an AO system is naturally more complex as in the seeing-limited case. The AO correction will always be limited by the number of fitted modes and the residual wavefront error, and as such is always partial.

3.1.3 Strehl ratio

For large telescopes, $D \gg r_0$, the point-spread function will be composed of a diffraction-limited core with flux F_{core} and a seeing-limited halo with residual flux F_{halo}. The performance on the final image is described by the Strehl ratio, the ratio of the observed normalised peak flux to the theoretically

expected normalised peak flux of a diffraction limited image,

$$S = \frac{F_{peak,obs}/F_{total,obs}}{F_{peak,theo}/F_{total,theo}} \tag{3.6}$$

Due to the fact that the wavefront can only be corrected down to a certain scale, r_{min}, below which the correction will be dominated by the residual wavefront error, the Fourier transform of the point-spread function, the optical transfer function of the system, will not be zero at scales $r < r_{min}$, but will tend to the limit

$$S^* = e^{-\langle\epsilon^2\rangle}, \tag{3.7}$$

a quantity called the *coherent energy*. $\langle\epsilon^2\rangle$ is the residual phase error, which is related to the telescope diameter D and the coherence length via $\langle\epsilon^2\rangle = \Delta_J(D/r_0)^{5/3} \sim (D\beta/\lambda)^{5/3}$, where the constant of proportionality Δ_J depends on the number of corrected modes. This asymptotic limit of the optical transfer function represents the fraction of the flux corrected by the AO system, reflecting the quality of the correction under given observing conditions. In intermediate- or high-order systems, the AO point-source image will be a compound of the (≈gaussian) seeing-limited PSF, PSF_{seeing}, called the *seeing halo*, and the diffraction limited core, PSF_{diff}. The shape of the resultant PSF can be represented as the sum of these two contributions

$$PSF_{AO}(\vec{r}) = S^* \cdot PSF_{diff}(\vec{r}) + (1 - S^*) \cdot PSF_{seeing}(\vec{r}) \tag{3.8}$$

where $\vec{r}$ is the radial distance from the center of the PSF. The total flux of a point source is then given by

$$F_{total} = F_{core} + F_{halo} = S^* \cdot F_{total} + (1 - S^*) \cdot F_{total} \tag{3.9}$$

and correspondingly for each circular aperture with radius r around the source. In particular, the flux in the peak ($\vec{r} = 0$) used above to determine the Strehl ratio will also be the sum of the peak flux from the diffraction limited core and the seeing limited halo. In the high-Strehl case ($S \gtrsim 20\%$), the peak flux will be dominated by the diffraction limited core with a negligible halo contribution, and the coherent energy will represent the Strehl ratio. At low Strehl ratios of only a few percent, as will be shown in the case of the Gemini data, this approximation is not valid anymore. In the low-Strehl case, a large fraction of the central peak flux is contributed by the seeing halo. Due to the low performance, the FWHM of the PSF widens, and the flux actually contained within the FWHM radius is much larger than estimated by the Strehl ratio. These effects will be discussed quantitatively when analysing the Gemini/Hokupa'a data set.

In order to demonstrate the effect of wavelength on the achieveable correction, we can study the coherent energy more closely. If S^* is known at a certain wavelength λ_1 for a given telescope with diameter D and seeing β, S^* may be calculated for the same system at any other wavelength as follows.

$$S^* = e^{-(D\beta/\lambda)^{5/3}\Delta_J} = e^{-c\lambda^{-2}} \tag{3.10}$$

where $c = \Delta_J(D\beta_0)^{5/3}$, with $\beta_0 = \lambda^{1/5}\beta$ as $\beta \sim \lambda^{-1/5}$, is constant for the given observational conditions. We can determine this constant from the known coherent energy S_1^* at wavelength λ_1 via

$$c = -\ln S_1^* \lambda_1^2 \tag{3.11}$$

The coherent energy S_2^* at wavelength λ_2 becomes

$$S_2^* = e^{-c\lambda_2^{-2}} = e^{\ln S_1^* (\lambda_1/\lambda_2)^2} \tag{3.12}$$

and the relative change in S^* can be written as

$$\begin{aligned} \frac{S_1^*}{S_2^*} &= \frac{e^{-c\lambda_1^{-2}}}{e^{-c\lambda_2^{-2}}} \\ &= e^{-c(\lambda_1^{-2}-\lambda_2^{-2})} \\ &= e^{\ln S_1^* \lambda_1^2(\lambda_1^{-2}-\lambda_2^{-2})} \\ &= e^{\ln S_1^*(1-(\lambda_1/\lambda_2)^2)} \end{aligned} \tag{3.13}$$

Assuming for demonstration purposes that the coherent energy S^* represents the Strehl perfectly, and given an excellent Strehl ratio of 0.5 (50%) at K-band wavelength, 2.2μm, we obtain a decrease in Strehl to J at 1.25μm by a factor of 4, resulting in a degraded Strehl ratio of 12 %. While this is still acceptable, we have to keep in mind that Strehl ratios as high as 50 % are very hard to reach even at K, such that with average performance the Strehl in J will be only a few percent. When considering even shorter wavelengths in the visual regime, $\lambda_2 = 0.5\mu$m, the quadratic dependence on the wavelength ratio in the exponent of the exponential function causes the coherent energy to decrease by a factor of $3{\cdot}10^5$ to formal values below one promille. This strong wavelength dependence of the residual wavefront error makes correction at visual wavelength very hard and requires significantly more complex systems. In addition to the fact that observations of young star forming regions - obscured in native material causing high foreground extinctions - are facilitated at infrared wavelength, the resolving power of AO systems can currently only be exploited in the NIR regime. In case of the densest star clusters observed in the Milky Way and in near-by galaxies, this spatial resolution allows to penetrate far into the dense cluster centers with ground-based observations.

3.1.4 Isoplanatic Angle

Images obtained with AO correction are almost diffraction limited. However, the correction is only ideal at the position of the reference source. The science target of interest may be offset from this position by some angular distance θ. At large angular distances, the atmospheric turbulence pattern will be decorrelated and the reference source will not yield the correction for the science target. This effect is called anisoplanatism.

The isoplanatic patch is defined as the radial area around the reference source within which the residual wavefront error due to anisoplanatism remains smaller than one radian. It is known from standard optics that a residual wavefront error less than one radian delivers diffraction limited images. This implies that, for a given number J of corrected low-order modes, the residual wavefront error of the *uncorrected* high-order modes, $\langle\epsilon^2\rangle = \Delta_J(D/r_0)^{5/3} \sim D^{5/3}/\lambda^2$, dominates the remaining wavefront distortion within the isoplanatic patch. This residual distortion was assumed above to be below one radian in the case of a reasonable AO correction allowing to obtain diffraction limited images (cf. eq. 3.3). Outside of the isoplanatic patch, i.e. at radial distances from the reference source larger than the isoplanatic angle, the mean-square error of the compensated wavefront increases to values larger than one radian, and will thus dominate the wavefront residuals. With increasing distance from the guide star, the compensation quality will decrease, causing the wavefront to degrade. In the following, the Kolmogorov atmosphere model is used to estimate the isoplanatic angle in dependence of the imaging wavelength and the characteristic turbulence altitude. Note that the assumption of a characteristic altitude instead of an atmospheric profile is a simplistic approach to demonstrate the wavelength dependence of the isoplanatic angle. For this reason, this approach will be refered to as the "simplistic model".

From the Kolmogorov structure function, a crude estimate on the isoplanatic angle can be derived. The dependence on spatial distance in the structure function can be expressed in angular distance using

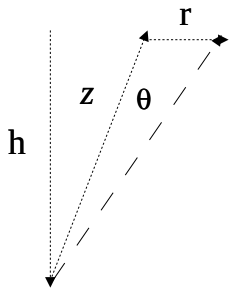

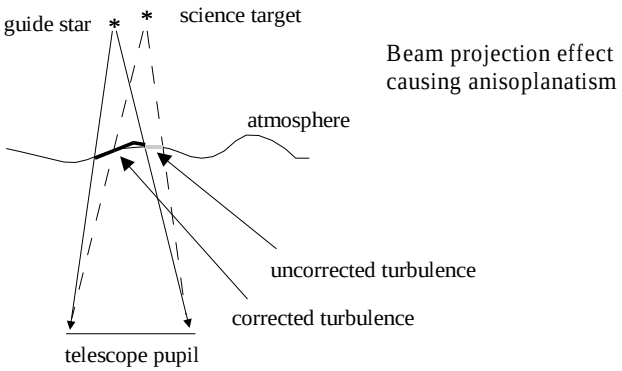

$$r \approx \frac{h\theta}{\cos z} \tag{3.14}$$

where h is the height of the atmospheric turbulence layer, z the zenith angle, and θ the angular distance between two points, e.g. the reference source and the science object. Inserting eq. 3.14 into eq. 3.5, the structure function becomes

$$D_\phi(\theta) = 6.88 \left(\frac{h\theta}{r_0 \cos z} \right)^{5/3} \tag{3.15}$$

By definition, the structure function describes the residual wavefront variation, $D_\phi = \sigma^2$. Solving the above equation for a residual wavefront error smaller than 1 radian, $D_\phi(\theta) \leq 1$ srd^2, yields an estimate for the "allowed" angular distance before the wavefront degrades, the isoplanatic angle θ_0

$$\theta_0 = 0.314 \frac{r_0 \cos z}{\bar{h}} \tag{3.16}$$

Here, the height of a single layer, h, has been replaced by a mean height, $\bar{h}$, constructed from the measured turbulence profile. This height does not represent a specific atmospheric layer, but serves as a theoretical average (calculated from the assumed turbulence profile of the atmosphere, see Roddier (1999) for details) to obtain a rough estimate on the isoplanatic patch size. Re-inserting θ_0 into eq. 3.15, the residual error due to anisoplanatism for any angular distance θ from the reference source simply becomes

$$\sigma^2_{aniso} = (\theta/\theta_0)^{5/3} \tag{3.17}$$

Remembering that the coherent energy is given by $S^* = e^{-\sigma^2}$ and approximately corresponds to the Strehl ratio yields an estimate for the degradation in Strehl ratio with distance from the reference source due to anisoplanatism alone (all other degradation effects neglected)

$$S \approx S^* = e^{-(\theta/\theta_0)^{5/3}} \tag{3.18}$$

At zenith, $z = 0$, for typical Paranal seeing of $\beta(Vis) = 0\farcs8$, and a mean turbulence altitude of $\bar{h} = 3$ km theoretically estimated from a typical turbulence profile (Flicker & Rigaut 2001), an isoplanatic patch size of $17''$ can be reached in K ($r_0 = 0.77$ m), decreasing to $13''$ in H ($r_0 = 0.58$ m) and $8''$ in J ($r_0 = 0.39$ m). Moving on to visible wavelength, the corresponding isoplanatic patch diminishes to $\approx 3''$ in V ($r_0 = 0.13$ m). Again, the advantage of long-wavelength observations is clearly demonstrated.

If the reference source is positioned in the center of the NACO field of the $27'' \times 27''$ camera (optimised for JHK observations and used to observe the Arches cluster, see Sec. 3.4), the above parameters cause a theoretical degradation in the Strehl ratio from center to edge of the CONICA field, $\theta = 13\farcs5$, by a factor of 2 in K, 3 in H, and 9 in J. Note, however, that these estimates are strongly dependent on the conditions assumed. If the seeing worsens, r_0 decreases, causing a much stronger degradation in the form of a decreased isoplanatic patch size and Strehl ratio over the desired field of view. From the above equations we see that the simple-minded assumption that adaptive optics liberates astronomers from the need of good seeing conditions is not true. While observations where the science target serves as the reference source may yield acceptable results under moderate conditions, observations exploiting the entire field of view are still dependent on good or - in the case of shorter wavelength observations - even excellent seeing conditions.

We have used the rough estimates above to demonstrate the problems faced when correcting at short wavelengths. The above model is, however, a very simplistic view assuming that the same turbulence layers affect both the seeing and the isoplanatic patch, i.e. a direct dependence between β and θ_0. In reality, the seeing β and thus the measured value of the coherence length r_0 is mostly dominated by atmospheric perturbations close to the ground ($h \approx 1$ km). The anisoplanatism, being a beam projection effect, is mainly determined by high-altitude turbulence ($h \approx 10$ km). This means that the seeing and the isoplanatic patch size are not correlated in a simple manner. The atmosphere is a complex, largely unpredictable system, and our experience shows that the probability for stable atmospheric conditions yielding good AO correction with large isoplanatic angles is enhanced under excellent seeing conditions.

Typical measured values of the isoplanatic angle range from $0\farcs5$ to $3''$ at visual wavelengths. In cases where the isoplanatic angle is known at any given wavelength λ no assumption of the relation between θ_0 and β has to be made. θ_0 may then be scaled to the imaging wavelength via $\theta_0(\lambda_i) = \theta_0(\lambda_{ref}) \cdot (\lambda_i/\lambda_{ref})^{6/5}$, and inserted directly into eq. 3.18 to obtain the degradation in Strehl over the field. Note that the approximation $r_0 = \lambda/\beta$ yields an isoplanatic angle of $2\farcs8$ at visual wavelength in the case of $\beta = 0\farcs8$, which corresponds to excellent conditions. The expected changes in Strehl over the CONICA field for this "ideal case" and the "worst case" of $\theta_0 = 0\farcs5$ are given along with one intermediate value for typical Paranal conditions in Tab. 3.1.

3.2 Gemini/Hokupa'a

3.2.1 Observations

H and K' images of the Arches cluster center were obtained in the course of the Gemini science demonstration at the Gemini North 8m telescope located on Mauna Kea, Hawai'i, at an altitude of 4200 m above sea level.
Gemini is an alt-azimuth-mounted telescope with a monolithic primary mirror and small secondary mirror optimised for IR observations. The telescope is always used in Cassegrain configuration with instruments occupying either the upward looking Cassegrain port or one of three sideward facing ports. The University of Hawai'i adaptive optics (AO) system Hokupa'a is a 35 element curvature sensing AO system (Graves et al. 2000), which typically delivers Strehl ratios between 5 % and 25 % in the K-band.

Hokupa'a is operated with the near-infrared camera QUIRC (Hodapp et al. 1996), equipped with a 1024×1024 pixel HgCdTe array. The plate scale is 19.98 milliarcseconds per pixel, yielding a field of view (FOV) of $20\farcs2$. The images are shown in Fig. 3.1, along with the HST/NICMOS images used for calibration.

The observations were carried out between July 3 and 30, 2000. 12 individual 60 s exposures, dithered in a 4 position pattern with an offset of 16 pixels ($0\farcs32$) between subsequent frames, were coadded to an H-band image with a total integration time of 720 s. In K', the set of 34 dithered 30 s

Table 3.1: Variations in Strehl ratio and isoplanatic angle with wavelength.
Changes were calculated using the wavelength dependence $\theta_0 \sim \lambda^{6/5}$. In the first model, a typical seeing of $\beta(Vis) = 0\farcs8$ is assumed and $r_0 = \lambda/\beta$ (simplistic approach). A low and intermediate value for θ_0 is included for comparison. The changes in coherent energy ($\approx$ Strehl ratio) due to anisoplanatism alone are for a distance of $\theta = 13\farcs5$, corresponding to the half-diameter of the CONICA S27 camera field of view. The coherent energy at the center of the field, $\theta = 0$, corresponds to a Strehl of 100%.

	K	H	J	V
	2.2μm	1.75μm	1.25μm	0.5μm
scaling factor $(\lambda_i/\lambda_V)^{6/5}$	5.9	4.5	3.0	1
simplistic model $r_0 = \lambda/\beta$ $\beta_V = 0\farcs8$				
$\beta_i = \beta_V\ (\lambda_i/\lambda_V)^{-1/5}$ [″]	0.59	0.62	0.67	0.8
$r_{0,i} = r_{0,V}\ (\lambda_i/\lambda_V)^{6/5}$ [m]	0.77	0.58	0.39	0.13
$\theta_{0,i} = \theta_{0,V}\ (\lambda_i/\lambda_V)^{6/5}$ [″]	16.6	12.6	8.4	2.8
$S^*(\theta = 13\farcs5)$	0.5	0.32	0.11	$1 \cdot 10^{-6}$
intermediate $\theta_{0,V} = 1.5''$ (assumed)				
$\theta_{0,i} = \theta_{0,V}\ (\lambda_i/\lambda_V)^{6/5}$ [″]	8.8	6.7	4.5	1.5
$S^*(\theta = 13\farcs5)$	0.13	0.04	$2 \cdot 10^{-3}$	0
minimum $\theta_0 = 0.5''$ (worst case assumed)				
$\theta_{0,i} = \theta_{0,V}\ (\lambda_i/\lambda_V)^{6/5}$ [″]	2.9	2.2	1.5	0.5
$S^*(\theta = 13\farcs5)$	$2 \cdot 10^{-6}$	10^{-9}	0	0

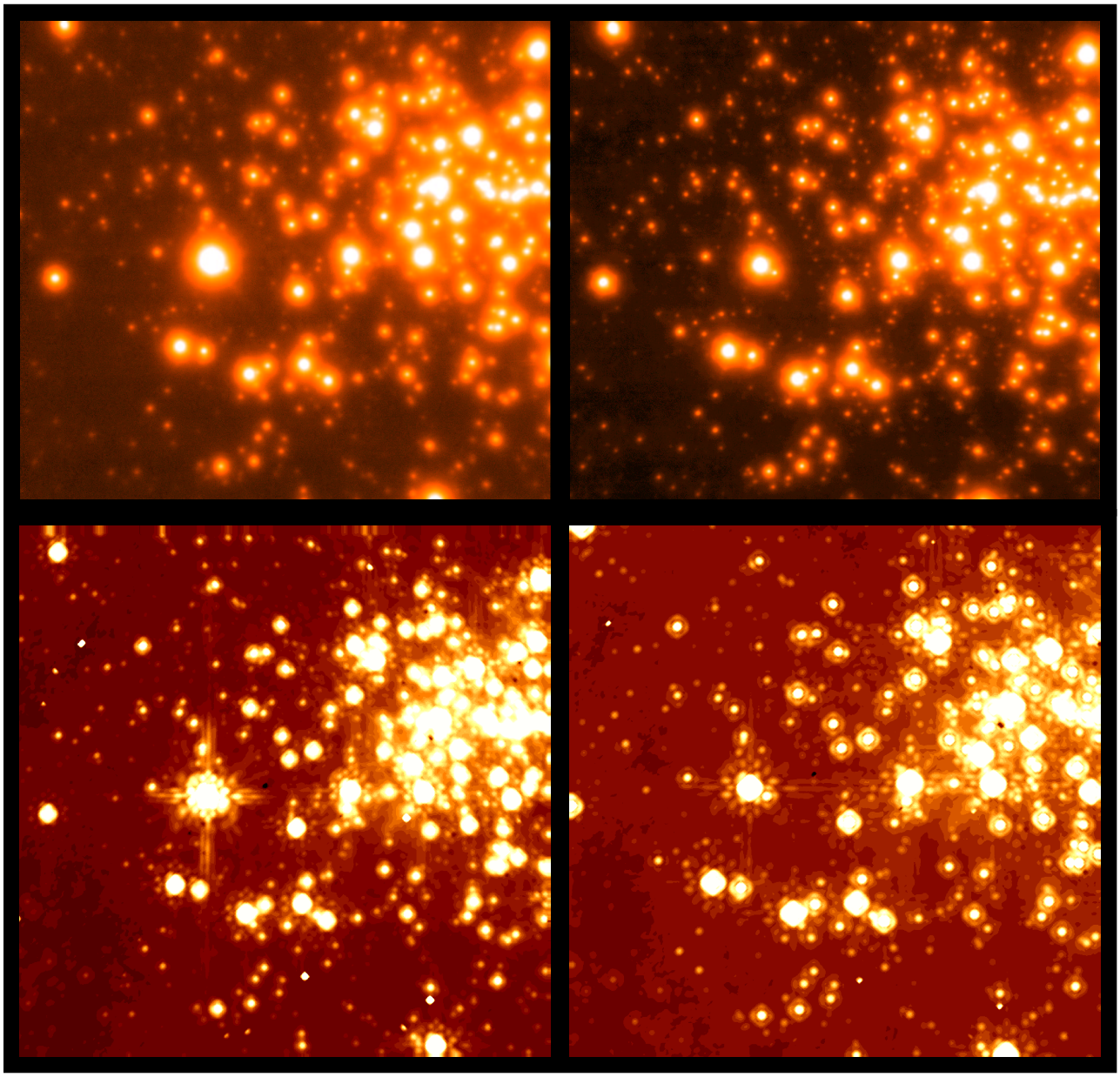

Figure 3.1: Gemini/Hokupa'a and HST/NICMOS images of the Arches cluster center.
Upper panels: Gemini/Hokupa'a H (left) and K' (right) images, $20''\times 20''$(0.8 pc $\times$ 0.8 pc) with a spatial resolution of less than $0''.2$. North is up and East is to the right. Lower panels: HST/NICMOS F160W and F205W images from Figer et al. (1999), geometrically transformed to the Gemini FOV.

Table 3.2: Gemini/Hokupa'a and HST/NICMOS observations

Date	Filter	single exp.	n_{exp}	exp. total	det. limit	σ_{back}	resolution	diffract. limit
				Gemini				
05/07/2000	H	1 s	3	3 s	18.5 mag	7.74	0.″17	0.″05
05/07/2000	H	60 s	12	720 s	21 mag	0.19	0.″20	0.″05
30/07/2000	K′	1 s	16	16 s	17.5 mag	3.73	0.″12	0.″07
09/07/2000	K′	30 s	34	1020 s	20 mag	0.22	0.″13	0.″07
				HST				
14/09/1997	F160W			256 s	21 mag	0.04	0.″18	0.″17
14/09/1997	F205W			256 s	20 mag	0.15	0.″22	0.″21

exposures obtained under the best observing conditions was coadded to yield a total exposure time of 1020 s. The full width at half maximum (FWHM) of the point spread function (PSF) was 9.5 pixels (0.″19) in H and 6.8 pixels (0.″135) in K'. The observations were carried out at an airmass of 1.5, the lowest airmass at which the Arches cluster with $\alpha = 17^{\rm h}45^{\rm m}50^{\rm s}$ and $\delta = -28°49'28''$ can be observed from Hawai'i.

The H-band data were oversampled, and 2×2 binning was applied to improve the effective signal-to-noise ratio per resolution element[2]. A combination of long and short exposures was used to increase the dynamic range. For the short exposures, 3 frames with 1 s exposure time were coadded in H, and 16 1s frames in K'. See Table 3.2 for the observational details. In the long exposures, the limiting magnitudes were about 21 mag in H and 20 mag in K'. Note that the completeness limit in the crowded regions was significantly lower. The procedure used for completeness correction will be described in detail in section 3.2.1.6.

3.2.1.1 Data reduction

The data reduction was carried out by the Gemini data reduction team, F. Rigaut, T. Davidge, R. Blum, and A. Cotera. The procedure as outlined in the science demonstration report[3] was as follows: Sky images, obtained after the short observation period when the Galactic Center was in culmination, were averaged using median clipping for star rejection, and then subtracted from the individual images. The frames were then flatfielded and corrected for bad pixels and cosmic ray hits. After inspecting the individual frames with respect to signal-to-noise ratio and resolution, and background adjustment, the images with sufficient quality were combined using sigma clipped averaging. The final images were scaled to counts per second. For the analysis presented in this paper, this set of images reduced by the Gemini reduction team has been used.

[2]During the course of the analysis of the NAOS/CONICA data, we realised that oversampling might improve PSF fitting. Unfortunately, this was not known at the time of the Hokupa'a data reduction and analysis.

[3]The description of the Galactic Center data set can be found at
http://www.gemini.edu/gallery/observing/release_doc/manual.html,
and the Gemini North science demonstration data are publicly available at
http://www.gemini.edu/sciops/data/dataSV.html.

3.2.1.2 Photometry

The photometry was performed using the IRAF[4] (Tody 1993) DAOPHOT implementation (Stetson 1987). Due to the wavelength dependence of the adaptive optics correction and anisoplanatism over the field, the H and K' data have been treated differently for PSF fitting. While in H the PSF radius increases significantly with distance from the guide star, with a radially varying FWHM in the range of $0\farcs18$ to $0\farcs23$ (see the science demonstration data description), the K' PSF was nearly constant over the field ($0\farcs125$ to $0\farcs135$). This behaviour is expected from an AO system, as the isoplanatic angle θ_0 varies as $\lambda^{6/5}$, yielding a 1.4 times larger θ_0 in K' than in H, resulting in a more uniform PSF in K' across the field of view.

As obscuration due to extinction decreases with increasing wavelength, many more stars are detected in K' than in H. For comparison, the number of objects found with $K' < 20$ mag and uncertainty $\sigma_{K'} < 0.2$ mag was 1017 (1020 s effective exposure time), while for $H < 20$ mag and $\sigma_H < 0.2$ mag we detected only 391 objects (720 s effective exposure time), where in both cases visual inspection led to the conclusion that objects with photometric uncertainties below 0.2 mag were real detections. The increased stellar number density in K' leads to increased crowding effects, such that we decided to use a non-variable PSF for the K'-band data after thorough investigation of the results of a quadratically, linearly or non-varying PSF. It turns out that, due to a lack of isolated stars for the determination of the PSF variation across the field, the mean uncertainty is *lower* and the number of outliers with unacceptably large uncertainties reduced when a non-variable PSF is used. From the uncertainty-magnitude distribution, the decrease in photometric accuracy may be estimated more quantitatively. The mean uncertainty in K' of all objects above a certain threshold, which was fitted as an upper envelope polynomial to the photometric uncertainty vs. magnitude distribution (Fig. 3.2), is $<\sigma_{K'}> = 0.090 \pm 0.075$ in case of a non-variable PSF, whereas the quadratically variable PSF yields $<\sigma_{K'}> = 0.111 \pm 0.084$. The same result is achieved if no lower threshold is applied, but less pronounced, as the bulk of the stars is found at low uncertainty values, which then dominate the determination of the mean.

Thus, the 5 most isolated stars on the K' image, which were well spread out over the field, were used to derive the median averaged PSF of the long exposure. In the case of the short exposure, where due to the very short integration time faint stars are lost in the background, leaving more 'uncrowded' stars to derive the shape of the PSF, 7 isolated stars could be used. In K', the best fitting function was an elliptical Moffat-function with $\beta = 2.5$.

Due to the lower detection rate on the H-band image crowding is less severe. As strong PSF variations are observed on the H-band frame as noted above, we used the quadratically variable option of the DAOPHOT *psf* and *allstar* tasks for our H-band images, with 27 stars to determine a median averaged PSF function and residuals. The best fitting function was a Lorentz function on the binned H-band image. In both filters, the average FWHM of the data has been used as the PSF fitting radius, i.e., the kernel of the best-fitting PSF function, to derive PSF magnitudes of the stars.

The short exposures have been used to obtain photometry of the brightest stars in the field, which are saturated on the long exposures. The photometry of the long and short exposures agreed well after atmospheric extinction correction in the form of a constant offset had been applied. The saturation limit on the long exposures was 13.0 mag in H and 13.3 mag in K'. At fainter magnitudes, the photometry of both images was indiscernible within the uncertainties for the bright stars, and the better quality long exposure values were used. Furthermore, a comparison of the bright star photometries was used to estimate photometric uncertainties (see Sec. 3.2.1.6 and Tab. 3.3).

[4]IRAF is distributed by the National Optical Astronomy Observatories, which are operated by the Association of Universities for Research in Astronomy, Inc., under cooperative agreement with the National Science Foundation.

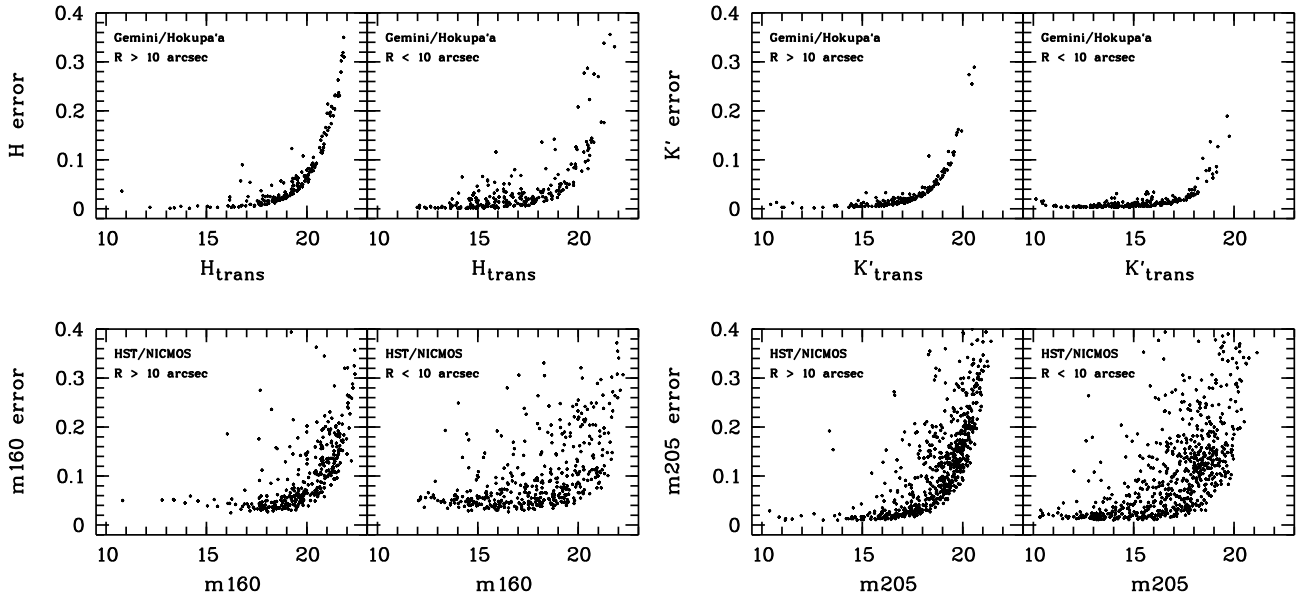

Figure 3.2: Formal DAOPHOT photometric uncertainties.
Upper panel: Gemini/Hokupa'a H and K' photometry transformed to HST/NICMOS F160W and F205W filter magnitudes, $m160$ and $m205$. Lower panel: HST/NICMOS $m160$, $m205$ photometry of the same $20'' \times 20''$ field (shown in Fig. 3.1).

3.2.1.3 Photometric Calibration

To transform instrumental into apparent magnitudes, we used the HST/NICMOS photometry of Figer et al. (1999) as local standards. The advantage of this procedure lies in the possibility to correct for remaining PSF deviations over the field, e.g., due to a change in the Strehl ratio with distance from the guide star or due to the increased background from bright star halos in the cluster center. Indeed, as will be discussed below, the spatial distribution of photometric residuals shows a mixture of these effects.

We were able to use approximately 380 stars to derive colour equations. The residuals obtained for these stars after calibration allow a detailed analysis and correction of field variations. The colour equations to transform Gemini instrumental H and K' magnitudes to F160W and F205W magnitudes, the HST/NICMOS equivalent filters for H and K broadband observations, were determined using the IRAF PHOTCAL package, yielding:

$$\begin{aligned} m160 &= H_{\rm inst} + 0.001(\pm 0.017) \cdot (H - K')_{\rm inst} - 0.028(\pm 0.031)\ {\rm mag} \\ m205 &= K'_{\rm inst} + 0.023(\pm 0.008) \cdot (H - K')_{\rm inst} - 1.481(\pm 0.016)\ {\rm mag} \end{aligned} \tag{3.19}$$

where $H_{\rm inst}$ and $K'_{\rm inst}$ are the Gemini instrumental magnitudes, and $m160$ and $m205$ correspond to magnitudes obtained with the NICMOS broadband filters F160W and F205W, respectively. After the transformation had been applied, it turned out that the residual magnitudes in the two independent fitting parameters $H - K'$ and K' still varied systematically over the field. As can be seen in Fig. 3.3, the variation is *not* a simple radial variation increasing with distance from the guide star (GS), but a mixture of displacement from the GS position (shown in the contour map in Fig. 3.3 as a cross), and the position with respect to the cluster center (marked by an asterisk) or bright stars in the field. Fortunately, the variation was well behaved in the Y-direction, and could be fitted by a fourth order polynomial. Close inspection showed that two areas on the QUIRC array showed a remaining photometric offset compared to the HST photometry. In the region $400 < X < 700$ pixels and $Y < 250$ pixels, the magnitude was underestimated by 0.1 mag. For $X > 850$ pixels and $Y > 850$ pixels, i.e., the upper right corner, the K' magnitude was overestimated by 0.25 mag (however, note that there

are only 7 stars in this region). For a discussion of these effects, see Sec. 3.2.1.4. We corrected for these offsets before deriving the Y-correction, which then showed remarkable homogeneity over the entire field. This smooth correction function is probably due to discrepancies in the dome flat field illumination versus sky exposures. The correction was then applied to transformed K' and $H-K'$ magnitudes, denoted $K'_{\rm trans}$ and $(H-K')_{\rm trans}$ from now on. The $H_{\rm trans}$ magnitude was calculated from the corrected $K'_{\rm trans}$ and $(H-K')_{\rm trans}$ values.

An additional advantage of this procedure is the independence on uncertainties in colour transformations at large reddening and non-main sequence colours, as opposed to colour transformations derived from typical main sequence standard stars. Using the HST photometry as local standards, we are naturally in equal colour and temperature regimes, allowing the direct comparison of the Gemini and HST photometry. For most parts of the paper, we remain in the HST/NICMOS system. We use the colour equations obtained in Brandner et al. (2001, hereafter B00) to transform typical main sequence colours and theoretical isochrone magnitudes into the HST/NICMOS system where indicated. This allows us to transform mainly unreddened main-sequence stars, for which the B00 colour transformations have been derived. The only exceptions are the two-colour diagram (Sec. 4.1.4) and the derivation of the extinction variation from colour gradients (Sec. 4.1.1), where the extinction law is needed to determine the reddening path. We will use the notation "$m160$" and "$m205$" as in F99 for magnitudes in the HST/NICMOS filters, and "$H_{\rm trans}$" and "$K'_{\rm trans}$" for the Gemini/Hokupa'a data calibrated to the NICMOS photometric system. HST magnitudes transformed to the ground-based 2MASS system will be denoted by $(JHK_s)_{\rm 2MASS}$ or simply JHK_s.

3.2.1.4 Discussion of the residual maps

The behaviour of the residual of the HST/NICMOS vs. Gemini magnitudes, $m_{\rm NICMOS}-m_{\rm Gemini,trans}$, can be analysed in more detail when studying the residual map and the smoothed contour plot. In (Fig. 3.3), positive (negative) residuals correspond to overestimated (underestimated) flux. From the map we denote a general tendency to overestimate the flux. The contour maps show that positive residuals are correlated with the position of bright stars on the K' image, both in the crowded cluster center as well as in the area to the lower left, where a band of bright stars is located (see Fig. 3.1). This is the area where the K' magnitudes were found to be underestimated in Sec. 3.2.1.3, and thus the flux overestimated. This suggests that the increased background due to the uncompensated seeing halos of bright stars (cf. Sec. 3.2.1.5), inherent to AO observations, causes an overestimation of the flux of bright ($K' \lesssim 13$ mag) sources. On the other hand, points with negative residuals are mainly correlated with fainter stars ($K' \gtrsim 16$ mag), suggesting that this enhanced background leads to an oversubtraction of the individually calculated background of nearby fainter stars. The result is an underestimate of the flux of companion stars in the vicinity of bright stars. The correlation of positive residuals with the position of bright stars seems to be less pronounced in the H-band image (Fig. 3.3). In H, the distance from the guide star is supposed to be more important due to the smaller size of the isoplanatic angle at shorter wavelengths and consequently more pronounced anisoplanatism. Indeed, the smoothed residual contour plot shows a symmetry in the residuals around the guide star, with close-to-zero residuals in the immediate vicinity of the guide star, where the best adaptive optics correction can be achieved. With increasing distance from the guide star, the residuals increase not only towards the bright cluster, but also to the west (left in Fig. 1) of the field, indicating that remaining distortion effects from the AO correction are mixed with the problem of the proximity to bright stars as seen in K'.

3.2.1.5 Strehl ratio

The Strehl ratio (SR) was defined as the ratio of the observed peak-to-total flux ratio to the peak-to-total flux ratio of a perfect diffraction limited optical system in eq. 3.6. This definition allows to

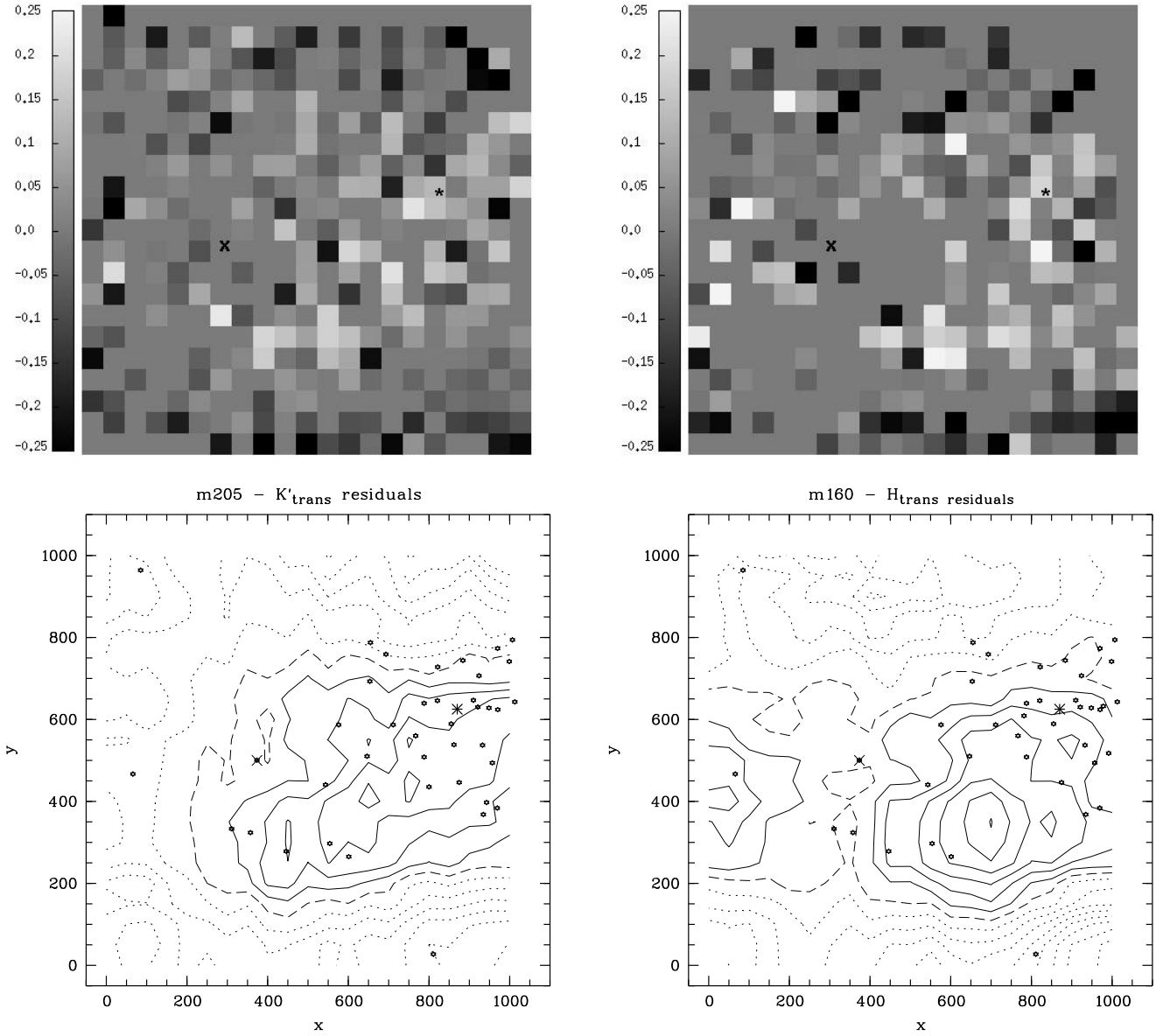

Figure 3.3: Map of residuals of NICMOS vs. Gemini photometry (orientation as in Fig. 3.1).
Left panels: $m205 - K'_{\rm trans}$, right panels: $m160 - H_{\rm trans}$
Stars have been binned into areas of 50×50 pixels, and the value displayed shows the average of all stars in each bin. Statistical fluctuations are large due to the varying number of stars in each pixel intervall, but the overall trends are clearly visible. The position of the guide star is marked by a cross, the cluster center as determined from the HST/NICMOS F205W image as an asterisk, and stars denote stars resolved in the Gemini images with magnitudes brighter than $K'_{\rm trans} = 13$ mag. The strong correlation between the position of bright stars and positive residuals reveals the tendency of PSF fitting photometry applied to AO data to overestimate the flux of bright sources, and underestimate the flux of faint sources in their vicinity (see text for discussion).

compare the quality and photometric resolution of different optical systems using a single characteristic quantity.

Diffraction limited theoretical PSFs have been calculated using the *imgen* task of the ESO data analysis package *eclipse* (Devillard 1997). The peak and total flux of several isolated stars was determined from aperture photometry, and scaled with the theoretical PSFs to obtain the Strehl ratio. The Strehl ratio on the Gemini H-band 720s exposure is found to be 2.5 % compared to $\sim 50-60$ % on the HST F160W image, and 7 % in K' (1020s) compared to $\sim 60-80$ % in the case of F205W. The low SRs measured in the Gemini science demonstration data indicate that more than 90 % of the light of a star is distributed into the resolution pattern of the AO PSF and the halo around each star induced by the natural seeing, while only a few percent of the flux expected from a diffraction limited image are truely concentrated into the PSF peak. It has turned out that these halos cause a significant limitation to the resolution and depth of the observations in a crowded field, as faint stars can be lost to the enhanced background in the vicinity of bright objects. When comparing the HST and Gemini luminosity functions (Sec. 3.3), this effect causes the main difference between both data sets.

In the case of very low Strehl ratios, the SR does not directly indicate the fraction of the flux concentrated in the FWHM area of the PSF. First of all, the PSF appears significantly widened, in case of the Gemini data by about a factor of 2 in K and 3 in H with respect to the diffraction limit of the telescope. In comparison to eq. 3.8, this means that the approximation of a dominating diffraction limited peak flux is not valid any more. In the prior simple assumption, $F(peak) = F_{diff}(peak) + F_{seeing}(peak) \approx F_{diff}(peak)$, the seeing-limited halo flux can no longer be neglected. This equation was derived from the coherent energy, the fraction of flux concentrated in the diffraction limited core, which was used as an estimate for the Strehl ratio. In the low-Strehl limit, the blurring of the image widens the FWHM, and the diffraction limited core does not stand out as depicted in the core + halo model anymore. As a consequence, the peak flux used for the Strehl calculation will not be representative for the percentage of the flux within the FWHM, i.e. the Strehl will not represent the fraction of flux found in the observed core. A much larger fraction of the source flux can be used for PSF fitting in this case, although the spatial resolution is limited by the large FWHM as compared to diffraction limited observations (cf. Tab. 3.2). The ratio of the flux in the FWHM kernel of the compensated stellar image to the total flux,

$$FR_{\rm obs} = F_{\rm FWHM}/F_{\rm total},$$

may be determined by creating curves of growth for individual stars (Stetson 1990). The larger number of nearly isolated stars found on the H-band image (used for PSF creation) allowed a reliable determination of $FR_{\rm obs}$ only in H, although many stars on the H-band image were still too influenced by neighbours to study the aperture curve of growth in detail. We were able to create well-behaved curves of growth for 7 stars. As in the PSF fitting routine, we have used the FWHM of the PSF as kernel radius and as the reference flux for the flux ratio determination. These ratios range from 0.47 to 0.58, with an average of 0.53 ± 0.05, i.e., $\sim$ 50 % of the integrated point source flux are used for PSF fitting. In addition, the variation of the flux ratio $FR_{\rm obs}$ over the field serves as an indicator of the Strehl ratio variation. If the AO correction mechanism is the dominant factor determining the concentration of the flux into the FWHM kernel, the Strehl ratio and thus $FR_{\rm obs}$ should decrease with distance form the guide star, as the seeing correction worsens. No correlation of the flux ratio with distance from the guide star is found. Though these are small number statistics, this supports the suggestion that the sensitivity variations over the field are not predominantly due to increasing distance from the guide star (Sec. 3.2.1.4).

3.2.1.6 Photometric uncertainties and incompleteness

For the incompleteness correction, artificial frames were created with randomly positioned artificial stars. Magnitudes were assigned automatically in a random way. Due to the very crowded field,

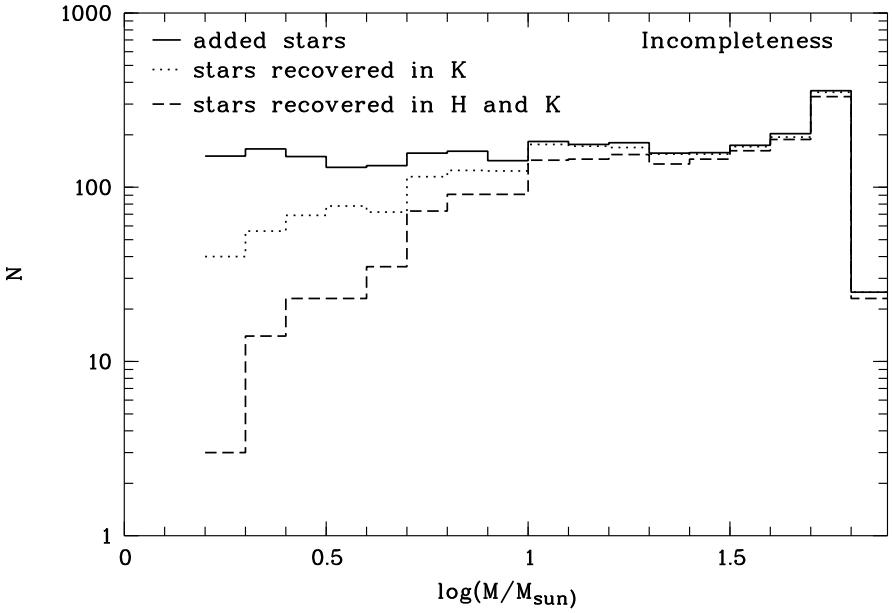

Figure 3.4: Incompleteness tests performed on the Gemini H and K' data. The plot demonstrates the necessity to include the matching between single filter observations to obtain a realistic estimate on the incompleteness, when matching of objects is needed to create colour-magnitude- and two-colour-diagrams.

only 40 stars were added to each artificial frame in order to avoid significant changes in the stellar density. A total of 100 frames was created for both the H and K' deep exposures, leading to a total of 4000 artificial stars used in the statistics. In addition to the individual incompleteness in each band, the enhanced scatter due to larger photometric uncertainties in the dense parts of the cluster was simulated. For this purpose the artificial K' stars were assigned a formal instrumental 'colour' of $(H-K') = 0.33$ mag (corresponding to 1.745 mag after photometric transformation), derived from the average observed instrumental colour of the main sequence, and via this transformed into instrumental H magnitudes. Artificial stars were inserted at the same sky positions in the H and K' frames to account for stars lost due to the matching of H and K' data. The artificial stars were calibrated using the colour equations shown in Sec. 3.2.1.3 , thus allowing to estimate the loss of stars in the mass function derivation due to the applied main sequence colour selection (see Sec. 5.1). This resulted in significantly larger corrections as compared to the individual filter recoverage without matching and colour selection. As an example, the results for the mass function calculation performed on the artificial stars are displayed in Fig. 3.4.

As the recovery rate depends strongly on the stellar density and thus radial distance from the cluster center, the incompleteness correction will be determined in dependence of the radial bin analysed when radial variations in the MF are studied (Sec. 5.1.3).

In addition to luminosity and mass function corrections, the artificial star tests were used to estimate the real photometric uncertainties by comparing inserted to recovered magnitudes of the artificial stars. The median difference between the original and the recovered magnitude of the artificial stars, $\Delta m_{\rm arti} = <m_{\rm added} - m_{\rm DAOPHOT}>$, has been used as an estimate of the real photometric uncertainty. To obtain the median uncertainty, the intervalls $0 < \Delta m_{\rm arti} < 1$ and $-1 < \Delta m_{\rm arti} < 0$ have been treated individually, and the mean of the absolute value of both median values, weighted with the number of objects in each intervall, is quoted in Tab. 3.3. The overall flux deviation, including positive and negative deviations, is close to zero for stars brighter than 20 mag ($< \pm 0.004$), and for fainter stars becomes -0.17 and -0.13 in H and K', respectively, showing a tendency to underestimate the flux of faint stars. This tendency is more serious in the cluster center, where comparably large uncertainties are already observed for magnitudes fainter than 18 mag in both pathbands.

Table 3.3: Photometric uncertainties derived from artificial star experiments (Δm_{arti}) and the comparison of short and long exposures (Δm_{sl}). The photometric uncertainties determined by DAOPHOT are given for comparison. Note that for the brightest bin, 10 - 12 mag, only the photometry of the short exposures was available. The higher starting bin in H is due to the calibration procedure of the inserted artificial stars. Magnitudes are given in the NICMOS system (F160W, F205W).

Band	mag	Δm_{arti}	Δm_{sl}	σ_{DAO}	Δm_{arti}	Δm_{sl}	σ_{DAO}	Δm_{arti}	Δm_{sl}	σ_{DAO}
		all			$R < 10''$			$R > 10''$		
H	12 - 14	0.007	0.059	0.004	0.012	0.052	0.005	0.004	-	0.002
	14 - 16	0.015	0.061	0.008	0.025	0.065	0.010	0.011	0.035	0.004
	16 - 18	0.044	0.128	0.015	0.077	0.120	0.017	0.038	0.134	0.009
	18 - 20	0.119	-	0.036	0.167	-	0.039	0.098	-	0.030
	> 20	0.264	-	0.142	0.514	-	0.142	0.265	-	0.144
K′	10 - 12	0.004	-	0.005	0.004	-	0.005	0.003	-	0.006
	12 - 14	0.008	0.042	0.005	0.011	0.048	0.005	0.007	0.028	0.005
	14 - 16	0.027	0.072	0.007	0.041	0.086	0.007	0.020	0.042	0.006
	16 - 18	0.071	0.121	0.016	0.125	0.166	0.017	0.057	0.088	0.016
	18 - 20	0.206	-	0.060	0.280	-	0.073	0.189	-	0.056
	> 20	0.411	-	0.274	0.520	-	-	0.360	-	0.274

In a second test, photometry of the bright stars in the short exposures was compared to the magnitudes of the deep exposures, yielding $\Delta m_{sl} = <m_{short} - m_{long}>$ using the same procedure as for artificial stars. Note, however, that the quality of the short exposures is much worse than the one of the long exposures due to the high background noise. Therefore, the artificial star experiments, for which only the deep exposures have been used, yield a more realistic estimate of the photometric uncertainties. The results of both tests are summarised in Table 3.3.

The resulting uncertainty is roughly a factor of 2 to 3 larger than the theoretical magnitude uncertainty σ_{DAO} determined from detector characteristics by DAOPHOT. The photometry in the cluster center shows a larger uncertainty than the photometry in the outskirts. As expected in a crowding-limited field, this also implies a reduced detection probability of faint sources in the center of the cluster.

3.2.2 HST/NICMOS data

HST/NICMOS observations have been obtained in the three broad-band filters F110W, F160W and F205W, roughly equivalent to J, H and K. The basic parameters are included in Table 3.2. A detailed description of the HST data and their reduction is given in Figer et al. (1999).

3.3 Luminosity Functions and incompleteness effects

3.3.1 Integrated luminosity function

In Fig. 3.5, we compare the Gemini with the HST luminosity function for the K'_{trans} vs. $m205$ observations. For direct comparison of the observational efficiency, no colour cut was applied, but the entire physically reasonable colour range from approximately 0 to 4 mag in $H - K'$, including reddened and foreground objects, is included in the luminosity function (LF). Therefore, these LFs are *not* the ones from which the mass functions are derived in Chapter 5. The only selection criterion that was applied is a restriction of the photometric uncertainty in both magnitude ($\sigma_{K'} < 0.2$ mag)

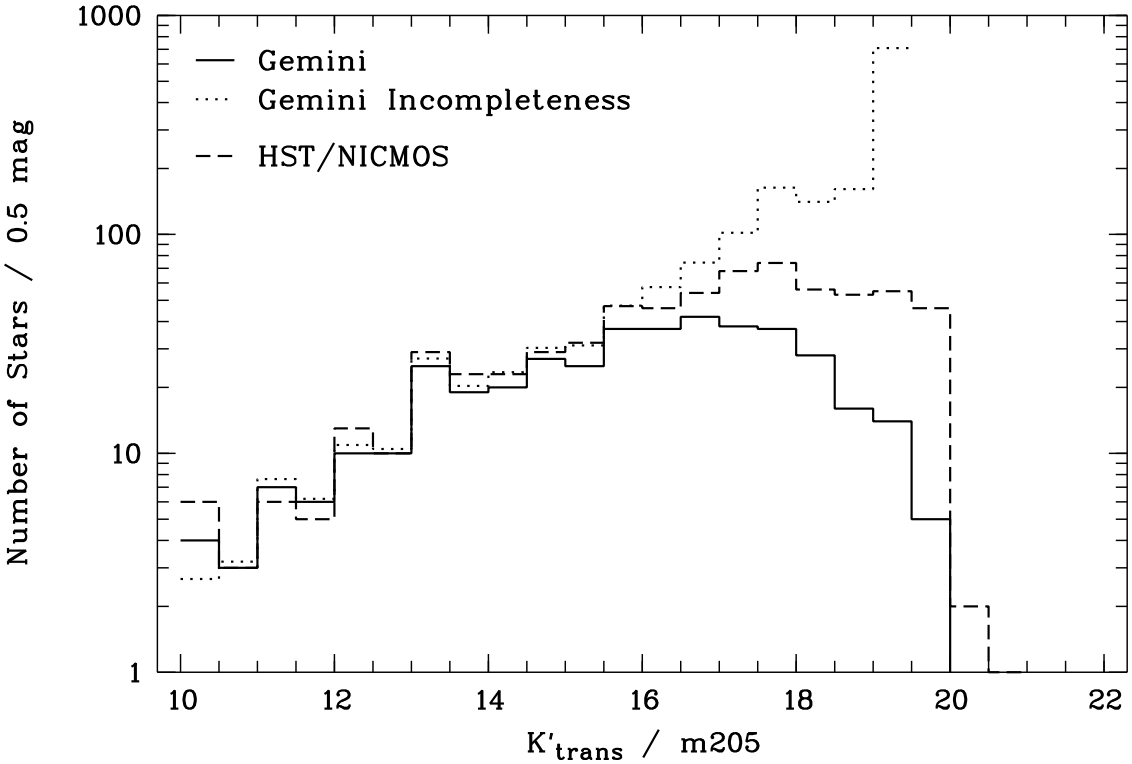

Figure 3.5: Comparison of Gemini versus HST luminosity functions.

and colour ($\sigma_{H-K'} < 0.28$ mag, corresponding to $\sigma_{K'} < 0.2$ mag and $\sigma_H < 0.2$ mag). The uncertainty selection in colour allowed us to select only those objects that have been detected with high confidence in both H and K' images in the Gemini data, and in the F160W and F205W filters in the NICMOS data, respectively. The colour-uncertainty selection on the HST data simulates the matching of H and K' detections used on the Gemini data for the selection of real objects. Thus, only objects that are detected in both H and K' have been included in the luminosity function in both data sets. This gives us some confidence that we do not pick up hot pixels, cosmic ray events or brightness knots in the Airy pattern of the NICMOS PSF (slightly variable over the NICMOS field). The area covered with Gemini has been selected from the HST photometry as displayed in Fig. 3.1.

As can be seen in Fig. 3.5, many objects are missed by Gemini in the fainter regime, though the actual limiting (i.e., cut-off) magnitudes are the same in both data sets. This is due to the fact that 50 % of the light is distributed into an extended seeing halo around each star. These halos prevent the detection of faint objects around bright sources, especially in the crowded regions. This effect is most obvious when examining the star-subtracted frames resulting from the DAOPHOT *allstar* task. In these frames the cluster center is marked by a diffuse background, enhanced by a factor of 10, or ~ 20 counts in K' and ~ 40 counts in H, above the observational background of 2 and 4 counts in the cluster vicinity, respectively. In addition to the simple crowding problem due to the stellar density affecting both data sets, the overlap of many stellar halos hinders the detection of faint stars in the Gemini data. At larger radial distances from the cluster center, more and more faint stars are detected both in the HST as well as in the Gemini data (Fig. 3.6).

The fact that the incompleteness corrected Gemini LFs follow closely the shape of the HST LFs supports the results of our incompleteness calculations, which will be used to determine the incompleteness in the mass function.

3.3.2 Radial variation of the luminosity function

Radial luminosity functions were calculated in $\Delta R = 5\ ''$ bins, using the same uncertainty selection as in Fig. 3.5 (Sec. 3.3.1). The resulting radial LFs are shown in Fig. 3.6, along with the incompleteness determined for each radial bin. In the cluster center (lowest panel), the very good match of the Gemini and HST LFs for $K'_{\rm trans} < 16$ mag reveals the comparable spatial resolution obtained in both data sets. Despite the strong crowding seen already in these bright stars, the Gemini AO data resolve the sources in the cluster center nicely. When we move on to fainter magnitudes, however, we are limited by the halos of these bright stars, as discussed above. The clear decrease below $K'_{\rm trans} = 16$ mag marks the point where stars are lost due to the enhanced background. When we move radially outwards, the limiting magnitude above which faint stars are lost shifts towards fainter magnitudes. The tendency to loose the faint tail of the magnitude distribution nevertheless remains clearly seen, though it becomes much less pronounced for $R > 10''$, where the Gemini and HST LFs resemble each other. For $R > 15''$ (upper panel) we are limited by small number statistics due to the small area in this radial bin. As it is hard to observe a well-defined LF at these radii, we will add the two upper bins when we create the radially dependent mass functions in Sec. 5.1.3.

The magnitude-dependent distribution of stars within the cluster is evident in these LFs. While bright stars are predominantly found in the cluster center, their number density strongly decreases with increasing radius. When we analyse the Gemini LFs more quantitatively, we find 25 (50) stars with $K'_{\rm trans} < 13(14)$ mag within $R < 5''$, but only 8 (23) such stars with $5 < R < 10''$, and beyond $10''$, we observe only 7 (11) such stars. The numbers for HST are comparable in the bright magnitude bins. On the other hand, the number of faint stars with $K'_{\rm trans} > 18(19)$ mag increases from 1 (0) to 14 (3) to 48 (16). As we see significantly more faint stars in the HST data, the corresponding numbers are higher, i.e. the number of stars with $m205 > 19$ mag is 0 in the innermost bin, 24 in the intermediate bin, and 81 in the outermost bin. Despite the fact that the area on the Gemini frame increases by about a factor of 3 between the inner and intermediate bin, the number of bright stars is strongly diminished beyond a few arcseconds, while the number of the faint stars increases by much more than the change in area can account for. Although for the fainter stars the effects of crowding and a real increase in the fainter population of the cluster cannot be disentangled, the decrease in the number of bright stars is a clear indication of mass segregation within the Arches cluster.

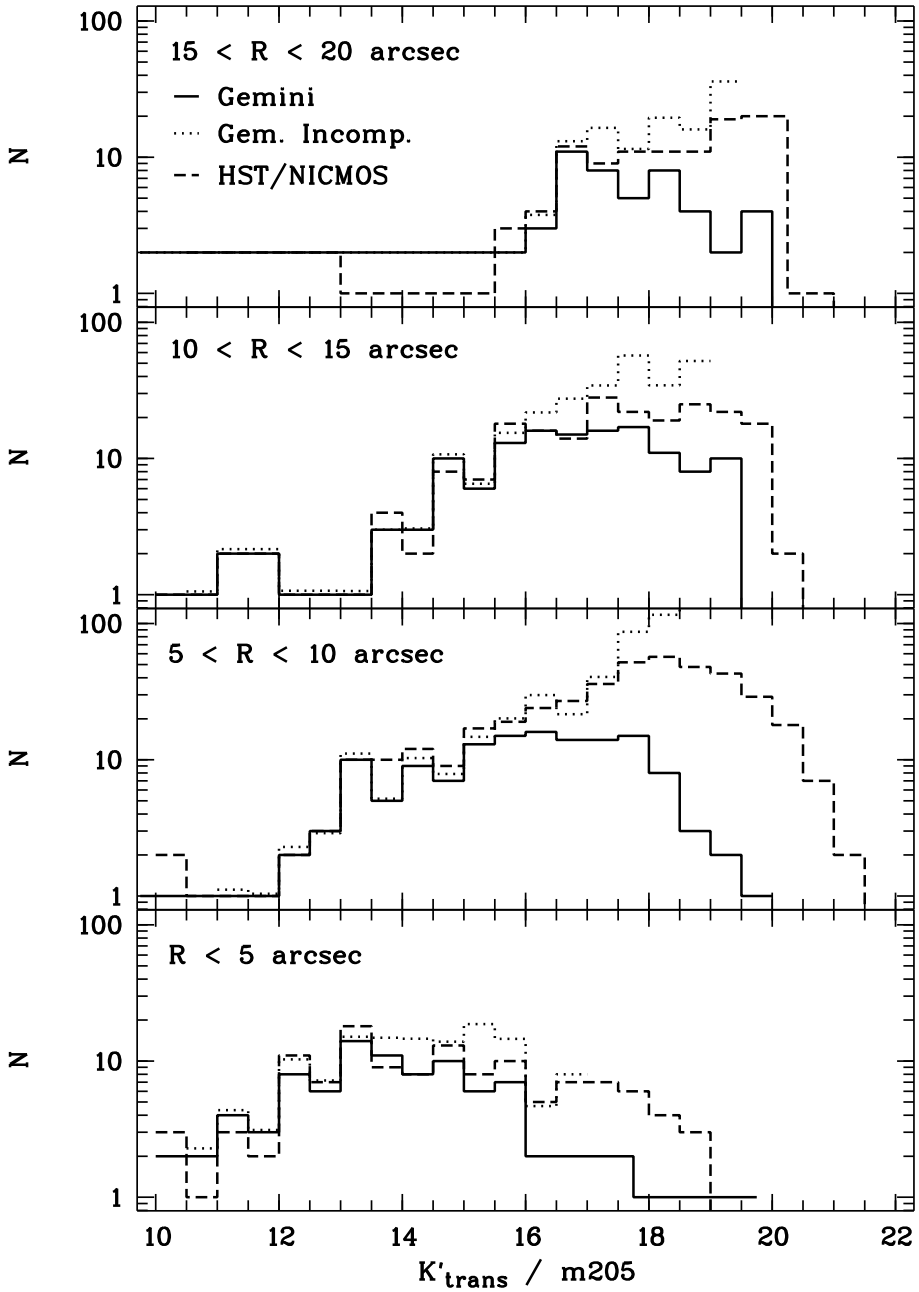

Figure 3.6: Radial variation of the luminosity function. The comparison of Gemini and HST LFs is shown together with the Gemini incompleteness calculation. The dependence of the magnitude limits on the distance to the cluster center is striking.

3.4 NAOS/CONICA

The work presented in this section was carried out at the European Southern Observatory under DGDF grant.

During Commissioning run 3 of NAOS-CONICA at the VLT 8m telescope YEPUN on Paranal, Chile, the Arches cluster was observed as a test object for NACO performance on a crowded stellar field. The Arches field was selected as commissioning target for NAOS/CONICA to allow comparison with the Gemini/Hokupa'a low-order correction data and the HST/NICMOS data set. The high spatial resolution of ~ 84 mas and moderate Strehl ratios of $14 - 20\%$ obtained with NACO allowed to conduct a comparison of crowded field performance with HST/NICMOS comparable to, but by far exceeding the analysis performed on the Gemini/Hokupa'a data presented in the previous sections. The higher Strehl ratios obtained with NACO yielded a spatial resolution better than HST/NICMOS by a factor of 2.4. As a consequence, the cluster population was resolved much more completely. The detectability of sources is discussed with respect to AO performance and observational conditions. In addition, the facilitated source finding and separation of close neighbours on the higher resolution images is revealed. The effects of image oversampling during the image combination process are discussed in detail, as this method has up to now not been shown to enhance source detectability. Furthermore, the influence of image deconvolution on source detection and photometry is discussed.

We again use luminosity functions to show the effects of enhanced resolution on a crowded stellar field, in comparison to the HST/NICMOS data, which have until now been the best resolved data of the Arches cluster. The achievements of ground-based AO on 8m class telescopes are revealed.

The mass function of the Arches cluster will be derived in Chapter 5.1 from the highest resolution photometry presented in this Chapter, and compared to the results obtained with Hokupa'a and NICMOS. With much better statistics due to the higher resolution, spatial variations in the MF slope can be analysed in more detail and with higher statistical significance. These data will be used to introduce cumulative functions in addition to MFs in order to eliminate the statistical effects caused by binning. A comparison with the expected power-law mass distributions of single-age stellar populations will be shown.

Combining all three data sets, source detection and photometric performance for low, moderate and high Strehl observations with varying spatial resolutions are studied with the goal of a deeper understanding of the adaptive optics characteristics inherent to the ground-based data sets, important for the careful scientific analysis of the mass functions in particular in the dense crowded center regions.

The previously introduced Strehl ratio, the flux ratio inside the PSF kernel, and peak flux above the background of a sample star will serve as quality parameters for a quantitative comparison. As in the case of the Gemini/Hokupa'a data, the residual distribution between the NACO and NICMOS photometries is derived. In addition, the effects of deconvolution on the photometry, and the possibility to use higher spatial resolution object lists as input to lower resolution data are discussed.

3.4.1 VLT/NAOS-CONICA observations

VLT/NAOS-CONICA data of the Arches field have been obtained during Commissioning 3 of the instrument in March/April 2002 on Paranal, Chile. As in the case of the Hokupa'a data, a combination of long and short exposures was used to increase the dynamic range, yielding photometry of all stars in the Arches field. In H-band, two data sets were taken under different observing conditions (see Tab. 3.4), 15 exposures á 30s detector integration time (DIT) under moderate seeing conditions, and 20 exposures á 30s DIT under excellent seeing. These two data sets will enter the comparison below as a "high"' (i.e. moderate on absolute scales) and "low" Strehl data set. In K_s, 15 exposures á 15s DIT were obtained under moderate conditions. For K-band observations, the seeing is lowered as compared to the visual seeing, and the AO performance does not depend as critically on the observing

Table 3.4: Summary of NACO observations. Visual wavefront sensor, reference source $V = 16^m$.

date	filter	seeing($''$)	mean	NDIT	DIT(s)	no. exp.	Strehl
long exposures							
30/03/2002	H	0.85-1.3	1.0	2	30	15	5 %
02/04/2002	H	0.45-0.85	0.64	2	30	20	14 %
30/03/2002	K_s	0.8-1.3	0.9	4	15	15	20 %
short exposures							
30/03/2002	H	1.1-1.8	1.4	8	1	15	3-4 %
30/03/2002	K_s	0.7-0.8	0.75	8	0.5	15	15-20 %

conditions as in the case of shorter wavelengths observations, as was discussed in Sec. 3.1. In addition to the long exposures, 15 exposures with 1s DIT in H and 0.5s DIT in K_s were obtained, respectively. The observational parameters are summarised in detail in Tab. 3.4.

A blue foreground giant was used as reference source for the NAOS adaptive optics system, with a visual magnitude of 16 mag ($R - V \sim 1$ mag).

Down to our detection limit of $K < 20.5$ mag, we detect 340 stars in the inner $5''$ of the cluster, such that the average stellar density in the central field is 4.3 stars arcsec^{-2}, visualising the challenge faced when resolving the center of the Arches cluster.

3.4.2 Data Reduction

All frames were normalised to the median of the background of each frame and background subtracted with a sky frame created from the average of the normalised images via rejection of the 80% brightest pixels to exclude stars. Afterwards, a flat field created from gradually changing twilight flats using the data reduction package *eclipse* has been applied to all frames. Most of the data reduction and analysis was performed using the IRAF DAOPHOT package.

50 Hz pickup:

The electronic system of the telescope and/or the instrument can impose a systematic noise pattern to the detector during read-out. This noise is observed as stripes with enhanced background flux at a certain spatial frequency characteristic for the frequency of the disturbing electronic signal.

In case of the long H exposures, the 50 Hz noise was exceptionally strong with an amplitude of ± 11 cts or $\sim 3\sigma$ above the background noise of ~ 4 cts. This noise pattern varies with time, but repeats on a somewhat regular basis, such that always 2 or 3 frames could be used to extract the pattern, again by averaging and pixel rejection. In order to minimise contamination from cluster stars, all pixels brighter than the noise pattern were set to 0 to avoid artificially increasing the noise. The remaining pixels containing the pattern information were then collapsed and averaged to a single column, and re-expanded to the original frame size. In this way, the pattern could be reproduced with only little disturbance from the dense cluster. The expanded frame was than subtracted from the images to which the pattern applied.

Hot pixels:

As the CONICA detector has a non-negligible number of hot pixels, and as these hot pixels vary in sensitivity on a timescale comparable to the individual exposure time, the bad pixel mask created

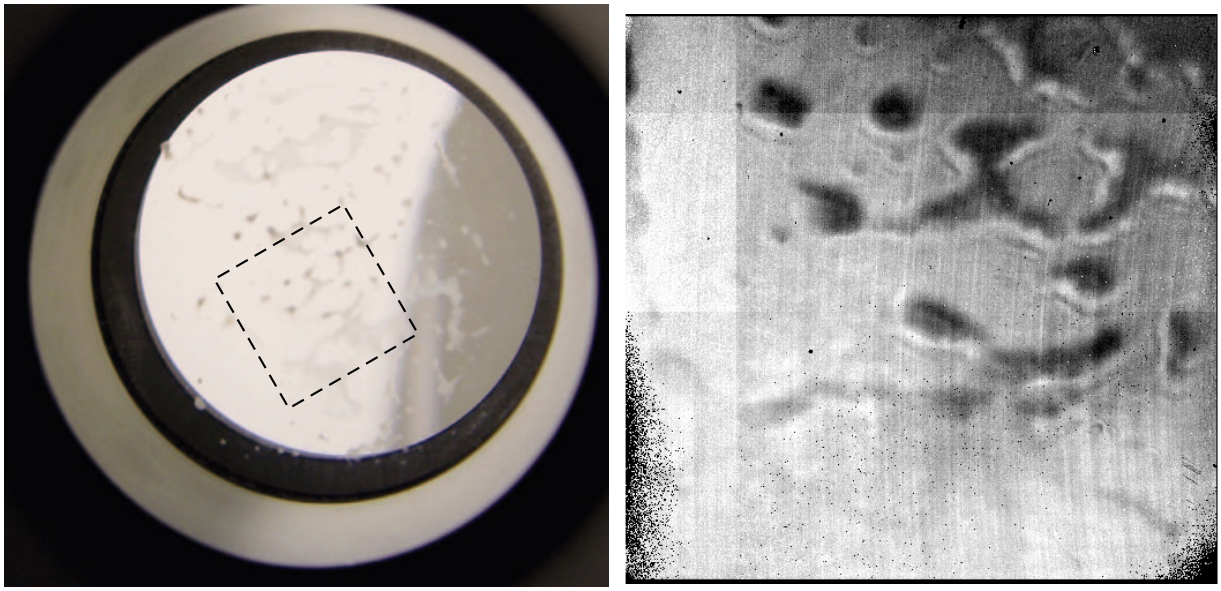

Figure 3.7: Contamination of the CONICA collimator lense during Comm 3 (solved in Comm 4).
Left: Image of the old CONICA collimator lense with perturbed surface. This collimator was exchanged against a new, uncontaminated lense during Commissioning 4. The approximate area reproduced on the sky frame (right) is marked by the box. Right: H-band sky frame showing a strong moon light contamination pattern. The pattern corresponds to the structure on the central collimator surface. Moon light reflections must have entered the optical path, as the moon was only 6 degrees from the target.

by *eclipse* from flat fields taken in the afternoon was not sufficient to reject most hot pixels. To obtain an additional bad pixel mask closer in time to the observations, we applied the IRAF procedure *cosmicrays* to two more frames in each data set, and combined the resulting bad pixel mask with the mask created by *eclipse*. The final mask was used to reject unreliable pixels during image combination.

Image selection:

In case of the long exposures, different sets of drizzled images have been created to allow quality comparison. In particular, selection of the best performance AO images vs. combination of all obtained images under loss of resolution was compared with respect to source resolution in the crowding limited cluster field, and detection of faint sources in less crowded regions. As the flux in higher Strehl data is more concentrated into a narrow peak, the combination of the highest resolution images can supercede a longer total integration time in photometric depth. The K-band data set was drizzled to one long 15 min image including all K_s frames, and one 7 min image including only frames with a FWHM of less than 3 pixels or 81 mas on the raw frame. In the same way, the higher Strehl H-band exposures with FWHM < 3.4 pix were used to create again one 7 min frame from the 7 best exposures, and one 14 min frame from all useable exposures.

The sky background on this data set strongly fluctuated due to moon light contamination, such that out of the 20 exposures taken only 14 could be used. By chance, the moon light imaged the perturbed surface of the collimator lense, shown in Fig. 3.7 in comparison to a sky frame displaying the resulting image background. The CONICA collimator lense is composed of bariumfluoride (BaF_2) and lithiumfluoride (LiF) without coating to allow the entire spectral range from $1-5\,\mu$m to progress into the subsequent optical system. The hygroscopic, sensitive lense surface is especially sensitive to dirt particles. As one of the coolest components, the collimator surface is preferentially exposed to condensations. During the extended test phase of the instrument, particles accumulated and corrupted the lense surface, most probably inserted in the evacuated dewar due to a vacuum leak detected

and closed during Commissioning (R. Lenzen, private communication). The structures damaged the surface such that the lense had to be exchanged and re-polished. Although the reproduction of the pattern is unambiguous, the optical path of the moonlight that led to the projection of the lense surface onto the detector could not be traced. These fluctuations significantly affect the H-band field photometry in the sparser regions.

In addition to these high-Strehl H-band images, the low-Strehl H-band data set (cf. Tab. 3.4) was used to create one 7 min frame with and without oversampling applied to allow quality comparison.

This procedure yielded K-band images with $\sim 20\%$ Strehl ratio and 7 min total integration time for the highest resolution exposures, and $\sim 16\%$ Strehl with 15 min integration time when all frames are used. Both the 7 min and the 14 min H-band frames display a Strehl ratio of $\sim 14\%$ as seeing conditions during the second H-band data set were very stable. The data set obtained under poor conditions yielded $\sim 5\%$ Strehl after combination of the 7 highest quality exposures. This data set will be used in the following as a low-Strehl comparison data set. The Strehl ratios of images combined in different ways are given along with the other quality parameters used in Tab. 3.5.

As will be shown in the following analysis, it turns out that the oversampled 7 min K_s image and 14 min H image yield the best photometric performance.

In case of the short exposures, only the 10 best frames in K and the 5 best frames in H have been used, leading to frames with total integration times of 40 s in each filter. These frames were used to fill in the bright end of the stellar population, and have not been used else in the technical analysis. All short exposures have been corrected for hot pixels prior to drizzling using the cosmicrays routine. Due to the very short DITs, the varying count rates of hot pixels was more pronounced than in the long DIT exposures, where such an extra correction was not required.

Combination of images:

The final images were combined using the *drizzle* task in IRAF. This task allows to apply subpixel sampling, which turned out to increase the efficiency in faint source detection.

The NAOS-CONICA data sets allowed us to perform several quality comparisons:

1. low vs. moderate Strehl performance in a crowding limited field (H-band)
2. long vs. short exposures, selecting the highest resolution frames
3. detectability of sources with natural sampling and subpixel drizzling (oversampling)
4. photometric performance in comparison to data taken with other instruments

3.5 Image Quality

3.5.1 Strehl ratio vs. flux ratio inside the PSF kernel

For a thorough comparison of AO images with varying performance, either due to diverse observing conditions, or due to changes in instrumental setup, e.g. in different filters or using different AO correction modes, it is necessary to define a set of standard quality parameters. The following three quality parameters are compared:

1. Strehl ratio (SR) - ratio of the observed peak over total flux to the diffraction limited peak over total flux of the PSF (see Sec. 3.1.3).
In the high Strehl case, the SR measures the percentage of flux concentrated into the diffraction limited PSF kernel. In the low Strehl case, the PSF kernel is widened with respect to the diffraction limit, and the flux in the seeing halo is partially included in the resultant PSF kernel, i.e. $Flux_{\mathrm{FWHM}} > \mathrm{SR}$,

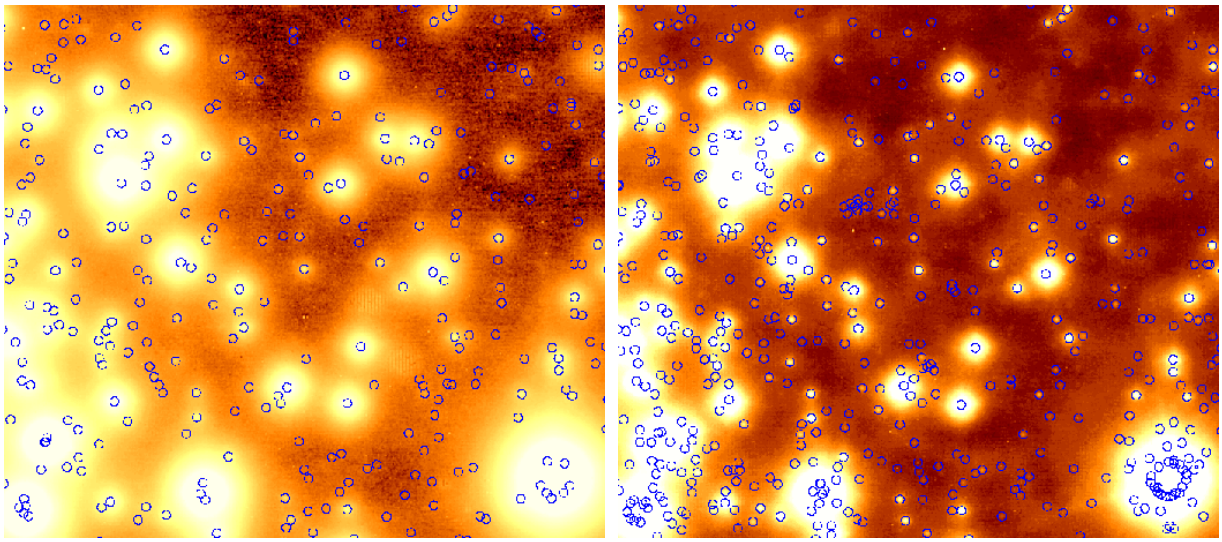

Figure 3.8: *H*-band 5 % Strehl (left) vs. 14 % Strehl (right).
All images shown in Figs. 3.8 to 3.13 are 8.3″ × 9.2″. Both images are a combination of 7 drizzled frames, resulting in 7min total integration time. The blue circles indicate 7 σ detections above the average background. While on the lower Strehl image more extended structures and background fluctuations are interpreted as sources due to the lower resolution, significantly more point-like (peaked) sources are found on the higher Strehl image. As expected, resolving and centroiding near neighbours is facilitated on the high Strehl image. As a consequence, also more detector artefacts (hot pixels) and saturation peaks are detected. These artefacts can be rejected effectively either by two-filter matching and error selection, or/and by masking bright objects.

but FWHM > diffraction limit (loss in resolution).

2. Flux ratio inside the PSF kernel (FR) - percentage of the stellar light within the (median) FWHM. In low Strehl data, FR can be significantly larger than SR (see Tab. 3.5). As the effective resolution varies for low Strehl ratios, this is a measure of the flux ratio used to derive the final PSF fitting photometry.

3. Peak over background σ for a sample star - ignoring varying exposure times and background noise, this measures the effective detectability of a source on the final frame. This allows the comparison of the image performance obtained with different data sets under various conditions.

3.5.2 Detectability of individual sources

To a first approximation, the detectability of sources on a frame can be probed by determining the ratio of the peak (in counts) over the local background variation (σ_{back}), i.e. the signal-to-noise ratio for one comparison star. The peak/σ value depends on the concentration of the star light into a peaked PSF, and its height above the background. In this sense, it is somewhat comparable to the Strehl for close-to diffraction limited observations, although it is not independent of the total integration time, as σ ($\sim \sqrt{t}$) raises less steeply than the peak flux ($\sim t$) with increasing integration time. When existing final combined frames shall be compared with focus on the resulting performance, however, the peak/σ value yields a simple comparison measure of the detectability of sources on a given frame. For this purpose, the same individual, bright (i.e. peak flux not influenced by background fluctuations) source has to be chosen on all frames. In this case, we have not taken into account the distribution of flux into frame pixels, which could have an effect on the peak/σ value if the PSF core consists of very few pixels i.e. in the case of strong undersampling. Except for NICMOS, the pixel sampling in all data sets is far from critical.

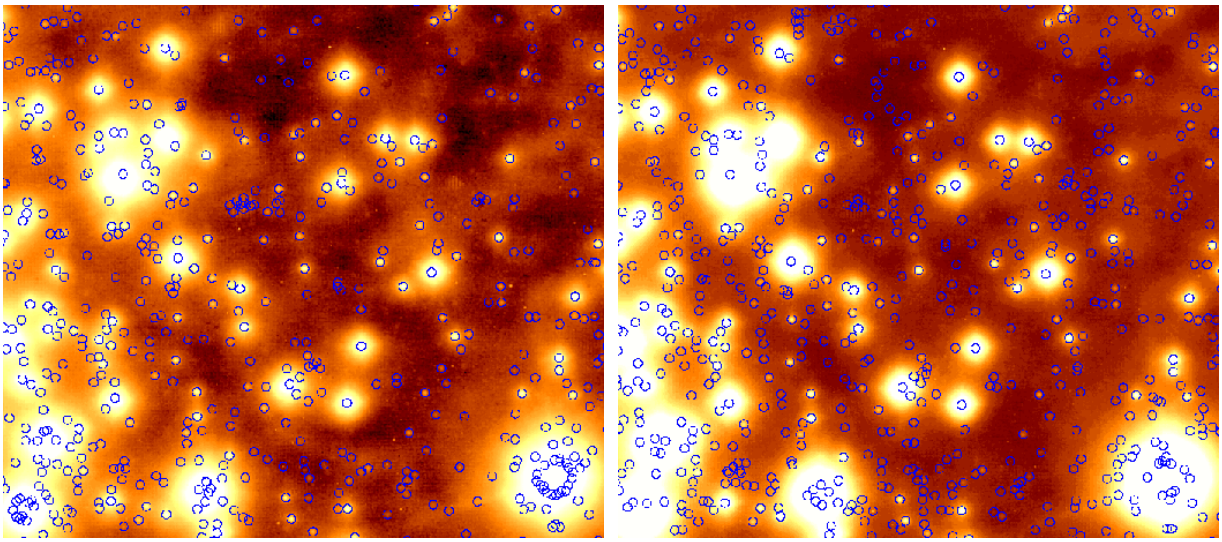

Figure 3.9: *H*-band 7 min (left, blue circles) vs. 14 min (right, green circles) oversampled image. Both images have 14 % Strehl and are combined from the same data set (2002-04-02). The observing conditions during the *H*-band observations were very stable, such that the resolution in the longer exposure image (14 frames) is equally good as in the shorter image combined from the 7 best frames only. As a consequence, the detectability of sources is comparable on both frames, except for the fact that the longer exposure is deeper, leading to more faint objects found. Note that the background variations seen on these images are due to moonlight contamination. Few faint sources are lost due to this strongly varying background. The photometric performance is not affected, as the background is determined locally by the daophot PSF fitting procedure *allstar*. The right image is the best image of Arches in *H*-band obtained during Commissioning, and has thus been used to obtain the final photometry.

The uncertainty in the final results mainly reflects the uncertainty in background fluctuations. This is particularly critical on the NICMOS frames, as the background is influenced by the extended NICMOS PSF pattern. To obtain an objective estimate on the background variation, we have chosen a field close to the analysed star without point sources, characterising the local background in the immediate vicinity of the star, but large enough to be representative for the performance in the crowded stellar field of the frame. A histogram plot has been created from the intensities in the background field. This historgram was then truncated beyond the maximum in the number count, such that the bright, slowly decreasing tail of detected background structure was excluded. The steep raise of the distribution to the maximum was mirrored around the peak to represent the underlying background. Assuming a normal distribution, a Gaussian was fitted to the resulting function, yielding σ. The same background field has been chosen in each image. Although this procedure allows a consistent treatment of all data sets, it turns out that several frames do not show a normal distribution in the background variation. The results are shown in Tab. 3.5.

In the case of the high-Strehl *H*-band data set (*H*-band 420 s and 840 s, oversampled), the background statistics are influenced by the large scale moonlight contamination shown in Fig. 3.7. The resulting distribution appears too wide, thus yielding a too large σ, and too low peak/σ. When the large scale fluctuations are excluded by measuring σ on small areas around the star (thus more locally biased), the peak/σ increases by a factor of 1.6, which is more representative for the higher Strehl in this data set. For comparison, the values are given in parentheses in Tab. 3.5.

The NICMOS data show a very distorted background flux distribution, which does not appear very Gaussian. The profile rather appears to consist of several Gaussian-like functions with varying height, and a sharp peaked maximum. It is very likely that the extended PSF structure folds into the detector and stellar background variation, resulting in the combination of different components. This is the reason why the locally determined background variation for our test star is about a factor of

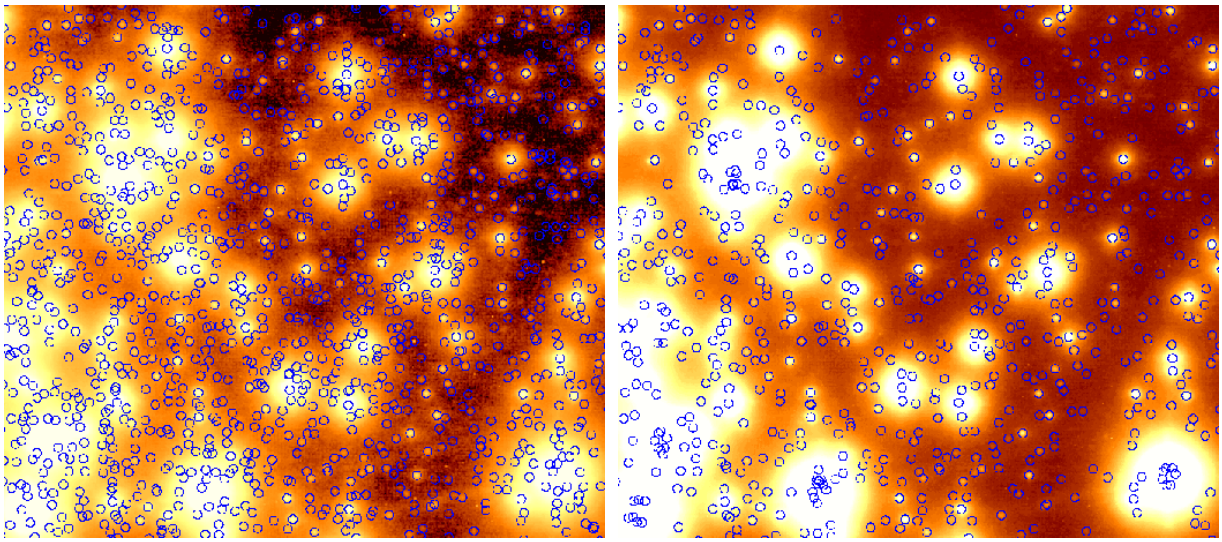

Figure 3.10: K-band 7 min (left, blue circles) vs. 15 min (right, green circles) oversampled image. While for the 7 min image only the 7 best frames have been used (seeing $< 0\farcs81$, FWHM < 3 pix), the 15 min image was combined from all frames without selection (seeing $0\farcs65$ to $1\farcs3$, $2.84 <$ FWHM < 3.6 pix). The limiting factor in this case is not the photometric depth, but the crowding, such that the detectability of sources on the slightly better resolved 7 min exposure is enhanced. Although the resolution changes only slightly from 84 mas to 87 mas, the Strehl (determined on both images in the same fashion and from the same sources) decreases from 20% to 16%. Faint peaks in less crowded regions are more readily detected on the 7 min frame, as point sources appear more peaked. On the 15 min frame faint peaks can be smeared out due to the spreading of their flux into a larger area. Thus, photometric depth is not only determined by the length of exposure time, but is as well as the resolution on the final frame determined by the AO performance.

10 larger than the global σ, which has been determined from more isolated parts of the frame. Such isolated areas are not available on all frames, and as crowding is the most limiting factor in object detectability in the case of the Arches cluster field, the same local background field has been used on all frames, including background fluctuations induced by surrounding stars.

Bearing in mind these uncertainties, this is an easy and straight-forward method to obtain a rough idea on the differences in data sets taken under varying conditions or over longer periods of time.

The quality parameters for several selected data sets of Arches are given in Tab. 3.5.

Higher Strehl:

As expected, the higher Strehl NACO data show a higher resolution and sensitivity than the lower Strehl data. The discrepancy is particularly pronounced in comparison to the low Strehl Hokupa'a data, where the loss in photometric depth is clearly reflected in the low peak/σ values.

Longer total integration time:

A longer integration time, effectively meaning a larger number of drizzled frames, should increase the peak flux by the factor $f = t_{long}/t_{short}$, while σ should only increase as $\sqrt{f}$. In the case of stable observing conditions, this causes enhanced detectability of objects. In the case of the 14 min H-band and 15 min K-band exposure, the total integration time is increased by about a factor of 2. Theoretically, this should enhance the peak/σ by $2/\sqrt{2} = \sqrt{2}$. When comparing the values in Tab. 3.5, we do not find an increase in performance on the H-band frame, and the increase in K-band is significantly smaller than expected. This is understandable, as the seeing variations during observations resulted in relatively large changes in the AO performance, and thus a degeneration of the Strehl on the combined

frame, causing the stellar image to be less peaked.

Oversampling:

On the oversampled images the flux, given in counts, is spread out into a factor of four more pixels than on the frames drizzled without oversampling. (Note that we have drizzled some of our frames using units of counts/second, to allow direct comparison in some cases. So, peak fluxes cannot be compared strictly on all frames, but the peak/σ has to be considered instead to draw conclusions.) The peak flux of the test star is decreased by a factor of 3.8 in H, and 3.5 in K, reflecting a more confined peak in the oversampled images. It turns out that σ, however, decreases only by a factor of 2.8. This effect is not quite understood at the moment, but may have to do with the correlation of noise when drizzling onto a finer grid. Thus, the overall performance appears to go down by a factor of ~ 0.8. The correlated noise, however, appears to affect source detection less than pure statistical fluctuations, leading to the significantly better result obtained in the final photometry of the oversampled images (see Sec. 4). Unfortunately, the many statistical effects entering here are very complex and not yet entirely clear.

NICMOS data:

The perturbed background in the NICMOS images strongly influences the peak/σ value. The increased background decreases the detectability of sources, which may well reflect a real effect in the crowded field, as each source finding and fitting algorithm has to cope with the background fluctuations induced by the spiky NICMOS PSF.

We show the performance in terms of object detection with *daofind* at a 7σ finding threshold in Figs. 3.8 to 3.10. The photometric performance described below is shown in Figs. 3.11 and 3.12, where now in case of the CONICA data only sources matched in H and K are shown. A comparison with NICMOS is given in Fig. 3.13.

Table 3.5: Comparison of data sets - Quality parameters.

Tele/Instrument	filter	exp. time	sampling	pix scale	FWHM	FWHM	σ_{back}	peak	peak/σ	flux(FWHM)	Strehl	remarks
				$''$/pix	pix	mas	cts	cts	cts			
VLT/NAOS-CONICA	H	420 s	natural	0.027	4.	110	8.41	490.2	58	27 %	4 %	7 best frames (30th March), natural sampling
	H	420 s	over	0.027	8.	110	2.97	126.9	43	27 %	4-5 %	7 best frames (30th March), 2x2 oversampled
	H	420 s	over	0.027	6.2	84	1.04 (0.6)[1]	72.5	70 (120)	37 %	12-14 %	7 best frames (4th April), 2x2 oversampled
	H	840 s	over	0.027	6.3	85	0.80 (0.5)[1]	55.3	69 (110)	33 %	12-14 %	14 useable frames (4th April), 2x2 oversampled
	H	720 s	natural	0.027	3.2	86	2.86	158.9	56	30 %	10-14 %	12 useable frames (4th April), pipeline reduced
Gemini/Hokupa'a	H	720 s	natural	0.020	9.7	194	0.18	7.07	39	46 %	2-4 %	Gemini low Strehl photometry
HST/NICMOS	F160W	256 s	natural	0.075	2.4	210	0.028	3.94	141	60-79 %	50-60 %	HST/NICMOS F160W
VLT/NAOS-CONICA	Ks	420 s	natural	0.027	3.2	86	5.60	2104.	376	44 %	20 %	7 best frames, natural sampling
	Ks	420 s	over	0.027	6.2	84	1.98	595.7	301	43 %	21 %	7 best frames, 2x2 oversampled
	Ks	900 s	natural	0.027	3.4	92	7.07	3252.	460[2]	37 %	15-17 %	all 15 frames, natural sampling
	Ks	900 s	over	0.027	6.4	86	2.48	908.5	366[2]	37 %	16 %	all 15 frames, 2x2 oversampled
	Ks	900 s	natural	0.027	3.2	86	0.07	29.2	417	38 %	20 %	all 15 frames, pipeline reduced
Gemini/Hokupa'a	K′	1020 s	natural	0.020	7.0	140	0.26	18.4	71	43 %	7 %	Gemini low Strehl photometry
HST/NICMOS	F205W	256 s	natural	0.075	2.9	220	0.24	17.5	73	60 %	70-80 %	HST/NICMOS F205W

general remarks:
The pixel scale is always given in arcsec/pixel for the CCD used. This is not the image pixel scale, which is dependent on the sampling. In the case of 2×2 oversampling, the resulting image scale is a factor of 2 smaller than the detector pixel scale.

The peak/σ value is meant as a comparison of the detectability of one individual star on each frame. The same star with a well-behaved PSF shape has been used to perform the comparison. σ has been determined from a Gaussian fit to the histogram of the background intensity distribution in a near-by field. The same field has been chosen on all frames. As peak/σ is strongly influenced by local variations, the peak/sigma is only a rough estimate on the performance.

3.6 The Effects of Oversampling

While experimenting with AO data, we realised that oversampling appears to help source detection. We have drizzled the NACO frames with highest quality applying 2×2 pixel oversampling, such that the subpixel grid, onto which the flux in each original image pixel is distributed, is finer than the original "natural" grid of the IR detector used for the observations. This feature is implemented in the drizzle task (Fruchter & Hook 2002), used to combine the images, via the "pixfrac" keyword. Due to the finer subpixel drizzling the sources appear more peaked and the flux is more concentrated into the kernel. The overall FWHM may only change slightly, but the better concentration of flux into the central pixel facilitates source detection.

Different finding routines have been tested to check whether or not this feature is intrinsic to DAOPHOT, our preferred reduction package. In addition to DAOPHOT testing, the FIND algorithm implemented in the IDL astro library (in principle, an older version of *daofind*), and the Starfinder package (Diolaiti et al. 2000) have been used. The quantitative results are given in Tab. 3.6.

A few general features can be found on the oversampled images, mostly from our thorough *daofind* testing:

1. the resolution of blended sources is facilitated on the oversampled images

2. faint point sources are more easily detected, especially in the broad wings of bright stars, as in the Arches cluster center
note that extended features (here due to background variations, but in other cases desired objects such as galaxies) are easier detected on the *naturally sampled* frames

3. PSF fitting appears to work better in the crowded regions, as more pixels are available for the fitting algorithm on the oversampled frame

Oversampling facilitates the separation of close objects and enhances the contrast, in particular in crowded regions. The resulting gain is strongly dependent on the data quality - the lower the Strehl, the higher the gain. For well resolved data the gain is not as significant as for low Strehl data (cf. Tab. 3.6).

We noticed that the FWHM fed into the finding algorithm is a very critical parameter. Especially when using *daofind*, a change in FWHM by 0.2 pixels (H-band NACO data set, 15 % Strehl, 6.2 vs. 6.4 pixels FWHM) can change the detection rate by almost a factor of 2! This is due to the fact that with a too narrow FWHM artificial peaks as well as background fluctuations can be chosen as sources. The first possibility is a large source of contamination due to the high hot pixel rate on the NACO detector, in particular as hot pixel positions appear to be time varying. Applying a standard cosmic ray rejection algorithm after basic reduction prior to image combination significantly reduces the number of hot pixels. The second possibility is particularly pronounced in regions with high background fluctuations, such as obscured star forming regions. In addition, the centroiding appears to work worse when the FWHM is chosen too small. On the other hand, a too large FWHM causes close sources to be missed or confused, such that the gain from oversampling is easily lost.

An additional handicap inherent to AO data is the fact that the FWHM of the stars varies across the field. This is not taken into account in standard available finding algorithms. From the above analysis it is clear that a single value for the FWHM causes the performance of the photometry routines to vary over the field, already at the stage of finding sources. Although the DAOPHOT PSF fitting task *allstar* allows for a spatially variable PSF, sources may already be lost at the stage of peak detection. Visual inspection of the detected sources is required to determine reasonable parameters.

In Tab. 3.6, we have systematically tested the detection rate of objects on several frames. The

remarks added in the last column give an idea on the performance obtained. We conclude that oversampling helps source detection, and in case of carefully chosen finding threshold and FWHM enhances the detectability of close sources. A special remark on *daofind*: The finding threshold for oversampled images may be chosen a factor of two higher (in units of σ) to obtain the same performance as on naturally sampled images. This reduces the number of artefacts found. Especially on frames with low Strehl ratios and thus only moderate resolution, oversampling significantly reduces the number of wrong detections and increases the number of resolved real sources. Very close sources are more reliably and easier detected and centered on the oversampled images. In the case of the low Strehl H-band data set, the frame with natural sampling never reaches the same performance as the oversampled frame. While an increasing number of artefacts is picked up with decreasing finding threshold, several faint sources in the cluster center and near neighbours remain undetected.

Note that in this crowding and background limited case, the photometry in the 15 min exposure is not significantly deeper than in the 7 min exposure, as the strongly fluctuating background is the main source of contamination.

Table 3.6: Source detection with *daofind* on NAOS/CONICA images with and without oversampling(peak detection only, no PSF fitting applied).

image	filter	exptime	sampling	σ_{back} cts	FWHM pix	FWHM mas	threshold σ	threshold cts	sources	remarks
h7nat	H	7 min	natural	8.0	4.	110	10	800	931	many objects are missed
							7	56	1238	fainter sources are found,
Strehl										but already more artefacts
							5	40	2196	picks up many artefacts,
5%										faint sources still missed
							2.5	20	11736	too many fake sources
h7m	H	7 min	over	2.0	8.	110	10	200	2459	most objects visually seen detected,
										few faint sources lost
5%							7	14	4423	more artefacts around saturated stars,
										faint sources in cluster vicinity detected
							5	10	11263	significantly more artefacts, but the faint
										sources in the cluster center are found
hnew7nat	H	7 min	natural	1.8	3.2	86	10	18	1198	way too many sources missed
							7	12.6	1460	close and faint sources not resolved
14%							5	9	1957	better, but close sources still unresolved
hnew7m	H	7 min	over	0.5	6.2	84	10	5	2286	faint sources missed
							7	3.5	4538	good performance, most sources found,
14%										only few faint sources in cluster center missed
							5	2.5	11597	apparantly way to many fake sources,
										however, this yields the best performance after
										matching with K
ks7nat	Ks	7 min	natural	5.	3.2	86	10	50	2717	way too few sources
							7	35	3704	slightly better, but many faint sources missing
20%							5	25	5269	good performance, few faint and close sources
										missed
ks7m	Ks	7 min	over	1.3	6.2	84	10	13	5278	faint sources in cluster center clearly missed
							7	9	9977	better performance in cluster center
20%							5	6.5	19996	many artefacts, very dense field of detections,
										good performance when matching H and K,
										but cannot be used without matching!
ks15nat	Ks	15 min	natural	8.5	3.4	92	10	85	2287	comparable, slightly worse than ks7nat
							7	60	3001	as ks7nat
16%							5	42	3855	as ks7nat
							3	25	6506	surprisingly good performance, not too many
										artefacts, faint sources ok
ks15m	Ks	15 min	over	2.3	6.4	86	10	23	4008	too many faint sources lost
							7	16	6086	rejects most artefacts, looses few real stars
16%							5	12	10765	many artefacts, but also more real faint sources

Table 3.7: Comparison of different finding routines: number of detected sources

image	threshold (sigma)	daofind (detections)	IDL find	Starfinder (PSF fitting)
ks7m	10	5278	3413	3539
	7	9977	5550	4243
	5	19996	11384	4729
ks7nat	10	2717	3227	-
	7	3704	4450	2671
	5	5269	6315	3209
	3	-	-	3880

IDL find and Starfinder: Detection rates for several thresholds are compared for the 7 min K-band frame in Tab. 3.7. The general differences in the finding procedures are that centroiding works much worse in IDL *find* and *Starfinder* than with *daofind*, and that the finding threshold has to be lower to obtain the same efficiency, which is probably an intrinsic feature of each code. Although on the naturally sampled frames the number of detected artefacts is much lower than with *daofind*, and also much lower than on the oversampled frames, a significant number of faint sources, in particular close to brighter objects, are lost.

There is a general tendency of all peak finding algorithms to detect many more sources on the oversampled frame, in particular faint stars and near neighbours, such that oversampling helps to resolve a dense stellar population. However, these additional detections have to be viewed carefully, as the detection of artefacts may also be enhanced. With a reasonably chosen detection threshold, within IDL FIND and Starfinder the discrepancy of objects found on the natural vs. oversampled frame is not as large as with *daofind*, where many more spurious sources are detected (with comparable FWHM).

In summary, oversampling facilitates source detection, in particular at the faint end and near brighter sources. Daofind appears to be the most efficient detection routine, but along with faint and close sources many artefacts are found. The FWHM and finding threshold, and thus σ, of the frame are very critical parameters for source detection. Starfinder, which combines source detection with PSF fitting, separates real objects more reliably from background fluctuations and artefacts.

3.7 Deconvolution and higher Strehl images as coordinate input

3.7.1 H-band low vs. high Strehl

It has been suggested to use high Strehl observations to determine the positions of sources in the field, and use the resulting coordinate list as input for photometry routines on data with worse performance. However, it turns out that photometry on the faint sources, lost to the background in the lower Strehl images, is not feasible. Even the photometry of bright, blended sources spatially resolved in the higher Strehl images can be miscalculated by as much as ± 2 mag.

3.7.2 Image deconvolution

Rainer Schödel (MPE, Garching) provided deconvolved images of the Gemini/Hokupa'a Arches data set based on a Linear Wiener Filtering deconvolution algorithm (see Ott et al. 1999 for details). The PSF used for deconvolution is a combination of an analytical PSF kernel determined by averaging over several isolated stars on the frame, plus wings fitted with a Moffat function to simulate the seeing

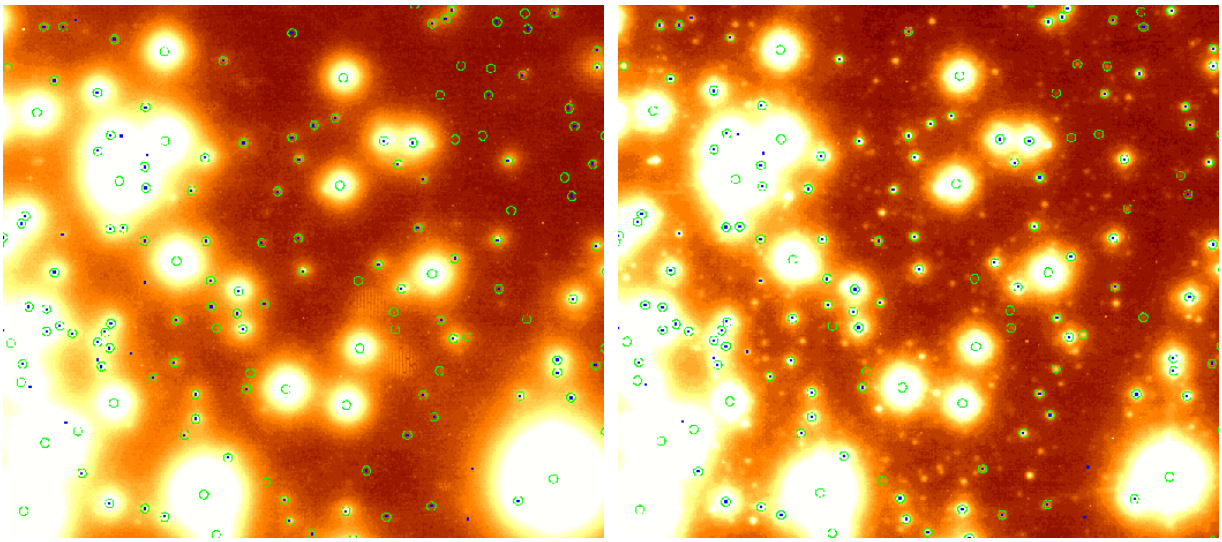

Figure 3.11: Matched H and K photometry with (green circles) and without (blue dots) oversampling overlaid on the 7min H-band image, 5% Strehl (left) and K-band image, 20% Strehl (right).
Bright sources are not included in the natural sampling photometry. With 2×2 oversampling applied during the drizzling process, faint sources and close neighbours are better resolved than with natural sampling. The effect is mainly due to the gain achieved with oversampling on the low-Strehl H-band image.

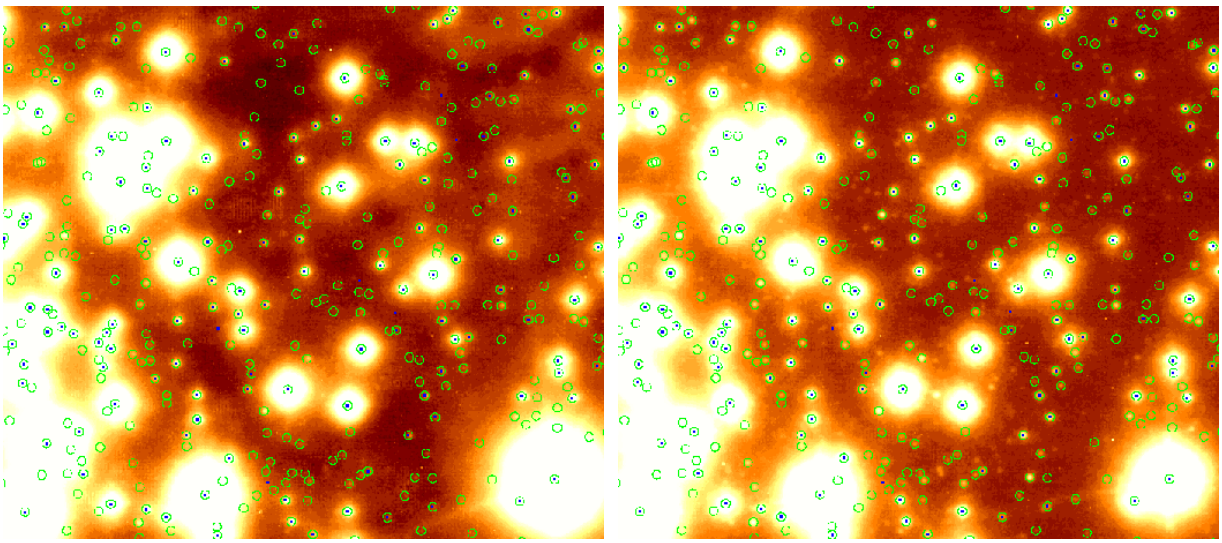

Figure 3.12: H-band 5% Strehl (blue) vs. H-band (green) 14 % Strehl plus K-band 20% Strehl, overlaid on the 14% Strehl H-band image (14 min, left) and the K-band image (20% Strehl, 7 min, right).
Due to the widening of the PSF, faint sources are missed in the low Strehl data, as their flux is distributed into more detector pixels. Seeing halos from brighter stars introduce a stronger background contamination, hindering photometry of faint stars. The resolution of 110 mas with 5% Strehl, as opposed to 85 mas with 14% Strehl, is a strong limitation in the crowded cluster.

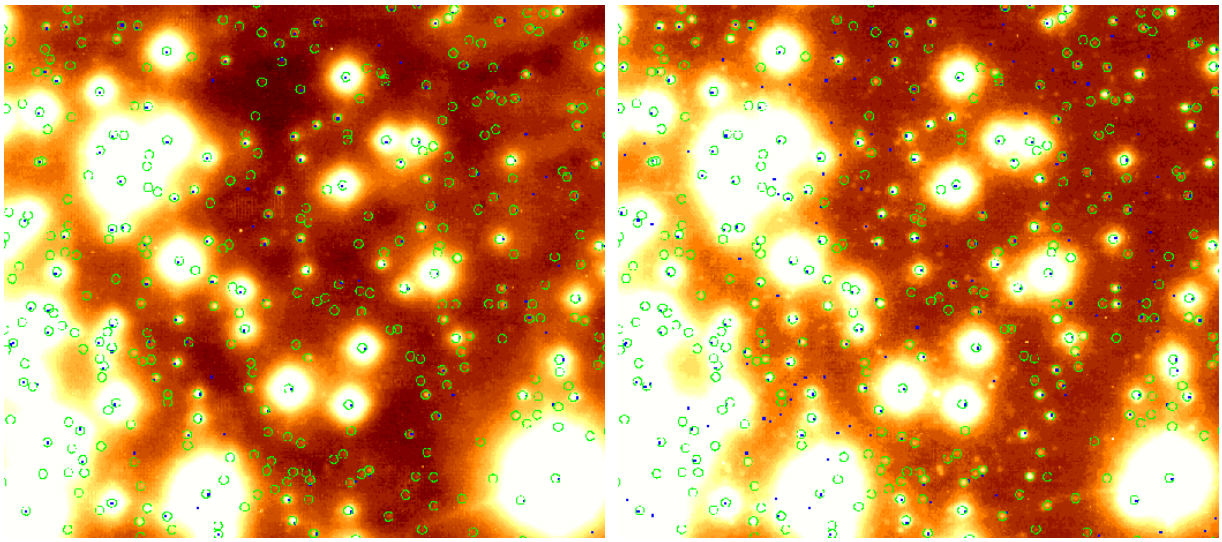

Figure 3.13: NAOS-CONICA (green circles) vs. HST/NICMOS (blue dots) sources overlaid on the best quality NACO H (14 min, 14 % Strehl, left) and K (7 min, 20% Strehl, right) image.
Note that the bad centroids of the NICMOS data are due to the few pixels available for centroiding. Overlaid on the H-band image, NICMOS detections in H and K are shown (NICMOS photometry provided by Don Figer), while on the K-band image K-only detections are plotted. The NACO sources are always detected both in H and K. On the one hand, the NACO data reach a higher photometric depth than the NICMOS data. On the other hand, the higher resolution on the NACO images causes an increase in dynamic range close to the bright cluster stars, thereby enhancing the detectability of sources.

halos.
Probing the efficiency of image deconvolution in terms of source detection and photometric performance requires a reference data set, where the locations and magnitudes of real sources are known. The higher resolution NACO data provide such a reference.

Detection of sources: The detection of sources within a crowded region is much more efficient on the deconvolved images. Due to ringing effects, however, care has again to be taken to reject artefacts. As in the undeconvolved case, the most efficient method for artefact rejection is the matching between two filters, as the ringing effects and resultant shape of the sources on the deconvolved image is dependent on the Strehl ratio, resolution, and shape of the original PSF. When comparing the sources detected on the deconvolved Gemini low Strehl (2.5 and 7 % in H and K, resp.) images, matched in H and K, with the NACO higher resolution K-band image, only very few artefacts remain. Most of the detected stars are real faint stars or neighbours to bright stars. In comparison with HST/NICMOS, several, but not all, of the stars detected with NICMOS are recovered. In addition, several stars *not detected* with NICMOS are found. Still, the loss is quite significant even after deconvolution. While 425 stars were matched in H and K on the observed Gemini images, 647 stars are found and matched on the deconvolved images, and 780 stars are detected with HST/NICMOS. When the coordinate list from the deconvolved images is used as daophot input to the observed images (no deconvolution), 698 objects are PSF fitted in both filters, of which 558 are spatially coincident with NICMOS sources. NAOS/CONICA observes roughly 1400 stars on the same field of view, but reaches about 1 mag fainter photometry. Down to a magnitude of 20 mag, the detection limit on the Hokupa'a and NICMOS K-band images, NACO detects 1207 sources.

Photometry: We have used daophot PSF fitting photometry with a spatially invariant PSF (a penny2 function) on the deconvolved images to test the photometric performance. The result was, unfortunately, not very satisfying (see Fig. 3.14, middle). Several problems were noticed when analysing

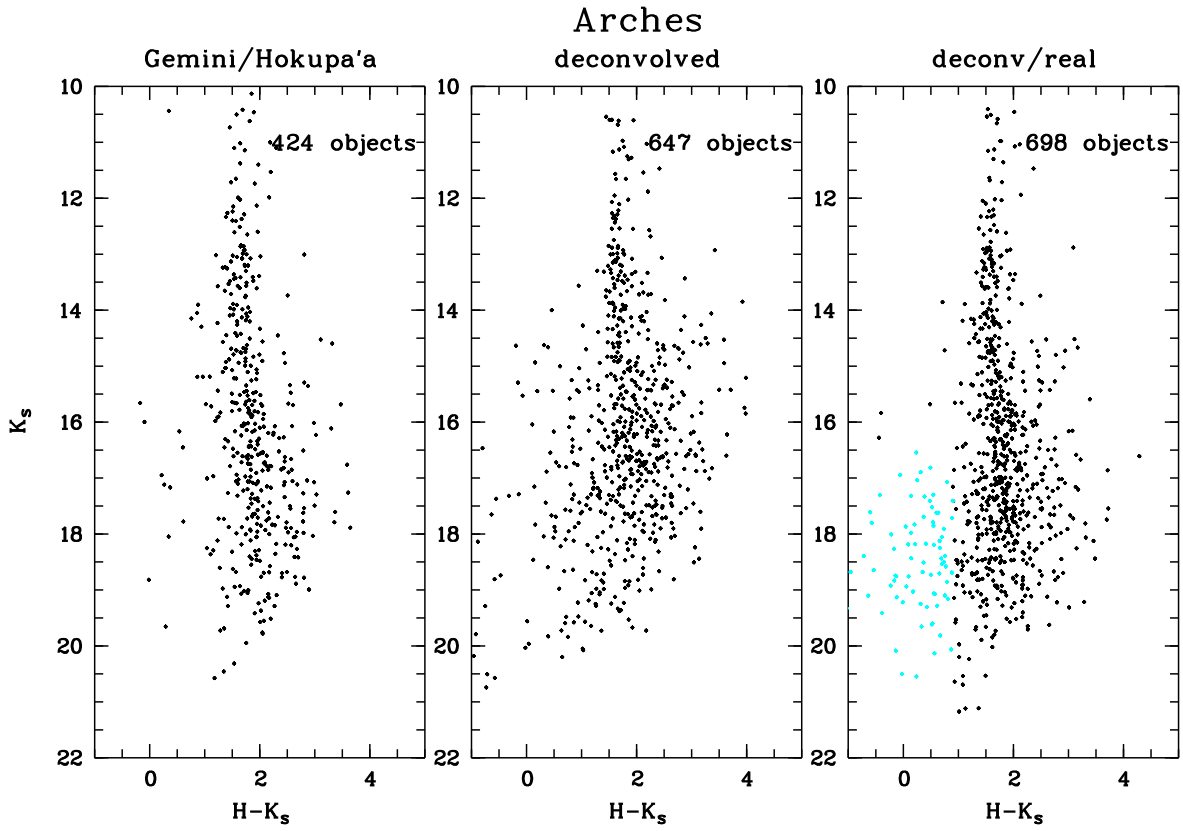

Figure 3.14: Colour-magnitude diagrams of Gemini/Hokupa'a photometry with and without deconvolution. Left: Photometry performed on the real frame, no deconvolution applied. Middle: PSF fitting photometry on the deconvolved frame. Right: PSF fitting photometry on the real frame, where the coordinate input was taken from the deconvolved image. Blue objects to the lower left of the main sequence have been excluded in the star count, as they are mainly artefacts. Clearly, the main sequence is much better populated in the right CMD than in the left CMD, and is well confined. While photometry on the deconvolved image itself does not yield satisfying results, using a coordinate list obtained from the deconvolved image as input for the final photometry on the original frames helps source resolution and fitting.

the residual images, where fitted stars have been subtracted. On the K-band image, the peak flux of faint sources was systematically overestimated by at least a factor of 2, such that these sources are scattered to higher K-magnitudes on the CMD. In H-band, the fitting performance on the faint sources was much better, but here the bright sources were severely overestimated, in particular due to oversubtraction of the ringing features around each bright star. With a single PSF function, the faint end and the bright end of the stellar population cannot be fitted with comparable photometric performance. As ringing was stronger in H than in K, we used a larger PSF radius to take into account the perturbance around each star. Despite the fact that the fitting should be performed within the FWHM radius, the larger PSF yielded a better performance on faint objects, while a smaller PSF Radius with the same FWHM yielded better performance on the bright sources. The different PSF shape and resolution on the H and K images may also be responsible for the significantly different PSF fitting performance. A more thorough selection of fitting parameters has still to be tested.

Resulting performance: Colour-magnitude diagrams of the original and deconvolved image photometries are shown in Fig. 3.14. Photometry with coordinate input from significantly higher resolution frames appears difficult as many sources are included which are not readily detectable in the lower resolution image. In addition to the decreased resolution causing faint objects to be lost due to the

distribution of flux into more pixels, the higher background and/or lower photometric depth hinders source detection of point sources as well as of extended objects. On the other hand, source detection from the deconvolved version of the same image ensures that only sources that are definitely detected in the frame are included in the coordinate list. In our preliminary analysis, it appears that the resulting photometric performance is much more reliable. We suggest to combine source detection on deconvolved images with subsequent photometry on the original images.

3.8 Photometric Residuals

As in the case of the Gemini/Hokupa'a data (Sec. 3.2.1.4), the calibration of the NAOS/CONICA photometry against the NICMOS photometry allowed to analyse the spatial distribution of photometric residuals. More than 1400 stars were found in common between the NICMOS and NACO photometries on the NACO field of view of $25'' \times 25''$. Note that this area is larger than the Hokupa'a FOV, which is chosen in the following discussion to allow direct comparison between all available data sets. The high number of several hundred stars in common between the different data sets yielded the positional dependence of photometric residuals over the field. In the case of the Gemini data, a linear dependence of photometric residual with distance from the cluster center was found (Fig. 3.15). While the flux of cluster center stars was overestimated, the flux of stars in the cluster vicinity was underestimated. Detailed analysis revealed the photometric performance to be magnitude dependent. While the flux of bright stars, most frequent in the cluster center, tended to be overestimated, the flux of faint stars tended to be underestimated. Our interpretation was that the wide seeing halos in the low-Strehl Gemini photometry led to an oversubtraction of the local background of neighbouring stars, thereby decreasing the faint stars' fluxes.

The dependence of photometric residual from the cluster center clearly dominated the photometric uncertainty in K-band (Fig. 3.15), while the anisoplanatism was negligible on the Gemini K-band frame. In H-band, however, it turned out that both effects mix. Although this is hard too see in the simple plots given in Fig. 3.15, residual maps (cf. Stolte et al. 2002) show the symmetry of photometric residuals around the guide star in addition to the dependence on cluster center distance.

We have performed the same kind of analysis on the NACO data. Only stars brighter than 20 mag with uncertainties less than 0.1 mag in H and K have been used for this comparison. When comparing the NACO data to NICMOS, no colour terms were found, such that we used simple zero-pointing for calibration. The residual behaviour also shows no evidence for colour terms. Although the photometric scatter in H is significantly larger than in K (which may in parts be due to the lower resolution NICMOS photometry), we cannot find a dependence of photometric performance on distance from the cluster center or the guide star.

In accordance with this we could also not find a clear change in FWHM over the field in both filters, although objects located at the field edges of the combined image appear slightly more elongated. As no distortion correction has been applied, this effect is probably a mixture of field distortion and anisoplanatism.

In Fig. 3.17 we show the photometric residuals vs. magnitude. Only the general trends observed are meaningful, as the higher resolution in the NACO data allows to resolve sources detected as single objects with NICMOS, thus causing large residuals even at the bright end. At very faint magnitudes, there may be a slight tendency to underestimate the flux in the AO data when compared to NICMOS (Fig. 3.17). About 20% of the stars with $K > 18.5$ mag have residuals $K_{HST} - K_{NACO} < -0.5$ mag, while only 10% have $\Delta K > 0.5$ mag (i.e. overestimated flux). A similar trend was observed with Hokupa'a, but would have to be confirmed with independent data sets, as an overestimation of fluxes in the NICMOS photometry can currently not be excluded. In H-band, the photometric scatter at the faint end appears random, and approximately the same fraction of stars is scattered towards brighter and fainter magnitudes, respectively. The width of the residual distribution at the faint end is about 1.4 mag, and the fraction of stars with H-band residuals larger ± 0.7 mag is below 10 % for stars with

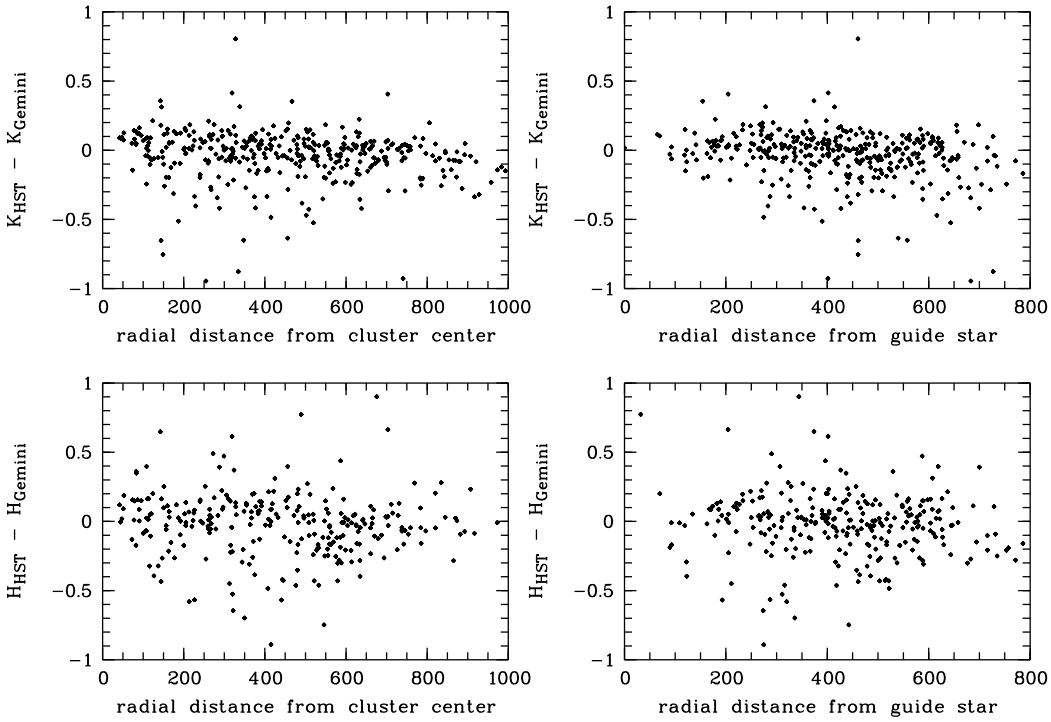

Figure 3.15: Gemini/Hokupa'a photometric residuals vs. distance from the cluster center (left) and distance from the guide star (right).
Stars brighter than 20 mag with uncertainties less than 0.1 mag in both H and K have been used for this analysis. The tendency to overestimate the flux of (bright) cluster center stars and underestimate the flux of (fainter) stars in the cluster vicinity is seen in the K-band photometric residuals when compared to HST/NICMOS photometry. In H-band, the scatter is very large, and the anisoplanatism washes out the clear trend seen in K.

$H > 20$ mag.

3.9 NAOS-CONICA luminosity functions

Fig. 3.18 shows the NACO H- and K-band LFs derived from the CMD shown in Fig. 3.21 (right). In the top panel, the LF of the entire field is displayed. Note that in all NACO LFs only the data matched in H and K are shown, to eliminate artefacts. Thus, the K-band LF is limited at the faint end by the requirement that objects need be detected in H, where extinction is more severe, leading to 1.5 mag stronger obscuration in H-band at a visual extinction of $A_V = 24$ mag, corresponding to the Arches cluster center. As a consequence, the H-band LF represents the total LF on the field more realistically, as it is not artificially truncated.

In the H-band LF of all stars on the Gemini field, which was chosen as the field in common between all data sets, first of all the much deeper photometry at the faint end is prominent. While the Hokupa'a and NICMOS LFs decrease beyond $H \sim 19$ mag, the NACO LF shows a strong increase in the number of stars out to $H = 21$ mag, and drops off sharply only beyond $H = 22$ mag. This behaviour is the expected behaviour for a background limited LF, while the flat decrease in the number of stars seen in the Hokupa'a and NICMOS data indicates loss of stars due to crowding. The K-band LF of the entire Gemini FOV is truncated at $K = 20$ mag by the H-band detection limit. Nevertheless, this LF clearly displayes the gain in the NACO data as opposed to previous data sets. Although the NICMOS K-band LF resembles the NACO LF very closely down to a mangitude of $K = 19$ mag, several stars are additionally resolved with NACO in each magnitude bin already at magnitudes as

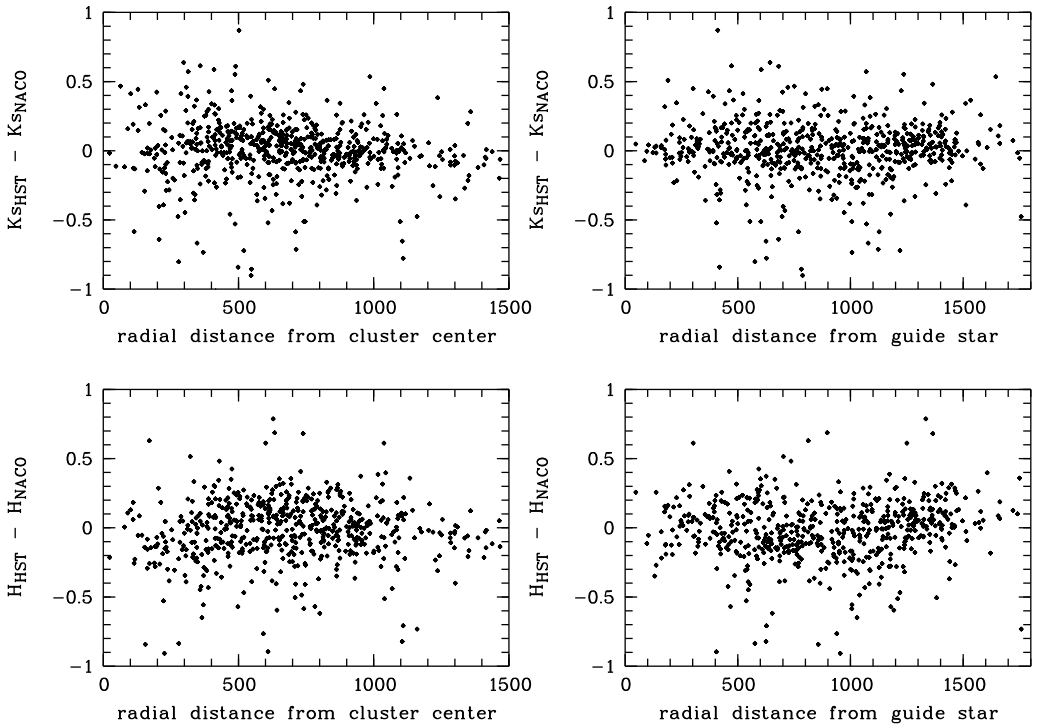

Figure 3.16: VLT/NAOS-CONICA photometric residuals vs. distance from the cluster center (left) and distance from the guide star (right).
Stars brighter than 20 mag with uncertainties less than 0.1 mag in both H and K have been included. No clear positional dependence of photometric performance is seen in this data set.

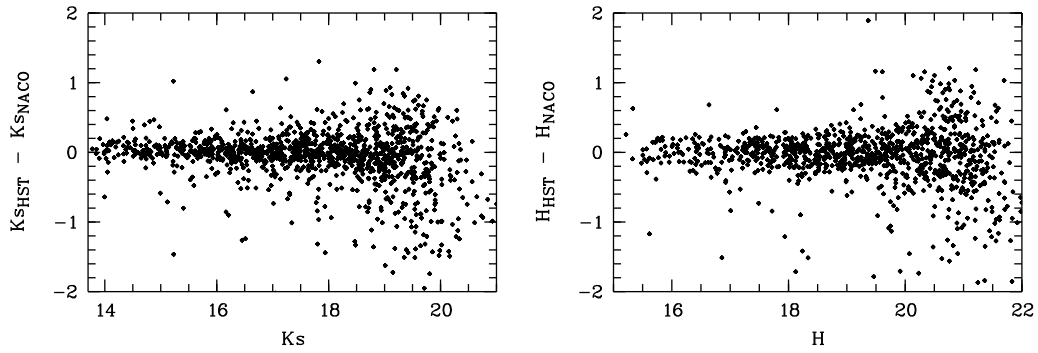

Figure 3.17: Photometric residuals vs. magnitude.
All stars with uncertainties less than 0.1 mag have been included. Note that the NICMOS detection limits are roughly 20 mag in K and 21 mag in H, and that the lower resolution in the NICMOS data may cause large outliers. Fainter stars are observed, but with relatively large uncertainties. For $K < 19$ mag and $H < 20$ mag, the photometric scatter of the bulk of the stars is less than ± 0.3 mag in both H and K, with stronger scatter in H at the bright end. A slight trend to underestimate faint fluxes in K-band is seen in the NACO data. As the corresponding magnitudes are close to the NICMOS detection limit of $K = 20$ mag, this effect has to be confirmed with deeper reference data.

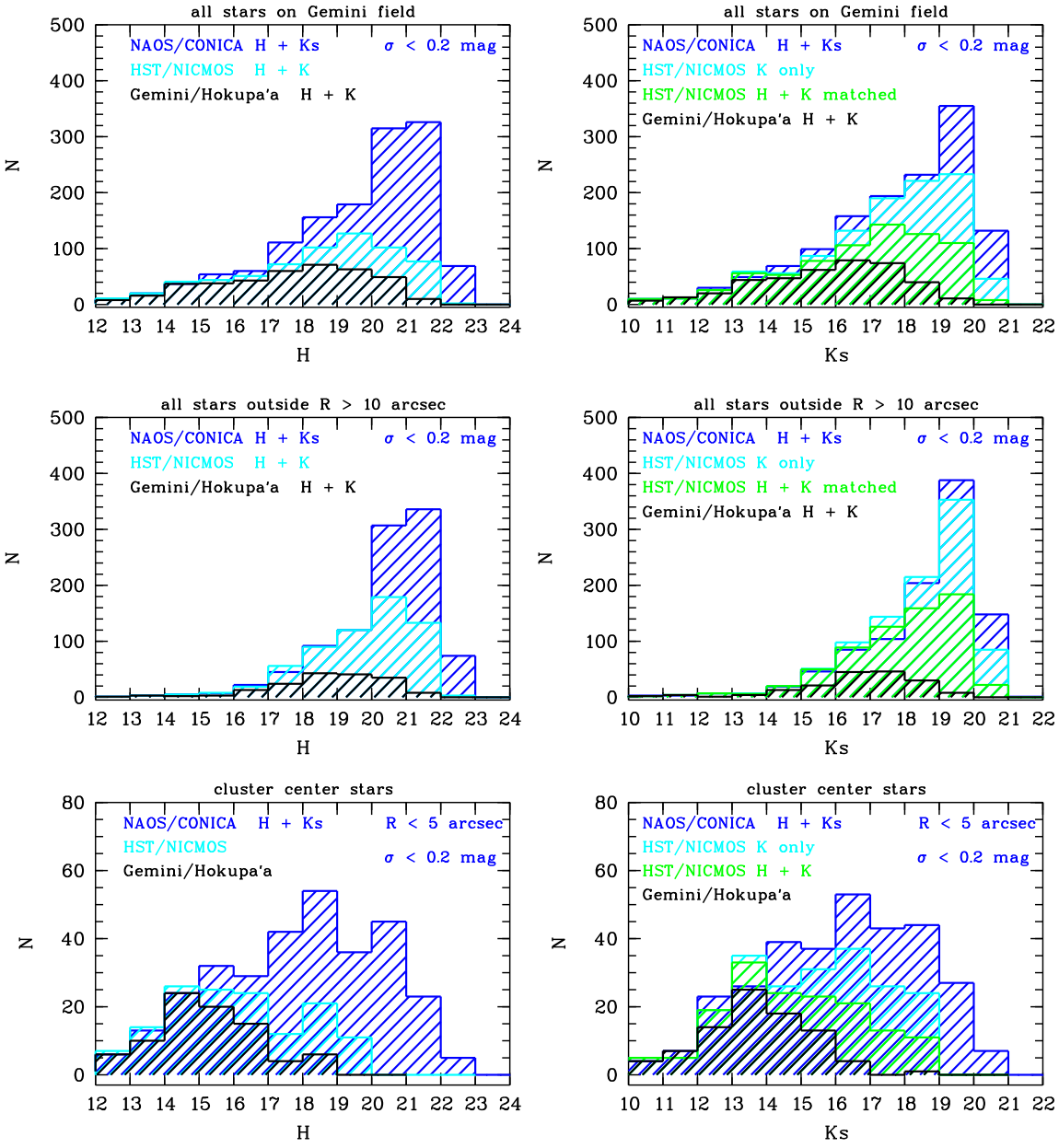

Figure 3.18: Luminosity functions of the Arches cluster derived from the NAOS-CONICA data. Top: H- and K-band LF of the entire Gemini FOV, which is the field in common in all data sets. Middle: LF of sources with radial distances $R > 10''$ from the cluster center, where the NACO LF is background limited (note that "background limited" means limited by faint background sources below the point source detection limit in this case, as opposed to neighbouring stars of the entire magnitude range as in the cluster center). Bottom: Cluster center LFs including sources with $R < 5''$, displaying the crowding-limited performance. While the NICMOS LF resembles the NACO LF closely in the background-limited case, the higher resolution of the NACO data causes a large gain in the detection of cluster center stars. This indicates that the cluster center population has been resolved entirely with NACO for the first time.

bright as $K = 15$ mag. The shape of the NICMOS K-band LF without matching with H-band data suggests that contamination by artefacts is much less severe than with NACO. However, even the K-band only LF cannot entirely reproduce the cluster population beyond $K = 15$ mag.

To disentangle the effects of the crowded cluster center from the background-limited performance on the surrounding field, the population was split up into cluster center stars ($R < 5''$) and "field" stars ($R > 10''$). The latter selection has nothing to do with real field objects, but was choses to reveal the performance on a region less limited by crowding. As can be seen in the middle panels of Fig. 3.18, stars outside $R > 10$ arcsec from the cluster center are detected with comparable completeness with NICMOS as with NACO. The H-band LF shows that within a factor of ~ 4 longer integration time, NACO can reach a detection limit about 2 mag fainter than HST with NICMOS. All the brighter bins, however, are indistinguishable. In K-band, the detection limits are roughly comparable when K-only detections with NICMOS are compared (somewhat unfairly) to H and K matches with NACO. Up to $K = 20$ mag, the LFs resemble each other very closely. Note that the detection limit for K-only detections with NACO is 1 mag deeper than displayed here, given only a factor of 1.6 longer integration time with NACO, which profits from the collecting area of the VLT 8m mirror as opposed to the HST 2.4m primary, but also has to cope with the infrared sky background.

A completely different picture arises in the cluster center. Here, the crowding severely affects the NICMOS detectability of sources. While the number of stars in the NACO LF increases out to magnitudes of $H = 19$ mag and $K = 17$ mag, the NICMOS LF cannot reproduce the resolved cluster population beyond $H = 17$ mag and $K = 14$ mag, beyond which a significant fraction of stars detected with NACO is missed by NICMOS. While the flat decrease of the NACO LF at magnitudes fainter than 20 in H and 17 in K may indicate crowding losses, where the NACO completeness fractions drop below 70 % in H and 80 % in K, the NACO LF shows an increase at brighter magnitudes, while the NICMOS LF already flattens at $H = 15$ mag. The completeness levels derived from artificial star experiments at the bright end suggest that the central population of the Arches cluster has been resolved nearly entirely, such that a mass function can be derived without the severe crowding limitations faced in previous observations.

Although it is apparent from all LFs displayed in Fig. 3.18 that the Hokupa'a data loose a significant number of stars due to the low Strehl ratio, the cluster center LF is not severely discrepant from the NICMOS LF. The shape of the LF is approximately reproduced up to $H = 17$ mag and $K = 16$ mag, explaining the consistent results obtained when deriving mass functions from the Hokupa'a and NICMOS data.

3.10 Radial variations in the NACO LF

A more detailed comparison of radial variations in the Arches LF is given in Fig. 3.19. Here, the cluster center LF is compared to successive annuli of equal areas, out to a cluster center distance of $R = 10''$. Except for the fact that more and more stars are missed by NICMOS due to the lower spatial resolution in this data set, as expected from the above discussion, a clear physical change in the shape of the LF of the cluster is seen in both data sets. Surprisingly, all of the outer annuli down to a radius of $R = 5''$ display a rather normal LF showing a strong increase in the number of stars with decreasing magnitude, as expected from a single-aged standard mass and luminosity distribution. Only a slight flattening in the nearest central annulus ($5'' < R < 7.1''$) is observed in the H-band LF in the bin between 19 and 20 mag. This tendency may also be seen in the K-band LF, where the increase in stars is reduced at $K = 18 - 19$ mag. A strong change in the shape of the LF is only seen in the densest cluster center region at $R < 5''$. Unfortunately, statistical uncertainties do not allow to split up the inner region further. Clearly, the LF in the cluster center is significantly flatter than in the outer annuli, suggesting an enhanced population of bright (i.e. massive) stars, while the relative fraction of moderately bright to faint stars is depleted. Note that the 75 % incompleteness limit for stars detected in both H and K (i.e., crowding losses taken into account) occurs at $H = 19.4$ mag

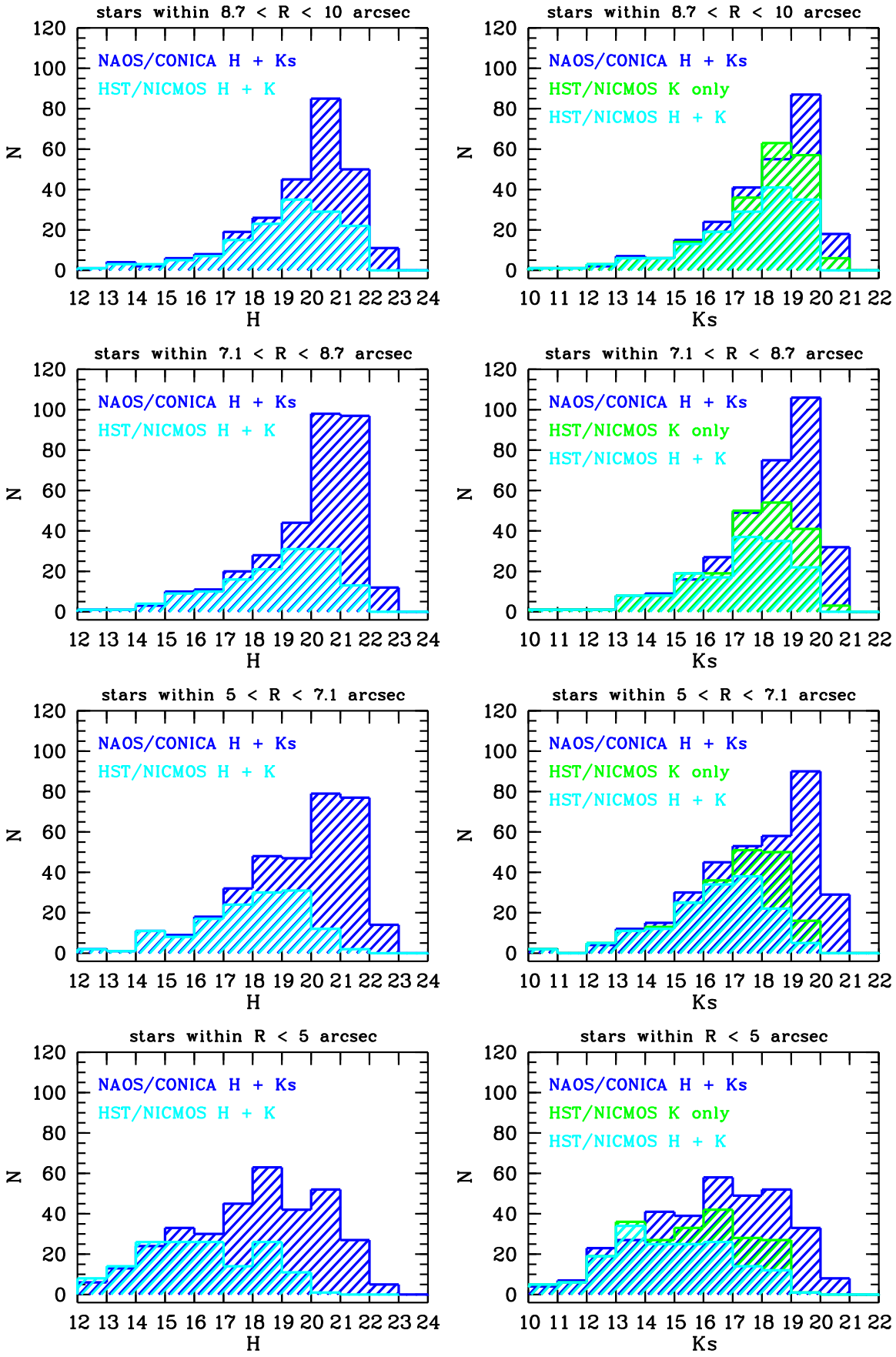

Figure 3.19: Radial changes in the luminosity functions observed with NACO.

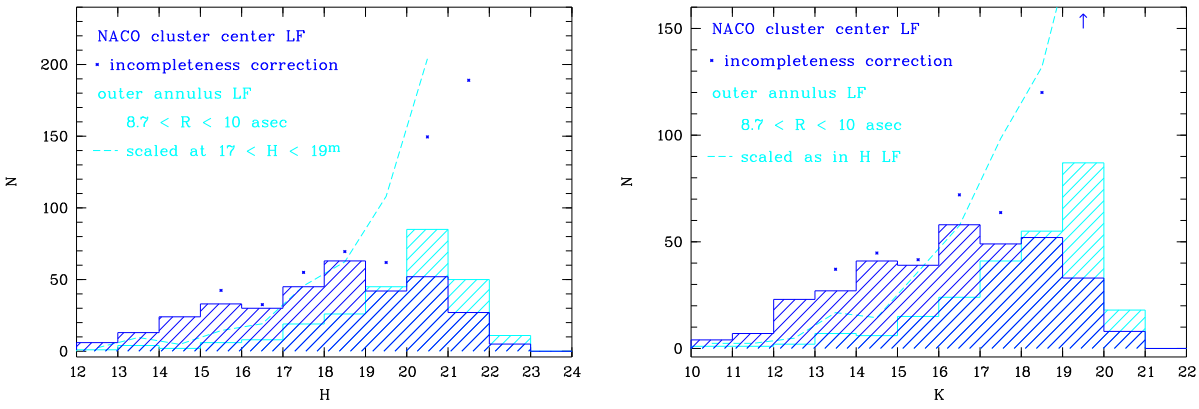

Figure 3.20: Luminosity functions in the Arches cluster center.
The H-band K-band LFs in the cluster center are shown in comparison with the outermost annulus used to trace the radial behaviour of the stellar population. The blue histogram shows the LF of stars with $R < 5''$, the cyan histogram represents the outer annulus with $8.7'' < R < 10''$. Asterisks correspond to the incompleteness corrected central LF. The dashed line is a scaled version of the outer LF, allowing to compare the shapes in more detail. A scaling factor of 2.4 has been applied to match the intermediately bright population ($16 < H < 19$ mag).

and $K = 17.7$ mag. The cluster center LFs stay constant or drop beyond these magnitudes.

To analyse the difference observed in the shape of the cluster center LF and the outer radial LFs, the cluster center LF is compared to the population of stars in the outermost annulus, $8.7'' < R < 10''$. Fig. 3.20 shows the superposition of both LFs in H and in K, including our preliminary incompleteness calculation in the cluster center (asterisks). Note that due to the restricted number of artificial stars used, statistical fluctuations are seen in the cluster center correction. Generally, each magnitude bin with $H > 17$ mag or $K > 15.5$ mag can be affected by up to 20% incompleteness in the cluster center due to crowding losses. The outer LF is complete by more than 70% in all the luminosity bins compared here, and has thus not been corrected for incompleteness in these diagrams.

First of all, we note a peak at $H = 15 - 16$ mag and $K = 14 - 15$ mag in the central LF, which is not seen in the outer population. Indeed, if we turn back to Fig. 3.19, this peak is only clearly seen at $R < 5''$, and vanishes rapidly at larger radii. Beyond 16 mag, there is a narrow region of regular increase in the H-band LF, which resembles the outer population, before the central LF drops off again at $H = 19$ mag. Although our incompleteness tests suggest the drop off to be real, thus indicating a lack of intermediate-mass stars in the central region, the next bins require strong incompleteness corrections. This could indicate that the incompleteness correction is too low in the $H = 19 - 20$ mag bin. To probe whether or not the completeness correction can account for the loss of stars in the faint bins in the cluster center, we scale the outer cluster LF by a factor of 2.4 to match the central LF at $17 < H < 19$ mag, where both LF shapes appear to be regular. Comparing the scaled LF (shown as a dashed line in Fig. 3.20) to the incompleteness corrected central LF (asterisks), we see that, even if we assume our incompleteness values to be too low in the $H = 19 - 20$ mag bin ($2.4 - 4\,M_{\odot}$), the incompleteness correction cannot explain the lack of faint stars with $H > 19$ mag in the cluster center as compared to the outer cluster regions.

Unfortunately, the situation is not as clear in the K-band LF, where incompleteness limits our analysis to magnitudes below $K = 19$ mag. The preliminary incompleteness fractions indicate again that a lack of stars is evidenced in the cluster center for stars with $K > 17$ mag. With the same scaling as applied for the outer H-band LF, the outer K-band LF matches well the central K-band LF at $15 < K < 17$ mag. Again, there is an indication of a lack of intermediate-mass stars at $K = 17 - 18$ mag ($3 - 5\,M_{\odot}$).

We have, however, ignored the fraction of field stars contaminating the outermost annulus. Without

field data comparable in depth and resolution to our cluster observations, we can currently not exclude these faint stars to be dominated by the bulge field population.

However, even if only the more than 75% complete, bright end of the luminosity distribution is considered, the shape of the central LF is much more irregular than in the outer annuli. The enhanced numbers of stars in the brightest bins is a strong indication of mass segregation effects, as observed in our previous Arches data sets. Thus, the much more complete census of stars observed with NACO does not eliminate the effects of mass segregation observed in the Arches cluster center. Quantitatively, this will be discussed in context with the mass functions derived from this more complete sample of cluster stars.

3.11 Colour-magnitude diagrams

The NAOS/CONICA colour-magnitude diagrams (CMDs) shown in Fig. 3.21 have been obtained selecting stars with formal photometric uncertainties less than 0.2 mag in H and 0.06 in K, respectively. This error selection ensures that most artefacts are rejected, as has been confirmed by visual inspection of source locations on the frame. Only few very close neighbours with separations very close to the FWHM (used as PSF fitting radius) are rejected this way. Else, mainly faint artefacts caused by hot pixels on the detector (in particular at the edges) or background fluctuations are rejected, as desired.

In case of the Hokupa'a and NICMOS photometries, an error selection of < 0.2 mag proved reliable.

The NACO CMD shows a very narrow, well-defined main sequence of the Arches cluster, which is - given a distance of 8 kpc and variable foreground extinction of more than 24 mag in the visual (still 2.7 mag at K-band wavelength, assuming a Rieke & Lebofsky 1985 extinction law) - not self-evident. Clearly, the photometric performance is more than comparable to NICMOS, which has the benefit of a significantly lower sky background. In stark contrast to this stands the low Strehl Hokupa'a photometry, where the strong seeing halos of bright stars artificially introduced an enhanced and strongly variable background. This hindered the detection of faint objects and severely limited photometric accuracy. The NICMOS data of the same field allowed us to transform all photometries to the same system. We used the NICMOS system as the reference system, such that all calibrated data refer to F160W and F205W filter magnitudes.

As can be seen in Fig. 3.16, the Hokupa'a photometric residuals show a strong dependence on distance from the cluster center, where the perturbance due to seeing halos is largest. In H-band, the separation from the guide star additionally worsens photometric performance due to the smaller isoplanatic angle at shorter wavelength. Both effects introduce a large photometric scatter thereby widening the main sequence (MS) of the cluster. As none of these effects is seen with NAOS-CONICA, the MS is very confined, in particular at the bright end, where crowded cluster center stars dominate.

When compared to the NICMOS CMD, a larger number of stars is seen at the faint end of the NACO CMD, and the main sequence is more populated. This is in accordance with the higher resolution causing a larger number of close neighbours to be resolved in the cluster center. The luminosity functions discussed in the previous section show the gain in stars detected in each magnitude intervall.

From Fig. 3.21 we conclude that with a moderate Strehl ratio good photometric performance can be obtained in a very crowded field.

3.12 Summary of the technical analysis

Adaptive optics data obtained with the Gemini/Hokupa'a and VLT/NAOS-CONICA AO systems were analysed with regard to their photometric performance and spatial resolution. A detailed comparison with space-based HST/NICMOS data showed the advantages of moderate (and high) Strehl ratio AO data exploiting the light collecting power and diffraction limited spatial resolution of an 8m class

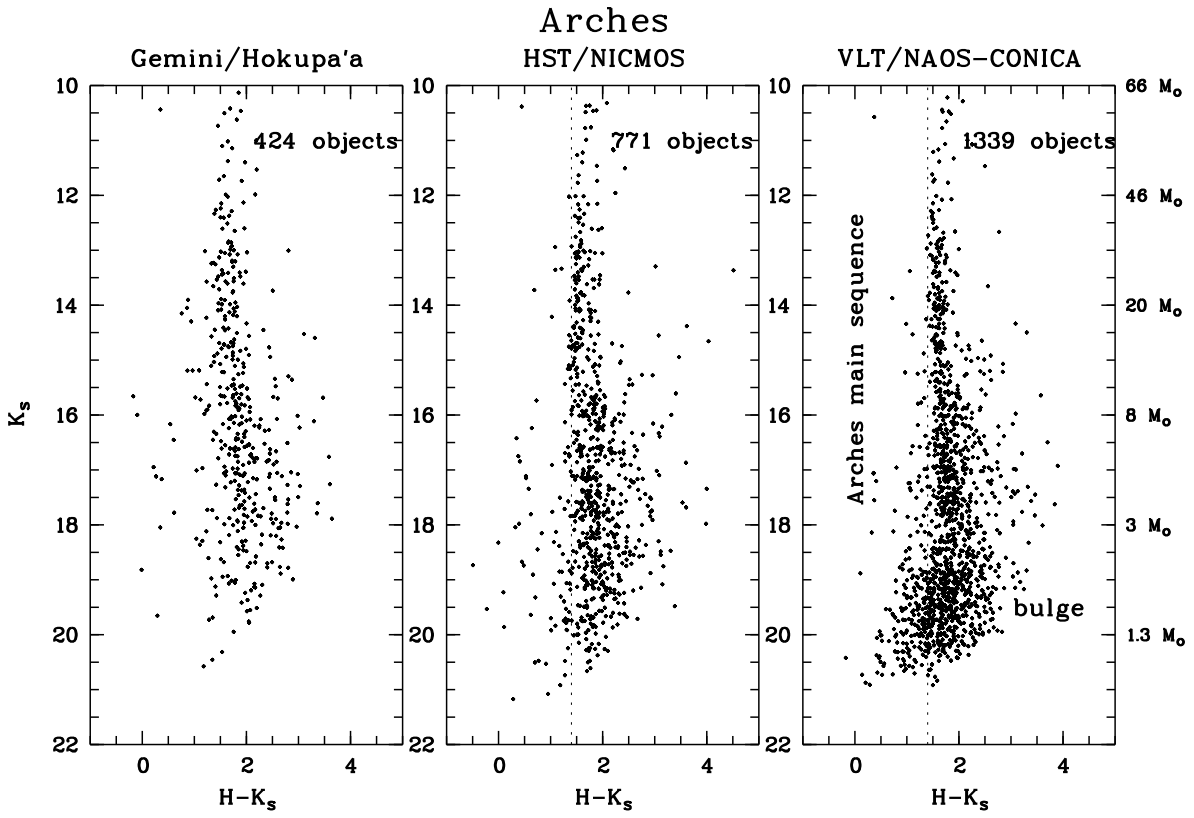

Figure 3.21: Colour-magnitude diagrams of the Arches Cluster.
CMDs of the Gemini/Hokupa'a, HST/NICMOS and NAOS/CONICA photometries are compared. Only stars located within the Gemini field of view are shown, which is the smallest of all fields, such that the spatial area covered is the same in all CMDs. The very narrow main sequence observed with NACO reflects the photometric quality of these moderate-Strehl data. At the faint end of the main sequence, bulge contamination dominates the CMD. For the first time, a slight break in the CMD at about 18 mag is seen, which may be the turn-on point of the young Arches MS population. In addition to the fainter photometry, the main sequence is also much more populated than in the NICMOS data. Indeed, the entire cluster population may be resolved for the first time. This leads to a more complete census of the Arches population, yielding a more realistic mass function.

telescope. On the other hand, the Gemini/Hokupa'a data showed that low-Strehl data can be severely limited by the extended seeing halos of bright sources, quenching the flux of nearby point sources. Maps of photometric residuals derived from the photometric calibration of Hokupa'a data against NICMOS clearly show a strong dependence of the photometric performance from the distance to bright sources and especially the bright cluster center. The fact that the flux of bright stars was overestimated with respect to the NICMOS flux, while the flux of faint stars underestimated, displayed the complexity of the AO PSF and the problems faced when analysing low-Strehl data. The suppression of faint-star detection in the denser cluster regions strongly influences the derived luminosity functions. Careful incompleteness testing is required, where the position on the field and thus the local stellar density has to be taken into account.

In contrast to the problems faced in the Hokupa'a data set, NAOS/CONICA moderate Strehl data of the central Arches field display a large gain when compared to NICMOS. The cluster center is nicely resolved into individual stars, including a large fraction of faint sources. A systematic variation of photometric performance is not seen, but a uniform performance can be reported over the CONICA field of view of $27''$. Remember that the simplistic model used in the introduction to demonstrate the

degradation of the performance over the CONICA field yielded a decrease in Strehl by about a factor of 2 in K and 3 in H under typical conditions (cf. Tab. 3.1). Note, however, that the isoplanatic angle is strongly varying depending on the interplay of turbulence in a diversity of atmospheric layers. The NAOS-CONICA data are one example of the high quality that may be achieved under excellent conditions even with a moderately bright reference star touching the limits of the wavefront sensor.

Indepent of the data quality, source detection and photometric performance of AO data strongly depend on the careful determination of parameters such as FWHM and detection threshold used by data reduction algorithms. Ideally, the spatial variation of the FWHM of the PSF kernel due to the anisoplanatism observed over the field should be taken into account in PSF fitting photometry. Fortunately, with the increase in performance and Strehl ratio using high order correction systems such as NAOS, the stellar flux can be confined into a narrow, concentrated peak facilitating the analysis. The example of the Arches cluster main sequence, with more than 1000 sources on the CONICA $27''$ field, shows that good photometry can be obtained even with a spatially constant PSF function. The photometric residuals obtained via calibration against the NICMOS Arches data also do not show any signs of spatially varying photometric performance on the combined $40'' \times 40''$ mosaic, including guide star distances of up to about $25''$. On low and moderate Strehl data, oversampling appears to reduce the limitations in crowded field data and facilitate the detection of close neighbours. Image deconvolution may also be an effective way to enhance the spatial resolution via source detection on the deconvolved image and subsequent photometry using the created coordinate list.

As expected, the AO performance is critical for the final resolution. In contrast to theoretical calculations, however, which predict a constant FWHM in the kernel of the AO PSF and a Strehl dependent peak flux (cf. Sec. 3.1), the PSF is found to widen with decreasing Strehl ratio. This may be due to the more difficult first order tip-tilt correction in the case of relatively faint guide stars such as the 16 mag guide star used for Arches, or other instrumental effects degenerating the PSF. As a consequence of this, one has to keep in mind that the Strehl ratio may not be sufficient to describe the photometric performance of moderate and low Strehl data . The flux within the (widened) PSF kernel has to be determined in dependence of observing conditions and AO system performance as well.

In summary, adaptive optics offer an excellent tool for high-resolution imaging from the ground. Moderate- to high-Strehl data allow to exploit the diffraction limit and light collecting power of 8 to 10m class telescopes. The remaining limitation on the photometric depth is thus dominated by the night sky, increasingly bright at longer wavelengths (e.g., $15 - 17$ mag in J vs. $12 - 14$ mag in K). It has to be kept in mind, however, as is demonstrated in the above sections, that the use of adaptive optics does not liberate astronomers from the seeing variations imposed by the Earth's atmosphere. The resultant AO and thus image performance is strongly dependent on observing conditions. Unique data in terms of resolution and photometric depth can be obtained under excellent conditions, but a low Strehl ratio can severely complicate the analysis. As explained in the introduction to this chapter, there is no simple dependence between AO performance and a single atmospheric parameter as e.g., the seeing. The complexity of atmosphere is to some extend reflected in the complexity of the data delivered by an AO system.

The Arches Cluster

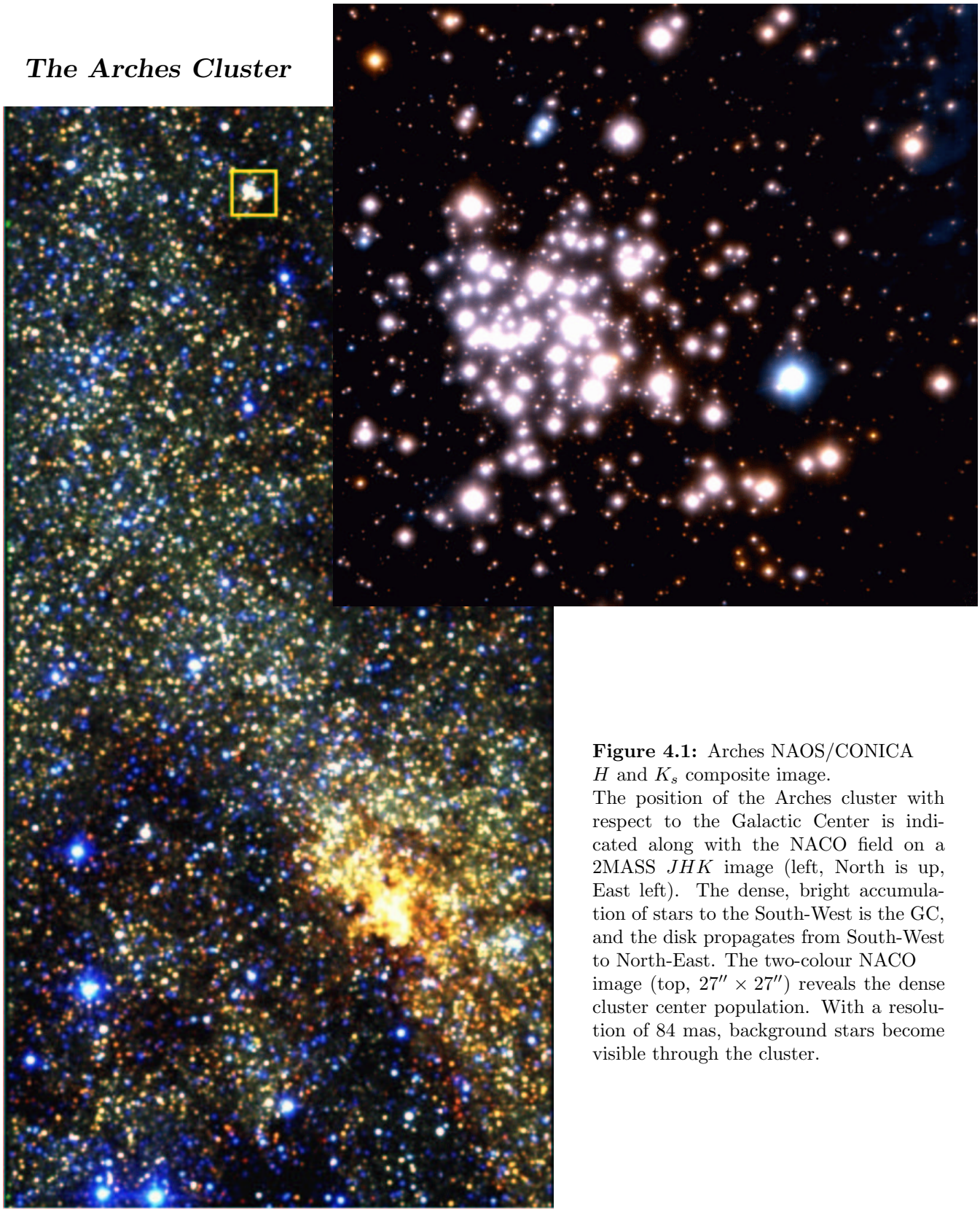

Figure 4.1: Arches NAOS/CONICA H and K_s composite image.
The position of the Arches cluster with respect to the Galactic Center is indicated along with the NACO field on a 2MASS JHK image (left, North is up, East left). The dense, bright accumulation of stars to the South-West is the GC, and the disk propagates from South-West to North-East. The two-colour NACO image (top, $27'' \times 27''$) reveals the dense cluster center population. With a resolution of 84 mas, background stars become visible through the cluster.

Chapter 4

The Arches Cluster

After the understanding of AO data gained in the previous chapter, we are now ready to move on to the scientific interpretation. First, the Gemini-Hokupa'a photometry is analyed to obtain the basis for the mass function derivation in Chap. 5. From a systematic variation of the colour over the Arches field of view, the radial variation in the extinction from the cluster core to the cluster outskirts is derived. The varying extinction will be a crucial correction factor in the mass function, as will be shown in the next chapter. The $H-K, K$ Hokupa'a colour-magnitude diagram and the NICMOS colour-colour diagram are presented. The extinction corrected colour-magnitude diagram, displaying a confined main sequence of the Arches cluster, is derived. The results of this chapter are published in Stolte et al. (2002).

4.1 Photometric results from Gemini/Hokupa'a data

4.1.1 Radial colour gradient

During the process of calibration we realised that a strong colour gradient is present in the Arches field. In Fig. 4.2, the $H-K'$ colour is plotted against radial distance from the cluster center. As the extinction law has not yet been derived for HST filters, the colour transformations in B00 were used to transform NICMOS into 2MASS magnitudes. Though the 2MASS filters deviate slightly from the standard JHK filters used to determine the extinction law (Rieke & Lebofsky 1985), the approximate amount of change in visual extinction across the field can be estimated to show the severe variation in the dust amount in the Arches cluster center. For the extinction correction performed to derive the corrected CMD and mass function, the trend as observed in the original HST data set is used, such that no assumption about the extinction law had to be made.

The extinction parameters from Rieke & Lebofsky (1985) are given by

$$A_J/A_V = 0.282 \quad A_H/A_V = 0.175 \quad A_K/A_V = 0.112, \tag{4.1}$$

where A_{Filter} is the extinction in the given filter. For a change in extinction of ΔA_V this leads to

$$\begin{aligned} \Delta A_V &= \Delta(A_J - A_H)/0.107 \\ \Delta A_V &= \Delta(A_H - A_K)/0.063 \\ \Delta A_V &= \Delta(A_J - A_K)/0.170 \end{aligned} \tag{4.2}$$

The right-hand side of each expression can be measured from the transformed HST/NICMOS JHK_s photometry. The resulting ΔA_V is given in each plot in Fig. 4.3, together with the fitting uncertainty from the rms scatter in the colour.

From the linear fits in Fig. 4.3, we see that A_V increases by about one order of magnitude over the entire field when moving outwards from the cluster center. The effect is most pronounced in the

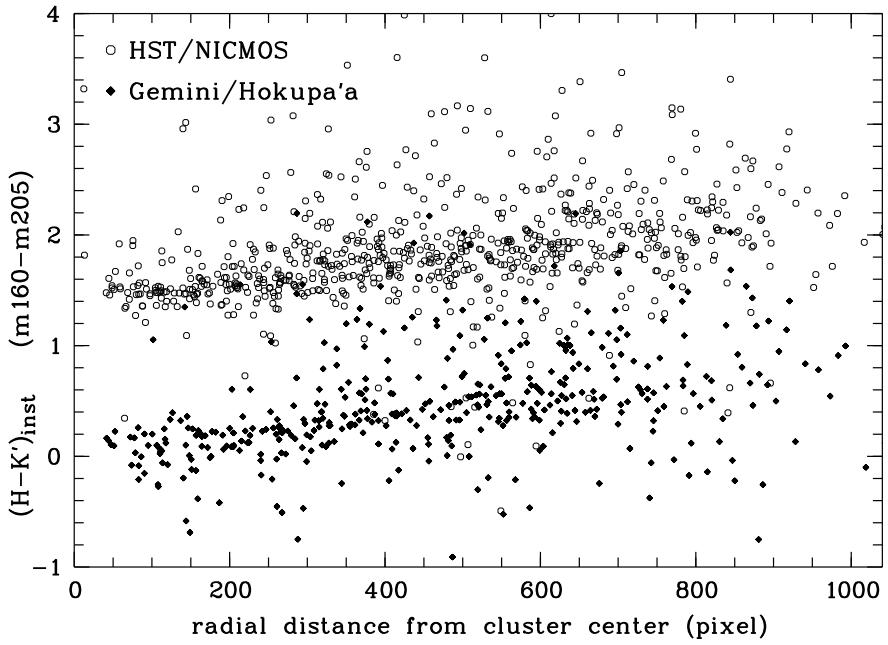

Figure 4.2: Colour variation across the Gemini field, as observed in instrumental Gemini magnitudes and HST/NICMOS data. As a trend of increasing colour excess with increasing distance from the Arches cluster center is observed in the two independent data sets, an instrumental effect as the cause for this variation is highly improbable.

HST $J - K_s$ vs. radius diagram (Fig. 4.3, bottom), where the longest colour baseline is used. A change in visual extinction of $\Delta A_V = 10.71 \pm 2.47$ mag is derived over the Gemini field (1000 pixels $\hat{=}$ 0.8 pc). Notably, if only the innermost $5''$ (250 pixels, 0.2 pc) are fitted, no variation in A_V is observed. Fitting the core separately yields $\Delta A_V = 0.77 \pm 1.12$ mag for $R < 5''$ (250 pixels) versus $\Delta A_V = 7.87 \pm 2.85$ mag for $5'' < R < 20''$ ($250 < R < 1000$ pixels). The latter value corresponds to $\Delta A_V = 10.5$ mag/1000 pix^{-1}, consistent with the trend over the entire field. The small radial trend and low extinction value in the cluster center indicates the local depletion of dust. This could be either due to winds from massive stars or due to photo-evaporation of dust grains caused by the intense UV-radiation field, or a mixture of both processes. As was discussed in the introduction, a low-extinction cavity is also observed in radio data of the HD 97950 cluster, and a similar analysis of the JHK data of this cluster will be shown in Sec. 6.4.

A change in A_V of $\sim$ 10 mag/1000 pix^{-1} is also consistent with the result found in $J - H$, 8.8 ± 2.1 mag/1000 pix^{-1}, while a larger value of $\Delta A_V = 14.9 \pm 3.2$ mag is derived from the $H - K_s$ plot. Due to the uncertainties, the final conclusion is drawn that the extinction varies by $\Delta A_V \sim 9-15$ mag across the Arches field of $20''$ or 0.8 pc, most likely closer to the lower value. This is in any case a tremendous change in the dust column density along the line of sight, with strong implications on limiting magnitudes and the potential detection of faint objects.

A linear fit to the colour variation with radius was used for $R > 5''$ to correct for the strong change in reddening observed in the outer cluster field. The values for cluster center stars ($R < 5''$) were left unchanged, due to the large scatter and the very small trend found. Thus, these adjusted colours are scaled to the cluster center, where A_V is lowest. From the Rieke & Lebofsky (1985) extinction law, the change in K-band magnitude with radius corresponding to the change in colour can be derived as $\Delta A_K = 0.112/0.063 \cdot \Delta A_{H-K}$. The K-band magnitudes are adjusted accordingly. The dereddened colour-magnitude diagrams will be shown in direct comparison with the observed CMDs in Sec. 4.1.3 (cf. Fig. 4.6).

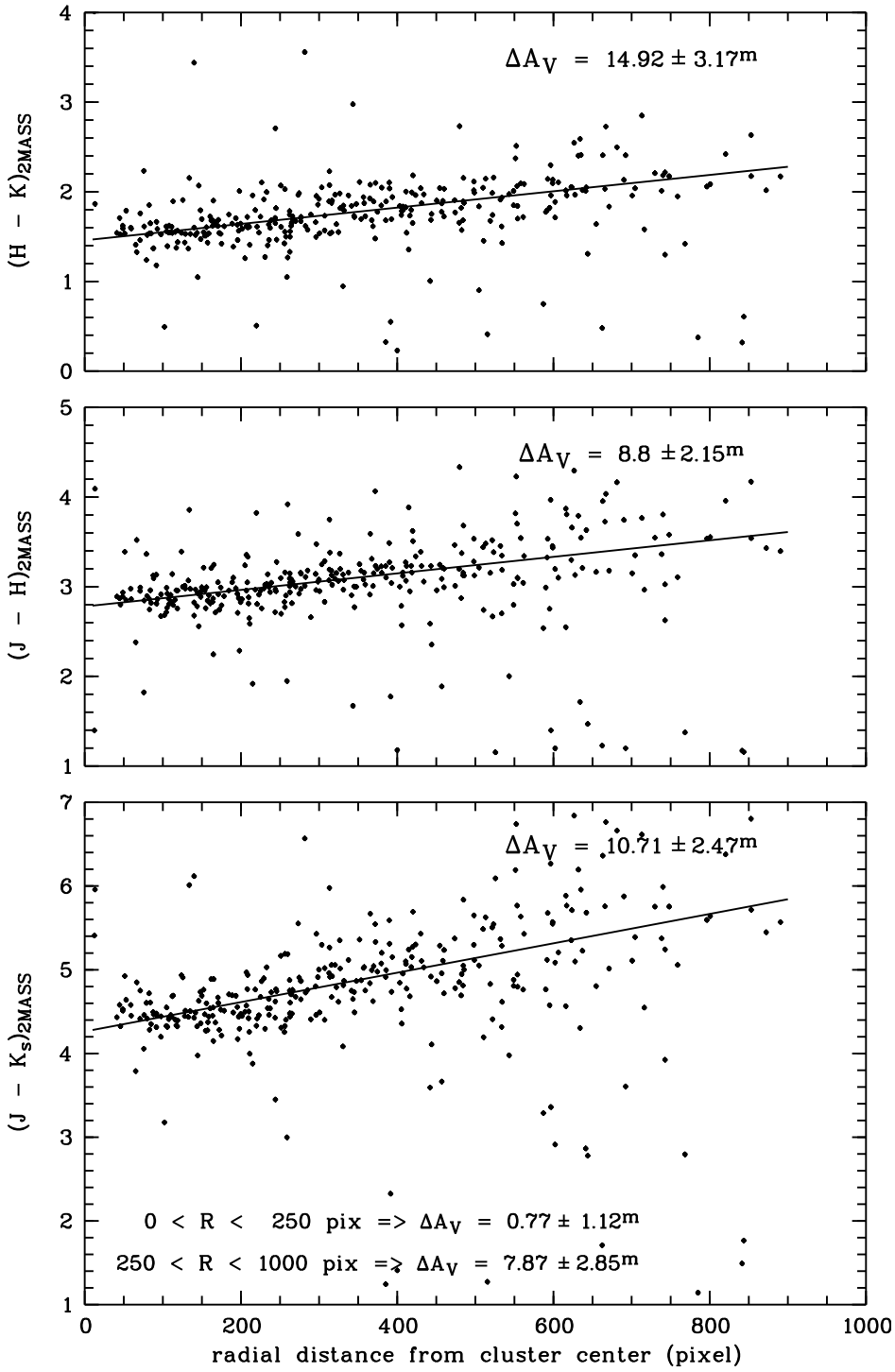

Figure 4.3: Colour trends over the Arches field as observed in the HST/NICMOS data set within the area covered by the Gemini observations. The radial distance from the cluster center is given in pixels on the Gemini scale. For the calculation of ΔA_V, the Rieke & Lebofsky (1985) reddening law has been assumed.

4.1.2 Extinction maps

The individual extinction for each object can be calculated by shifting it along the reddening vector onto the isochrone. If we assume that intrinsic reddening plays only a minor role for most of the stars within the cluster, the individual reddenings derived for each star can be combined to estimate the average spatial extinction variation. In practice, an arbitrary reddening of $A_V = 15$ mag was applied to a 2 Myr isochrone of the Geneva set of models (Lejeune & Schaerer 2001), and the relative shifts are then corrected to $A_V - 0$ mag. This choice of reddening ensures that the isochrone serves as a blue envelope for the bulk of the cluster stars, which are significantly more reddened ($A_V \approx 30$ mag) . The choice of the isochrone will be discussed in the context of the mass function (Sec. 5.1), where the physical effects of the population model used are more important. As discussed in Grebel et al. (1996), colours of main-sequence stars also depend on binarity, stellar rotation, and intrinsic infrared excess. These effects are ignored here since they cannot be distinguished from reddening effects. In the worst case, the reddening for some stars will be overestimad due to the imposed scatter towards redder colours in the CMD. The median value in each combined area is chosen instead of the average to reject the most extreme outliers. Each star is shifted along the reddening path in colour-magnitude space until the intersection with the isochrone is found, again assuming that the relative slopes of the extinction law approximately follow a Rieke & Lebofsky (1985) law. The relative shift yields the individual reddening ΔA_V of each star. These values are combined into areas of 50×50 pixels to display large-scale spatial extinction variations. The resulting extinction map for the Hokupa'a photometry is shown in Fig. 4.4.

Since the original HST/NICMOS field has twice the area of the Gemini central Arches field, the extinction map is also calculated for the entire NICMOS field following the same procedure. The corresponding map is shown in Fig. 4.5.

The extinction measured with this procedure in the K-band lies in the range $1.9 < A_K < 4.1$ mag, with an average value of 3.1 mag, corresponding to $16 < A_V < 37$ mag, $<A_V>= 27.7$ mag. Cotera et al. (2000) derive a near-infrared extinction of $2.8 < A_K < 4.2$ mag, with an average value of $<A_K> = 3.3$ mag for 15 lines of sight towards several Galactic Center regions, corresponding to an average visual extinction of $<A_V> = 29.5$ mag (transformed using Rieke & Lebofsky (1985)). They obtain the highest extinction towards a field close to the Arches cluster, $A_V = 37.5$ mag. This is very close to our highest extinction value. The average value determined from individual dereddening here is the same as the average extinction obtained by Figer et al. (1999), $< A_V > = 27.7$ mag. Note that the typical random scatter $\sigma(A_K)$ from foreground dust density fluctuations found in GC fields is linearly related to the average extinction within a field. The relation determined by Frogel et al. (1999) from giant branch stars in 22 pointings towards fields within 4° of the GC is given by $\sigma(A_K) = 0.056(\pm 0.005) <A_K> + 0.043(\pm 0.005)$. This yields an expected natural scatter from GC clouds of only $\sigma(A_K) = 0.22$ mag for $< A_K > = 3.1$ mag, much below the difference in reddening observed in the Arches field. Thus, the change in extinction cannot be explained by the natural fluctuations of the dust distribution in the GC region.

Comparison of the cluster center main sequence population with the main sequence colour of a theoretical 2 Myr isochrone from the Geneva set of models (Lejeune & Schaerer 2001), later-on used for the derivation of the mass function, yields an average extinction of $A_V = 24.1 \pm 0.8$ mag in the cluster center. This extinction value has been used to transform isochrone magnitudes and colours into the cluster magnitude system. It has been suggested that the brightest and most massive stars in Arches are Wolf-Rayet stars of type WN7 (Cotera et al. 1996; Blum et al. 2001). Fundamental parameters of Wolf-Rayet stars are compiled in Crowther et al. (1995). For stars of subtype WN7 they find typical colours of $(H - K) \sim 0.2$ mag. The observed $H - K$ colour of ~ 1.77 mag for the WN7 stars, which were identified by comparison with the Blum et al. (2001) narrow band photometry, leads to an extinction of $A_V = 24.9 \pm 2.4$ mag . This value is in very good agreement with the A_V determined from the main sequence colour in the cluster center.

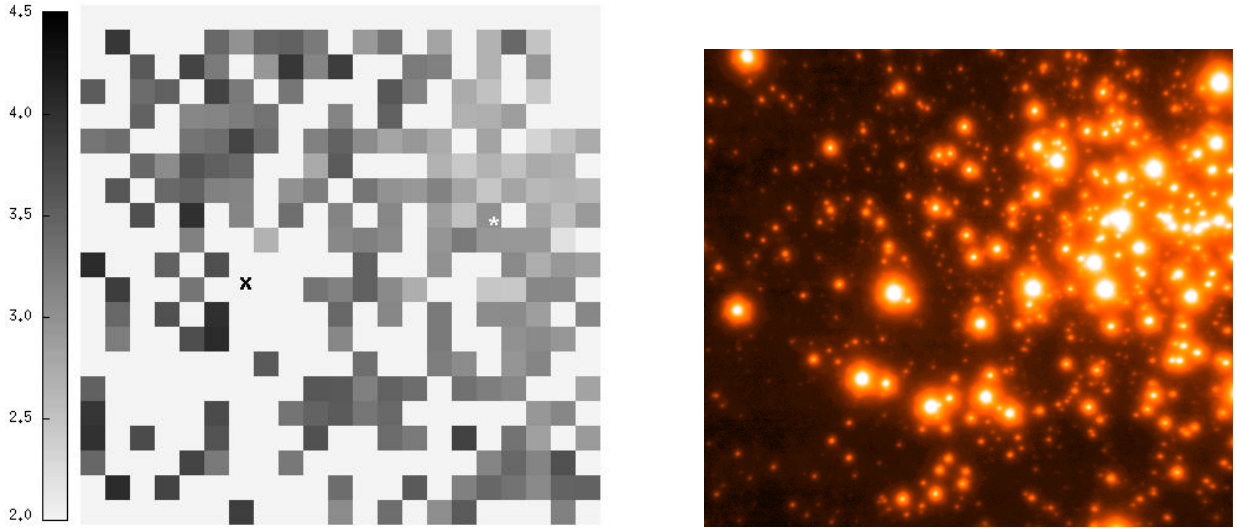

Figure 4.4: Extinction map of the Arches cluster center derived from Gemini/Hokupa'a K-band.
A_K extinction map, binned into areas of 50×50 pixels ($1'' \times 1''$), with each value representing the median individual reddening of all stars in each bin (North is up, East is to the right). White spots are positions without stars for evaluation. The individual extinction was calculated by shifting the stars in the K vs. $H-K$ colour-magnitude diagram to a 2 Myr isochrone. This results in a minimum A_K of 1.86 mag, and a maximum of 4.08 mag, assuming a Rieke & Lebofsky (1985) extinction law.

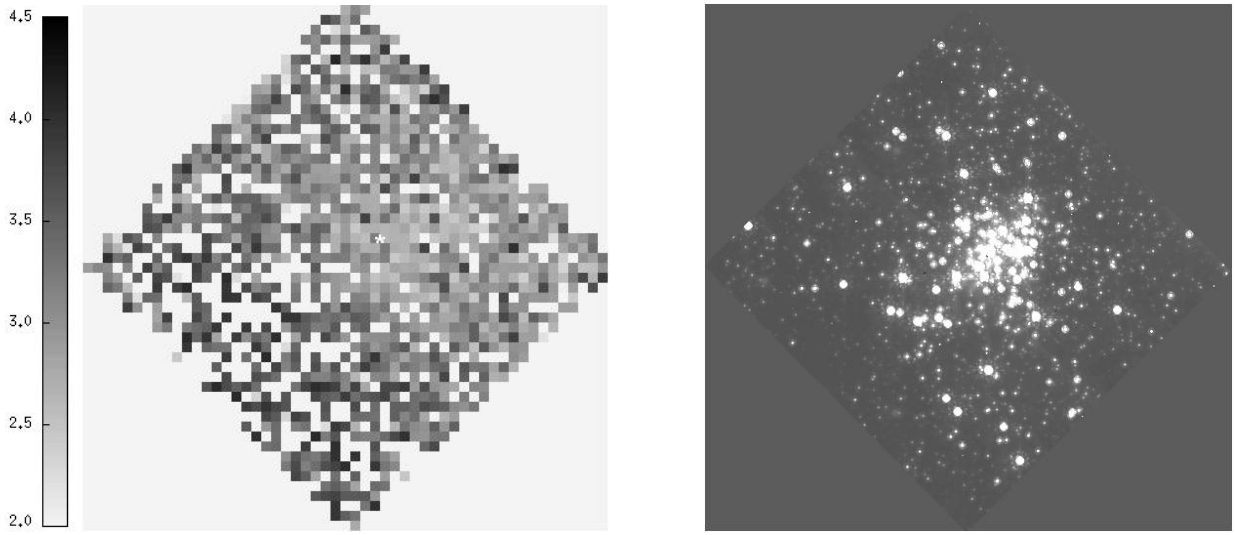

Figure 4.5: A_K extinction map derived from HST $m205$ photometry.
See Fig. 4.4 for details. The coordinate transformed HST/NICMOS F205W image is also shown for comparison. Note the different scales (HST/NICMOS: $40'' \times 40''$, Gemini/Hokupa'a: $20'' \times 20''$).

4.1.3 Colour-magnitude diagrams

The resulting colour-magnitude diagrams for Gemini and HST are presented in Fig. 4.6 (upper panel). Two important differences are seen when inspecting the CMDs. First, the scatter in the main sequence is significantly larger in the ground-based photometry. While the HST/NICMOS CMD reveals a narrow main sequence in the cluster center (marked in cyan in Fig. 4.6), the same stars display a much larger colour range in the Gemini CMD. The poor Strehl ratio in the Gemini/Hokupa'a data as compared to the HST/NICMOS data (see Sec. 3.2.1.5) causes a high, non-uniform additional background due to uncompensated seeing halos around bright stars, which decreases photometric accuracy. In the dense regions of the cluster center, where crowding problems are most severe, the photometry is most affected. The number of faint, unresolved companion stars that merge into the high stellar background underneath the bright cluster population is very high. As discussed in Sec. 3.2.1.4, the halos of the bright stars hinder the detection of faint objects despite the principally high spatial resolution seen in individual PSF kernels. Operating at the diffraction limit, NICMOS is not restricted by these effects, yielding a better effective resolution especially in the dense regions. A tighter main sequence and less scatter is the consequence. In Fig. 4.6, the innermost $5''$ of the Arches cluster are marked in cyan. It is clearly seen that most massive (bright) stars are located in the cluster center.

A second effect observed is the much larger number of faint objects seen in the HST data (cf. Fig. 3.2). As the limiting magnitude and the measured spatial resolution of the images are similar in both data sets, this, too, has to be a consequence of the low Strehl ratio in the AO data.

The lower panel of Fig. 4.6 shows the "dereddened" CMDs, corrected for the radial colour gradient found and the corresponding change in extinction, ΔA_K (Sec. 4.1.1). The colours of stars beyond $R > 5''$ have been adjusted to the colour of the cluster center. Comparison with the original CMDs shows that most of the bright, seemingly reddened stars fall onto the same main sequence after correcting for the colour trend. These stars are located at larger distances from the cluster center and thus suffer from more reddening by residual dust. As will be discussed in the context of the mass function (Sec. 5.1), these stars might have formed close to the cluster at a similar time as the cluster population. At the faint end of the CMD, there are, however, a large number of objects that remain unusually red after the correction is applied. These objects may either be pre-main sequence stars or faint background sources. Unfortunately, it is not possible to disentangle these two possible contributions, such that objects significantly reddened with respect to the main sequence will be excluded when deriving the mass function.

4.1.4 HST/NICMOS colour-colour diagram

For comparison with the reddening path and a main sequence in standard colours, the NICMOS filters have been transformed into the 2MASS JHK_s system. In Fig. 4.7, the transformed HST/NICMOS colour-colour diagram is shown, including all stars bright enough to be observed in all three filters. The A_V values are from the Rieke & Lebofsky (1985) extinction law for standard JHK photometry. Though some uncertainty remains due to the transformation of severely reddened stars, the proximity of the reddening path to the data points supports the validity of the equations derived by B00. Changing the transformation parameters slightly results in a large angle between the data points and the reddening path.

A wide spread population of stars is clearly seen along the reddening path, as expected from the colour trend discussed in Sec. 4.1.1 (no correction for the varying extinction is applied in this diagram). Again, the stars with the lowest reddening within the cluster population are the bright stars in the Arches cluster center. Moving along the reddening line towards higher values of A_V mainly means moving radially outwards from the cluster center. As in the CMD, a correction for the observed colour gradient causes the bulk of the stars to fall onto the main sequence with a reddening of $A_V = 24$ mag, corresponding to the cluster center.

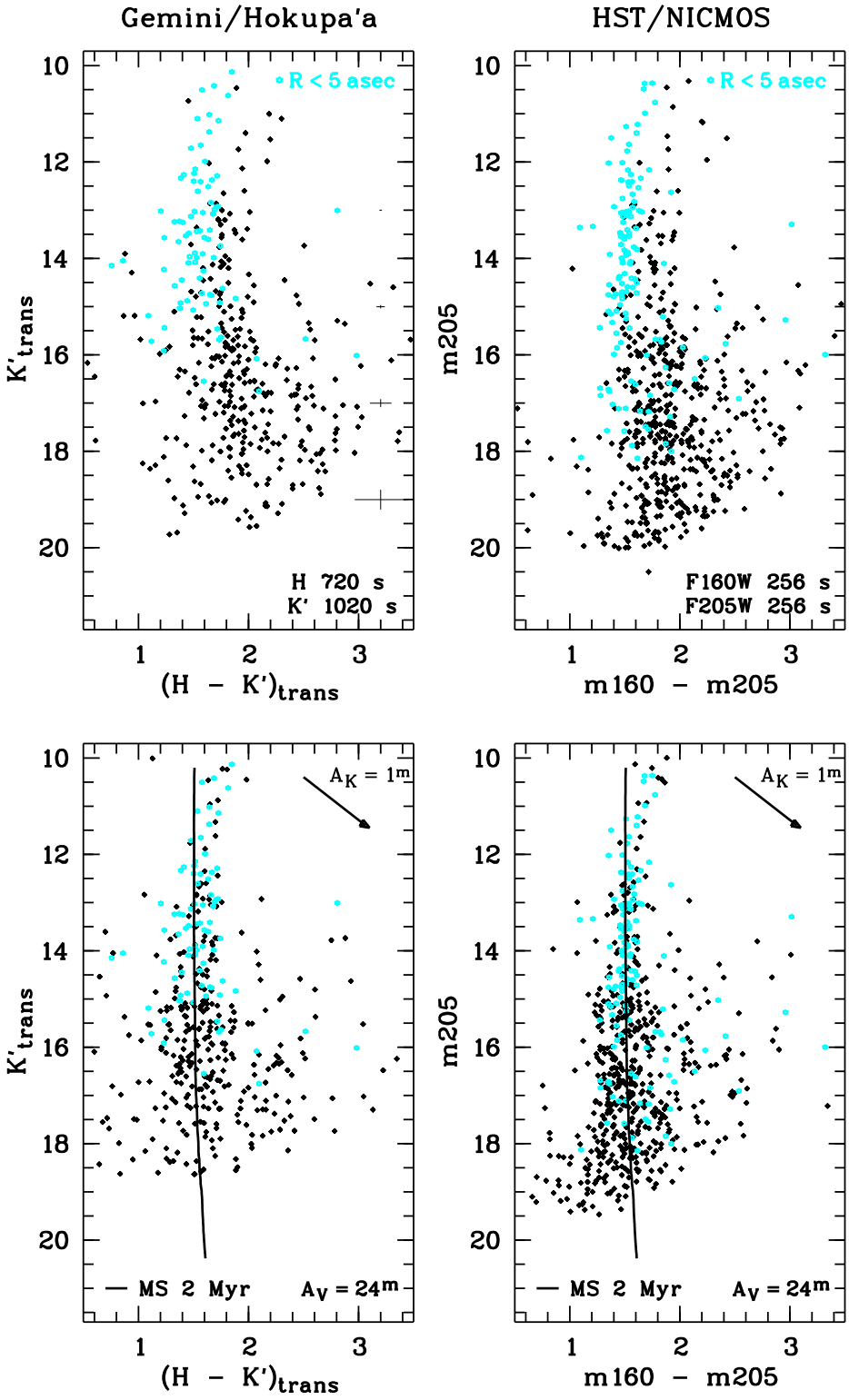

Figure 4.6: Colour-magnitude diagrams.
Left: Gemini/Hokupa'a, right: HST/NICMOS
Lower panel: CMDs corrected for radial reddening gradient (Sec. 4.1.1)
Blue stars mark objects in the cluster center ($R < 5''$), displaying a tight main sequence in accordance with a constant reddening observed in the cluster center. The center stars mark the blueward boundary of the Arches population in the CMD, consistent with the lowest extinction found in the field. The uncertainties in colour and magnitude in the Hokupa'a photometry are indicated in the upper left diagram, as derived from artificial star tests. In the corrected CMDs (lower panels), the 2 Myr Geneva isochrone (Lejeune & Schaerer 2001) used to transform magnitudes into masses is overlaid as a thick line. The reddening vector is also shown.

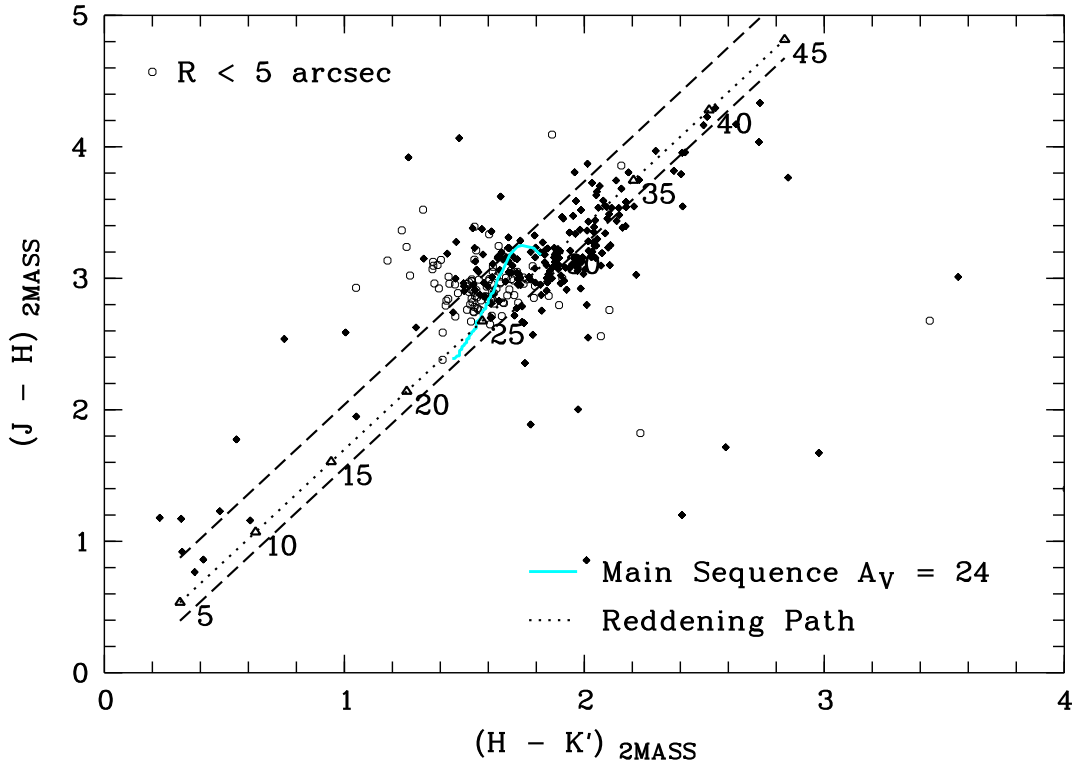

Figure 4.7: Two-colour diagram from HST observations.
For comparison with the standard reddening law, F110W, F160W and F205W magnitudes are transformed to 2 MASS JHK_s photometry using the colour equations in B00. The reddening path according to Rieke & Lebofsky (1985) is shown as a straight line labeled with A_V values, and the main sequence is indicated by the thick grey line. The area between the dashed lines marks the region of reddened main sequence stars. Cluster center stars ($R < 5''$), marked as open circles, are predominantly found around $A_V \approx 25$ mag, while stars at larger radii populate increasingly redder loci along the reddening path.

4.2 Implications for the mass function derivation

The extinction variation causes stars at larger cluster center distances to be more severely reddened than stars in the cluster center. These stars will appear fainter in the CMD. Cluster center stars, on the other hand, occupy a locus without additional extinction bias, and the average extinction applied allows a straight-forward mass determination. As the cluster center is dominated by the bright, massive stellar population, while intermediate-mass stars become increasingly important at larger radii, the masses of intermediate-mass stars are systematically underestimated. The correction of this extinction bias is thus a critical ingredient to an unbiased mass function derivation.

As these effects and, in particular, the contamination with field stars become increasingly important when progressing to fainter stars, the NAOS/CONICA colour-magnitude diagram is much more affected than the Gemini/Hokupa'a CMD. As the details observed in the NACO CMD are reflected in the resultant mass function, the CMDs are shown and discussed in the context of the MF calculation in Sec. 5.2.1.

Chapter 5

The Mass Function of the Arches cluster

The mass function as defined in Sec. 2.3 is derived from the $H-K, K$ colour-magnitude diagram in the following sections. First, the present-day MF as obtained from the Gemini/Hokupa'a data is discussed in Secs. 5.1.1 and 5.1.2, and radial variations in the mass function slope are analysed in Sec. 5.1.3. Preliminary cumulative functions are created from the Hokupa'a mass distribution to emphasise the effects of mass segregation. In Sec. 5.2.1, the Arches MF is re-derived from the more complete NAOS/CONICA data set. The better resolution of the Arches cluster center increases the available number of stars for the MF derivation. Several methods are introduced to circumvent the strong dependence of binning in the mass function derivation, and cumulative functions are studied in comparison to the theoretically expected single power-law shape.

5.1 The mass function from Gemini/Hokupa'a data

5.1.1 Integrated mass function

The present-day mass function (Fig. 5.1) of the Arches cluster has been derived from the colour-magnitude diagram by transforming stellar luminosities into masses via a 2 Myr isochrone from the Geneva basic set of stellar evolution models (Lejeune & Schaerer 2001). Enhanced mass loss models were also used, but did not alter the resultant mass function. Stellar evolution (mass loss, giant evolution) is not important on timescales of the Arches age of ~ 2 Myr for stars with initial masses of $M < 50\,M_\odot$ ($\log(M/M_\odot) < 1.7$, i.e. stellar evolution affects the two upper mass bins (see below) of the MF at most). No attempt has been made to reconstruct the initial mass function (IMF) from the present-day MF for $M > 50\,M_\odot$. A distance modulus of 14.5 mag and an extinction of $A_V = 24.1$ mag, corresponding to the cluster center, were applied to the isochrone prior to the transformation.

The slopes of all mass functions discussed have been derived by performing a weighted least-squares fit to the number of stars per mass bin. The size of the mass bins was chosen to be $\delta \log(M/M_\odot) = 0.1$ as the best compromise between mass function resolution and statistical relevance. This bin size is significantly larger than the photometric uncertainty in the corresponding magnitude range. Only mass bins with a completeness factor of $\geq 75\%$ have been included in the fit.

Note that no attempt was made to subtract the field star contribution. As can be seen in Fig. 3.1, the Gemini field is mostly restricted to the densest cluster region. When comparing to an arbitrary part of the GC field, we cannot expect to observe the same distribution of stars as in the Arches field, as the faint, reddened background sources are undetectable due to the high density of bright sources in the cluster area. The strong variability of the stellar density in the GC renders the determination of the field star contribution from neighbouring fields even more difficult. Neither the Gemini nor the HST field covers enough area to estimate the field star population in the immediate vicinity of the cluster.

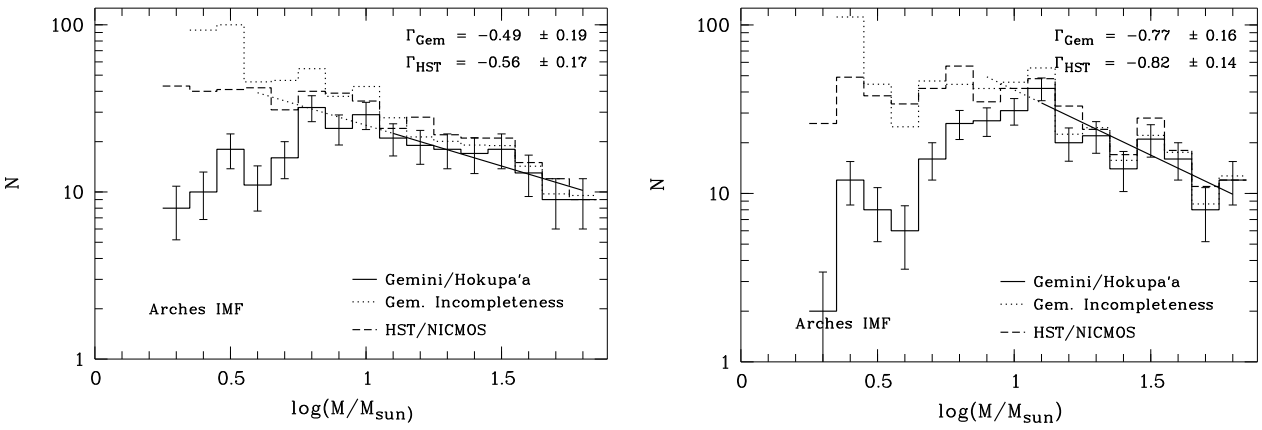

Figure 5.1: Arches mass function as derived from Gemini/Hokupa'a.
The Arches MF was calculated from the colour-magnitude diagram shown in Fig. 4.6. A 2 Myr main sequence isochrone from the Geneva set of models (Lejeune & Schaerer 2001) was used to transform magnitudes into stellar masses. The mass function has been derived for bins of $\delta \log(M/M_\odot) = 0.1$ with a lowest mass bin $\log(M/M_\odot) \geq 0.20$. Left panel: without A_K correction; right panel: with A_K correction

A main sequence colour cut ($1.15 < H - K < 1.90$ mag) has been applied to the colour-corrected CMDs to select Arches members, excluding blue foreground and red background sources.

To allow for a direct comparison with the results obtained in F99, isochrones calculated for a metallicity of $Z = 0.04$, twice the solar metallicity, are used for all MF derivations. The derived MFs with and without prior extinction correction are displayed in Fig. 5.1. The overall mass function derived from the dereddened Gemini data displays the same slope as derived from NICMOS within the uncertainties, namely $\Gamma_{\rm Gemini} = -0.77 \pm 0.16$ and $\Gamma_{\rm HST} = -0.82 \pm 0.14$ fitted for $10 < M < 65\ M_\odot$, which may be extrapolated down to 6 $M_\odot$ when taking into account the incompleteness correction. The present-day upper mass of 65 $M_\odot$ corresponds to an *initial* mass of about 100 $M_\odot$ according to the Geneva models. F99 derive an overall slope of $\Gamma = -0.7 \pm 0.1$ in the inital mass range $6 < M < 120\ M_\odot$, in good agreement with these results. The remaining difference in the maximum mass is due to the different extinction and the extinction corrections applied, which represent one of the largest uncertainties in the mass function derivation. As in particular the correction of the K magnitude for the varying extinction is uncertain due to the unknown extinction law of the NICMOS filters, the mass function was also derived for uncorrected K magnitudes, with only the colour correction applied, which is independent of the extinction law assumed. In this case, the MF appears flatter with a slope of $\Gamma \sim -0.5 \pm 0.2$ (Fig. 5.1, left panel). The discrepancy in the derived slopes clearly shows that the effects of differential extinction are not negligible, especially when deriving mass functions for very young regions, where the reddening varies significantly.

Furthermore, the effect of the binning on the MF was checked by shifting the starting point of each bin by one tenth of the bin-width, $\delta \log(M/M_\odot) = 0.01$. The resultant slopes range from $-0.69 \pm 0.13 < \Gamma_{\rm Gemini} < -0.90 \pm 0.15$ and $-0.79 \pm 0.12 < \Gamma_{\rm HST} < -0.98 \pm 0.13$. The average slopes for Gemini and HST, $\Gamma_{\rm Gemini} = -0.77 \pm 0.15$ and $\Gamma_{\rm HST} = -0.86 \pm 0.13$, respectively, agree well within the errors. The slightly flatter slope observed in the Gemini data may reflect the more severe incompleteness due to crowding. Although all slopes are consistent within the errors, the range in slopes derived by scanning the bin-step shows that statistical effects due to the binning may not be entirely neglected in the MF derivation.

The metallicity within the immediate Galactic Center region has been a matter of discussion during the past decade. Several authors report supersolar metallicities derived from CO index strength and TiO bands in bulge stars (Frogel & Whitford 1987; Rich 1988; Terndrup et al. 1990, 1991). Carr et al. (2000) measure [Fe/H] $= -0.02 \pm 0.13$ dex for the 7 Myr old supergiant IRS 7, and Ramirez et al.

(2000) derive an average of [Fe/H] = $+0.12 \pm 0.22$ dex for 10 young to intermediate age supergiants, both very close to the solar value.

Using a 2 Myr isochrone with solar metallicity Z=0.02, the average slope of all bin steps is $\Gamma_{\rm Gemini} = -0.84 \pm 0.13$ and $\Gamma_{\rm HST} = -0.91 \pm 0.12$. The mass function is thus not significantly altered when using solar instead of enhanced GC metallicity. We note, however, that a lower metallicity (i.e., in this case solar) steepens the MF slightly, thus working into the same direction as the incompleteness correction.

F99 report a flat portion of the MF in the range $15 < M < 50\ M_\odot$, which is not seen in the Gemini MF. This plateau can, however, be recovered, when we create a MF from K-band magnitudes uncorrected for differential extinction, and use a lowest mass of $\log(M_{low}/M_\odot) = 0.25$. For $\log(M_{low}/M_\odot) = 0.20$ the plateau is seen neither with nor without extinction correction. This, again, shows the dependence of the shape of the MF on the extinction corrections applied, as well as on the chosen binning.

From the considerations above, the overall mass function of the Arches cluster is found to display a slope of $\Gamma = -0.8$ to -0.9 in the range $6 < M < 65\ M_\odot$. Although the uncertainty of missing lower mass stars in the immediate cluster center remains, the incompleteness correction strongly supports the derived shape of the MF. If the flat slope would be solely due to a low recovery rate of low-mass stars in the cluster center, this should be visible in a much steeper rise of the incompleteness corrected MF in contrast to the observed MF. In summary, the MF slope observed in the Arches cluster from Gemini/Hokupa'a data appears significantly flatter than the Salpeter slope of $\Gamma = -1.35$. When compared to the average MF slope of $\Gamma = -1.1$ observed in star-forming regions in the Milky Way, however, the slope in the Arches cluster displays only a slight flattening. Although the evidence for flattening in the integrated MF is not very pronounced, the derived slope yields the first indication of the efficient production of high-mass stars in the Arches cluster and the GC environment.

When the radial variation in the MF is discussed in Sec. 5.1.3, this suggestion will be strengthened from the strong bias of the stellar mass distribution in the cluster center to high-mass stars.

5.1.2 Effects of the chosen isochrone, bin size, and metallicity

Blum et al. (2001) estimate a cluster age of $2 - 4.5$ Myr for Arches assuming that the observed high-mass stars are of type WN7. If we compare the Geneva basic grid of isochrones with fundamental parameters obtained for WN7 stars (Crowther et al. 1995), a reasonable upper age limit for this set of isochrones is ~ 3.5 Myr. Crowther compares the parameters derived for WN stars with evolutionary models at solar metallicity from Schaller et al. (1992) and with the mass-luminosity relation for O supergiants from Howarth & Prinja (1989), yielding a mass range of $20 - 55\,M_\odot$, but with high uncertainties at the low-mass end. The more reliable mass estimates for the colour and magnitude range observed for WN stars in Arches are restricted to $35 < M < 55\ M_\odot$. From spectroscopic binaries, the masses of two WN7 stars are determined to be $\sim 30\ M_\odot$ and $> 48\ M_\odot$ (Smith & Maeder 1989). The theoretical lower limit to form Wolf-Rayet stars is $25\ M_\odot$ for the Geneva models (Schaerer et al. 1993).

In the Geneva basic grid of models with $Z = 0.04$, the 3.5 Myr isochrone is limited by a turnoff mass of $32\,M_\odot$. We have thus calculated mass functions for isochrones with ages 2.5, 3.2, and 3.5 Myr in addition to the 2 Myr case discussed above. Though the derived slopes scatter widely, irrespective of the isochrone used, the average slope of the MF tends to be even *flatter* for any of the older population models. We thus conclude that, regardless of the choice of model and parameters, the Arches mass function displays a flat slope.

5.1.3 Radial variation in the mass function

The radial variation of the mass function is particularly interesting with respect to the evolution of a young starburst cluster. For this purposed, the stellar population in Arches was analysed within three different radial bins, $0'' < R < 5''$, $5'' < R < 10''$ and $10'' < R < 20''$. The resulting mass functions

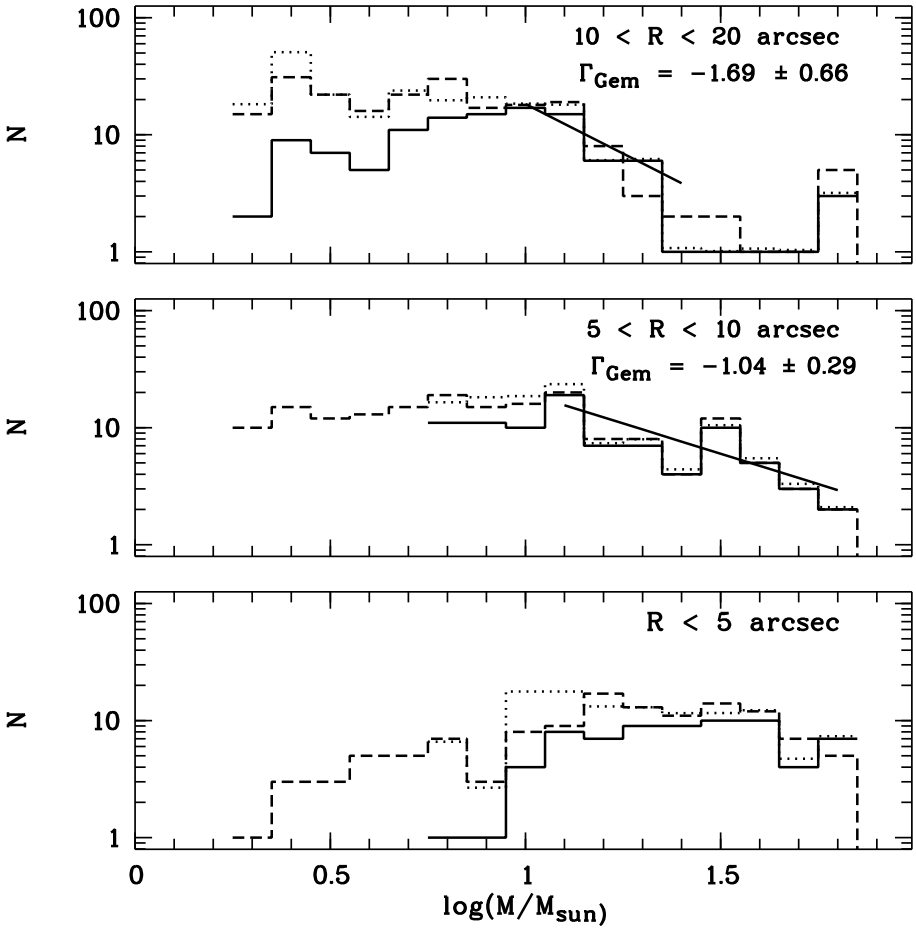

Figure 5.2: Radial change of the mass function as observed in the Gemini/Hokupa'a data.
A very flat mass function is seen in the inner cluster regions, where predominantly massive stars are found. The slope of the mass function increases towards the Salpeter value ($\Gamma = -1.35$) already at a radial distance from the cluster center of $> 10''$ (0.4 pc at a distance of 8 kpc).

for the Gemini and HST data sets, along with the radius dependent incompleteness correction for the Gemini MFs, are displayed in Fig. 5.2.

The flat mass function observed by F99 in the innermost regions of the cluster is confirmed ($R < 5''$), steepening rapidly with increasing radii beyond the innermost few arcseconds. Most of the bright, massive stars are found in the dense cluster center, where the mass function slope is very flat. F99 derive a slope of $\Gamma = -0.1 \pm 0.2$ from the HST data in this region, which is consistent with Fig. 5.2. It is obvious from the lowest panel in Fig. 5.2 that in the case of the Gemini data the strong limitation due to crowding in the innermost cluster region prohibits to fit a slope for $R < 5''$.

In the next bin, $5'' < R < 10''$, the mass function obtained from the weighted least-squares fit has already steepened to a slope of $\Gamma = -1.0 \pm 0.3$. Again, the MF in this radial bin remains significantly flatter ($\Gamma = -0.5 \pm 0.4$) when no A_K-correction is applied. Beyond $10''$ (0.4 pc, upper panel), a power law can only be defined in the range $10 < M < 30\ M_\odot$ ($1.0 < \log(M/M_\odot) < 1.5$), where a slope of $\Gamma = -1.69 \pm 0.66$ is found, consistent with a Salpeter ($\Gamma = -1.35$) law. The large error obviously reflects the small number of mass bins used in the fit. The depletion of high-mass stars at large radii seen in Fig. 5.2 reveals the effects of mass segregation very soon beyond the cluster center most clearly.

For a more quantitative confirmation of the mass segregation present in the Arches cluster, we created cumulative functions for the mass distributions in the three radial bins (Fig. 5.3). Cumulative functions, where each star is counted individually, have the advantage of independence from the

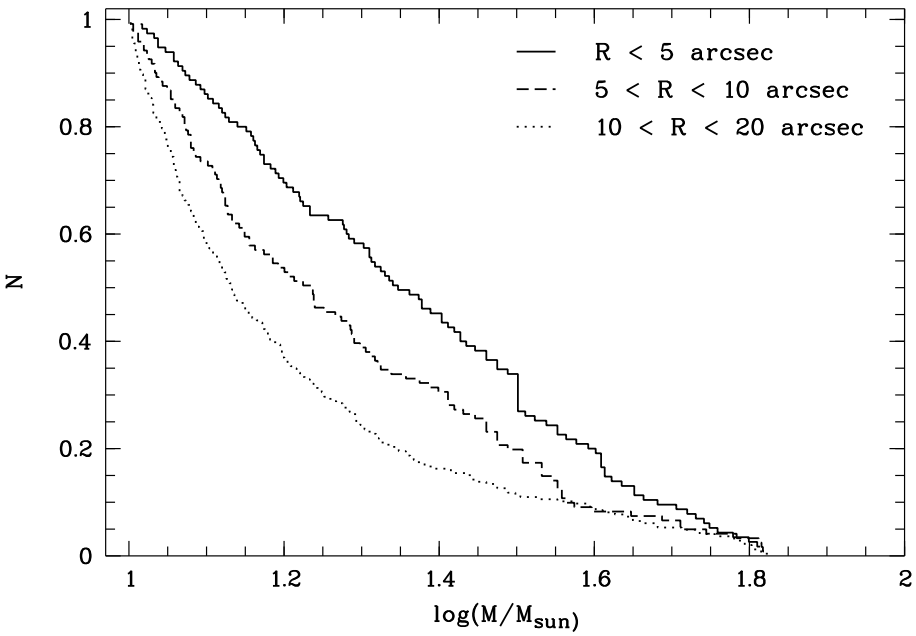

Figure 5.3: Cumulative mass distributions of the stars in radial annuli obtained from HST/NICMOS data. Each radial annulus corresponds to one radial mass function in Fig. 5.2. The cumulative distributions have been normalised at $10\,M_{\odot}$, the limit where all MFs are more than 75 % complete.

statistical uncertainties inherent to binning. The concept of cumulative functions will be introduced in more detail in Sec. 5.2.4, where a comparison with the expected single power-law distributions is performed. Here, we are only interested to obtain a more quantitative estimate on the variation in the radial mass distributions. A Kolmogorov-Smirnov test was applied to quantify the observed differences of these functions. When the central, intermediate, and outer radial bins are compared pairwise, we obtain in each case a confidence level of more than 99 % that the mass distributions do not originate from the same distribution.

Thus, the inner regions of the cluster are indeed skewed towards higher masses either by sinking of the high mass stars towards the cluster center due to dynamical processes or by primordial mass segregation, or both. The causes for this segregation will be discussed in more detail in the context of dynamical timescales and cluster evolution models in Sec. 5.1.5.

5.1.4 Formation locus of massive stars

Several (5) high mass stars are found beyond the cluster center, at larger radii in the cluster vicinity. These stars fall onto the Arches main sequence after applying the reddening correction (Sec. 4.1.1). When the entire HST field is separated into two equalsize areas, the first area being a circle of radius $16''$ around the cluster center, and the second the surrounding field, no additional comparably high-mass stars are found with Arches main sequence colours except for the two bright stars found at the edges of the Gemini field. In the dynamical models of Bonnell & Davies (1998) there is a low, but non-zero probability that a massive star originating outside the cluster's half-mass radius might remain in the cluster vicinity. High-mass stars formed near the center show, however, a tendency to migrate closer to the cluster center. The disruptive GC potential might enhance the ejection process of low-mass stars, but according to equipartition, it is unlikely that the most massive stars gain energy due to dynamical interaction with lower mass objects. We have to bear in mind, however, that interactions between massive stars in the dense cluster core could cause the ejection of high-mass stars.

N-body simulations performed by Portegies Zwart et al. (1999) show that the inclusion of dynamical mass segregation in cluster evolution models enhances the collision rate by about a factor

of 10 as compared to theoretical cross section considerations. For a cluster with 12000 stars initially distributed according to a Scalo (1986) mass function, a relaxation time of 10 Myr, and a central density and half-mass radius comparable to the values found in Arches, about 15 merging collisions occur within the first 10 Myr ($1\,t_{relax}$) of the simulated cluster. Shortly after the start of the simulations, frequent binary and multiple systems form from dynamical interactions leading to the ejection of several contributing massive stars. The flat MF in the Arches center as compared to a Scalo MF, containing a larger fraction of massive stars to interact at a given total number of stars, may even increase the collision rate.

Though it is likely that the high-mass stars seen in the immediate vicinity of the Arches cluster have formed from the same molecular cloud at the same time as the cluster, a final conclusion on the possible ejection of these stars from the cluster core due to dynamical processes can only be drawn when velocities for these cluster member candidates are available.

5.1.5 Comparison with cluster formation models

In this section, the simple analytical approach summarised in Binney & Tremaine (1987) is first used to analyse internal cluster dynamics, and derive dynamical timescales for the Arches cluster. These timescales for dynamical cluster evolution are then compared to published N-body simulations, where the tidal force of the Galactic Center potential is considered.

From the mass distribution, a rough estimate of the timescale relevant for dynamical cluster evolution can be made. For larger area coverage, the HST/NICMOS data are used in the calculation below. The timescales characterising cluster evolution are the cluster's crossing time, t_{cross}, which is simply given by some characteristic radius divided by the average velocity, i.e., the mean velocity dispersion of the cluster, $r_c/\langle\sigma\rangle$, and the relaxation time, t_{rh}. The median relaxation time is the time after which gravitational encounters of stars have caused the system to equilibrate to a state independent of the original stellar orbits (Binney & Tremaine 1987, Chap. 8, eq. 8-72, hereafter BT87)

$$t_{rh} = \frac{6.63 \cdot 10^8 \mathrm{yr}}{\ln(0.4N)} \left(\frac{M}{10^5\,M_\odot}\right)^{1/2} \left(\frac{1\,M_\odot}{m_*}\right) \left(\frac{r_c}{1\,\mathrm{pc}}\right)^{3/2}, \tag{5.1}$$

where M is the total mass within some characteristic radius r_c, m_* is a characteristic stellar mass, here defined as the median of the observed mass distribution, and N is the number of stars in the cluster. t_{rh} may also be expressed in terms of the crossing time, $t_{rh} \approx 0.1\,N/\ln N \cdot t_{cross}$. In this expression, the simplification of a median density inside the characteristic radius is made, implying the assumption that the total gravitational potential inside r_c determines the relaxation process (see BT87, Chap. 8, for a detailed discussion). While in principle the relaxation time at each radius and for each considered stellar mass is different, the overall relaxation time within some characteristic area of the cluster can be estimated by introducing the characteristic mass m_*. The resultant dynamical timescale represents the *average* relaxation time expected for the entire population.

To evaluate the above formula, we need to know the total mass of the system, M, a characteristic radius, r_c, the number of stars, N, and the characteristic stellar mass, m_*. In principle, most of these quantities can be derived from isochrone fitting, by assigning each star a mass corresponding to its K-band luminosity, and analysing the resulting spatial distribution of masses. Naturally, these individual masses cannot be accurate for each star, as they depend strongly on the choice of the isochrone and inherit the uncertainties of the photometry. The integrated properties are, however, not very sensitive to the age of the model isochrone used, within the reasonable age range of Arches, $\sim 2-3$ Myr (results will be given below). The attempt was made to create a density profile from the HST/NICMOS data, but as the profile appears to be very distorted, the core radius cannot easily be derived, such that the half-mass radius, r_{hm}, is chosen as a characteristic scale. r_{hm} was obtained from the observed stellar population of the cluster under the assumption that the mass in the cluster center, relevant for the spatial scale on which gravitational interactions are important, is dominated

by the detected high-mass stellar population in the cluster center. The relaxation time derived from r_{hm} is usually referred to as the "half-mass relaxation time" (cf. Portegies Zwart et al. 2002).

The mass distribution within the cluster as derived from the isochrone yields estimates for r_{hm}, M, and m_*. Taking all stars within a certain radius with Arches main sequence colours as cluster members, N can also be estimated.

A half-mass radius of $r_{hm} = 10'' \hat{=} 0.4$ pc is obtained, irrespective of the age of the isochrone used (2 Myr or 3.2 Myr) to transform K-band magnitudes into masses. The total mass measured within this radius is $M(r_{hm}) = 6300\,M_\odot$ ($5400\,M_\odot$ for the 3.2 Myr isochrone). By extrapolation of the mass function down to $0.1\,M_\odot$, F99 derived a total mass of $12000\,M_\odot$ within $9''$ radius. To estimate the total mass in the cluster center, they used the relative fraction of stars with $M > 40\,M_\odot$ in two annuli separated at $R = 3''$ as a scaling factor. This procedure ignores the segregation of high-mass stars. As the cluster shows strong evidence for mass segregation (see Sec. 5.1.3), this may overestimate the total cluster mass (within $R < 9''$). On the other hand, the mass estimate derived above, ignoring incompleteness and the lower mass tail, is a lower limit to the total mass within $R < 10''$. Combining these number, a total mass of $10^4\,M_\odot$ within the half-mass radius of 0.4 pc is a good approximation for the order of mangitude estimate of the relaxation time anticipated here. This yields an average mass density of $\rho(R < r_{hm}) \approx 4 \cdot 10^4\,M_\odot\,\mathrm{pc}^{-3}$.

The calculation of the relaxation time requires an estimate of the characteristic stellar mass and the number of stars. The median mass within $R < 10''$ is $7.3\,M_\odot$ in the observed mass range of $1.4 < M < 65\,M_\odot$ in the HST sample, and the number of stars actually observed is 486. The median mass is chosen as a more realistic mass estimate than the mean for individual stars participating in interaction processes, as the mean is highly biased by the high fraction of high-mass stars in the cluster center. Nevertheless, it has to be kept in mind that this median value is still unrealistically high as the low-mass tail of the mass distribution is missed, which also has the highest number of stars.

As the low-mass tail of the distribution is highly incomplete, we estimate N to be at least $10000\,M_\odot/7.3\,M_\odot \sim 1400$. This results in $t_{rh} = 1.2$ Myr. Decreasing the characteristic mass and increasing the number of stars lengthens the relaxation time. For instance, lowering m_* to $1\,M_\odot$, where the fact that the cluster center is mass segregated as opposed to a standard Salpeter mass function ($\langle m \rangle = 0.4\,M_\odot$) is taken into account and thus the characteristic mass of a star is higher, and raising N to 10000 stars, would result in $t_{rh} = 6.2$ Myr. If a significant fraction of low-mass stars would have been formed and survived in the cluster center, the half-mass relaxation time would increase even more. The present-day relaxation time is thus at least on the order of or longer than the age of the Arches cluster.

A relaxation time longer than the lifetime of the cluster would imply that not yet sufficient time has passed for dynamical mass segregation to take place, thereby indicating that primordial mass segregation was present at the time of cluster formation. However, we have so far ignored the Galactic Center tidal forces accelerating the dynamical evolution of the cluster. Kim et al. (2000) performed N-body simulations using the observed parameters of the Arches cluster to trace the dynamical evolution of the cluster and constrain initial conditions. They use a total mass of $2 \cdot 10^4\,M_\odot$, tidal radius of ~ 1 pc and a single power-law IMF with slopes of $\Gamma = -0.5, -0.75, -1.0$ and -1.35. The number of stars ranges between 12700 for a lower mass cutoff of $m_{low} = 0.1\,M_\odot$ and 2600 for $m_{low} = 1\,M_\odot$. From comparison with the HST/NICMOS data of F99 their models yield a power law with $\Gamma = -0.75$ as the most probable initial mass distribution. Although this slope is very close to the observed present-day MF, they also note that mass segregation takes place on timescales as short as 1 Myr, such that the cluster looses all memory of the initial conditions shortly after formation. Portegies Zwart et al. (2002) use a Scalo (1986) MF to model the Arches cluster, and derive a total cluster mass of $4 \cdot 10^4\,M_\odot$, and an initial relaxation time of 20-40 Myr. When comparing with the same set of HST/NICMOS observations, they conclude that a standard IMF can evolve into the current MF due to dynamical segregation, and that the IMF did not need to be overpopulated in high-mass stars. Their computations indicate that the relaxation time is strongly variable. During the dynamical evolution,

t_{rh} increases strongly after core collapse, which occurs within ~ 2 Myr, due to cluster re-expansion, and only starts to decrease after 10 Myr or later. The observed relaxation time does thus probably not trace the cluster's initial conditions, but reflects the current dynamical state in the evolution of Arches. In particular, a present-day relaxation time larger than the cluster's age does not necessarily imply that the cluster is not dynamically relaxed.

Unfortunately, this means that we are not able to distinguish between primordial and dynamical mass segregation from the estimated relaxation time. For the Orion Nuclear Cluster (ONC) and its core, the Trapezium, which has been studied in greater detail (e.g., Hillenbrand 1997, Hillenbrand & Hartmann 1998), Bonnell & Davies (1998) derive dynamical timescales too long to explain the segregation observed in high-mass stars within the Trapezium by dynamical evolution, concluding that a significant amount of primordial segregation must have been present. In the case of the Arches cluster, the external gravitational field acts towards a fast disruption, thereby impeding the equilibration process, such that dynamical segregation may well be under way.

As the different model calculations do not agree with respect to the IMF required to create the observed present-day mass distribution, a final conclusion on whether or not the Arches *initial* mass function had to be enriched in massive stars, thus supporting high-mass star formation models, cannot be drawn. During the comparison with other massive star-forming environments given in Chap. 8, this issue will be discussed in more detail.

The evaporation time, setting the scale for dynamical dissolution by internal processes, can be estimated as $t_{evap} \approx 136\, t_{relax} \sim 177$ Myr (857 Myr for $m_* = 1\, M_\odot$, BT87). Kim et al. (1999) have shown that the time required to disrupt an Arches-like cluster within the GC potential is only 10 Myr, much shorter than evaporation by internal processes will ever be relevant. The models by Portegies Zwart et al. (2002) suggest somewhat longer evaporation times in the range $30 < t_{evap} < 50$ Myr for an Arches-like cluster. The external potential is thus the dominating factor in the dynamical evolution of Arches. Note that, however, even a cluster as dense as Arches would not survive for more than 1 Gyr independent of its locus of formation.

5.2 The Arches mass function derived from NACO data

5.2.1 Integrated mass function

The Arches mass function has been derived from NACO data using the same method as described in Sec. 5.1. The trend in visual extinction was re-determined from this data set and corrected accordingly, showing no significant deviation from the change in extinction observed over the Gemini field before. In particular, the constant extinction in the innermost $5''$ is confirmed. The same 2 Myr isochrone was used to transform K-band magnitudes into masses to allow direct comparison of the derived mass functions.[1]

Prior to the MF derivation, the $H, H-K$ colour-magnitude diagram obtained with NACO has to be investigated. The NACO colour-magnitude diagram is shown in Fig. 5.4, along with the CMD corrected for the systematic change in extinction. The 75 % completeness limit in the cluster center ($K = 17.6$ mag) and the lower-density field ($K = 19.3$ mag) are indicated, corresponding to mass limits of 2 and $3.7\, M_\odot$, respectively. The prior Hokupa'a completeness limit in the cluster center, $M = 10\, M_\odot$, is also shown. This fitting limit is adopted for the NACO MF as well not only to compare the derived MFs, but also because the field contamination is expected to be large below $K \sim 15 - 16$ mag ($\sim 10\, M_\odot$). For comparison, a 10 Gyr isochrone is overlaid to indicate possible bulge star loci in the CMD, both for the cluster center extinction of $A_V = 24$ mag and the average

[1] The current best age estimate for Arches is 2.5 Myr as given in Figer et al. 2002. A direct comparison of determined slopes would be blurred with evolutionary effects, such that we postpone the detailed re-calculation of the MF to the complete, field-subtracted data set.

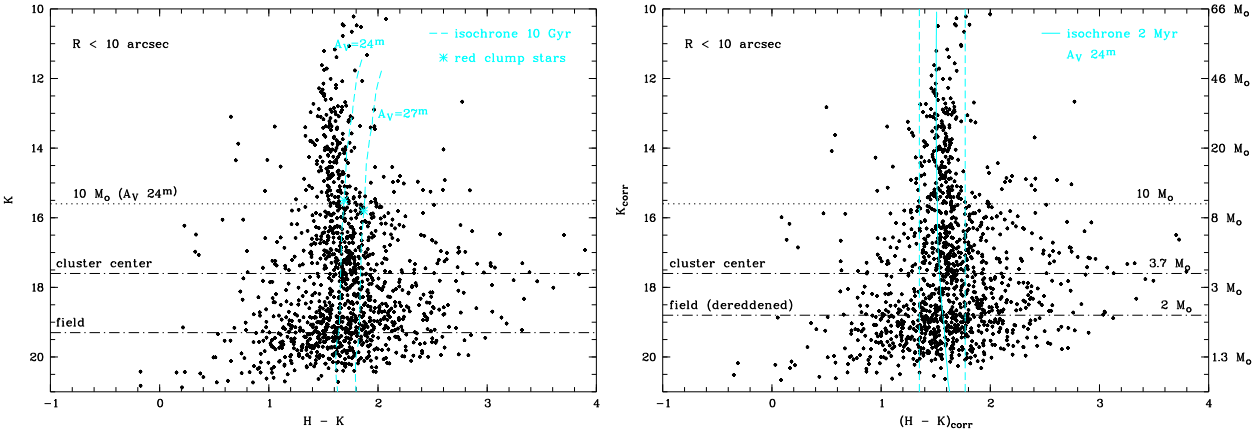

Figure 5.4: Arches colour-magnitude diagram derived from NACO data.
Left panel: Raw CMD, without extinction correction. 2 isochrones with age 10 Gyr and $A_V = 24^m$ and $A_V = 27^m$ are overplotted to indicate possible contamination from old bulge stars, the asterisk denotes the red clump location. Note that contamination indicated by the $A_V = 24^m$ isochrone is only expected in the immediate cluster center ($R < 5''$), where the foreground extinction is this low. 75% completeness limits for the cluster center ($R < 5''$) and the field ($R > 13''$) are shown as dash-dotted lines. The fitting limit of 15.6 mag $\sim 10\,M_\odot$ is also given for comparison with the 10 Gyr isochrones.
Right panel: CMD corrected for extinction variation over the field. Again, 75 % completeness limits are shown, with the field limit adjusted according to the change in extinction. Stars above the $10\,M_\odot$ limit were used to fit the MF slope. The vertical lines represent the colour selection applied to reject blue foreground and red background stars ($1.35 < (H-K)_{corr} < 1.77$ mag).

extinction of 27 mag observed on the Arches field (see Fig. 5.4, left panel). These isochrones blend into the cluster population close to the $10\,M_\odot$ fitting limit. Note that contamination by old bulge stars could also be non-negligible above $K = 15.6$ mag, but from the sample isochrone locus ($A_V = 24$ mag) this influence would increase with fainter magnitudes, thus steepening the MF. Unfortunately, we cannot disentangle field and cluster population due to the limited field size, and the severely varying stellar density in the GC region prohibits to estimate the field star density from population models. The small field of view and the confined Arches main sequence, however, provide some confidence that the population is dominated by cluster members.

The Gemini/Hokupa'a data were not influenced by this severe bulge contamination, as mainly the bright, massive population above $K < 15.6$ mag was traced. When investigating the NACO CMD below this limit, a gap is observed at $K \approx 16$ mag. Although the feature is weak, this tentatively suggests a low-mass truncation in the Arches mass function. This feature cannot correspond to the main sequence turn-on point, as a 2 Myr old pre-main sequence population enters the hydrogen burning phase at around $2 - 3\,M_\odot$. In addition, although more reddened, most probably background sources are observed towards fainter magnitudes in consistence with bulge contamination, there is no indication of a rich, severely reddened population hinting at variable extinction superimposed on the systematic radial increase in A_V. The bulk of the population down to the completeness limit in the cluster center falls into the colour range chosen to select cluster members (vertical lines in Fig. 5.4, right panel). As will be seen more quantitatively in the MF, the cluster population is indeed heavily depleted below this point.

The mass function derived over the entire NACO mosaic from a colour-selected sample of cluster stars is displayed in Fig. 5.5, now limited to the narrower colour range of $1.35 < H - K < 1.77$ mag. The narrower colour cut is applicable as a consequence of the confined Arches main sequence from the more accurate NACO photometry. As before, MF slopes are derived by scanning through each mass bin in steps of one tenth of the binwidth ($\log M/M_\odot = 0.1$). The derived MF slopes are in the range $-0.99 < \Gamma < -1.21$ with fitting errors of the weighted least-squares fit between 0.12 and 0.15, yielding

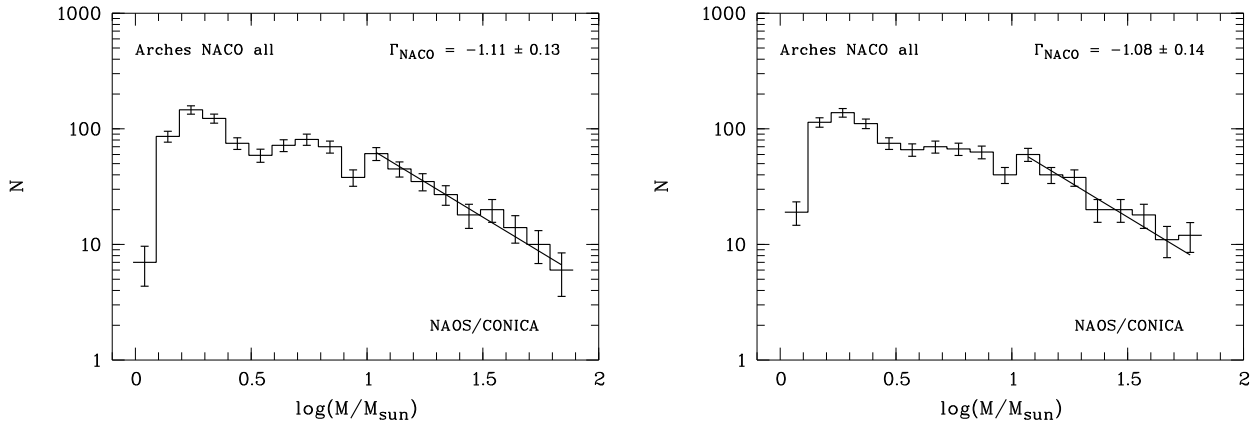

Figure 5.5: Mass function of the Arches cluster derived from NAOS-CONICA data.
The Arches MF has been derived as before, using a 2 Myr Geneva isochrone after correcting K-band magnitudes for the change in extinction observed over the field. The entire NACO field is included, and a colour cut $1.35 < H - K < 1.77$ mag was applied to select cluster members. Two different starting points for the MF calculation are shown. Left: Binning representing the mean slope from all binning choices. Right: Binning showing different fine structure to display the statistical uncertainties inherent to this MF derivation procedure.

a mean of $\Gamma_{\rm NACO} = -1.10 \pm 0.15$ in the mass range $10 < M < 65\,M_{\odot}$. A characteristic MF for the total NACO field is displayed in Fig. 5.5. Below $10\,M_{\odot}$, the MF is consistent with a very flat slope of $\Gamma \approx 0$. As discussed with respect to a thinning out of the CMD below this point, this flattening strongly suggests a depletion in low-mass stars in the Arches cluster. This is even more emphasised as the remaining low-mass population is expected to be severely contaminated by bulge stars.

A binning with a different starting point is also shown to illustrate the difference in the shape of the MF. It is obvious that even the much larger and more complete sample of stars observed with NACO is subject to binning uncertainties. In Fig. 5.5 (right), a plateau is seen at $1.3 < \log M/M_{\odot} < 1.6$, for which no evidence is observed in the first binning shown. Again, we see that care has to be taken when discussing the detailed structure in mass functions. Two methods will be presented to circumvent these statistical uncertainties in the next sections, after discussing the radial MFs obtained with NACO.

Comparison to Gemini MF:

When only the Gemini field of view is selected from the NACO data, the resultant average slope turns out to be slightly shallower, with $\Gamma_{\rm NACO} = -0.91 \pm 0.15$ (where $-1.05 < \Gamma < -0.82$). This slope agrees within the errors with the slope derived from Gemini data, $\Gamma_{\rm Gem} = -0.77 \pm 0.15$, and closely resembles the average slope derived from NICMOS data, $\Gamma_{HST} = -0.86 \pm 0.13$. A characteristic MF of the extracted Gemini field is shown in Fig. 5.6 (left panel). The MF derived from NICMOS for the same bin starting point (different from the binning displayed in Fig. 5.1) is shown for comparison in the right panel. Although some differing fine structure is seen, the slopes for the same binning agree extremely well.

These resulting integrated MF slopes allow two remarks. First and most important, the derived results from Gemini and NICMOS are confirmed by the more complete NACO sample of cluster stars. In particular, the incompleteness correction applied to the Hokupa'a data was successful in predicting the flat portion of the MF below $10\,M_{\odot}$ (cf. Fig. 5.1). The integrated mass function displays a comparable result as the NACO MF down to $\log m = 0.7$ or $M = 5\,M\odot$. This shows that incompleteness simulations in crowded stellar fields are efficient tools to estimate the number of stars lost. The slight trend to steepen the slope with more complete data observed in the comparison

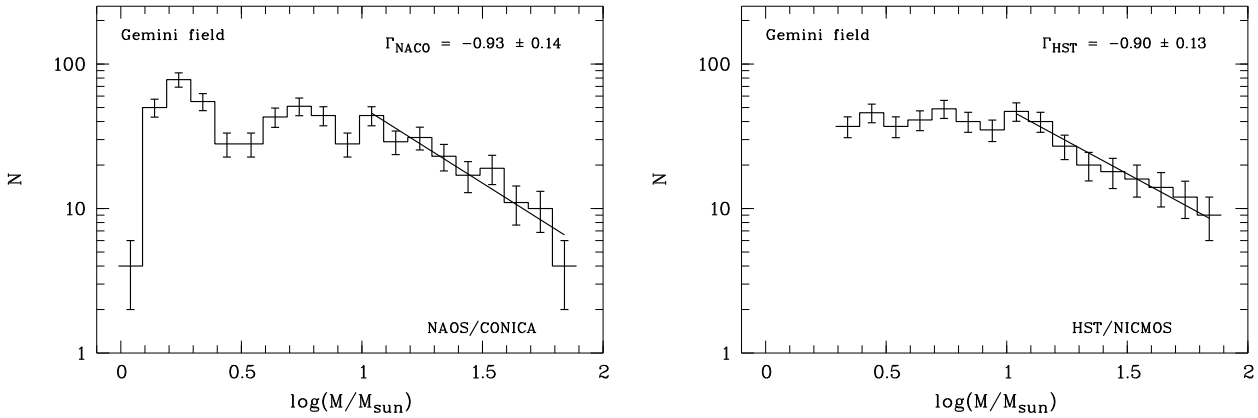

Figure 5.6: Integrated Arches mass function derived from NACO data (left).
Only stars in the area of the Gemini field are chosen in this case. For comparison, the MF derived from HST/NICMOS data is shown in the right panel for the same binning. This MF has a different bin starting point as the MF displayed in Fig. 5.1, such that the slopes deviate slightly as discussed in Sec. 5.1.

between HST and Gemini is confirmed by NACO, but an expected further increase in the slope due to the significantly more complete data set is not observed at least on the same field of view.

The steeper MF observed over the larger NACO field may arise from increasing amounts of field star contamination, although the possibility that a more complete census of stars steepens the MF to normal values cannot be entirely excluded. Clearly, with higher resolution data a larger number of field stars is also included in the sample, in particular at larger radii from the cluster center. To solve this ambiguity, a thorough background subtraction is urgently required in particular in the outer cluster regions.

5.2.2 Radial variations in the NACO mass function

The radial dependence of the Arches mass function with the improved statistics from NAOS-CONICA data is illustrated in Fig. 5.7. For statistical reasons, the size of the mass bins has been increased by a factor of two to $\Delta \log M/M_{\odot} = 0.2$. Again, two different binnings are shown in Fig. 5.7 to demonstrate the uncertainty in the shape and derived slope of the MF. The flattening of the MF towards the cluster center observed already in the Gemini and HST data is clearly seen in the NACO radial MFs. Significant changes are visible when comparing the two different binnings shown. In particular at the high-mass, i.e. low-number, end of the MF, the shift in the bin starting point causes seemingly random fluctuations in the MF due to the distribution of the few stars into changing bins. The average slopes obtained for the displayed annuli are shown in Tab. 5.1. The results in the MF slope with the inherent large errors will be discussed in the next sections, where more binning-independent methods are presented to derive the MF slope.

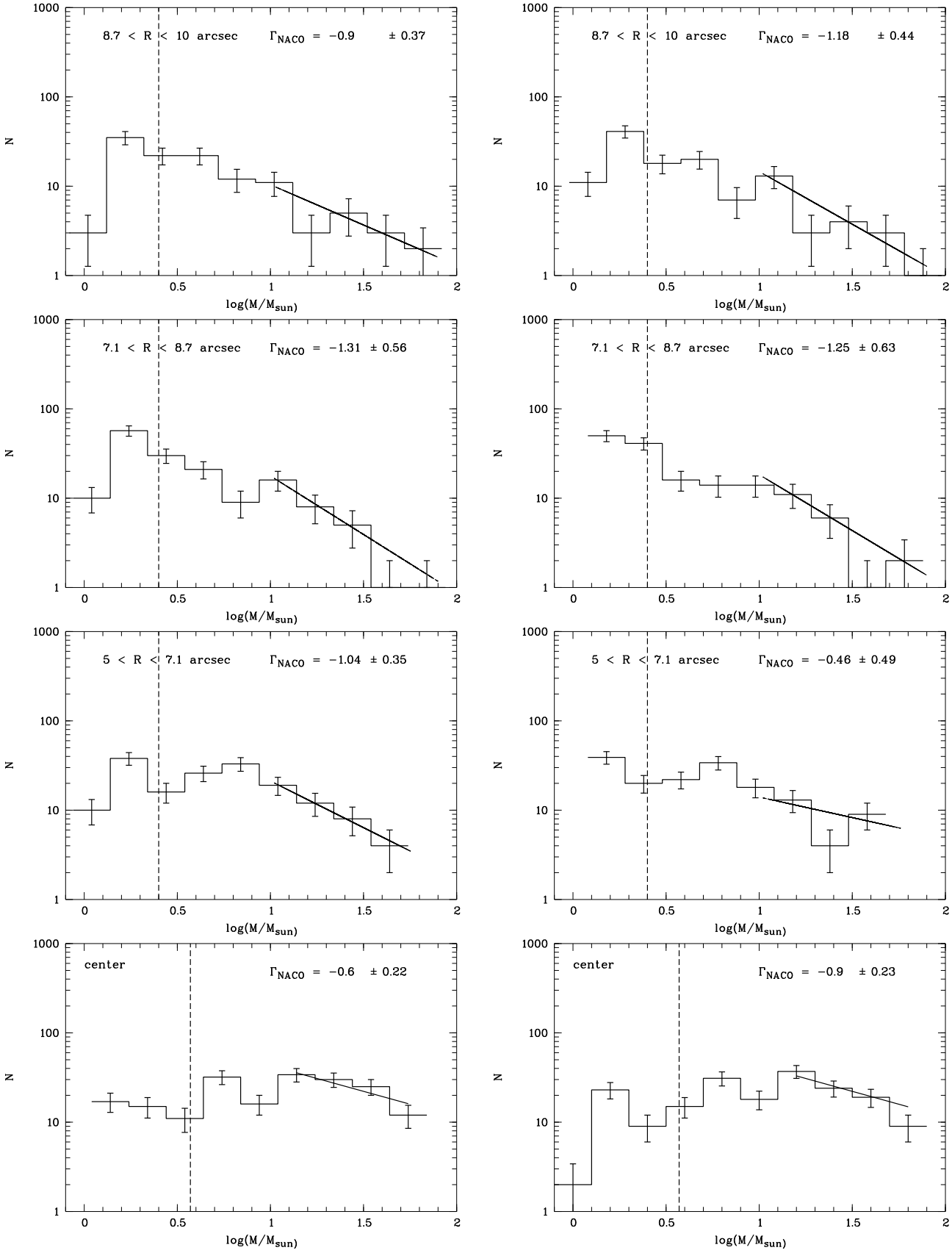

Figure 5.7: Radial variations in the Arches MF from NACO data.
The MF progresses inwards from top to bottom, with subsequent equal-area annuli. Note that the MF is different from the LFs presented, as a colour cut has been applied to select Arches cluster members. Two different binnings are shown for each annulus. Clearly, the uncertainty in the derived slope is large due to the limited number of stars in each bin, and individual details observed in the MF are strongly influenced by statistical effects. The general trend of a flattening of the MF in the cluster center is nevertheless prominently seen.

Table 5.1: Average MF slopes derived from different calculation starting points. The fitting range is given in units of $\log M/M_\odot$. $\langle\Gamma\rangle$ is the average slope obtained from shifts in the starting point of the calculation, and Γ_{all} is derived from the fit to all shifted MFs shown in Figs. 5.8 and 5.9 for the mass range $10-65\,M_\odot$. Γ_1 and Γ_2 are slopes for different sections of the MF displaying power-law like shapes.

annulus	fit range	$\langle\ \Gamma\ \rangle$	Γ_{all}	fit range	Γ_1	fit range	Γ_2
all	$1.0-1.9$	-1.08 ± 0.14	-1.1 ± 0.04				
$R<5''$	"	-0.59 ± 0.21	-0.60 ± 0.06	$1.2-1.7$	-0.73 ± 0.11	>1.7	-3.19 ± 0.90
$5''<R<7.1''$	"	-0.74 ± 0.42	-0.82 ± 0.13	$1.0-1.4$	-1.47 ± 0.80		
$7.1''<R<8.7''$	"	-1.33 ± 0.58	-1.26 ± 0.16	$1.0-1.4$	-1.10 ± 0.89	$1.4-1.6$	-3.02 ± 2.18
$8.7''<R<10''$	"	-0.89 ± 0.46	-0.97 ± 0.13				
$R>13''$ (field)	"	-1.61 ± 0.68	-1.70 ± 0.18	$1.1-1.3$	-3.68 ± 0.83		

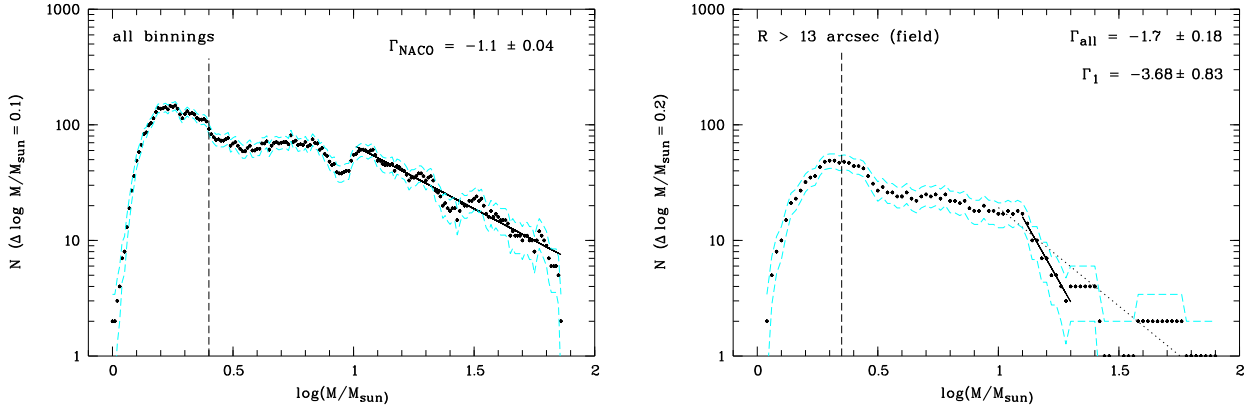

Figure 5.8: Arches MF including all used starting points (left).
N is again the number of stars per $\Delta \log M/M_\odot = 0.1$. The 75 % completeness limit is shown as a vertical line, and enveloping dashed lines indicate Poisson errors for each mass intervall $\Delta \log M/M_\odot = 0.1$. Note, however, that only each 10th data point is statistically independent. The finer resolution is an effect of the shift in the starting point of the MF, shifted by $\delta \log M/M_\odot = 0.01$. Combining the knowledge from all MF derivations allows to decrease the statistical fluctuations in the MF slope, and pronounces real variations, as e.g. the dips seen at $\log M/M_\odot = 0.95$ and $\log M/M_\odot = 1.4$.
For comparison, the MF derived with the same isochrone from stars with $R > 13''$, assumed to be largely field stars, is also shown (right). A larger bin width, $\Delta \log M/M_\odot = 0.2$, is chosen for statistical reasons. The solid line is a linear fit between $1.1 < \log M/M_\odot < 1.3$, the dotted line covering all mass bins above $\log M/M_\odot = 1$. is included for comparison. The field star distribution indicates that the plateau seen below $10\,M_\odot$ contains a large fraction of field stars.

5.2.3 Combining different binnings - a step towards binning independence

As demonstrated in Fig. 5.7, the effects of binning strongly influence MF derivations. For the derived MF to be meaningful, the bin width cannot be chosen arbitrarily small, as the shape information will then be lost. On the other hand, if the bin width is chosen small enough to trace the MF shape even in outer annuli of a star cluster, where the stellar density decreases, statistical fluctuations can influence the derived MF. There is a simple way, however, to improve the statistics *on the derived MF slope*. As the MFs for each radial bin or the total cluster are derived from the same stellar population using different starting points only, the points of each MF are found on the same curve. This allows us to include all calculated MFs into the same diagram. Of course, we cannot artificially increase our statistics, i.e. the number of stars in each bin is still the number of stars within $\Delta \log M/M_\odot = 0.2$, but the statistical fluctuations are reduced due to the fact that many more points are now located on the *same* curve. Including all the derived MF points in a combined diagram thus allows to determine the slope more accurately, avoiding fluctuations in individual bins arising from a certain MF calculation.

The results are shown in Fig. 5.8 for the integrated Arches MF (NACO field, see Fig. 5.5), and in Fig. 5.9 for the same equal-area annuli as displayed in Fig. 5.7. Note that consecutive dots at the same N-level indicate that the bin shift did not change the mass-bin in which the contributing stars have fallen. This is particularly evident at the high-mass end, where low-number statistics affect the MF most severely. From Fig. 5.9, it is obvious that the Arches MF is already changing significantly beyond the immediate cluster center. In each annulus with $R > 5''$ the contribution of high-mass stars decreases as the slope steepens. The core MF, displayed to the lower right of Fig. 5.9, shows a pronounced high-mass distribution, with a significant drop below $15\,M_\odot$ ($\log M/M_\odot = 1.2$). This dip is also seen in the second and third annulus. Although this has to be confirmed taking into account the field star contribution on all mass scales, this indicates a severe depletion of cluster stars below $10\,M_\odot$. Very cautiously, one might ask whether these stars have merged into more massive objects, or whether the initial mass function was already depleted in low-mass stars. At the highest masses, a population

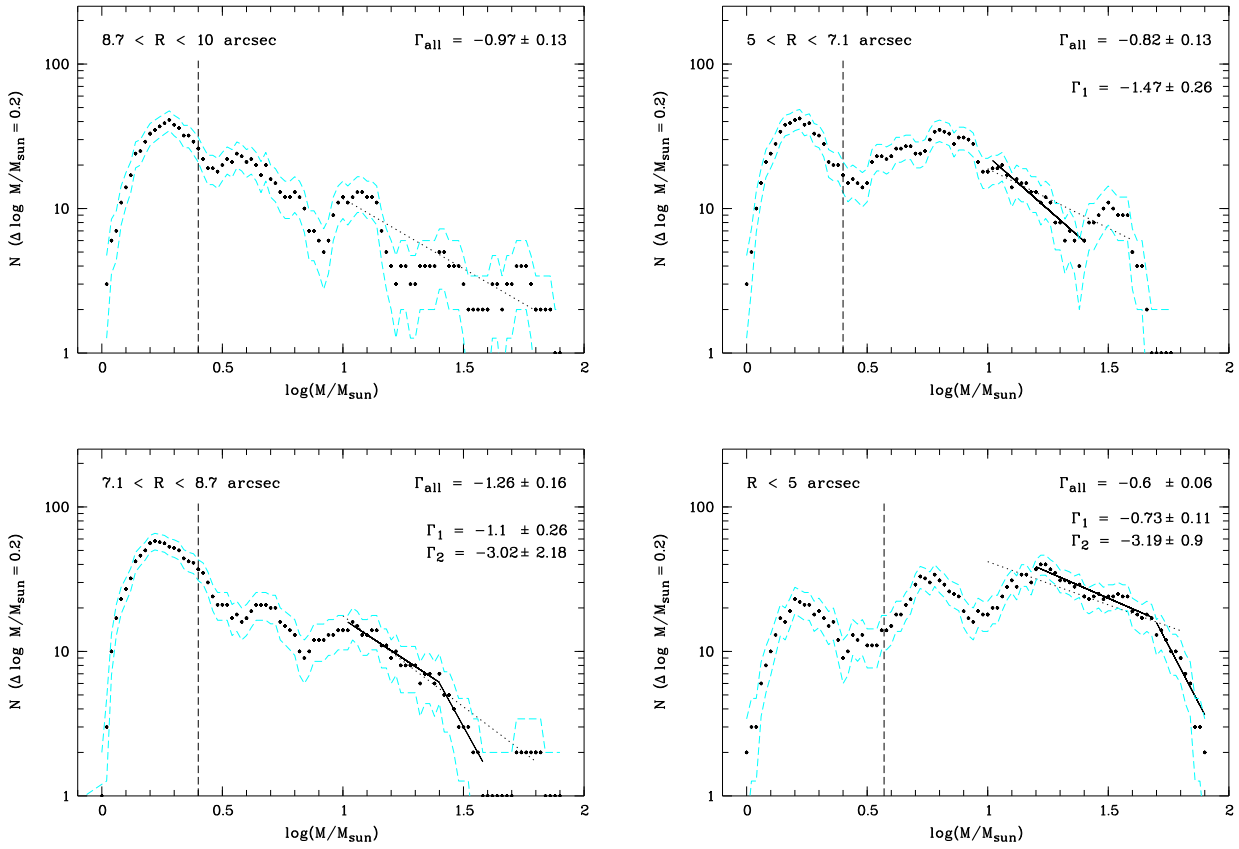

Figure 5.9: Arches MF radial variations including all starting points.
N is the number of stars per $\Delta \log M/M_\odot = 0.2$, and the starting point for the MF calculation has been shifted subsequently by $\delta \log M/M_\odot = 0.02$, resulting in 10 different solutions for the MF. The same radial annuli as in Fig. 5.7 are used to display radial variations in the MF from outer annuli to the cluster center. The dashed line indicates the incompleteness in each bin, taking into account the change in extinction over the field. The dotted line is a least-squares fit to all data points with $\log M/M_\odot > 1$ as before. A change in Γ is seen around $\log M/M_\odot = 1.4$. Where apparent, two power laws have been fitted to account for this change (solid lines).

with $M > 50\,M_\odot$ ($\log M/M_\odot > 1.7$) is present, which is only marginally found in all the outer annuli. Although the MF in the cluster center shows a pronounced bend beyond $\log M/M_\odot = 1.7$, this shape is still regular. A similar bend is observed in the second annulus, but at lower masses. To account for the change in shape observed in the MF, we have fitted two power laws to the distribution. In the cluster center, the weighted least-squares fit results in slopes of $\Gamma = -0.73 \pm 0.11$ for $15 < M < 50\,M_\odot$, significantly flatter than the Salpeter slope. Beyond $50\,M_\odot$, the MF falls off rapidly. If fitted by a power law, the corresponding slope is with $\Gamma = -3.19 \pm 0.9$ very steep.

The flat slope observed in the cluster center between 15 and $50\,M_\odot$, now much less affected by statistical uncertainties, indicates the efficient production of massive stars in the Arches cluster center, and thus confirms our prior findings. One explanation for the drop at the high-mass end is stellar evolution due to the use of *actual* masses to derive the present-day MF instead of *initial* masses. Stellar evolution of high-mass stars is influenced by mass-loss and stellar wind properties, which are not well understood, such that the extrapolation to initial masses adds additional uncertainties to the MF derivation. Fig. 5.10 demonstrates the mass-loss effects due to stellar evolution on the 2 Myr evolutionary timescale of the model isochrone. Mass-loss becomes prominent for $M > 60\,M_\odot$ or $\log M/M_\odot = 1.77$, very close to the observed turnover in the MF.

The behaviour in the *initial* MF is displayed in Fig. 5.11 for the cluster center, where the bulk of

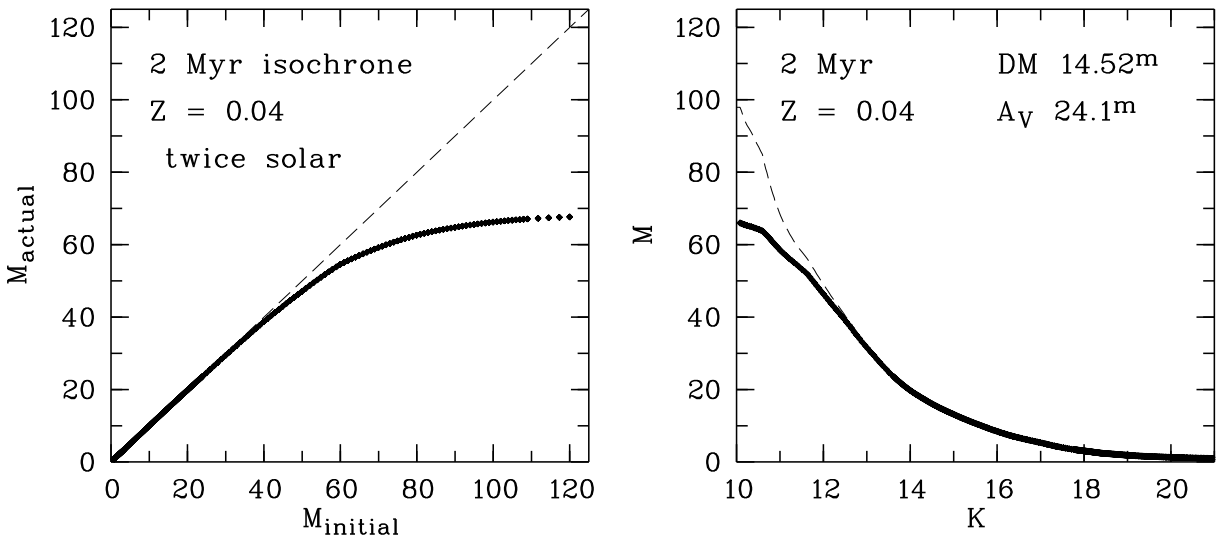

Figure 5.10: Effects of stellar evolution in the Geneva 2 Myr model.
Left: Mass loss model included in the Geneva 2 Myr isochrone. Present-day (actual) masses are compared to initial masses. Mass loss becomes significant for masses above $60\,M_\odot$ ($\log M/M_\odot = 1.77$). Right: Actual (solid line) and initial (dashed line) mass vs. K-magnitude. For stars with $K < 12$ mag ($60\,M_\odot$) mass loss causes deviations of the actual from the initial MF.

the high-mass stars are found. As expected, mass loss causes the slope at the high-mass end to become steeper, while more and more very massive stars are moved to lower mass bins. Stellar evolution can, however, not explain the strong change in the MF observed at $\sim 50\,M_\odot$ ($\log M/M_\odot = 1.7$). Monte-Carlo simulations with random sampling from a flat MF indicate that the steepening is caused by random sampling of the high-mass MF.

Beyond the immediate cluster center, at radii $R > 5''$, the MF becomes much more irregular. Note that field contamination is lowest in the cluster core, where the dense population is dominated by cluster stars, such that more and more field stars contaminate the outer annuli. The second annulus, although displaying a comparably flat MF slope as the cluster center when fitting the entire mass range above $M > 10\,M_\odot$, peaks near $\log M/M_\odot = 1.5$ ($32\,M_\odot$), and shows a quite normal MF slope when only the mass range $1.0 < \log M/M_\odot < 1.4$ is fitted. This slope, $\Gamma = -1.47 \pm 0.28$, is entirely constistent with a Salpeter slope. Although massive stars are still present in this annulus, and remain present in low numbers in the outer parts of our limited Arches field of view, this is a strong indication for mass segregation in the cluster center. When moving further into the next annulus, the integrated slope is already close to Salpeter, indicating a rather normal population of young stars at radii $R > 7''$ (0.3 pc) from the cluster center. Although statistics are very low at the high-mass end of the third annulus, the tentative fit to the high-mass end of the MF is included for completeness.

The outermost bin at $R > 8.7''$, although tentatively fitted with a power law, shows a very irregular behaviour. As the stellar density of cluster stars is already significantly decreased, there must be a significant number of field stars contaminating the MF in this region. A thorough field subtraction, including the effects of differential extinction and spatially varying incompleteness, is needed to study the MF out to larger distances in a physical meaningful way. In particular, the existence of bright, massive stars observed in the outer cluster field is very interesting with respect to interaction scenarios and dynamical cluster evolution, as has been discussed in the context of the Gemini data. A deep understanding of the field population will provide the basis to draw further conclusions on the probability that the observed bright objects have indeed formed out of the same molecular cloud, presumably even in the denser cluster regions. In Fig. 5.12 the radial MFs of Figs. 5.8 and 5.9 are overplotted to demonstrate the contribution of each radial MF to the integrated cluster MF. For a first estimate on the field star contamination, we again use the outer Arches field with

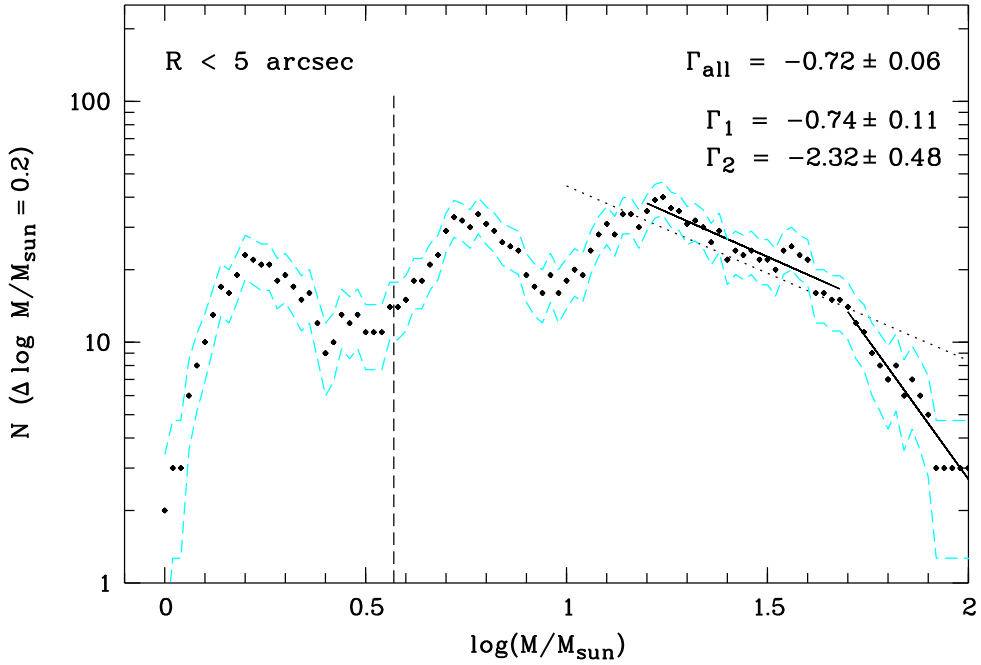

Figure 5.11: Effects of stellar evolution on the MF.
The cluster center MF calculated from initial masses of the same isochrone. As the early phases of high-mass stellar evolution are not yet well quantified, in particular with respect to wind mass loss, this MF may not represent the true IMF in the cluster center. Although the slope at the high-mass end is slightly flatter, the turnover in the MF remains clearly present.

$R > 13''$. The corresponding distributions of the entire NACO area and the field stars are subtracted in Fig. 5.13. Most prominently, the high-mass end remains clearly seen in the subtracted distribution, while stars below $10\,M_\odot$ again appear to be depleted. Note that the bump at low masses can be explained by the change in extinction over the field, which has not been taken into account here. This shows once more the importance of the correction for differential extinction, as artificial overdensities can be produced when the obscuration in the selected background field is larger than in the cluster. This may easily be the case when a massive cluster population has evaporated a large fraction of the surrounding molecular material. In particular at the low-mass end, where MFs and the IMF are very uncertain, caution has to be taken when the distribution shows unexpected structures.

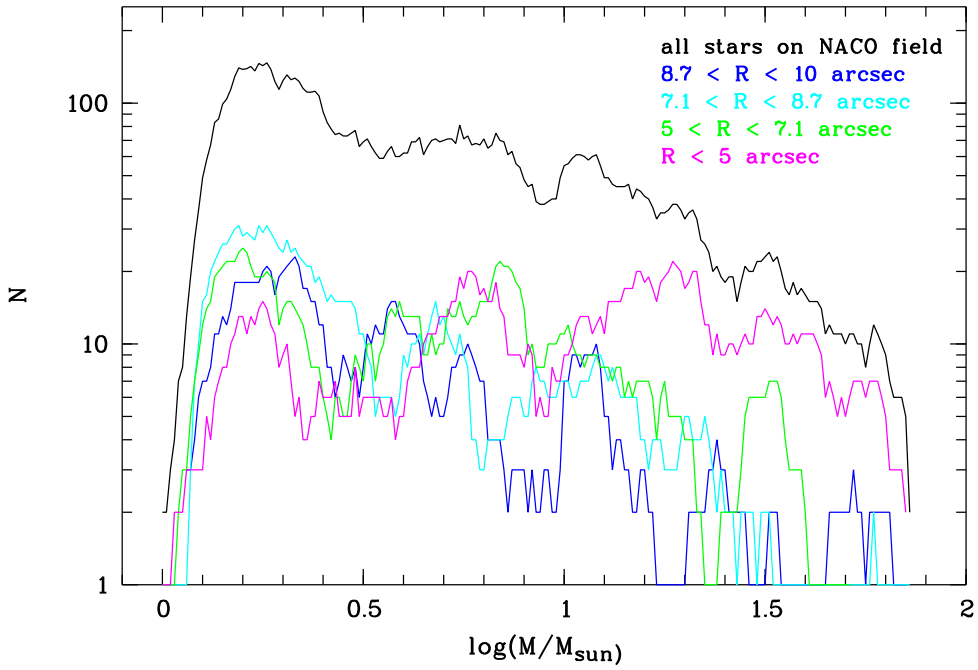

Figure 5.12: MF of the Arches cluster with all binnings.
This plot contains all radial MFs from Figs. 5.8 and 5.9 to allow direct comparison. The comparison with the MF derived for the entire NACO field demonstrates which part of the total MF is dominated by which cluster or field population.

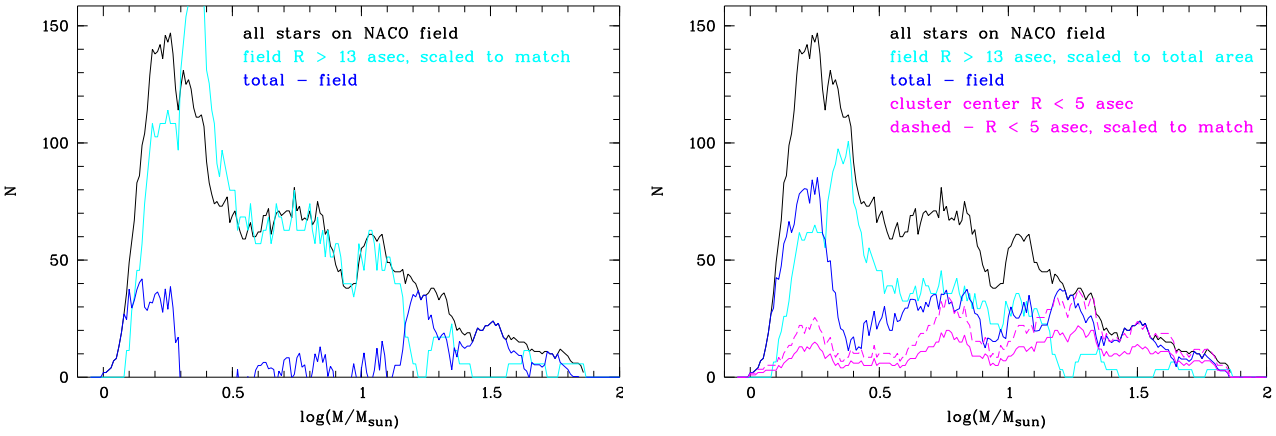

Figure 5.13: MF of the Arches cluster including all binnings.
The same distributions as in Fig. 5.8 are shown, but now on a linear scale to pronounce individual features. The black line includes all stars on the NACO field, the cyan line contains only stars with $R > 13''$, assumed to be dominated by field stars. In the left diagram, the field has been scaled to match the total distribution between 4 and 10 $M_\odot$, yielding an upper estimate on the field star contamination, while in the right diagram the field has been scaled to the same area, yielding a more realistic estimate on the field star contribution. The field subtracted MF is shown as a blue line. In the right panel, this MF is compared to the cluster center, $R < 5''$, distribution. When the cluster center MF is scaled to match the total MF, the distribution above $M = 15\,M_\odot$ ($\log M/M_\odot = 1.2$) may completely be reproduced, indicating that this part of the MF is indeed completely comprised of cluster stars.

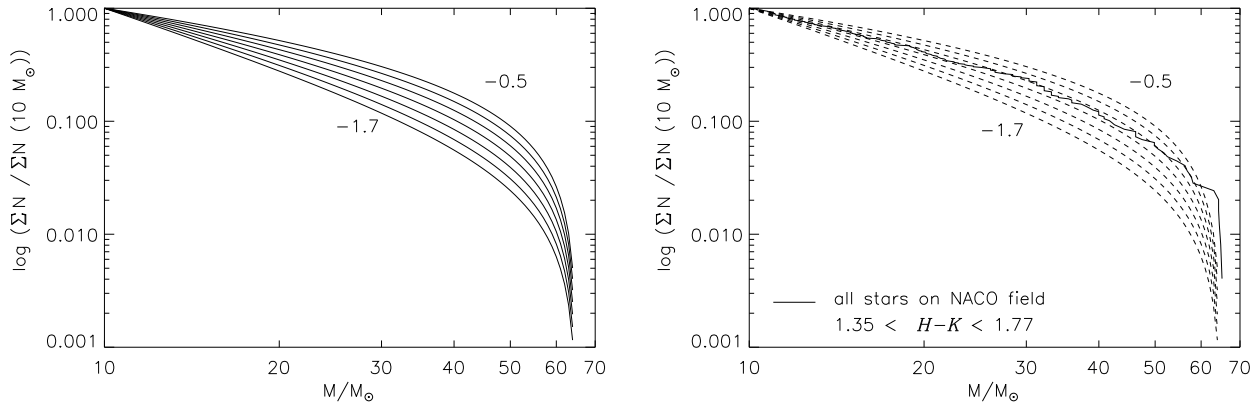

Figure 5.14: Cumulative functions
Left: Cumulative functions as expected from power laws with different slopes Γ. Γ is steepening from top to bottom in bins of $\delta\Gamma = 0.2$, progressing from $\Gamma = -0.5$ to $\Gamma = -1.7$. Right: The integrated CF over the entire NACO field, colour selected for Arches main sequence stars, is overplotted over the grid of theoretical CFs. The observed CF matches well the shape expected from a power law distribution with an index between -0.9 and -1.1, consistent with the derived MF slopes.

5.2.4 Away from binning - Cumulative Functions

In the previous sections, we have seen that mass functions derived from isochrone fitting can be influenced by statistical effects caused by the finite bin width applied during luminosity-mass transformation. Mass functions are a simple and straight-forward way to study the stellar distribution in equal-age, equal-metallicity populations, and have thus been widely used to characterise resolved stellar populations. There are, however, other approaches which are independent of the statistical uncertainties inherent to binning.

Cumulative functions, i.e. the number of all stars summed up to a certain mass, do not require binning of any sort. Each star is simply counted, and the number of the function increased star by star with decreasing mass. In the case of a stellar population, where incompleteness sets in at the faint and low-mass end, the star count has to be started at the most massive star. The resultant function may finally be compared with a power-law.

There is only one disadvantage in CF derivation as compared to MF derivation. As each star is considered individually, providing the independence of bin width and starting point, each star has to be assigned a mass individually. This means that photometric uncertainties enter the CF directly. Of course, photometric uncertainties also enter the MF, but here the use of luminosity bins eliminates random fluctuations. Only systematic effects, such as a decrease in the number of detected objects at small radii due to crowding, or at large radii in the case of Arches due to increased extinction, affect the slope and shape of the MF.

Most populations are mainly limited by the number of stars in a young cluster or association. Low number statistics can veil spatial variations in the mass distribution. In the following, we demonstrate the use of cumulative functions in the context of mass function fitting to avoid statistical binning fluctuations.

From the definition of the mass function,

$$\xi(\log m) \sim m^{\Gamma} \tag{5.2}$$

or

$$\frac{\mathrm{d}\log\xi(\log m)}{\mathrm{d}\log m} = \Gamma \tag{5.3}$$

we can reconstruct a cumulative function by integration. Integrating over the number of stars per $\log m$-Intervall yields

$$\begin{aligned}
\int_{m_{max}}^{m_x} \xi(\log m)\,\mathrm{d}(\log m) &\sim \int_{m_{max}}^{m_x} m^{\Gamma}\ \tfrac{\mathrm{d}\log m}{\mathrm{d}\,m}\ \mathrm{d}\,m \\
&\sim \int_{m_{max}}^{m_x} \tfrac{m^{\Gamma}}{m}\mathrm{d}m \\
&\sim \int_{m_{max}}^{m_x} m^{\Gamma-1}\mathrm{d}m \\
&\sim \tfrac{1}{\Gamma}(m^{\Gamma})_{m_{max}}^{m_x} \\
&\sim \tfrac{1}{\Gamma}(m_x^{\Gamma} - m_{max}^{\Gamma})
\end{aligned}$$

The integrated number of objects in the given power law is derived by scaling. We have used again the $10\,M_\odot$ mass limit for scaling, which is more than 90% complete in all bins, and allows comparison with our prior deviations.

Fig. 5.14 (left panel) displays the theoretically expected functions for MF slopes of $-0.5 < \Gamma < -1.7$, and the integrated cumulative function of the Arches cluster field observed with NACO (right panel). The observed distribution matches the expected shape from a power law very well. As indicated before, deviations are apparent at the highest masses, as well as close to the $10\,M_\odot$ limit. In the intermediate range, the CF lies between the lines corresponding to MF power laws with $\Gamma = -0.9$ and $\Gamma = -1.1$. There is more indication at the high-mass end towards flattening. Although this part of the CF consists of only very few stars, it represents the part of the MF dominated by the massive cluster center population. Indeed, a flat slope has been found in the central region, as discussed before. A drift towards shallower Γ values is seen in the integrated CF.

The radial variations in the CF are displayed in Fig. 5.15. In each diagram, the integrated CF is included for comparison. The central CF, $R < 5''$, basically follows the $\Gamma = -0.5$ function, although with some scatter. Beyond $5''$, the CF shape appears very perturbed. At the high-mass end, the irregular rise reflects the few stars found randomly distributed in the outer cluster field. For masses below $M = 30\,M_\odot$, the CF of the second annulus shortly tangents the $\Gamma = -0.7$ line, and then turns over to the $\Gamma = -1.1$ line, reflecting the normal slope observed in this annulus. Beyond $R = 7''$, the CF only displays a regular shape for $M < 20\,M_\odot$, now closely following the integrated CF with $\Gamma = -1.1$. The outermost annuli appear more and more irregular. Two effects cause the irregular shape of the outer CFs, both acting towards a strong deviation from the theoretically assumed power law shape. On the one hand, the high-mass end of the MF becomes increasingly depleted, and only very few stars contribute to the CF (see Tab. 5.2 for actual numbers). As observed in the MFs before (cf. Fig. 5.9), statistical fluctuations become prominent and perturb the shape of the distribution. On the other hand, the comparison with the distribution beyond $R > 13''$ reveals the onset of field contamination and increasing deviation from a power-law like behaviour. All these effects are evidenced in the CF. More detailed modelling and a deeper understanding of the CF distribution will be required to deduce the observed MF features from these functions in detail. It is apparent from Fig. 5.15 that a single-exponent power law is not a very good description of the mass distribution at least ar larger radii.

In addition to the cumulative distribution, the number of stars found in each bin, and in particular the relative fraction of massive stars, yields quantitative evidence for mass segregation. The number of stars in each annulus, the fraction of massive stars in each annulus, and the median present-day mass is given in Tab. 5.2. Incompleteness has not been taken into account, i.e. the numbers of stars are influenced by the varying stellar density and extinction over the field. The content of massive stars ($M > 10\,M_\odot$), however, is not influenced by incompleteness, as has been shown before. Again,

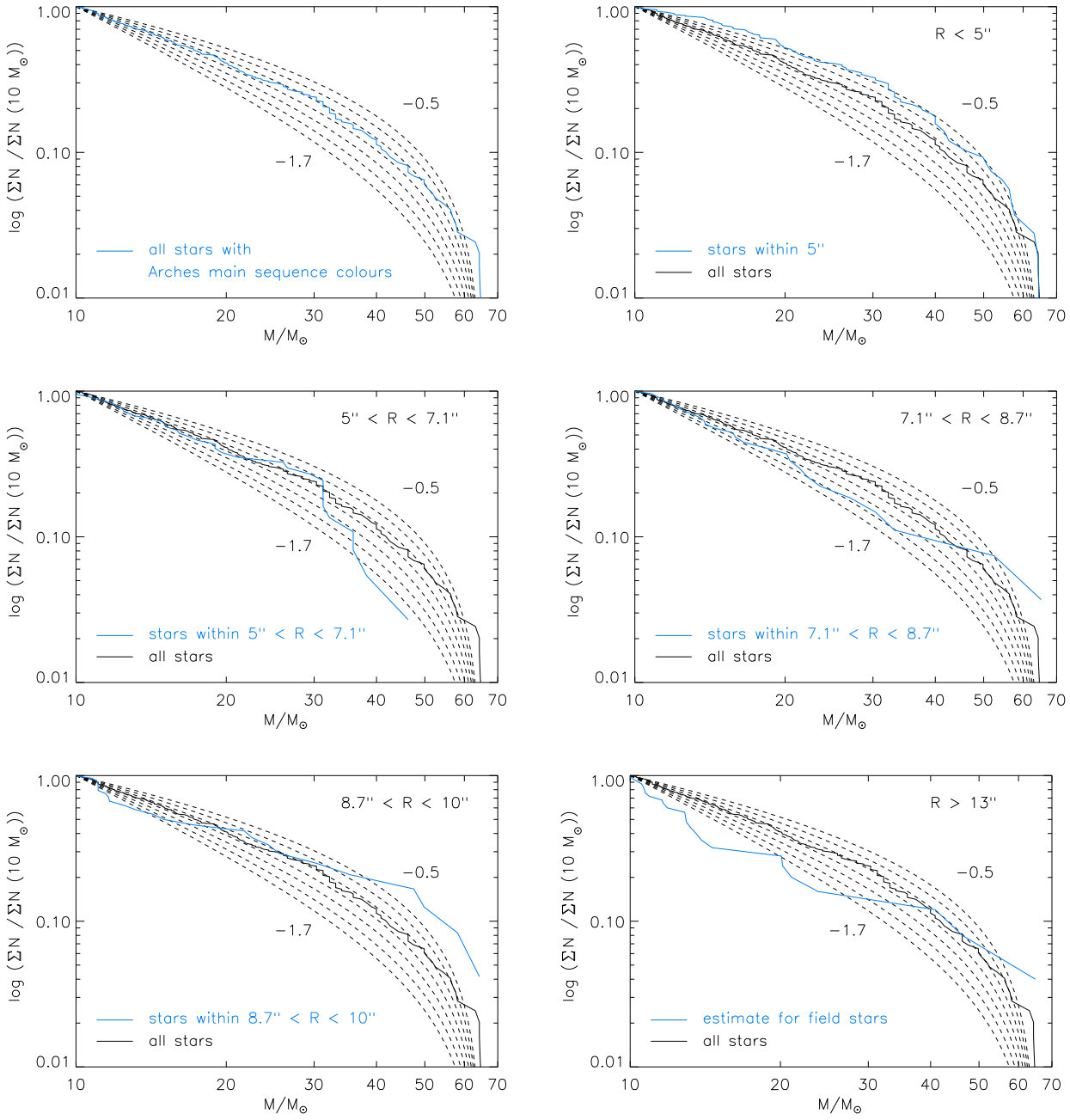

Figure 5.15: Radial variations in cumulative mass functions of Arches.
Radial annuli are identical to the annuli used for radial LF and MF determinations. All CFs are normalised at $M = 10\,M_{\odot}$. A grid showing theoretical functions expected from power-law distributions is underlaid (dashed lines, cf. Fig. 5.14). The CF of each annulus is shown in blue, and the CF of the entire field is included in black for comparison. The number of stars included in each CF is given in Tab. 5.2. Note the increasing deviation of the CF from a single power law shape, as was already indicated in the radial MFs (Fig. 5.9).

Table 5.2: Number of stars contributing to each radial CF.

annulus	all stars	$M > 10\,M_\odot$	f($M > 10\,M_\odot$)	$< m >$	$< m > (M > 10\,M_\odot)$
$R < 5''$	196	107	55 %	11.7 $M_\odot$	21 $M_\odot$
$5'' < R < 7.1''$	170	36	21 %	4.7 $M_\odot$	17 $M_\odot$
$7.1'' < R < 8.7''$	163	26	16 %	2.5 $M_\odot$	16 $M_\odot$
$8.7'' < R < 10''$	117	23	20 %	3.4 $M_\odot$	15 $M_\odot$
$R > 13''$	60[a]	9[a]	15 %	3.2 $M_\odot$	13 $M_\odot$
all	1030	247	24 %	4.0 $M_\odot$	17 $M_\odot$

[a]Number of field stars scaled to area of annuli ($N_{field}/2.63$)

the core is clearly mass segregated when compared to even the next annulus. More than 50 % of the observed core stars have masses in excess of $10\,M_\odot$, and the median mass observed in the core, $\langle M \rangle = 11.7\,M_\odot$ is nearly a factor of 3 larger than the median mass even in the subsequent annulus, $\langle M \rangle = 4.7\,M_\odot$. The median mass then decreases quickly down to $\sim 3\,M_\odot$ and stays at this level. On the other hand, the median mass of stars with $M > 10\,M_\odot$ decreases only slowly, providing weak evidence that the massive end of the stellar distribution on the entire field is dominated by Arches main sequence stars. In contrast to the large fraction of massive stars in the cluster core, however, only about 20 % of all observed stars have $M > 10\,M_\odot$ at *all* radii beyond $R > 5''$. This yields very strong evidence for a highly mass segregated core.

5.2.5 Summary of Arches results from NACO

The NAOS-CONICA data of the Arches cluster allowed a much more detailed and thorough analysis of the stellar population of the cluster. The improvement in spatial resolution yielded significantly improved number statistics, and consequently a deeper understanding of the statistical properties, and thus the mass function.

There is indication from the integrated MF that the MF slope appears flatter when crowding effects are severe. This was already slightly indicated in the comparison of Gemini and HST data, although the slopes all agree within the fitting uncertainties. The flattening of the observed MF in the case of a crowding limited field can be understood as a predominant loss of intermediate- and low-mass stars. The high-resolution NACO data allow the confirmation of the Gemini results, and show that thorough incompleteness correction as has been performed on the Gemini data is capable to reveal most crowding losses. Nevertheless, the resolution of the cluster population clearly supercedes all statistical correction methods.

In addition to the overall MF slope, the mass-segregated core is confirmed with NACO, and the flattening towards lower masses marginally suggested from the Gemini and HST data, is clearly depicted. In the mass range $4 < M < 10\,M_\odot$, the MF is consistent with a flat slope of $\Gamma \approx 0$. As the faint population in the Arches cluster is also most contaminated by field stars, this flat MF provides strong evidence for a mass function truncated at the low-mass end.

A similarly truncated MF is suggested for the nearby starburst galaxy M 82. From infrared imaging and spectroscopy of the highly obscured nucleus, used as input for starburst population models, Rieke et al. (1993) deduce a bias against low-mass stars, while the high-mass end of the MF is consistent with a standard MF slope. The modelled IMF reproducing the observational constraints best requires either a depletion of stars below a few $M_\odot$ and a normal high-mass IMF, or an overall strong bias

towards high-mass stars in the form of a flattened IMF. Recent evidence for a truncated MF is obtained from a detailed analysis of the dynamical properties and mass-to-light ratio in two young, massive starburst clusters in M82 (Smith & Ghallagher 2001). A low-mass cut-off of $2-3\,M_\odot$ yields the best agreement with the observations, implying a normal high-mass MF. The same authors argue that these massive clusters, formed in the starburst environment in M 82, despite total masses of $10^6\,M_\odot$ consistent with globular cluster masses, will probably not evolve into globular clusters, but dissolve in less than 2 Gyr. The same conclusion was already drawn for the Arches cluster in Sec. 5.1.5, and will be confirmed in the next section from NACO data. The behaviour observed in the Arches MF and the consequences on the survival of the cluster are very similar to the starburst clusters in M 82. The Arches cluster may provide a template for these and comparable unresolved extragalactic objects.

Even in a resolved cluster, the derived MF slope inherits large uncertainties from the binning of stars into magnitude and mass intervalls. Introducing two new procedures to study the MF, the statistical uncertainties could significantly be reduced. As a consequence, the radial change in the MF could be discussed in more detail, leading to a deeper understanding of the MF behaviour. While the cluster center was severely limited by crowding before, stars down to $\sim 4\,M_\odot$ are now resolved with a completeness of more than 75%. From number counts and radial MFs the cluster core appears not only extremely mass segregated, but there are also indications that the largest fraction of massive stars is indeed spatially restricted to the core. On the other hand, the outer annuli all display relatively normal slopes, at least in a significant part of the mass range, very close to the average value of Γ observed in young star forming regions in the Milky Way.

Further conclusions on the cause of mass segregation, i.e. whether primordial mass segregation is required to explain in the observed spatial distribution of stellar masses, or whether dynamical relaxation can cause the strong core segregation, has to await a detailed analysis of the field star contribution. Thorough field subtraction and a more detailed incompleteness calculation has to confirm the above findings. Field data will in particular allow to extend the MF considerations presented here down to the completeness limit of a few $M_\odot$. This in turn will allow more detailed dynamical and evolutionary modelling of the cluster population, promising to disentangle primordial from dynamical segregation.

5.2.6 Dyamical parameters revised from NACO data

When the NACO data are used to re-estimate the integrated cluster properties, a larger sample of stars and a wider mass range are available than in case of the Hokupa'a data set. Using the same procedure as in Sec. 5.1.5, the half-mass radius appears smaller due to the larger number of stars resolved down to at least $M \geq 3\,M_\odot$ in the cluster center, $r_c = 0.24$ pc as opposed to $r_c = 0.4$ pc before. Ideally, the core radius would be derived from the density profile fit. However, a profound knowledge of the field contamination is required to obtain the proper cluster profile, which is currently not available.

The determination of the relaxation time is still limited by the unknown total mass in stars and the characteristic stellar mass. As we have a larger sample at hand, several extreme cases may be considered. 1) Include all stars measured with Arches main sequence colours and $M \geq 3\,M_\odot$, as the low-mass hump observed is suspected to contain mainly field stars. 2) Calculate the relaxation time formally for $M \geq 10\,M_\odot$ only, assuming all stars below $10\,M_\odot$ to be dominated by field stars, as indicated by comparison with stars beyond $R > 13''$. 3) Extrapolate the high-mass end of the MF, $\Gamma = -1.1$, down to lower mass. 4) Extrapolate the flat MF between 3 and $10\,M_\odot$ down to lower masses, and add to the observed high-mass end.

The results of these calculations are presented in Tab. 5.3. Each of these procedures bears significant caveats that should be mentioned.

1) Although incompleteness tests indicate that the observed mass distribution is more than 75% complete down to $M \geq 3\,M_\odot$ at every cluster radius, some ill-understood selection effect may prohibit

the detection of lower mass members. The low total mass measured for $M \geq 3\,M_{\odot}$, and the high median mass in this distribution, both tend to decrease the relaxation time strongly. The same is true, but even more extreme, for case 2), where only the high-mass end of the distribution has been included. Hence the very short relaxation times of only a few $\times 10^5$ yr characterise the dynamical timescales of intermediate- and massive stars only, neglecting any low-mass contribution. Methods 3) and 4) represent the standard method to extrapolate mass functions in order to estimate the total amount of stellar mass found in a star cluster. Extrapolation of the high-mass end was used by Figer et al. (1999) to arrive at a cluster mass of at least $12000\,M_{\odot}$, and possibly close to $2 \cdot 10^4\,M_{\odot}$. From the lack of stars below $10\,M_{\odot}$ we now know, however, that the MF does probably not continue down to the lowest masses in a regular way. Extrapolating the high-mass MF thus leads to an upper limit of M_{total}, and to a lower limit of the median mass m_*, and therefore to an upper limit of the relaxation time, $t_{rh} \sim M_{total}^{1/2}/m_*$. This extrapolation is an artificial construct to derive an upper limit to t_{rh}, and should not be overinterpreted, as the MF clearly flattens below $M \leq 10\,M_{\odot}$. In order to obtain a more realistic estimate closer to the observed mass distribution, the flat portion of the MF can be extrapolated into the low-mass regime and combined with the measured high-mass population to obtain M_{total} and m_*. This represents method 4). As 4) exploits the data down to $M \geq 3\,M_{\odot}$, field contamination is, just as in method 2), the most limiting factor, as we assume all stars on the field with Arches main sequence colours to be cluster members. As in 2), field contamination would, however, most probably decrease the relaxation time even further.

A wide range of values is derived from the above analysis (Tab. 5.3). These values range from the minimum for the high-mass population only with $t_{rh} \sim 0.1$ Myr, suggestive of a very short relaxation time in the core, to $0.7-1.5$ Myr (depending on r_c) for the extrapolated MF ($\Gamma = -1.1$) down to $1\,M_{\odot}$ and for the flat MF down to $0.1\,M_{\odot}$. The maximum relaxation time derived for extrapolation of the steep, high-mass MF ($\Gamma = -1.1$) down to $0.1\,M_{\odot}$ yields $\sim 10-20$ Myr, depending on r_c. Although the cluster mass was probably overestimated in case of the latter values, these numbers allow to constrain the dynamical timescale for cluster evolution and mass segregation to $1 \lesssim t_{rh} \lesssim 20$ Myr, with a clear tendency to lower values. As already suggested by the Gemini data, a short relaxation time indicates dynamical segregation in Arches. Although a longer timescale hinting at primordial segregation can not be completely excluded, a relaxation time of 1-2 Myr is most likely from the currently observed mass distribution.

Two severe limitations to the above analysis should be mentioned. First of all, the relaxation time as given in BT87 is estimated for a bound cluster potential. Models by Kim et al. (2000) and Portegies Zwart et al. (2002) suggest strong tidal disruption on short timescales. As a consequence, a large fraction of the Arches population at larger cluster radii may already be unbound. Speculatively, the flattened portion of the MF might hint at tidal stripping, and the short estimate of t_{rh} simply reflects the incomplete cluster population. Secondly, no realistic assumption on the field contamination can be made. When discussing the MF above, stars beyond $R > 13''$ have been used to trace the "field". This is not necessarily true. It is highly probable that a large fraction of stars observed on the Arches field belong or once belonged to the cluster population, now strongly influenced by turbulent dynamical interactions and tidal stripping. Thus, it is not unreasonable to include all stars in the estimated cluster mass to obtain an upper mass limit. In all these considerations, the implicit assumption is made that the derived MF is correct. We should not forget, however, that several prerequisites as e.g. the cluster age and metallicity, as well as the extinction variation, entered this MF derivation. The observed flattening has to be confirmed independently.

The complex processes acting together on the Arches cluster internally and externally, distort the cluster profile heavily, and prohibit a final statement about the cause of the observed mass segregation. Velocities and proper motion studies are required to probe model predictions such as an extended low-mass stellar halo with a large velocity dispersion as compared to the central high-mass cluster population. Such a velocity gradient between high- and low-mass stars would yield additional evidence for a dynamically relaxed system, supporting the short dynamical timescales. A smooth velocity

Table 5.3: Dynamical timescales of the Arches cluster derived from different extrapolations of the mass function (see text for details).

low-mass cut-off	M_{total} $M_\odot$	$< m >$ $M_\odot$	N_{total}	$t_{rh}(r_c = 0.4\text{pc})$ Myr	$t_{rh}(r_c = 0.24\text{pc})$ Myr
measured stars $M \geq 3\,M_\odot$					
$M \geq 3\,M_\odot$	7420	7.7	586	0.30	0.14
measured stars $M \geq 10\,M_\odot$					
$M \geq 10\,M_\odot$	5485	17.5	244	0.11	0.05
high-mass IMF extrapolated, $\Gamma = -1.1$					
$M \geq 3\,M_\odot$	9417	5.0	1041	0.52	0.24
$M \geq 1\,M_\odot$	13446	2.0	3748	1.54	0.72
$M \geq 0.1\,M_\odot$	23040	0.2	47440	19.61	9.12
flat IMF extrapolated, $\Gamma = 0.$					
$M \geq 1\,M_\odot$	8107	4.0	966	0.57	0.26
$M \geq 0.1\,M_\odot$	8236	1.4	1656	1.52	0.70

distribution, on the other hand, would point towards primordial segregation, with imprinted stellar velocities from birth in the turbulent molecular cloud.

It should be noted in passing that the total cluster mass has been overestimated by all previous extrapolation procedures if the flattening in the MF turns out to be real. One significant impact of such a flattening would be a lower-mass cutoff in the *initial* cluster mass function, as the intermediate mass stars, even if ejected, should still be visible in the surrounding field. If the cluster is strongly dynamically segregated, enhanced collisions and merging in the cluster center as suggested by Bonnell et al. (1998) could also consume a fraction of the low-mass population.

NGC 3603

Figure 6.1: NGC 3603 and the central starburst cluster HD 97950.
The VLT/ISAAC JHK co-added image (field of view $3\farcm2 \times 3\farcm2$) visualises the beauty and obstacles of the giant HII region. The rims and elephant trunks indicate strong photo-evaporation, and gaseous filaments are signposts of the variable extinction in the remnant molecular cloud. The starburst cluster is located in an excavated cavity, exposing the rich stellar population to our view.

Chapter 6

NGC 3603

The second starburst cluster close enough to resolve the stellar population in detail is the central cluster in NGC 3603, HD 97950. As discussed in the introduction to NGC 3603 in Sec. 2.4.2, HD 97950 forms in the more moderate star-forming environment of the Carina spiral arm than the Arches cluster in the Galactic Center. If the environment is a crucial parameter shaping the emergent stellar mass distribution, we may expect that the mass spectrum of HD 97950 displays different characteristics than the Arches mass function. On the other hand, if the influence of the environment is minor and internal processes in the starburst cluster determine the final mass distribution, similar mass functions are expected for both starburst clusters.

The population in HD 97950 is studied using deep, high-resolution near-infrared VLT/ISAAC data. With a detection limit of 21 mag in K, this is the deepest photometry available of HD 97950, allowing to study the stellar mass distribution down to $0.1\,M_{\odot}$. The basic data reduction and photometric results are presented in this chapter. The ISAAC $JHKL$ photometry is complemented by HST Hα photometry, allowing to discuss the survival of circumstellar material in the presence of a rich O-star population. The mass function in HD 97950 will be derived on the basis of the colour-magnitude diagrams in Chap. 7.

6.1 NGC 3603 ISAAC data

VLT/ISAAC JHK data of the central starburst cluster HD97950 in the giant HII region NGC 3603 were obtained in service mode under excellent seeing conditions (seeing $< 0\farcs4$) in April, 1999. The data reduction of the JHK data will be discussed below, while the L-band data will be described in Sec. 6.1.4. These raw data were provided by Wolfgang Brandner and Bernhard Brandl. Preliminary J and K photometry is published in Brandl et al. (1999).

The data were taken when NGC 3603, located at $\alpha = 11^{\rm h}15^{\rm m}07^{\rm s}$ and $\delta = -61°15'33''$ (cluster center), was almost in culmination, such that the airmass ranged from 1.2 to 1.5. Airmass variations were taken into account during data calibration. The individual exposure time was 1 min, with detector integration times as short as 1.77 s to avoid saturation of bright stars as far as possible. This is the shortest DIT available with ISAAC. As all frames were taken with this short DIT setup, it was neither necessary nor possible to analyse the bright and faint end of the distribution on seperate frames (as in the case of the Arches cluster). Nevertheless, even these shortest DITs caused a loss of the brightest stars in the cluster center, and consequently a loss of the massive tail of the mass function. The upper end of the MF can therefore not be derived from this data set alone and will not be discussed in this work, as no JHK photometry with comparable resolution is currently available for the brightest cluster stars. The saturation of the brightest stars implies the loss of the innermost $7''$ of the cluster core, where the population is dominated by high-mass stars.

As in the case of the Arches cluster, these data are not limited by integration time, but by crowding

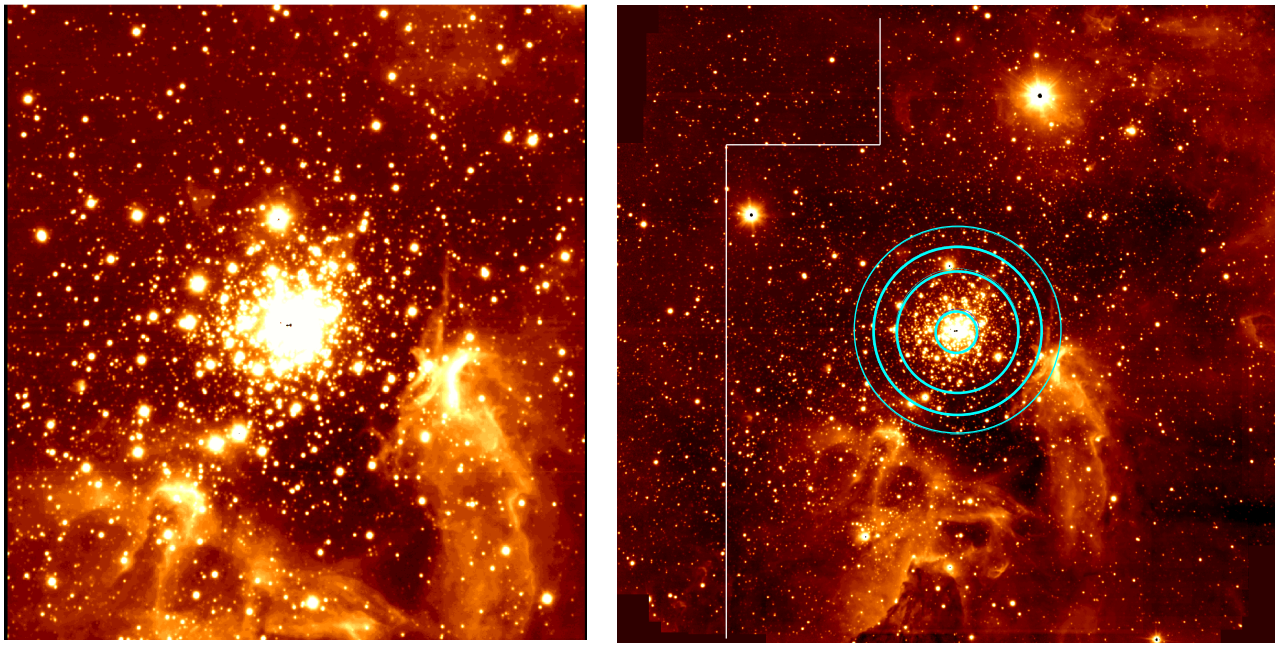

Figure 6.2: J_s combined 9 min and K_s 39 min ISAAC images (North is up, East left).
The high-resolution J_s $2' \times 2'$ image covers the smallest field of view available, while the K_s image reveals the entire observed region with $3\farcm4 \times 3\farcm4$ FOV. Selection of main cluster center, $R < 33''$ as suggested by enhanced stellar density and field selection to the East of the cluster are shown on the K_s image. Circles mark radial annuli with $7''$, $20''$, $27''$, and $33''$.

in the central cluster regions. With the lower resolution of seeing-limited imaging, crowding is even more critical given the comparable distance and stellar density of Arches and NGC 3603. As the procedure proved very successful in case of Arches, the highest resolution frames were selected to yield combined images in J_s, H and K_s of 9, 15 and 11 min total integration time, respectively. These data are limited by small area coverage of only $2' \times 2'$ surrounding the cluster due to the rejection of fields with lower resolution.

As the field is not as crowding limited as the cluster, a larger area with slightly lower resolution allows to determine a statistically complete sample of field stars. Thus, all useable data in all three filters were also combined yielding 35, 37 and 39 min integration time in J_s, H and K_s with a field of view of $3\farcm4 \times 3\farcm4$. As a seperate background field is not available, the outer regions of these images will be used to estimate the field contribution.

The observations are summarised in Tab. 6.1. The final high-resolution J_s image with the smallest field of view as well as the K_s image with the largest field coverage are shown in Fig. 6.2, where the cluster center ($R < 33''$), radial annuli and field star areas used in the following analysis are indicated.

6.1.1 Basic Data Reduction

Standard data reduction of ISAAC frames includes removal of electrical ghosts generated by the HAWAII detector, flat fielding and sky subtraction. During several observing periods, a strong odd-even column effect was detected. The data were checked with respect to column-to-column variations, and no indication of the odd-even column effect is found. Thus, prior to standard data reduction, only the *isaacp ghost* routine under *eclipse* was used for electrical ghost removal.

A special feature of the ISAAC HAWAII detector is the reset of the upper half of the detector prior to integration to avoid over-exposure due to accumulated dark current. This causes a separation of the field into two distinct regions, the lower half with rows 1-512 and the upper half with rows 513-1024, both with a strong background gradient. As the strength of the gradient varies among

Table 6.1: VLT/ISAAC observations of NGC 3603. The total integration time refers to the final combined images. All JHK frames were taken with a detector integration time of 1.77 s and 34 integrations, leading to a total exposure time of 60 s in each individual frame. L-band frames were taken with 135×0.104 s, or a total integration time of 14 s per frame.

date	Filter	detec. limit	satu. limit	N(frames)	t_{int}	final resolution	remark
JHK high-resolution images ($2' \times 2'$)							
April 1999	J_s	21.8 mag	11.7 mag	9	9 min	$0\farcs38$	
April 1999	H	21.2 mag	11.5 mag	15	15 min	$0\farcs41$	
April 1999	K_s	20.3 mag	11.6 mag	11	11 min	$0\farcs35$	
JHK entire field ($3\farcm4 \times 3\farcm4$)							
April 1999	J_s	22.0 mag	11.5 mag	35	35 min	$0\farcs40$	
April 1999	H	20.8 mag	11.4 mag	37	37 min	$0\farcs44$	
April 1999	K_s	20.4 mag	11.4 mag	39	39 min	$0\farcs37$	
L (2 fields á $1\farcm2 \times 1\farcm2$)							
July 2000	L	15.0	7	27	6.3 min	$0\farcs5$	Cluster field
July 2000	L	15.1	7	24	5.6 min	$0\farcs5$	East field

subsequent exposures, the background had to be subtracted before any image combination could take place. The ISAAC detector is read out in the y-direction, such that each row has a constant background, while the gradient affects the detector columns. This allowed to collapse each frame along rows, simultaneously rejecting $\sim 90\,\%$ of the brightest pixels to avoid stellar contamination, and using the average of the remaining faint pixels in each row as background estimate. Due to the strong HII region emission observed on all frames, however, individual rows still varied significantly. As the read-out contribution is known to be a smooth gradient, the values derived from each row were fitted by a third order polynomial, which was then subtracted from the frame. This procedure resulted in very flat images, except for the transition region around rows 511-515, where jumps persisted. In the final image combination, these rows have therefore been excluded.

After this pre-handling, as many images as possible were used for sky determination. The IRAF task *imcombine* allows to reject bright as well as faint pixels. Due to the high stellar density, the brightest $\sim 80 - 90\,\%$ of all pixels were rejected. In addition, to avoid bias to statistical fluctuations towards exceptionally low values, the lowest 2 pixels were also excluded. With a total number of available frames of about 40, this resulted in typically 4 averaged values for the background. Despite these low statistics, the resultant sky frames were very smooth, in particular avoiding bright residuals from cluster or HII region contamination. Rejecting less pixels caused strong, artificial background fluctuations from stellar residuals. Note that the images were already at a mean sky level of zero due to the prior gradient reduction.

The combined sky frame was subtracted from all science frames, which were then divided by the flat field corresponding to each filter, as derived with *eclipse* from twilight flats taken during the observing run. The geometric distortions over the ISAAC field were corrected. The distortion coefficients were kindly provided by Morten Andersen.

6.1.2 Image combination

From the pre-reduced images, the frames with the smallest FWHM were selected to achieve the highest resolution on the cluster center. In J band, where the seeing affects the image resolution most severely, this limit was set to FWHM $< 0\farcs37$ (2.5 pixels at a pixel scale of $0\farcs147$), thus allowing to combine the 9 highest quality exposures to a 9 min image with a FWHM of $0\farcs38$. The H band data display the lowest resolution of all three filters, such that a limit of FWHM$<$ 2.7 pixels or $0\farcs4$ had to be used to include a sufficient number of frames for area coverage. While only few frames had a lower resolution, 15 frames could be identified matching this criterion, which were combined to one 15 min H band image with a resultant FWHM of $0\farcs41$. As the K-band seeing is usually smaller than at shorter wavelengths, this data set displays the highest spatial resolution. 11 frames with FWHM$<$ 2.4 pixels or $0\farcs35$ could be co-added to one 11 min integration with a final resolution of $0\farcs35$ (no degradation due to image dithering is observed). The resultant field of view is limited by the J-band frame with the smallest area coverage ($1\farcm9 \times 2\farcm1$), constraining the field available for the high-resolution analysis of the cluster and surrounding population.

In addition, 35 exposures in J, 37 exposures in H and 39 exposures in K were combined yielding final resolutions of $0\farcs40$, $0\farcs44$, $0\farcs37$ in JHK, respectively. These data resulted in a larger field of view of $3\farcm4 \times 3\farcm4$ to allow estimates on the field contamination.

All frames were combined using the *drizzle* task in IRAF with 2×2 oversampling to enhance the peak flux and avoid resolution losses during image combination.

6.1.3 Photometry

Photometry was again performed using the IRAF implementation of the DAOPHOT package. Detection thresholds were set such that most artifacts due to sensitivity variations were rejected. The strong rims of the HII region, however, caused a large number of peak detections related to no obvious point source. As these intensity enhancements due to nebular emission are very bright, they could not be rejected using a higher detection threshold. For aperture photometry, the FWHM measured on each image was used as the aperture radius, and subsequently as the fitting radius in the final PSF fitting routine (*allstar*). The FWHM changed linearly over the field in all images, such that a linearly variable PSF was fitted. In all cases, the best fitting function turned out to be a penny function comprised of a Gaussian kernel with Lorentzian wings. As the stellar density is too high to allow a reasonable number of isolated stars to fit the FWHM variation over the field, the final PSF was determined iteratively after neighbour subtraction.

The sky background of each star was fitted individually to account for the highly variable background. PSF fitting with *allstar* allows for a simultaneous PSF and background fit, where the mode of the underlying residual intensity distribution is determined. An annulus of twice the PSF radius (15 to 20 pix depending on image resolution) was used to derive the sky, with rejection of the innermost 5 to 6 pix (i.e., the FWHM), as the peak flux causes the largest artefacts.

The calculated PSF magnitudes were then calibrated using the zero points derived from standard stars, with airmass and aperture corrections applied. For airmass correction the average atmospheric absorption, f_{abs}, of 0.06, 0.06 and 0.07 mag per airmass in J, H and K, resp., as given on the Paranal web page was used, where $\Delta mag = (AM - 1.) \cdot f_{abs}$. The aperture correction was determined from the most isolated stars on each frame, i.e. the most isolated of the stars used to derive the PSF.

The analysis presented below will be based on sources detected in all 3 filters simultaneously to reject artefacts as well as faint nebular emission peaks. The final photometry includes all sources detected in JHK with photometric uncertainties below 0.2 mag in J and 0.15 mag in both H and K. A stricter selection criterion resulted in the rejection of a significant fraction of the cluster center stars, where PSF fitting is complicated by crowding.

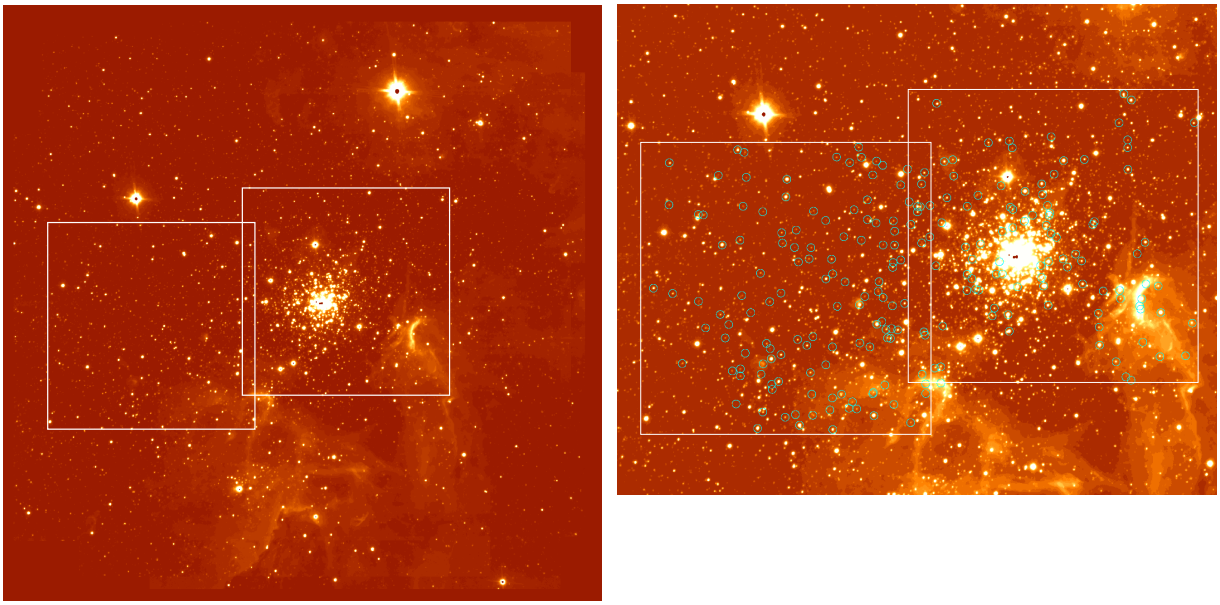

Figure 6.3: Fields observed in L-band, overlaid on the K-band image.
Left panel: The cluster center and East L-band fields shown on the $3\farcm4 \times 3\farcm4$ K-band image.
Right panel: L-band fields with sources detected in L and JHK marked as circles.
The field covers approximately $2\farcm5 \times 2'$. North is up and East to the left.

6.1.4 L-band observations

L-band observations were carried out in July, 2000, using the ISAAC long wavelength (LW) facility. The data were taken in chopping mode on two neighbouring fields, with the first field including the cluster, and the second field adjacent to the East of the first. Images were taken with the ISAAC LW Aladdin 1024×1024 pix^2 array at a pixelscale of $0\farcs071$, covering a FOV of $1\farcm2 \times 1\farcm2$. Dithering was applied to avoid saturation artefacts. The average seeing varied between $0\farcs35$-$0\farcs5$, such that only reduced frames with a resolution better than $0\farcs5$ entered the final images. The L-band fields are shown in Fig. 6.3 overlaid on the K-band image.

The shortest detector integration time for this camera, 0.104 s, was chosen to avoid saturation. 27 chopped and subtracted frames were combined to yield a total integration time of 380 s on the cluster field, and 24 frames on the East field, yielding 338 s integration time. The photometric limit was ~ 15 mag due to the large sky background of ~ 4 mag faced in long wavelength observations.

The reduced and calibrated photometry was provided by Wolfgang Brandner. Reduction included standard flat fielding and sky reduction using the chopped frames. Image combination of the reduced frames was conducted with the specialised *eclipse jitter* package for ISAAC observations, which allows automated sky fitting by image background interpolation, and rejection of frames from the sky estimate in case of large gradients. This procedure is optimised for the large sky background contaminating L-band observations, yielding smooth backgrounds and the best photometric performance. The remaining limitation is given by the negative stellar residuals introduced during chopped sky subtraction. These residuals are unavoidable in the given observing mode. Special care was taken to exclude spurious detections, in particular close to the negative images of the cluster and the bright HII features, using the allstar PSF fitting quality parameters. The final photometry file contains only objects identifiable as stellar point-sources. On a field as crowded as the NGC 3603 region, negative images can occasionally fall exactly onto the same position as a positive stellar image. These exact matches should, however, be rare and random, such that the overall statistical results are not altered. As it is not straight forward to correct for this effect, no attempt was made to reject these coincidences.

Due to the artefacts and higher background, the L-band photometry is more uncertain than JHK

photometry. Consequently, a conservative limit of $\sigma_L < 0.1$ mag is chosen as opposed to 0.2 mag in J_s and 0.15 mag in K_s. This selection rejects faint sources with uncertain photometry and outliers in the resultant two-colour diagram efficiently. The comparable final resolution on the L-band frames and the JHK images allows the resolved sample of $JHKL$ sources to be statistically complete.

Photometric Results

In the following sections, the results of the photometric analysis, such as colour-magnitude and colour-colour diagrams, extinction variation, near-infrared excesses and Hα emission of stars in the HD 97950 cluster and its immediate vicinity are discussed. The colour-magnitude diagrams shown below are in $J_s, J_s - K_s$ space, as these data sets yield the best photometric performance and will be used for the derivation of the mass function in the next chapter. The H-band data are less accurate especially in the densest cluster regions, and will therefore only be used for two-colour diagrams to study the underlying population in a more general way.

6.2 Colour-Magnitude diagram of HD 97950

6.2.1 Colour-magnitude diagram and pre-main sequence turn-off

The $J_s, J_s - K_s$ colour-magnitude diagram is derived from the highest resolution J_s and K_s frame, covering a field of view of approximately $2' \times 2'$. Photometry of all stars on this field is shown in the left panel of Fig. 6.4, while the central $33''$ of the cluster are displayed in the right panel. This radial selection will be used in the following analysis to select the main cluster area. This area is confined to the cluster center with obvious enhanced stellar density with respect to the field population (cf. Fig. 6.2). A prominent main sequence population stands out in the left panel of Fig. 6.4. At the fainter end below $J_s > 15$ mag, the entire stellar population on the FOV (right panel) is dominated by field stars. The restriction to $R < 33''$ depicts a densely populated pre-main sequence with a pre-main sequence/main sequence transition region at $14 < J_s < 16$ mag and $0.6 < J - K < 1.4$ mag. The overdensity of stars between $15 < J_s < 16$ mag and $0.7 < J - K < 0.9$ mag marks the point where hydrogen core burning is ignited, i.e. where the PMS joins into the MS (PMS turn-off point). The transition region where the PMS turns over towards the MS is - in comparison to the fainter PMS - only sparsely populated. PMS evolutionary models by Palla & Stahler (1999, hereafter PS99) yield a very narrow mass range for this transition state of only $2.5 - 4\,M_\odot$, while the entire PMS covers a mass range between at least ~ 0.1 and $4\,M_\odot$, such that only a minor fraction of the stars is currently in the transition stage. The apparent extension of the main sequence towards fainter magnitudes seen strongly in the field, but also slightly in the cluster CMD, most probably represents the young population associated with and widely distributed in NGC 3603, as this population falls onto the zero-age main sequence at the same distance and foreground reddening as the central cluster. In addition, the PMS shows significant redward scatter, suggesting a fraction of the PMS population to be still embedded in native material. The extinction properties will be discussed in Sec. 6.4 with respect to individually reddened objects.

6.2.2 Distance, extinction and age derived from the PMS turn-off

In Fig. 6.5, isochrones with various distances and extinction values are overlaid to the MS/PMS transition. The parameters yielding the best fit to the PMS turn-off imply a distance modulus of 13.9 mag, $d = 6$ kpc, and a foreground extinction of $A_V = 4.5$ mag to the PMS. This choice also matches the bulk of the PMS stars towards fainter magnitudes. The PMS tracks with these parameters included in the CMD in Fig. 6.6 depict the transition locus clearly. The left panel shows a 1 Myr Palla & Stahler

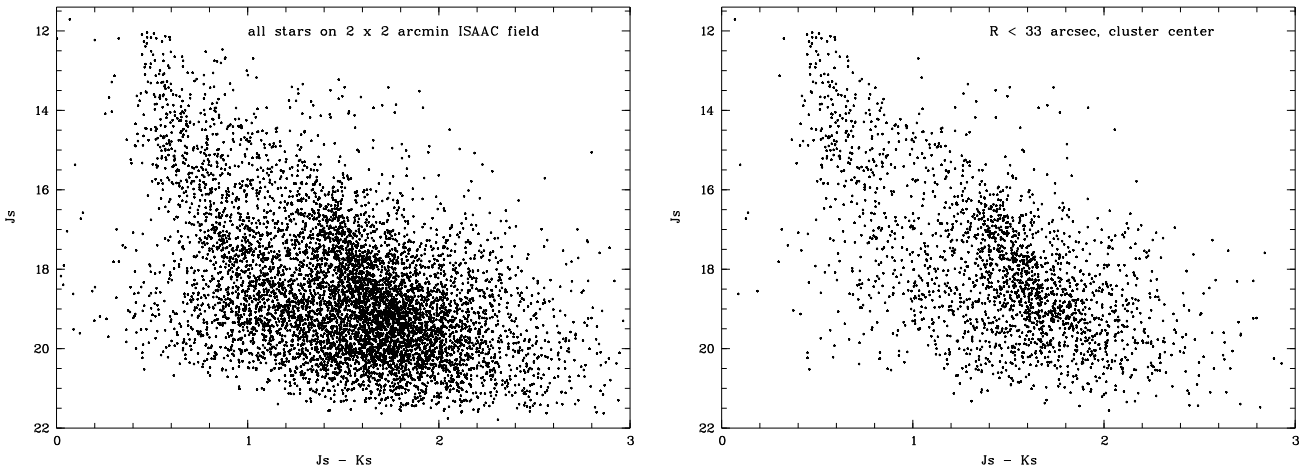

Figure 6.4: J_s, $J_s - K_s$ colour-magnitude diagrams of the central region in NGC 3603. Left panel: All stars on the high-resolution $2' \times 2'$ frame are shown. 7122 stars with photometric uncertainties $\sigma_J < 0.2$ mag and $\sigma_K < 0.15$ mag are included in this diagram. The uncertainty limits are selected such that artefacts are rejected, while cluster members with relatively high photometric uncertainty due to the crowded nature of the cluster center are not a priori excluded from the analysis. Right panel: CMD of the central $33''$ of the HD 97950 cluster. The same selection yields 2247 stars within a physical radius of ~ 1 pc at a distance of 6 kpc. The central $7''$ had to be rejected due to crowding and saturation. The main sequence is clearly depicted in the upper left part of the CMD, leading via the transition region at $J_s \sim 15$ mag into the pre-main sequence of the cluster to the lower right.

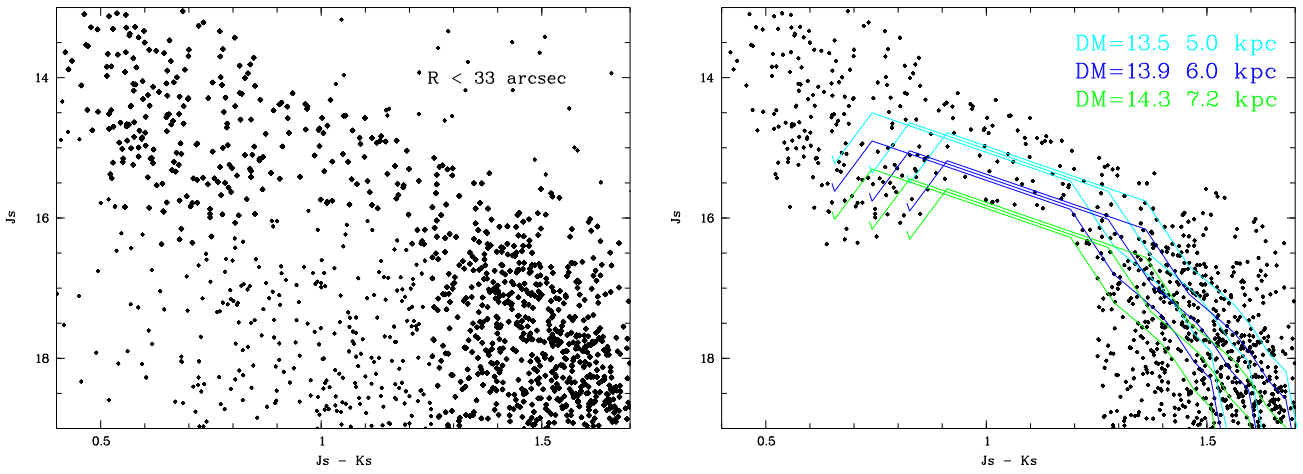

Figure 6.5: Isochrones with varying distance and extinction.
The left panel shows the selected MS/PMS stars (thick dots) compared to isochrones in the right panel. Distance moduli between 13.5 and 14.3 mag, $5 < d < 7.2$ kpc, and extinction values of $A_V = 4$, 4.5, and 5 mag are applied. The PMS turn-off at $J_s = 15.5$ mag and $0.7 < J_s - K_s < 0.9$ mag is best reproduced with $DM = 13.9$ mag, $d = 6$ kpc, and $A_V = 4.5$ mag. The main sequence appears less reddened than the PMS, and a common value for the extinction cannot be fitted.

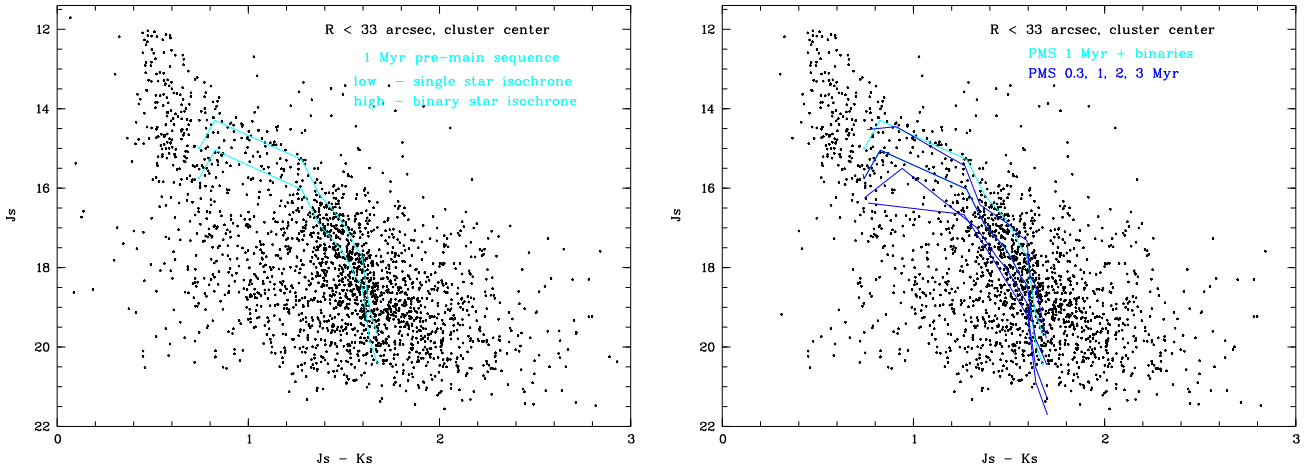

Figure 6.6: Colour-magnitude diagram of the central 33″ of HD 97950. Left panel: 1 Myr pre-main sequence isochrone from Palla & Stahler (1999) overlaid on the CMD, with distance modulus 13.9 mag (6 kpc) and foreground extinction $A_V = 4.5$ mag applied. The lower isochrone represents the locus of single stars, while the upper isochrone is shifted by $\Delta J_s = -0.75$ to display the expected positions of equal-mass binaries. The single-star PMS turn-off lines up very well with the PMS/MS transition point marked by a density enhancement at $15 < J_s < 16$ mag and $0.7 < J - K < 0.9$ mag. The binary locus emphasises a band of stars located above the transition region, where the PMS turns towards the MS. Right panel: PMS isochrones from the Palla & Stahler set of models for ages 0.3, 1, 2 and 3 Myr. The younger 0.3 Myr isochrone matches closely the 1 Myr binary locus. The 2 and 3 Myr models deviate significantly from the observed stellar distribution.

PMS isochrone overlaid on the CMD (lower curve), along with the analogous isochrone for equal-mass binaries shifted up by $\Delta J_s = -0.75$ mag (upper curve). These isochrones match the characteristic features of the PMS population very well. First of all, the overdensity at the PMS/MS transition (PMS turn-off point) is reproduced by the 1 Myr single-star isochrone, including the strong knee suggested by the models. Secondly, the width of the transition region of the isochrone corresponds to the width in $J - K$ colour observed in the transition region of the PMS, such that the fainter end of the isochrone falls on the average locus of the PMS stars. Last not least, the distinct sequence above the transition region is outlined by the equal-mass binary sequence, which will be discussed in detail in Sec. 6.2.4.

In the right panel of Fig. 6.6, PMS isochrones of various ages from the Palla & Stahler set of models are shown. As mentioned in Sec. 2.4.2, the age of the cluster is confined to less than 3 Myr by the Wolf-Rayet star population, and the pre-main sequence population is suggested to be younger than 1 Myr from comparison with PMS isochrones, such that isochrones with ages of 0.3, 1, 2 and 3 Myr are selected. Clearly, the 2 and 3 Myr isochrones are not consistent with the observed PMS transition. As described above, the 1 Myr isochrone models the features observed in the CMD very well. In previous works (Eisenhauer et al. 1998, Brandl et al. 1999), an age spread was suggested for the PMS in HD 97950. From Fig. 6.6 (right), this interpretation is not at all surprsing. The youngest 0.3 Myr isochrone almost exactly falls onto the 1 Myr equal-mass binary sequence, such that the scatter in the transition region was assigned to an age distribution. Although an age spread cannot be entirely ruled out from photometry alone, the offset of the bright edge of this population along with the additional shifted main sequence observed in the ISAAC data is very suggestive of the existence of an equal-mass binary sequence (see Sec. 6.2.4 for details). This has the main consequence that no age spread is needed to explain the observed scatter in the PMS/MS transition region.

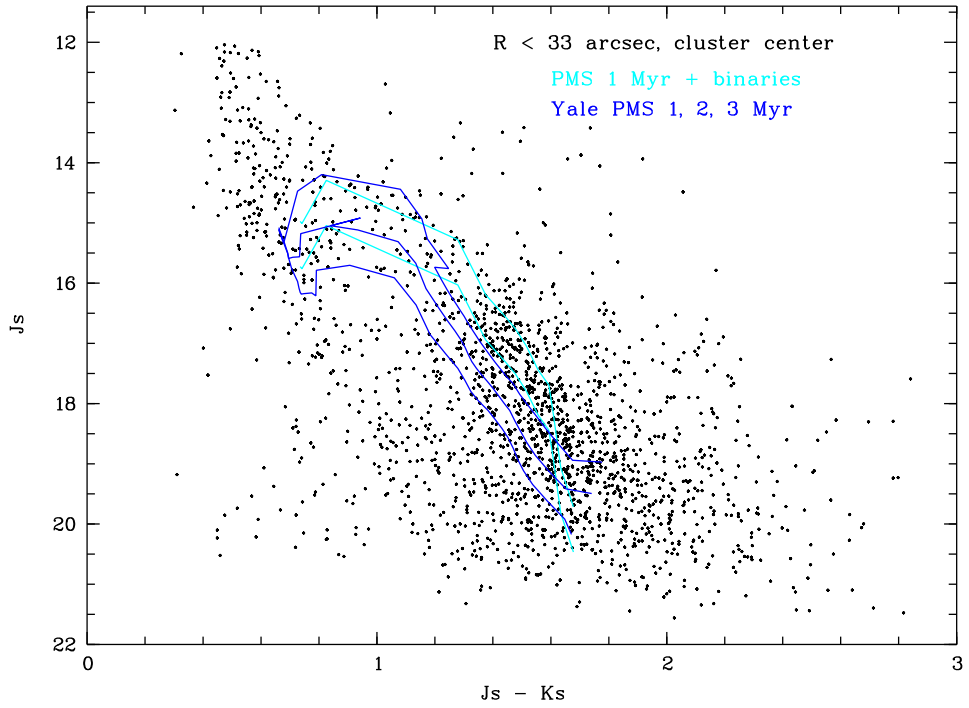

Figure 6.7: Yale isochrones (Yi et al. 2001) of various ages in comparison with the 1 Myr Palla & Stahler isochrone and binary locus. While the PS99 isochrone matches the turn-off point of the pre-main sequence, the width of the transition region as well as the average location of the bulk of the PMS stars, the transition region modelled in the Yale isochrones appears too narrow to reproduce these features. Note, however, that the 2 Myr Yale isochrone ($DM = 13.9^{\mathrm{m}}$, $A_V = 4.5^{\mathrm{m}}$) falls onto the 1 Myr PS99 isochrone. The duration of pre-main sequence evolutionary stages is not precisely known yet, and different sets of models are ambigious. As the PS99 isochrone reproduces the observed colour-magnitude distribution very well, it will be chosen for all mass function derivations.

6.2.3 Comparison with Yale evolutionary models

As stellar pre-main sequence evolution is not yet entirely understood, the existing sets of models deviate significantly (see, e.g. Baraffe et al. 2002 for a discussion). Although a detailed discussion of the model parameters and their consequences is beyond the scope of this thesis, a second set of PMS isochrones is compared to the data in Fig. 6.7. This set is deduced from the Yale database of evolutionary models as presented in Yi et al. (2001). The youngest PMS isochrone available in this set has an age of 1 Myr, such that the 1, 2 and 3 Myr isochrones are compared to the data, again with $DM = 13.9^m$ and $A_V = 4.5^m$ applied. On a first glance, these models also fall onto the pre-main sequence locus of the cluster stars. The subtle feature in the CMD resembling closely the PS99 1 Myr isochrone (and binary sequence), however, are not as exactly recovered by the Yale models. The same distance modulus and extinction reproduces the observed PMS turn-off with the 2 Myr isochrone, which however falls below the PMS locus at fainter magnitudes as the consequence of a too narrow transition region. While the 1 Myr isochrone is able to reproduce the PMS locus at the faint end, it overestimates the brightness at the PMS turn-off point, and falls above the transition region. If our interpretation of a binary sequence would be wrong, this isochrone would resemble the data more closely than the 2 Myr isochrone, but still fails to depict the exact transition point at $J_s - K_s = 0.7$ mag and $J_s = 15.5$ mag, where a pronounced overdensity is seen (cf. Fig. 6.4). As in the case of PS99, the 3 Myr model fails to reproduce the data completely, neither matching the faint bulk of the PMS stars nor the transition region. Therefore, the 3 Myr age is ruled out from PMS models in any event,

while some age ambiguitiy is still present due to the close resemblance of the 2 Myr Yale model with the 1 Myr PS99 model.

As the 1 Myr PS99 isochrone is able to reproduce the subtle features such as the width of the transition region, the main sequence turn-on point, and the average PMS locus observed in the CMD better than any other model, this isochrone will be used for the transformation of PMS luminosities into masses for the derivation of the mass function.

6.2.4 Binary candidate sequence

As mentioned above, a sequence of stars is offset above the PMS transition region as well as above and to the right of the main sequence. The shifted transition region lines up very well with the equal-mass binary locus suggested by the 1 Myr PMS isochrone (PS99). While it is very tempting to interpret this sequence as a binary sequence comparable to the binary sequence seen in young open clusters such as the Pleiades (Kähler 1999), several tests were performed to substantiate this assumption. First of all, the photometry was thoroughly checked against a systematic error. The stars selected as shown in Fig. 6.8 are neither exceptionally close neighbours indicating problems in the PSF fitting procedure (although some of them are, of course, close pairs given the high stellar density in the cluster), nor do they have unusually large photometric or fitting uncertainties (see Fig. 6.9, left panel for formal photometric uncertainties). Additionally, aperture photometry on several individual stars out of this selection as well as stars from the regular main sequence with comparable luminosity was performed to exclude systematic fitting errors not mirrored in the uncertainties assigned by the DAOPHOT *allstar* task. For this purpose, no fitting was involved at all, but simple flux counts in a circular area centered on the test star were determined. For the 12 stars sampled in this way, with half of the stars on the regular main sequence and half on the offset sequence, the gap remains, i.e. stars on both sequences are still found on approximately the same locus as derived from PSF fitting, except for the larger scatter due to ignorance of close companions and the fluctuating background.

In Fig. 6.9, the binary candidates are shifted down by $\Delta J_s = +0.75$ mag corresponding to a factor of two in luminosity, assuming equal-mass binaries. Despite the fact that the offset in the upper part of the main sequence appears to be a colour offset rather than a shift in luminosity, which would call the binary scenario into serious doubt, the down shifted stellar population lines up closely with the general shape of the stellar distribution in the CMD. At the least, no clear deviation from the underlying population of cluster stars is observed. The additional shift in colour at the upper main sequence is consistent with the scatter imposed on the CMD due to varying extinction, which will be discussed below.

How can the binary assumption be tested? Clearly, spectroscopy of the binary candidates would be ideal. As most objects in HD 97950 are relatively bright in the visual due to the low extinction along the line of sight, FORS multi-object spectroscopy of the PMS/MS transition stars has been initiated, and will be conducted shortly after the finalisation of this thesis. As long as spectroscopy is not available, comparison with higher spatial resolution observations might still give a clue on the nature of the objects. HST/PC data of HD 97950 were provided by Eva Grebel (private communication, see also Moffat et al. 2002) with a nearly diffraction limited resolution of $0\farcs06$, corresponding to 360 AU at a distance of 6 kpc. In contrast, the $0\farcs4$ resolution of the ISAAC images corresponds to 2400 AU. The average binary separation observed in solar-type main sequence stars in the solar neighbourhood by Duquennoy & Mayor (1991) is 35 AU, and a median separation of 30 AU with a maximum of 480 AU is found by Köhler (2001) in the η Chameleontis star-forming region, such that the spatial resolution of the ISAAC data is not expected to resolve typical systems. On the other hand, the HST/PC resolution allows to resolve the wider end of the binary separations persisting in the dense cluster environment with $a > 360$ AU.

Fig. 6.10 shows the selected binary candidates on the PC V-band frame (HST F547W filter). Blue

circles mark binary candidates unresolved with HST, and cyan circles indicate objects either clearly resolved into 2 stars with comparable luminosity or into one object with pronounced elongation. Of the 50 binary candidates included in the $37'' \times 37''$ FOV of the PC chip, 9 objects (18 %) are clearly resolved or elongated. Prosser et al. (1994) resolve 35 visual binary systems in the Trapezium cluster using the HST PC chip. They span a range in separations from $44 - 440$ AU at a distance of 450 pc, with 20 % (7) of these systems having separations of $a > 360$ AU. This is in excellent agreement with the resolved systems among our binary candidates.

The same authors derive a binary fraction of 12 % for the separations accessible with the HST Trapezium survey. Petr et al. (1998) confirm this result finding 10 % visual binaries for $63 < a < 225$ AU for low-mass stars. In the case of high-mass stars, Petr et al. note that of the 6 OB stars with spectroscopy in the central $40''$ (0.1 pc) of the Trapezium cluster 2 are binaries, and speculate that the higher fraction of high-mass binaries may indicate that high-mass systems form from three-body interactions. With a central density in HD 97950 exceeding the core density in the Trapezium by one order of magnitude, such encounters should be even more frequent. The binary selection displayed in Fig. 6.8 suggests a fraction of 30 % equal-mass binaries for stars earlier than type A down to $J_s \sim 16$ mag. Although the Petr et al. study is limited to a low number of objects, the 30 % binary fraction observed close to the cluster center of HD 97950 in the ISAAC data supports this scenario.

All these visual surveys are limited by the spatial resolution to a certain lower limit in separation. The photometric offset in the CMD identified in the ISAAC data is susceptible to all separations *below* 2400 AU, where two neighbouring stars would be resolved on the ISAAC frame. From the distribution of binary separations in the solar neighbourhood as well as in the Trapezium, this upper cut-off essentially includes all (physically bound) binary systems. We conclude that the observed sequence is very likely comprised of equal-mass binaries.

For the derivation of the mass function, these stars will either be treated as binaries or be rejected completely, or included as if they were single stars with larger reddening or brightness, to investigate the effects of binary treatment on the resultant mass function. It will be shown, nevertheless, that the resultant slope of the MF is not altered significantly by the treatment of the binary candidate sequence.

6.2.5 Binary sequence and Hα emission

Another aspect supporting the binary scenario is the strong anti-correlation between binary candidate selection and Hα excesses observed with HST/WFPC2. Of the 54 binary candidates and 40 Hα emitters marked on the J-band image in Fig. 6.11 only 4 coincide. This is to be expected if the Hα emission arises from circumstellar disks, as disks around binaries are observed to disrupt faster than around single stars (Osterloh & Beckwith 1995). The Hα data will be discussed in the next section.

6.2.6 Stars with enhanced Hα emission

In regions younger than 10 Myr, Hα is frequently used as an indicator for remnant accretion disks. The lifetime of circumstellar disks in the presence of O-stars is suggested to be as short as a few 10^5 yr from photoevaporation models (Johnstone et al. 1998). The richer the massive stellar population in O-stars, which are the primary emitters of photoevaporating UV radiation, the faster disks and circumstellar material around near-by stars will be disrupted. The distance to the ionising sources is critical for the lifetime of a disk, such that a larger fraction of disk systems is expected at larger distances from the central cluster population, where the massive O-stars reside. The lack of gas in the cluster center observed in radio data in the form of a bubble of 0.6 pc radius (Balick et al. 1980), suggests that circumstellar material will also be largely evaporated. On the other hand, young stars that formed at the same time as the cluster, but are found at larger cluster center distances, either because they formed at larger radii or were ejected from the dense cluster by interaction processes early-on and migrated outwards, are expected to display disk signatures. In brief, Hα emission is

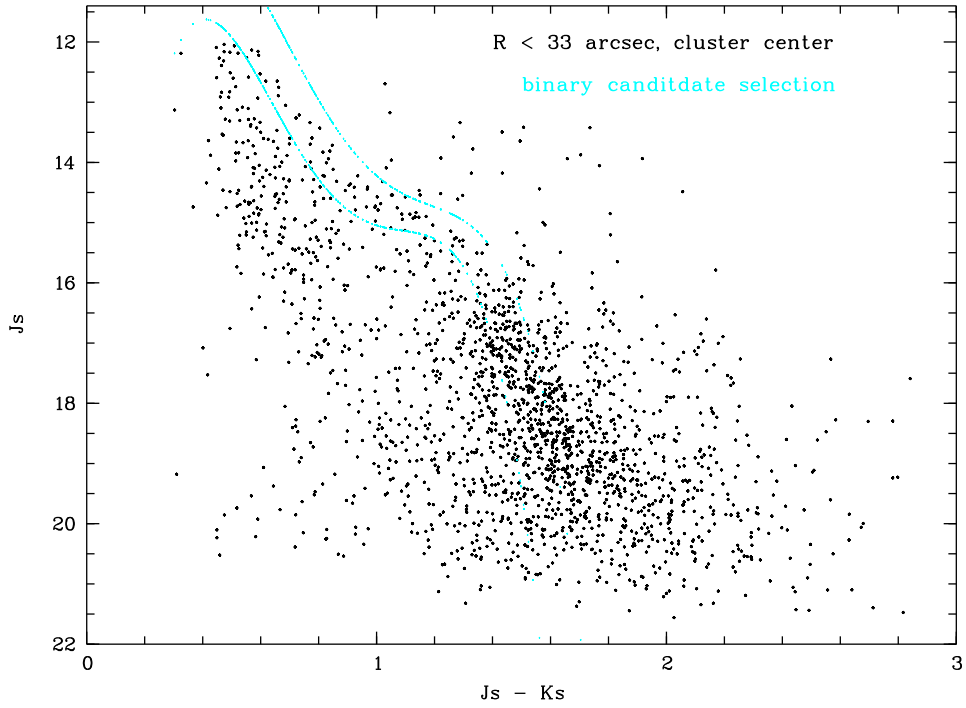

Figure 6.8: Binary candidate sequence. A sequence of stars positioned above the main stellar population in the CMD suggests the existence of a significant fraction of equal-mass binaries. This feature is particularly pronounced above the transition region of the PMS. As the nature of these stars cannot be conclusively determined from photometry alone, various assumptions will be chosen when deriving the mass function.

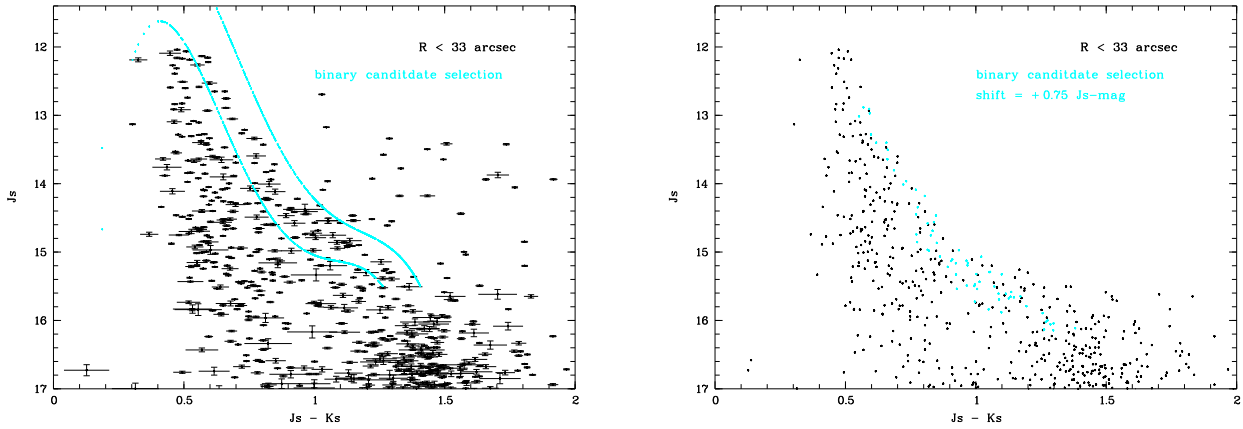

Figure 6.9: Zoom-in on the binary candidate sequence.
Left panel: The binary candidate selection as in Fig. 6.8 is shown with $J, J-K$ uncertainties included in the CMD. The offset above the transition region and off the main sequence is significantly larger than the photometric uncertainties. Right panel: In this CMD the binary candidates (cyan) are shifted down by $\Delta J_s = +0.75$ mag, as expected for equal-mass binaries with twice the luminosity of a single star of the same colour. The positions of binary candidates line up well with the CMD of the main stellar distribution.

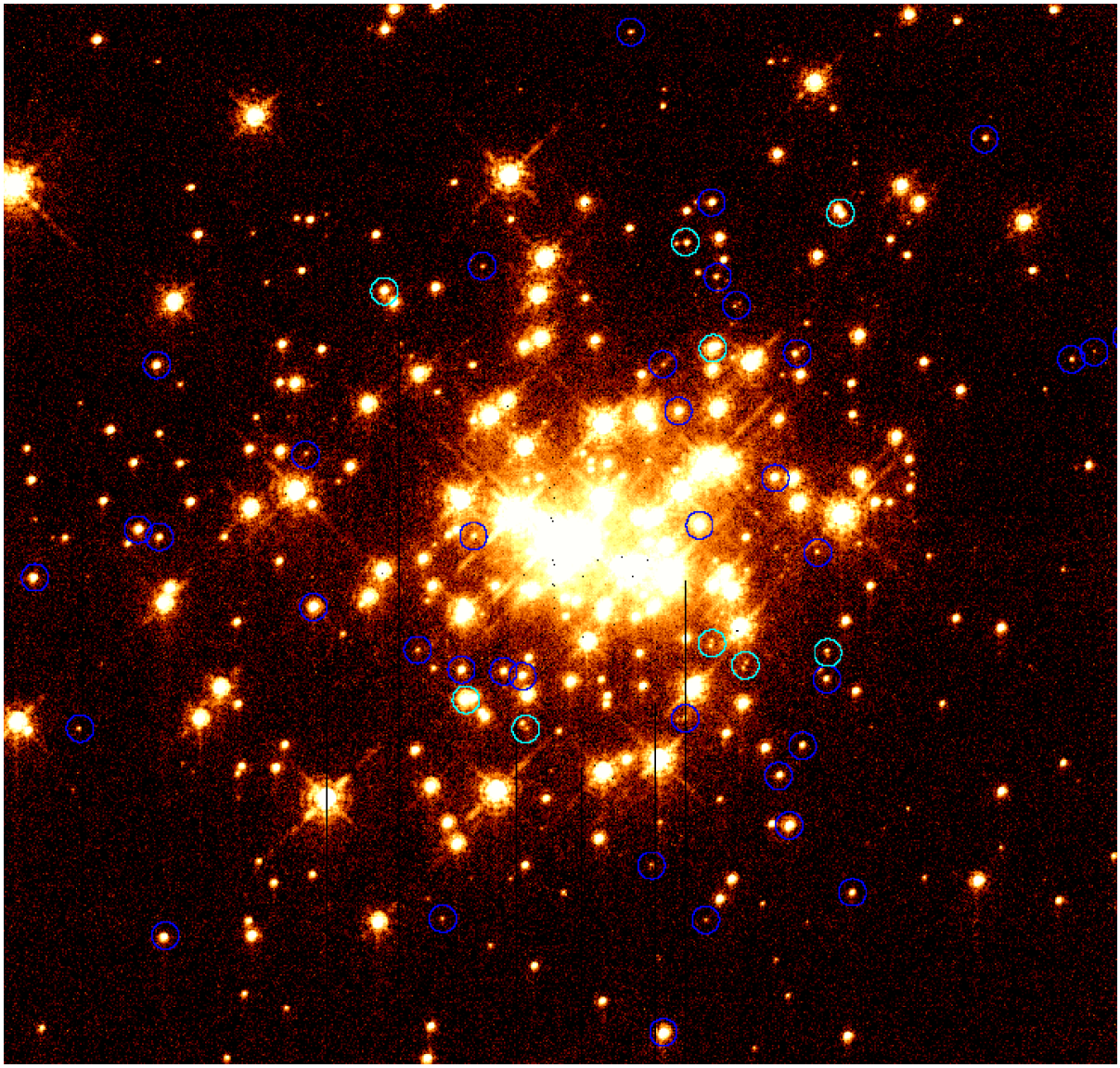

Figure 6.10: Binary candidates resolved with HST.
Diffraction-limited HST/PC optical V-band data with a resolution of $0\farcs06$, or 360 AU at $D = 6$ kpc. Blue circles mark all stars selected as binary candidates according to Fig. 6.8, and stars resolved on the PC chip are displayed in cyan. Out of 50 binary candidates common to the PC and ISAAC areas, 9 candidates are resolved binaries with HST. Note that individual extinction may cause visual magnitudes to deviate.
North is up and East is to the left.

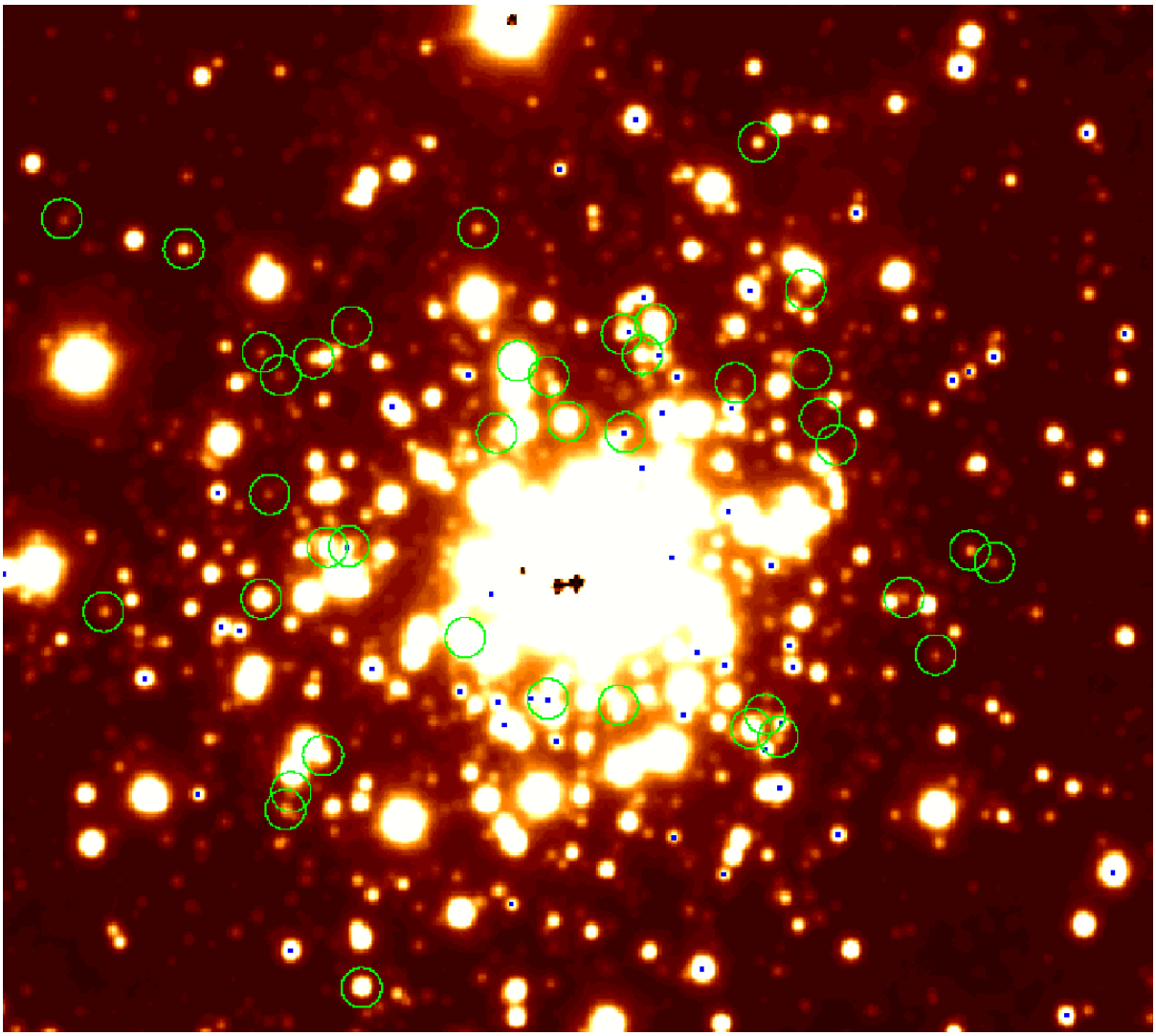

Figure 6.11: Binary candidates vs. Hα emission stars.
J_s-band image of the central cluster region (FOV $42'' \times 38''$), with binary candidates marked as blue dots and Hα emitters as green circles. Only 4 out of 50 binary candidates show Hα excess.

expected to be frequent among stars at larger distances from the massive cluster population, while stars in the cluster center itself should not show disk features.

HST/WFPC2 Hα data were provided by Eva Grebel to allow observations of radial variations in the Hα emission properties in and around the starburst cluster, in particular of pre-main sequence stars comprising the least evolved objects in NGC 3603 with ages ~ 1 Myr.

NGC 3603 was observed in the narrow-band Hα filter (F656N) with HST/WFPC2 under GO program 7373 (PI: Grebel) in March, 1999. The PC chip was centered on the blue supergiant Sher 25 North of HD 97950 in order to study wind structures around this exceptional star. The main area of the starburst cluster consequently was located on the WF chips with slightly lower resolution, but larger field coverage. The resolution on the WF images was $0\farcs1$, and $0\farcs064$ on the PC chip. The continuum measurement used to zeropoint the Hα emission was provided by R-band data taken earlier under program GO 6763 by L. Drissen. Details on these observational programs and the description of the data reduction can be found in Grebel et al. (in prep.).

The narrow-band images as provided were corrected for geometric distortion effects. The final Hα frame was combined from two deep 500 s exposures to yield 1000 s total integration time. PSF fitting photometry was performed under DAOPHOT, using essentially the same procedure as for the ISAAC broad-band photometry. The three WF chips and the PC chip were treated separately, allowing to account for slighly different resolution and PSF variation across each field. A quadratically varying Lorentz function provided the best fit to the diffraction-limited data, allowing for a narrow, peaked PSF kernel. As the R-band data yield the continuum to the Hα filter, the chosen zeropoint was taken from Dolphin (2000) for the F675W HST R-band filter.

The Hα magnitudes have been corrected for the chip-to-chip offset, derived by Dolphin (2000), and the newly determined offset of the PC to the WF photometry of -0.44 mag. We flux-calibrated the Hα data using the PHOTFLAM keyword, as described in the WFPC2 manual. The newest set of available values for PHOTFLAM have been used in the flux calculation. The R $-$ Hα colour has been adjusted to the magnitude difference corresponding to the full width at half maximum (FWHM) of the filters as an additive offset as described in Grebel et al. (1993), $\Delta\lambda = 889.5$ Å for F675W, and 21.5 Å for F656N, which results in an instrumental magnitude difference of 4.04 mag. After zeropointing, point sources without Hα emission have the same magnitude in R and Hα, yielding $R - \mathrm{H}\alpha = 0$ mag, as expected when only continuum emission from the stellar atmosphere is present.

As the uncertainties in the final $R - \mathrm{H}\alpha$ calibration were on the order of 0.2 mag, objects with $R - \mathrm{H}\alpha > 0.4$ mag were selected as Hα emitters. To distinguish objects with strong and weak emission, three different colour selections were used, $0.4 < R - \mathrm{H}\alpha < 0.8$ mag, $0.8 < R - \mathrm{H}\alpha < 1.2$ mag, and $R - \mathrm{H}\alpha > 1.2$ mag. The position of Hα emission stars is shown in the $J_s, J_s - K_s$ colour-magnitude diagram in Fig. 6.12. The right panel shows the cluster center including stars within $33''$, while the left panel shows the region beyond $33''$. Note that the independent R-band and Hα HST data sets shared only a small area of ~ 1.56 arcmin^2, only a factor of four larger than the area covering the cluster center (0.32 arcmin^2), where the stellar density is very high. In addition, the overlap region extended mainly to the West of the cluster, where the extinction is high. As a consequence, no statistically meaningful conclusions can be drawn with respect to the increase of Hα emission with cluster center distance.

In contrast to the expectations, a significant fraction of Hα emitters is found very close to the cluster center, within the evacuated cavity. In the right panel of Fig. 6.12, these objects are found on and redwards of the pre-main sequence, as expected for very young stars with accretion disks or remnant circumstellar material. Nevertheless, the total number of Hα emitters in the PMS locus with $15 < J_s < 17.5$ mag, beyond which the Hα detection limit prohibits further objects to be found, is only 19 out of ~ 280 PMS objects (expected number of field stars excluded), or 7 %. Clearly, this fraction cannot be compared to the 50 % disk fraction found in star forming regions with lower stellar density such as Orion or Taurus (Haisch et al. 2001). An additional 9 Hα emission stars are found in the PMS/MS transition region, where the density of objects in the CMD is much lower. The total

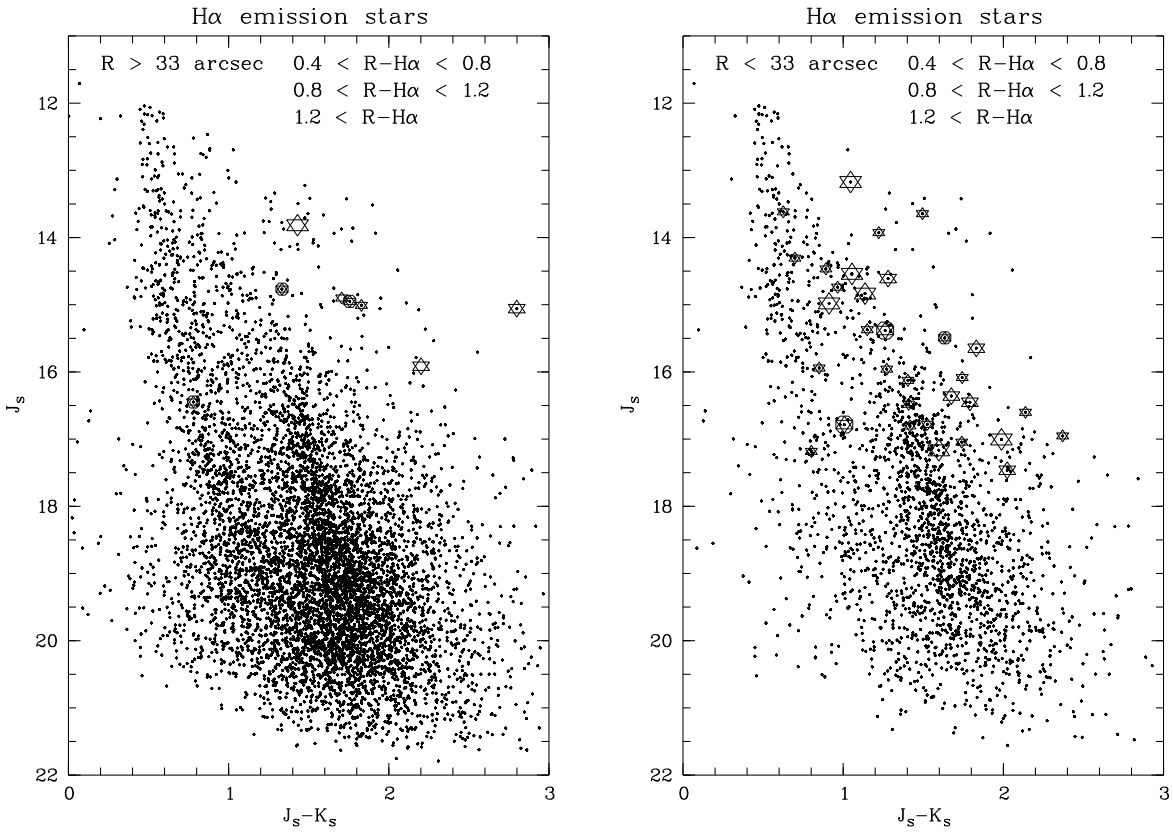

Figure 6.12: Hα emission stars and their locus in the $J_s, J_s - K_s$ CMD.
Stars denote objects with enhanced Hα emission, with the symbol size indicating Hα emission strength above the continuum, selected in three bins according to $0.4 < R - \mathrm{H}\alpha < 0.8$ mag, $0.8 < R - \mathrm{H}\alpha < 1.2$, and $R - \mathrm{H}\alpha > 1.2$ mag, where R refers to the continuum emission. Encircled stars mark objects with uncertain Hα photometry. The left panel shows the wider cluster environment with $33'' < R < 120''$, including the position of the few Hα sources found in the vicinity of HD 97950. The low number of sources may be a selection effect, as the field area covered in Hα lies mainly to the West of the cluster, where enhanced nebular emission is found, thus complicating the detection of emission objects.
The right panel shows the cluster center with radii $R < 33''$. Most Hα emitters are found on and close to the pre-main sequence, in particular in the transition region. This yields evidence that part of the scatter observed in the PMS/MS transition is due to reddening by circumstellar material. The large number of emission objects in the cluster center is remarkable given the intense UV radiation field arising from the rich O-star population.

number of objects found between $0.7 < J-K < 1.4$ mag and $14.2 < J_s < 15.7$ mag, roughly outlining the transition region, is only ~ 100, indicating a slightly larger fraction (9 %) of emission stars than on the PMS. These stars are found very close to the cluster center, down to radii of $3''$. According to the Palla & Stahler 1 Myr isochrone, objects at the borderline to hydrogen burning have masses of $\sim 4\,M_\odot$, and the transition region covers a range between 2.5 and $4\,M_\odot$, such that these Hα emitters are candidates for Herbig Ae and late Be stars.

The existence of stars with enhanced Hα emission in the transition region indicates reddening from disks as a second cause - in addition to binaries - for the large scatter observed in the PMS/MS transition. With this evidence, an age spread in HD 97950 becomes less and less probable as a cause for the observed scatter. The nature of the enhanced Hα emission observed in the transition stars is hard to deduce from photometry alone, although these objects will be discussed further with respect to their location in the colour-colour diagram in Sec. 6.3. Again, spectroscopy is required to reveal the diverse physical phenomena.

The very low number of Hα emitters found in the field suggests that the disk fraction is not significantly larger in the field than in the cluster. This would provide evidence that young stars found in the immediate vicinity of HD 97950 have not formed independently in the field, but might have formed close to the massive population or even inside the cluster center and migrated outwards later-on. A final conclusion can, however, not be drawn until a larger field surrounding HD 97950 has been investigated, without the bias to a highly extincted region mentioned above.

6.2.7 *L*-band photometry

The sources detected in L-band down to the detection limit of ~ 15 mag on both the cluster and the adjacent East field are overlaid on the $J_s, J_s - K_s$ diagram in Fig. 6.13. The cluster center population ($R < 33''$) is underlaid for reference of the stellar population features in the CMD. The main sequence and the pre-main sequence/main sequence transition are well covered with the L-band photometry, while the lower pre-main sequence is mainly too faint except for objects with exceptionally red colours. These objects are most probably embedded in circumstellar material or host disks, which enhances their long-wavelength radiation. This interpretation is supported by comparison with Fig. 6.12, as objects with L-band emission occupy the same loci in the CMD as Hα emitters. Reddened background sources, on the other hand, are not expected to show increased L-band brightness, and should thus be excluded due to their faintness in L. In the next section, the matched $JHKL$ photometry will be analysed in the two-colour plane, allowing physical deductions on the properties of the stellar population in and around the cluster.

6.3 Colour-colour diagrams of HD 97950

Near-infrared two-colour diagrams (TCDs) come mainly in two flavours - as $J-H, H-K$ and - if the more complicated L-band observations are available - as $J-H, K-L$ diagram. The advantage of TCDs as opposed to CMDs is first, that main sequence and pre-main sequence stars occupy distinct loci in the TCD, and secondly and more important that infrared excesses caused by circumstellar material in envelopes or disks are distinguishable from standard reddening by foreground material. As discussed in detail by Lada & Adams (1992), the TCD locus allows to distinguish stars in their protostellar phase from classical and weak-line T-Tauri stars. While stellar radiation passes a foreground cloud homogeneously, and is re-emitted homogeneously over the surface of the cloud, the temperature gradient of a disk causes the re-emission peak at a certain wavelength to originate in different surface areas of the disk. The flat tail of a characteristic r^{-1} disk profile results in increasing emission areas with increasing wavelengths. Thus, the long-wavelength radiation emitted in the cooler parts of the disk at larger radii covers a larger area, thereby increasing its relative luminosity in comparison to shorter wavelength emission. The spectral energy distribution (SED) will thus exhibit strong near-

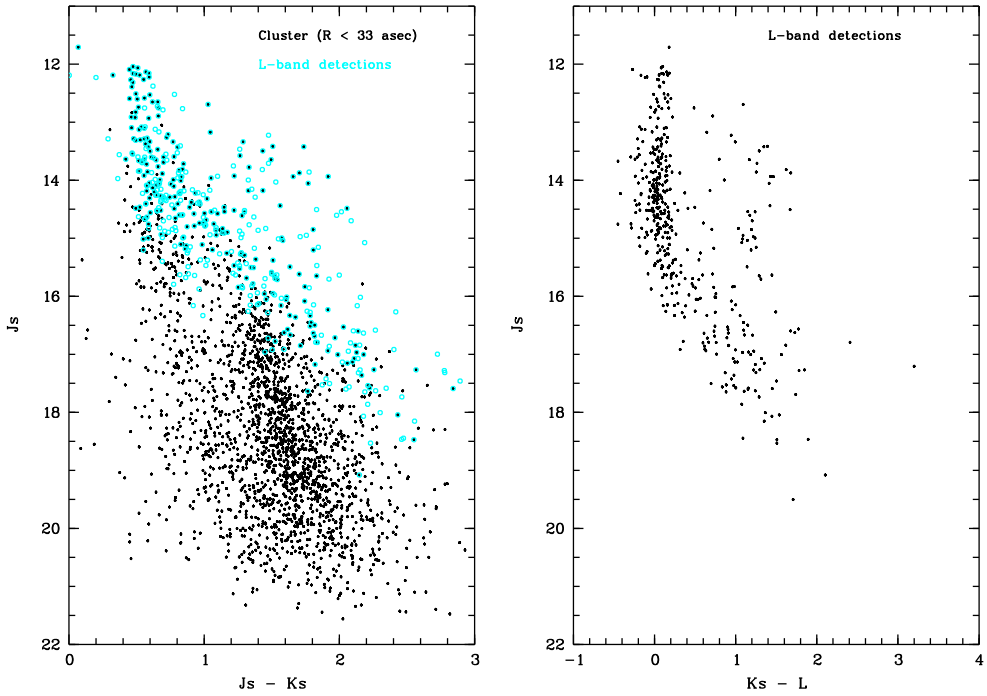

Figure 6.13: Colour-magnitude diagram including L-band detections.
Left panel: $J_s, J_s - K_s$ CMD displaying all sources detected on the two L-band fields (cyan). The main sequence and infrared excess objects redwards of the MS as well as the PMS/MS transition are completely covered by the L-band photometry. On the lower pre-main sequence, only the reddest objects are detected due to their enhanced L-band brightness. Note that faint background sources should not show enhanced L-band luminosity. The central cluster population ($R < 33''$) is underlaid for reference of the stellar population features.
Right panel: $K_s - L$ colours shown versus J_s magnitude, indicating the colour range covered in the $J_s - H, K_s - L$ two-colour diagram. The truncation to the lower left indicates the L-band detection limit.

infrared emission beyond the stellar radiation maximum, visible in star-disk systems in the form of a pronounced hump in the near-infrared regime. Consequently, the surface structure of a disk allows to distinguish dense, optically thick stellar disk emission from reddening by foreground material by observing at long wavelengths. In the two-colour plane, where the standard reddening in most star forming regions is determined by the re-radiation properties of interstellar dust, this excess emission reveals itself by unusually red colours. For a more detailed discussion on the physical processes involved see Adams, Lada & Shu (1987, 1988).

The $J - H, H - K$-plane is frequently used to derive disk fractions, although there has long been indication that the disk fraction is severely underestimated as the K-band does not extend far enough into the long-wavelength regime of the SED to trace disks. Due to the shallow temperature profile in the outer parts of a disk, L-band emission originates on a much larger disk surface area, such that the excess will be more pronounced when L-band data are included, and disks are sampled efficiently. Haisch, Lada & Lada (2001) derive a disk fraction of 86 % from the $J - H, K - L$ plane for the massive cluster NGC 2024 in Orion, while only 60 % excess stars are recovered in the $J - H, H - K$ plane. In addition, K-band excesses are more severely influenced by nebular emission, which biases the distribution of excess objects in dependence of the surrounding molecular cloud. The disk fraction - usually underestimated in the $J - H, H - K$ plane - can be enhanced in gas- and dust-rich regions as has been shown for the cluster center of NGC 2024 in Orion by Haisch, Lada & Lada (2001). Such a bias affects NGC 3603 in the other direction, where the amount of molecular material *increases* with distance from the cluster center. As L-band data are less affected by nebular emission, the L-band

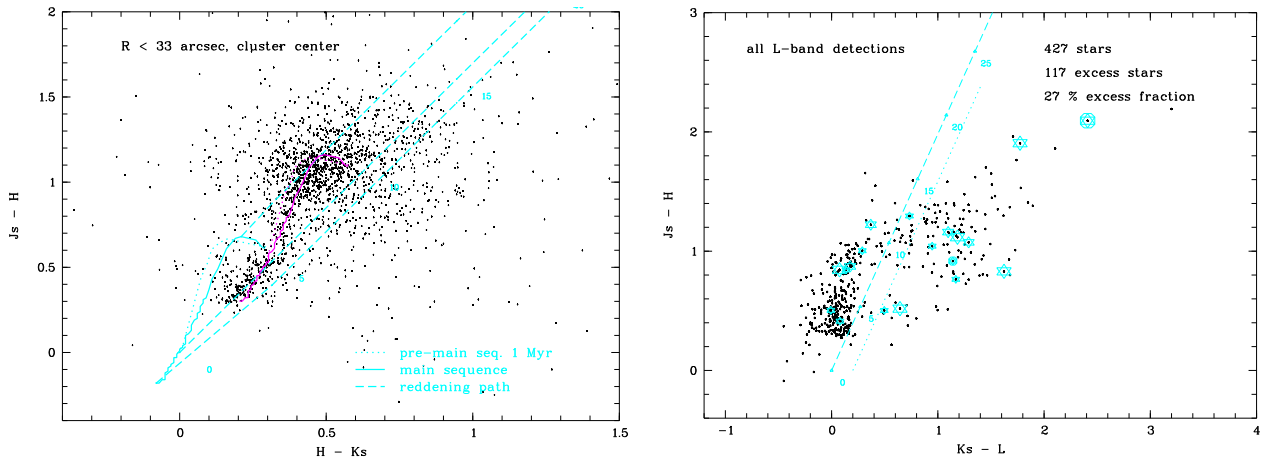

Figure 6.14: Two-colour diagrams of HD 97950.
Left panel: $J_s - H, H - K_s$ plane including the unreddened main sequence (solid line) and pre-main sequence (1 Myr, dotted line), as well as both sequences shifted to the $A_V = 4.5$ mag. The reddening path following Rieke & Lebofsky (1985) is also shown (dashed line). The cluster center ($R < 33''$) is selected, revealing the main sequence of massive stars at the blue end of the isochrones, and the dominant pre-main sequence population in the upper part of the TCD. Only few stars fall on the unreddened main sequence, indicating a low foreground contamination.
Right panel: $J_s - H, K_s - L$ plane and reddening path. While the bulk of the stars displays only atmospheric L-band emission (bluewards of reddening path), several sources with strong excess emission are seen redwards of the reddening path. The lower dashed line falls 0.2 mag below the reddening path. Sources redwards of this limit were counted as excess sources to obtain the disk fraction. Star symbols mark Hα emitters.

excesses are particularly well suited to derive radial variations in the disk fraction.

This effect is particularly important when conclusions on the possible disruption of circumstellar material by photoevaporation and stellar winds from O-stars shall be drawn. In the center of HD 97950 reside ~ 40 O-stars creating an intense UV radiation field photoevaporating nearby molecular material. Vivid evidence for photoevaporation is given by the pillars and rims displaying bright emission surfaces pointing in the direction of the central cluster (see Fig. 6.1). As the cluster excavated a large region of the molecular cloud exposing HD 97950 to our view even at optical wavelengths, residual molecular material should face the same fate in the immediate cluster center. The fraction of surviving disks after a lifetime of more than 1 Myr is thus expected to be small in the cluster center, but might increase when moving radially outwards with increasing distance from the central O-star population.

The $J_s - H, H - K_s$ and the $J_s - H, K_s - L$ diagrams are shown in Fig. 6.14. With the aim to show the features displayed by the cluster population, the inner $33''$ were selected for the $J_s - H, H - K_s$ TCD. The main sequence and pre-main sequence loci are clearly depicted as a blue and red clump, respectively. The number of foreground stars falling onto the unreddened main sequence is very low compared to the cluster population. This provides some confidence that the selection of the innermost densest cluster region within $R < 33''$ is dominated by cluster members.

Although several objects show L-band excesses, the number of excess stars can clearly not compete with the numerous main/pre-main sequence population to the left of the reddening line, indicating normal atmospheric L-band luminosity. The fraction of excess stars is estimated from the $J_s - H, K_s - L$ TCD (right panel) to 27 % on the total area covered in L.

While only 21 Hα sources have L-band detections, out of which only one Hα emission star is located outside the $33''$ chosen main cluster area, and 20 emission stars are found in the denser cluster parts, 429 stars are found in $JHKL$. This allows to test the hypothesis that disk fractions (here identified with L-band excess fractions) decrease towards the cluster center, where the photoevaporating UV radiation is generated. For this purpose, the cluster area is split up in three annuli with approximately identical area, covering $R < 20''$, $20'' < R < 27''$, $27'' < R < 33''$, and the outer field with $R > 33''$. A

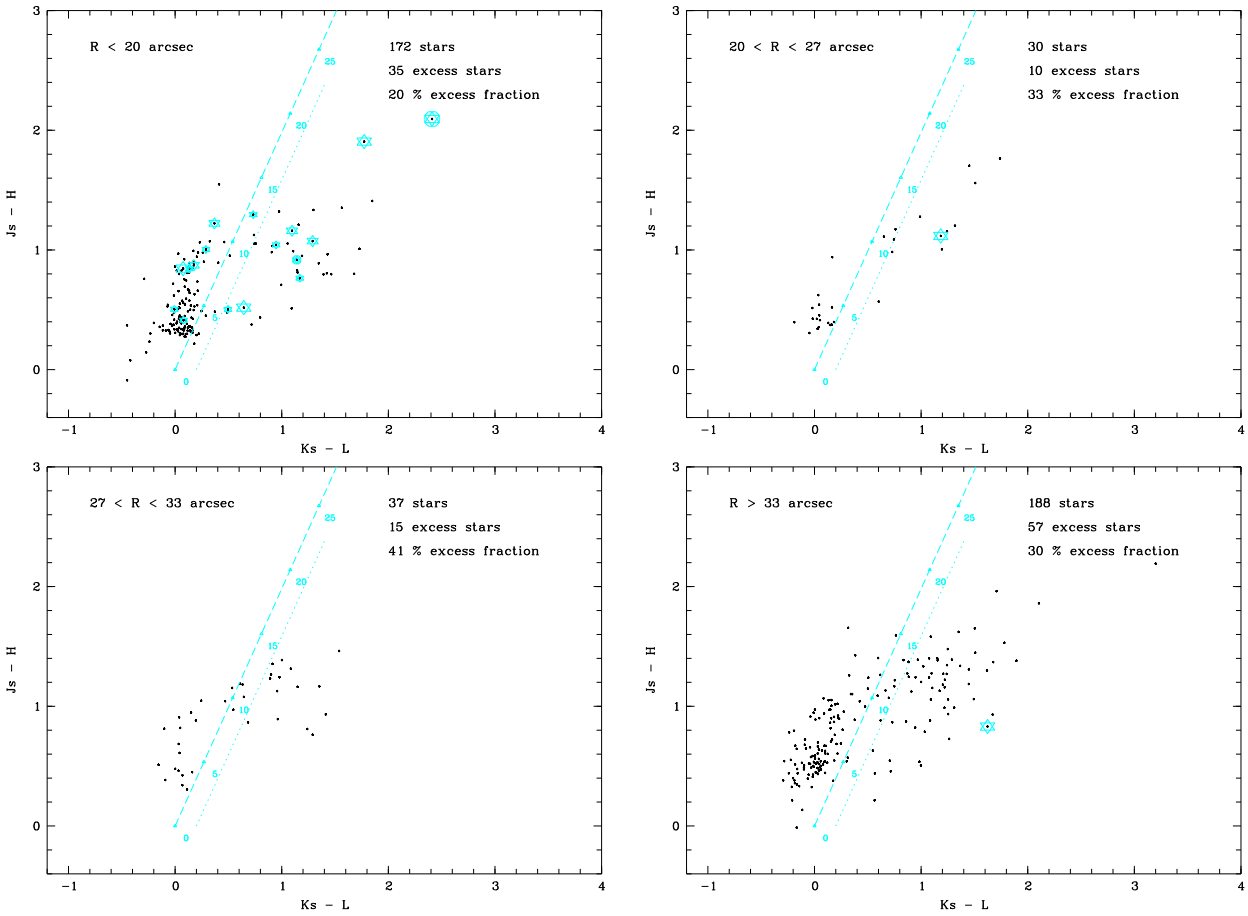

Figure 6.15: Radial variation in the $J_s - H, K_s - L$ distribution of stars.
From upper left to lower right the cluster center with $R < 20''$ and consecutive annuli with $20'' < R < 27''$ and $27'' < R < 33''$ (covering comparable areas) are selected. Stars at larger radii $R > 33''$ are displayed in the lower right panel. The L-band excess fraction increases with radius, indicating an increasing disk fraction with increasing distance from the central O-star population, supporting the photoevaporation scenario. In the cluster vicinity (lower right), field stars contaminate the main sequence population, thereby decreasing the relative fraction of L-band excess sources. Hα emitters are shown as in Fig. 6.12.

similar selection will be used in Sec. 7.3 when radial variations in the mass function of HD 97950 are derived. The corresponding $J_s - H, K_s - L$ TCDs are shown in Fig. 6.15. The reddening path and the chosen limit for excess objects, $K_s - L = +0.2mag$ of the reddening path, indicate the fraction of excess sources. The number of stars detected redwards of this limit is given along with the total number of stars in each plot. From the ratio, the excess fraction is determined. Although the cluster center ($R < 20''$) hosts most Hα emitters, the fraction of L-band sources is only 20 %. When progressing to the subsequent annuli, this fraction increases to 33 % and 41 %, respectively, and is thus doubled out to a radius of $33''$. This trend supports the photoevaporation scenario for disks in the innermost cluster region. Outwards of $33''$, however, the disk fraction seems to stabilise at 30 %. This is probably due to field star contamination on the main sequence displaying no L-band excess, thus increaing the number of detected stars without excess. One has to keep in mind, however, that faint pre-main sequence stars exhibiting L-band excess may be lost due to crowding in the densest cluster region. As no incompleteness tests are available so far (and are very much complicated on the L-band images due to the negative residuals from sky subtraction), the exact number of lost objects cannot easily be determined.

From the CMD (Fig. 6.13), we know that stars on the main sequence are not affected by the L

detection threshold. Thus, to obtain the excess fraction for a sample unbiased to the low detection limit in L, the main sequence fraction can be used. With a limiting magnitude of 15 mag, and a main sequence colour of $K_s - L \sim 0$ mag, the main sequence contains a statistically complete sample of stars. In addition, stars redwards of the main sequence locus are neither limited by the L nor by the K detection limit. If only main sequence stars are used, the above fractions *decrease* to 12 % for both inner annuli ($R < 27''$), and to 25 % in the third annulus. The reduction in the excess fraction is understandable as the large number of reddened PMS sources is now excluded from the analysis. Beyond $33''$, the disk fraction decreases again to 14 %, which is also the average for the entire population. Note, again, that bright field stars are a strong source of contamination in the latter area. In the cluster center, the trend of increasing disk fraction is still observed, but care has to be taken as number statistics are low. Combining the above estimates, the final conclusion can be drawn that the disk fraction in the cluster center is with 10-20 % very low compared to the expected disk fraction in star forming regions as young as one to a few Myr. A slight increase is observed towards larger cluster center distances, supporting the photo-evaporation of disks by UV radiation from massive O-stars.

Haisch, Lada & Lada (2001) find a disk fraction of 86 % in the Orion NGC 2024 cluster at an age as young as 0.3 Myr from L-band excess fractions, and 52 % in the 3.2 Myr old NGC 2264 cluster. In NGC 2362, at an age of 5 Myr, 12 % of the stars retain their circumstellar disks. These authors derive a linear decrease in the disk fraction with cluster age from a systematic study of 7 young clusters spanning an age range of 0.3 to 30 Myr. Even if the age of HD 97950 is larger than indicated by our analysis, at an age of 3 Myr - the oldest age suggested for the cluster in the literature - a disk fraction of 50 % would still be expected from the suggested disk lifetimes. Clearly, the processes in the dense cluster center shorten the lifetime of disks causing only a small fraction of disks to survive with respect to the given cluster age.

From Fig. 6.15, a low disk fraction is found in particular in the densest cluster regions. Nevertheless, most of the Hα emission stars are located close to the cluster center. Fig. 6.17 (left) shows the $J_s - H, H - K_s$ TCD including the position of the Hα emitters. The location with respect to the cluster center is colour-coded in the sense that light blue stars indicate Hα emission stars inside the inner $33''$, while dark blue denotes stars with $R > 33''$. The low number of stars detected in the cluster environment is due to the small area coverage. The fact that Hα emitters are, however, not exclusively observed at large radii, but that 34 Hα emission stars are located in the innermost $33''$ (1 pc) of the cluster center, suggests that disks are capable to survive in the presence of massive O-star radiation. If these stars are indeed Herbig Ae/Be stars harbouring prominent disks as suggested by Hillenbrand (1992), this indicates the survival of *massive* disks over the 1 Myr lifetime of the starburst.

Fig. 6.17 (right) shows the location of binaries in the $J_s - H, K_s - L$ plane along with the Hα emitters. The anti-correlation between binary candidate and Hα positions observed on the K-band image (Fig. 6.11) already suggested that these two groups belong to physically distinct stars. In the two-colour plane, binary candidates are predominantly found on the main sequence locus, showing no signs of infrared excess emission except for very few (4) sources. In stark contrast to the binaries, Hα emission stars are scattered widely over the $J_s - H, K_s - L$ plane, displaying either enhanced standard reddening (shift above the main sequence locus in the direction of the reddening vector), or infrared excesses. More than 60 % of the Hα emission stars detected in all filters show strong excess emission in Hα as well as in L-band. The anti-correlation between binary candidates and Hα emitters is extremely pronounced in the two-colour diagram, supporting the assumption of physically distinct populations.

Disk formation models indicate that the survival of disks is hampered by the existence of a binary companion due to the disruptive tidal forces acting in the system (Papaloizou & Pringle 1977, Artymowicz & Lubow 1994). The binary candidates in HD 97950 support this scenario by their strong anti-correlation with L-band as well as Hα excess, both being strong indicators for disk emission around young stars. As the binary candidate sequence selected from the $J_s, J_s - K_s$ diagram assumes a mass ratio of 1, Fig. 6.17 provides clear evidence that the formation of equal-mass binaries prohibits

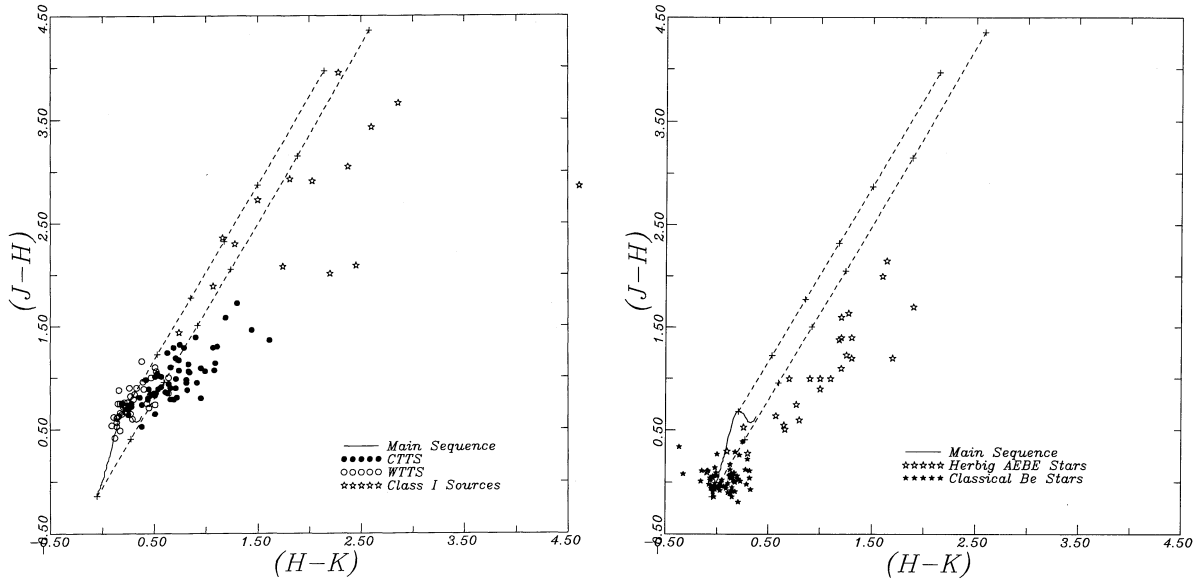

Figure 6.16: Interpretation of colour-colour diagrams from Lada & Adams (1992).
The left panel shows the classical and weak-line T Tauri loci along with the widely scattered protostellar (Class$\tilde{\text{I}}$) phase displaying strong NIR excesses. The distribution of Herbig Ae/Be stars over the TCD is shown in the right panel. Herbig Ae/Be stars are widely scattered as well due to individual reddening and NIR excess from massive disks, causing them to fall in the same region as embedded protostars.

disk survival around most of these systems.

6.3.1 Location of Hα emission stars in the two-colour diagram

Hα emitters, shown as stars in all TCDs, fall into both the excess region and the MS/PMS locus. Most Hα emission stars above the PMS are located in the PMS/MS transition region of the CMD (cf. Fig. 6.12). For a 1 Myr old population, late B and early A type stars are evolving from the PMS to the hydrogen burning phase. Stars with Hα emission are very likely in a Herbig Ae/Be state. 12 of the 21 Hα emitters with L-band detections fall into the L-band excess region, indicating that the Hα emission originates from accretion disks or photoionisation of the disk surface. Lada & Adams (1992) analyse the loci of young stars in the $J-H, H-K$ diagram (Fig. 6.16), and find that objects classified as Class I protostars from their IRAS luminosities (Kenyon et al. 1993) display individual reddening *and* infrared excess, falling into the upper part of the TCD redwards of the reddening path (see Fig. 6.16). These protostar loci are clearly distinct from the weak-line and classical T Tauri loci. While weak-line T Tauri stars appear in the unreddened portion of the TCD, classical T Tauri star/disk systems display infrared excesses, but not the unusually large individual reddening added to protostars, indicative of their remnant native envelopes. Herbig Ae/Be stars classified from spectra and their distinct locus in the $H-K, K-L$ TCD (Finkenzeller & Mundt 1985), are found by Lada & Adams to coincide with the reddened, widely scattered protostellar population (Fig. 6.16, right panel). From disk modelling, Lada & Adams concluded that Herbig Ae/Be stars are most probably hosts to massive, optically thick dust disks. These disks increase the extinction of the central star and the optically thick dust re-radiates the stellar radiation at infrared wavelengths, thus causing similar NIR colours as in the case of embedded protostars.

As the protostellar phase of low-mass stars lasts only a few $\times 10^5$ yr (e.g., Parker 1991), no significant protostar fraction is expected at a cluster age of 1 Myr if no age spread is present. The Hα emitters in the excess region of the TCD are thus probably Herbig Ae/Be stars with significant remnant disks. These disks might have survived evaporation as they are more massive than the disks

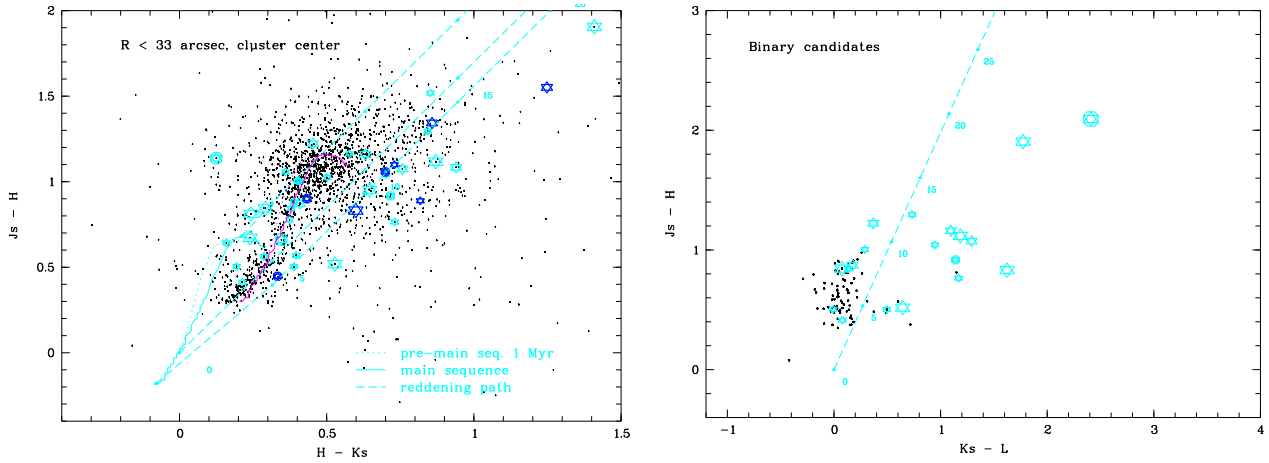

Figure 6.17: Locus of Hα emitters vs. binary stars in the two-colour plane.
Left panel: Hα emission stars are shown as stars coded as in Fig. 6.12. Cyan stars are emitters located close to the cluster center within $R < 33''$, dark blue stars are emitters found at larger radii. Note that the relative fractions of cluster to field emission sources are not meaningful due to the small field area covered.
Right panel: Binary candidates and Hα emission stars in the $J_s - H, K_s - L$ plane. While equal-mass binaries mainly cover the main sequence locus with standard foreground reddening, Hα emitters scatter widely and frequently show moderate too large infrared excesses.

around low-mass stars, resulting in a longer evaporation time to dissolve them completely. Hillenbrand (1992) derives disk lifetimes of isolated Herbig Be stars of ~ 1 Myr, in principle consistent with the existence of disks in HD 97950, although the UV radiation field from the massive O-star population should decrease the disk lifetime. Hα emitters redwards of the pre-main sequence at fainter NIR magnitudes coincide with the locus of classical T Tauri stars, of which the Herbig Ae/Be stars are the more massive counterparts. The survival of disks around these systems is even more surprising due to their lower mass, suggesting that at least a fraction of the PMS population has massive disks. We note in passing that strong dynamical segregation provides an alternative explanation for the existence of massive Herbig Ae/Be star disks close to the cluster center.

Hα emission of stars on the main sequence locus can have several causes as discussed in Hillenbrand (1992). While the IR excess sources studied above display steep spectral energy distributions between 2 and 100 μm, comprising an intermediate-mass analogue to classical T Tauri stars, enhanced Hα emission is also found in intermediate mass stars with flat or rising IR spectral energy distributions. Hillenbrand suggests that gas and dust in remnant infalling envelopes *not* confined in a disk is resposible for this emission. In addition, she also identifies a third group of Hα emitters with small IR excess and SEDs comparable to classical Be stars, which may host gaseous, dust-free disks or envelopes, representing the intermediate-mass analogue to weak-line T Tauri stars. These objects most probably form an evolutionary sequence, such that in a cluster as young as HD 97950 a larger fraction of strong excess sources would be expected. However, the high stellar density and strong UV radiation field can easily explain the depletion of dust disks in approximately half the Hα emission stars.

6.4 Extinction map

For a general view on the global extinction variation over the region around the central cluster in NGC 3603, stars in the colour-magnitude diagram were dereddened individually. The procedure used to derive individual reddenings is essentially the same as used for the Arches cluster (cf. Sec. 4.1.2). Each star was shifted along the reddening vector in the $J_s,\ J_s - K_s$,-plane to derive an extinction value for each star as $\Delta A_V = \langle A_V \rangle \cdot \Delta A_J / 0.282$, where $\langle A_V \rangle$ is the average foreground extinction applied to the isochrone, i.e. $\langle A_V \rangle = 4$ mag for the MS isochrone and $\langle A_V \rangle = 4.5$ mag for the PMS

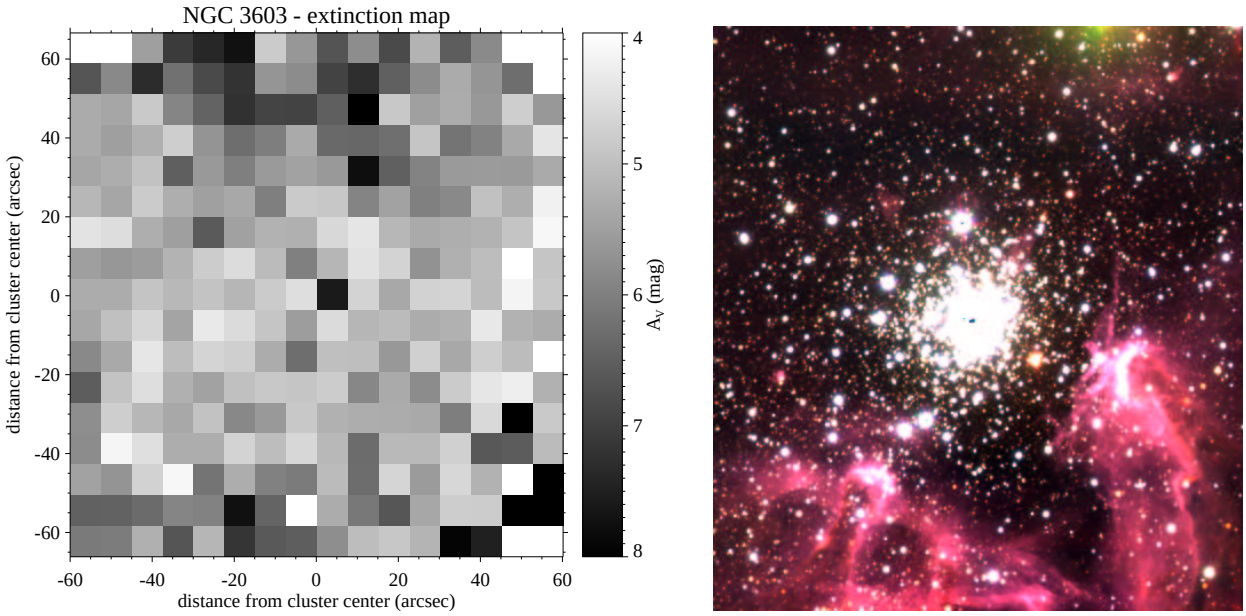

Figure 6.18: Extinction map of the central NGC 3603 region. The map covers the high-resolution $2' \times 2'$ field centered on HD 97950. The combined JHK image of the same field is shown for comparison in the right panel, with a scale chosen to enhance nebular features indicating areas rich in gas and dust. The oversampled ISAAC data (pixelscale $0\farcs0735$) were binned into areas of 100×100 pixels, or $7\farcs3 \times 7\farcs3$ corresponding to 0.22 pc at a distance of 6 kpc. The extinction in each pixel of the map was derived from individual dereddening of the stars to the $A_V = 0$ mag MS/PMS isochrone. With the aim to show the extinction properties in NGC 3603, blue foreground stars were excluded.

isochrone. The resultant A_V values therefore correspond to the dereddening to $A_V = 0$ mag. While all stars redwards of the PMS isochrone are selected, an envelope including only stars blue-shifted by less than 0.25 mag from the isochrone are included to reject the bulk of the foreground stars. In case of the main sequence, several very red objects known from spectroscopy to be severely embedded Of stars (Brandner, private communication), were excluded as well as blue foreground stars by choosing $-0.25 < \Delta(J-K) < +0.35$, where $(J-K)$ refers to the colour of the isochrone at each magnitude. In addition, stars on the binary candidate sequence are excluded from the extinction calculation. Binary stars shifted above the PMS/MS transition simulate stars with unusually red colours and thus large extinction, thereby introducing a bias in the extinction map. Although only 83 out of a total of 6700 stars are rejected in this way, these brightest cluster members are predominantly found close to the cluster center, thus biasing the spatial extinction variation in the cluster center.

From the dereddening procedure, ΔA_J was transformed into A_V using the Rieke & Lebofsky (1985) extinction law as denoted above. Stars were then binned into 100×100 pixel areas ($7.3'' \times 7.3''$), and the median value of A_V yields the intensity represented in the extinction map. The median was chosen instead of the mean in order to obtain typical values of the extinction along the line of sight unbiased from heavily embedded young objects. Between 10 and 30 stars are typically included in each point of the extinction map shown in Fig. 6.18. In the lower left and upper right corners, statistics are poorer with only a few stars in each bin, such that statistitical fluctuations are more severe. White pixels in the map indicate undetermined points due to a lack of stars. The cluster center corresponds to the dark central position in the map, as heavy saturation prohibits photometry in the innermost $7''$. Bright intensity symbolises low extinction, while dark areas show higher extinction.

Although statistical fluctuations are unavoidable in such a complex region of gaseous and molecular emission and absorption structures, the general trend displays a lower extinction of ≈ 4 mag in the cluster center, as already expected from radio data (Balick et al. 1980). On the other hand, the outskirts of the field, in particular to the North and South of the cluster, show a higher extinction of

≈ 8 mag in accordance with the appearance of the HII region (Fig. 6.18, right). Over the $27''$ (1 pc) cluster field of view, this indicates an increase in extinction by 4 mag. This variation is much lower than the 10 mag observed over the Arches $20''$ (0.8 pc) field, emphasising the overall low extinction towards the NGC 3603 region.

It is interesting to note that the bright rim observed to the South-West of HD 97950, beyond which stars appear depleted even on the K-band image, is outlined by a diagonal sequence of dark spots. Beyond this, fine-structure interpretation would go to far for a scientifically founded analysis, and the more detailed comparison between the extinction map and the K-band image is left to the imagination of the reader.

6.5 Consequences for the mass function derivation

In the previous sections, we were faced with a wide variety of phenomena influencing a young stellar population. Disks and envelopes of molecular material remnant from the star formation process, as well as binarity of varying mass ratios, and stellar rotation may all contribute to the scatter observed close to the PMS/MS transition point, where the horizontal bend in the PMS distribution reveals a spread in brightness and colour.

The variable extinction over the cluster field imposes additional colour variations and uncertainties to the colour-magnitude distribution. While varying extinction can be considered in the MF derivation by dereddening each star individually, phenomena such as disk excesses and binarity cannot easily be taken into account. The large scatter observed in particular at fainter magnitudes in the PMS/MS transition and PMS region of the CMD suggests that these evolutionary stages are especially affected. These uncertainties for masses below $4\,M_{\odot}$ have to be kept in mind during the derivation and interpretation of mass functions.

In order to resolve these ambiguities and understand in detail the inherent physical processes in the young starburst population, multi-object spectroscopy of the transition stars is under way.

Chapter 7

The Mass Function in the central NGC 3603 cluster

In this chapter, various methods will be used to derive the mass function in HD 97950. Before the methods suggested from the complex physical properties observed in the cluster and discussed in the previous chapter are described, the main physical parameters such as the distance, the age and the metallicity of HD 97950 are recalled. In many respects, the situation is not as straight-forward as in the Arches cluster, and a much more sophisticated analysis is required.

7.1 Physical parameters of NGC 3603 entering the MF

7.1.1 Distance to NGC 3603

Despite numerous efforts, the distance to NGC 3603 is still not known very precisely. Kinematic as well as photometric distances show significant scatter, yielding values between 6 and 10 kpc. A kinematic distance of 6.1 ± 0.6 kpc was derived by DePree et al. (1999) from radio line width, while Nürnberger et al. obtain 7.7 ± 0.2 kpc with a similar method. The large differences in the velocity determined for different parts of the molecular cloud complicate a consistent distance determination. Photometric distances have been derived from UBV colour-colour and colour-magnitude diagrams by Moffat et al. (1983) to $m - M_0 = 14.24 \pm 0.45$ mag, $d = 7.0 \pm 0.5$ kpc, and $m - M_0 = 14.3$ mag, $d = 7.2$ kpc by Melnick et al. (1989). The early photometric distance determinations were restricted to the main sequence population. Isochrone fitting of the pre-main sequence/main sequence transition yields a distance modulus of $DM = 13.9$ mag and a foreground extinction of $A_V = 4.5$ mag for the pre-main sequence population (cf. Sec. 6.2.1, Fig. 6.5). The corresponding distance, $d = 6$ kpc, is slightly lower than previously derived values, but consistent with distance estimates from DePree et al. (1999). The foreground extinction is consistent with the reddening observed in the colour-colour diagram. As these values allow the closest agreement between the isochrone used for mass function derivations in Sec. 7.3 and the colour-magnitude distribution of the cluster stars, they will be used throughout the thesis.

7.1.2 Metallicity of NGC 3603

No thorough analysis of NGC 3603 with respect to metallicity is available in the literature. Solar metallicity was assumed in other work (e.g. Eisenhauer et al. 1998). NGC 3603 is located at a Galactoccentric distance of 8 kpc, comparable to the Sun. The radial gradient in metallicity observed in the Milky Way supports that the metallicity in NGC 3603 is comparable to the solar value, which will be adopted.

7.1.3 Age of HD 97950

The age of the starburst cluster has essentially been constrained by the existence of hydrogen-rich WNL6 stars. Wolf-Rayet (WR) stars in this evolutionary state have ages between 2 and 3 Myr. The WN6 sources in HD 97950 have a factor of 10 higher luminosity than normal Milky Way WRs. Moffat et al. (2002) argue that the WR stars in HD 97950 are "probably main sequence stars of extremely high luminosity with strong wind-produced emission lines" from the correlation observed between X-ray and radio flux, which is uncorrelated for normal Galactic (single) WRs. Care has to be taken as at least one of the central WRs in HD 97950 is known to be in a binary system, such that colliding winds could produce the unusual observed X-ray properties. Massey & Hunter (1998) compare the spectra of the 3 WRs in HD 97950 to similar stars observed in R 136, and conclude that these are probably "super O stars". If the WN6 stars are in fact main sequence stars in their core hydrogen burning phase, they have to be more massive than O3 stars, indicating a very young cluster age of ~ 1 Myr due to their short lifetime.

Comparison of the pre-main sequence population observed by Eisenhauer et al. (1998) and Brandl et al. (1999) with PMS isochrones (Palla & Stahler 1999) is consistent with ages of 0.3-1 Myr for the PMS/MS transition region. Similar to the main sequence turn-off, used for age dating in more evolved populations such as globular clusters, the pre-main sequence turn-off can be used to estimate the age of a young population. With the above parameters for distance, reddening and metallicity, the best fit obtained for the ISAAC data presented in Fig. 6.6 yields an age of 1 Myr, consistent with previous pre-main sequence age dating. The high-resolution ISAAC photometry is very precisely fitted by a single isochrone, and does not require an age spread. A 1 Myr old stellar population is entirely consistent with the observed colour-magnitude diagram, and will mainly be used for HD 97950.

As stars on the MS do not evolve severely, light deviations in the age determination are not critical for the derivation of the main sequence MF. In the early evolutionary stage of the cluster population, stellar evolution is almost negligible except for the highest mass objects, such that mass function derived from a 1 Myr isochrone should not deviate significantly from MFs using a 3 Myr model. The MFs derived in the following are therefore comparable to the results of previous studies. The rapid evolution on the PMS, however, comprising a large part of the mass functions derived below, requires exact age dating. Here, the use of the model representing the stellar population most closely is critical, as was shown in Fig. 6.6.

7.2 General remarks on the mass function derivation in HD 97950

As a consequence of the existence of a visible binary (candidate) sequence, and the clear separation of a pre-main sequence and a main sequence population observed in the central CMD of HD 97950, the mass function derivation has to include different physical assumptions as in the case of the Arches cluster. First of all, two different sets of evolutionary models are required to represent the MS and the PMS population at a given age. As the 1 Myr pre-main sequence isochrone from the Palla & Stahler set of models fits both the transition of the PMS into the MS as well as the lower PMS distribution best, this isochrone is chosen for the MF derivation on the PMS. According to the arguments given above, a cluster age of 1 Myr is consistent with our data and with prior evidence from massive stellar spectra. For most of the MFs derived below, the 1 Myr isochrone from the Geneva set of models will consequently be used.

In addition, the case of a 2 and 3 Myr isochrone, used in prior MF derivations, will also be tested to compare the effect of MS evolution (mass-loss in high-mass stars, which is, however, expected to be minor for stars below the giant stage.

The identification of a binary sequence poses an additional challenge to a realistic MF derivation. As no prior data set resolved this feature clearly, the MF will be shown with and without binary

correction to allow comparison with prior MF derivations.

The strong variability of the extinction observed for individual objects in NGC 3603 additionally blurs the distribution of stars in the CMD. In particular, the PMS and MS populations cannot be fitted with a single foreground extinction. While the 1 Myr PMS isochrone fit is completely consistent with a foreground exinction of $A_V = 4.5$ mag, as derived in several works for the stellar population in the immediate vicinity of HD 97950 before (see, e.g. Moffat et al. 1994), the MS cannot be fitted reasonable well with this value. Note that without reddening, the MS and PMS tracks line up perfectly, as the transition point of the Palla & Stahler isochrones is calibrated to the Lejeune & Schaerer main sequence. Beyond the transition region in the CMD of HD 97950, the MS appears to turn bluewards, indicating decreasing extinction with increasing stellar brightness (and mass). A reasonable fit can be achieved with $A_V = 4$ mag, such that the main sequence model has been transformed using this lower extinction value (see Fig. 7.4).

As a consequence of the variable extinction observed in the NGC 3603 region, we decided to use individual dereddening as the safest method to derive realistic stellar masses. Each star in the colour-magnitude diagram has thus been shifted along the reddening vector onto the PMS or MS isochrone. Although this procedure is more accurate in the sense that individual reddening is taken into account, it implicitely assumes that all scatter observed in the CMD is due to reddening variation. This is clearly not the case. Besides the photometric scatter inherent to the data, other processes such as binarity, stellar rotation, and intrinsic IR excesses (see Sec. 6.2.7) contribute to the scatter as well. Most of the additional processes influencing a very young stellar population are difficult to quantify, and will be ignored in the following analysis. The uncertainty inherent should, however, be kept in mind when interpreting the MF slopes. The photometric uncertainties are expected to introduce random scatter, such that their combined effect averages out.

Another problem imposed by the fact that PMS and MS are both mixed up in the young stellar population of HD 97950 is the treatment of the transition region. Fortunately, the ISAAC data allowed to resolve the transition point, and the overdensity of stars observed at exactly this position matches the turn-off point of the 1 Myr PMS isochrone extremely well. Thus, stars in this area have been allocated PMS transition masses, which are in the narrow range between 2.5 and 4 $M_\odot$. There is a slight ambiguity in the Palla & Stahler isochrone in the sense that stars with 3.5 to 4 $M_\odot$ cannot be distinguished, but this is not relevant for the resultant MF as these stars all fall into the same mass bin. The continuation of stars along the main sequence beyond the PMS turn-off point is then counted into the MS population, where only masses above the MS turn-on of 4 $M_\odot$ enter the combined MF. Although this facilitates the analysis as a clear cut is introduced between MS and PMS contributions, the transition region is clearly physically more complex than envisioned in this simple treatment. In particular, stars contributing to the MS may be scattered away from the narrow range beyond the PMS turn-off in the CMD. The transition mass will be marked in all derived MFs, such that the combination of MS and PMS contributions is clear, and in particular the last PMS and first MS bin should be observed with care.

The procedures used to derive the stellar mass distribution in HD 97950 are outlined in the next section.

7.3 Mass function derivations

7.3.1 Incompleteness correction

Artificial star tests were performed on each science frame to determine the recovery fraction per magnitude. Between 200 and 250 stars were inserted in the smaller $2' \times 2'$ "cluster" frames and the larger $3\farcm4 \times 3\farcm4$ "field" frames. The inserted number of stars correponds to less than 1% of the total number of stars detected on each image. Magnitudes and positions were assigned randomly using the *addstar* task in IRAF, as in the case of the Arches cluster. As the cluster itself covered only

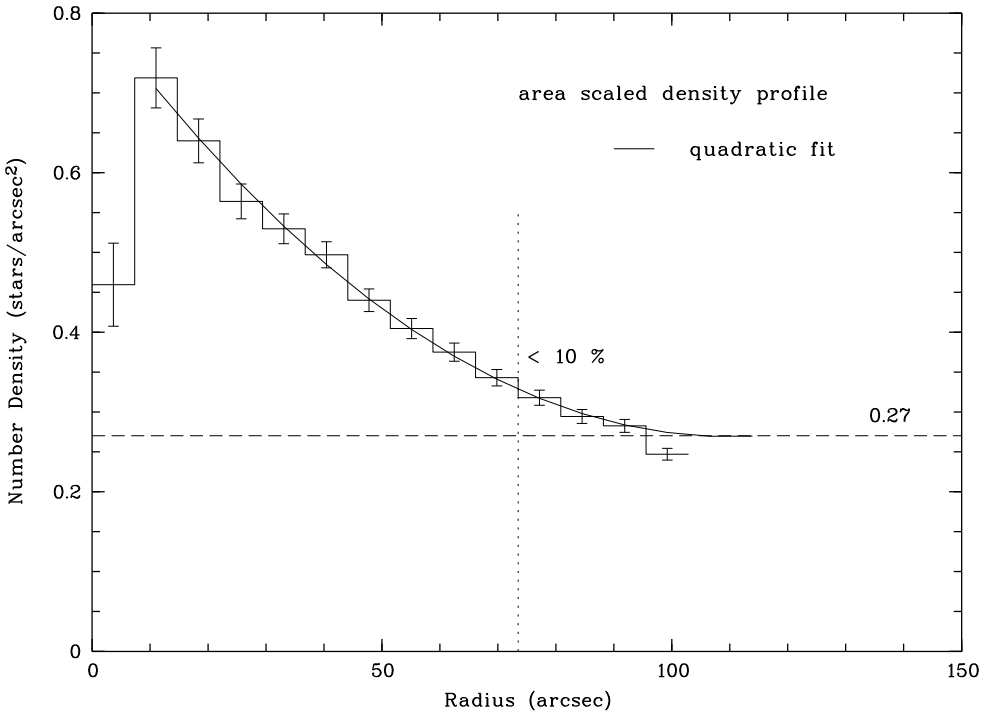

Figure 7.1: Density profile of HD 97950, indicating the radius where the field star contamination falls below 10%.

a small area on the high-resolution frames, additional simulations were performed on the innermost $60'' \times 60''$, with 100 to 150 artificial stars or $\leq 2\%$ of the stellar population found in the cluster center. Source detection and PSF fitting was conducted with the same parameters as when deriving the stellar photometry. The procedure was repeated to yield the recovery fractions for ~ 6000 stars in the field frames, and ~ 11000 stars in total on the cluster frames, with 5000 stars distributed randomly over the entire image, and 5000 stars confined to the central region. The resultant recovery fractions were applied in two steps during the analysis: 1) during field star correction and 2) during incompleteness correction of the mass function.

7.3.2 Field star correction

The field star fraction was derived from an area to the North and East of the cluster center. This region is particularly well suited to estimate field stars in the low-extinction cluster center, as it is neither influenced by strong HII region emission nor shows evidence of variable or enhanced extinction. Field stars were subtracted randomly in each 0.5×0.5 mag colour-magnitude bin of the CMD. Prior to statistical field star subtraction, the number of field stars had to be corrected for the varying stellar density (crowding) with radial distance from the cluster center. For this purpose, the field and cluster recovery fractions, f_{field} and $f_{cluster}$, were fitted in dependence of the magnitude as a third order polynomial as displayed in Fig. 7.2. The number of field stars is corrected for field incompleteness as $n_{field,corr} = n_{field}/f_{field}$, i.e. to a field completeness of 100%. This number was then reduced according to the expected recovery fraction of stars in the radial annulus studied, yielding a combined correction of $n_{field,final} = f_{cluster} \cdot n_{field,corr} = f_{cluster}/f_{field} \cdot n_{field}$, with $f = f_{cluster}/f_{field}$ denoting the final correction factor applied to the measured number of field stars.

The incompleteness simulations yielded independent correction factors for each filter. In principle, the combined probability to find a field star in each colour-magnitude bin in the $J, J-K$ plane is then given by the product of the individual probabilities, $f_{JK} = f_J \cdot f_K$. In the colour and magnitude range

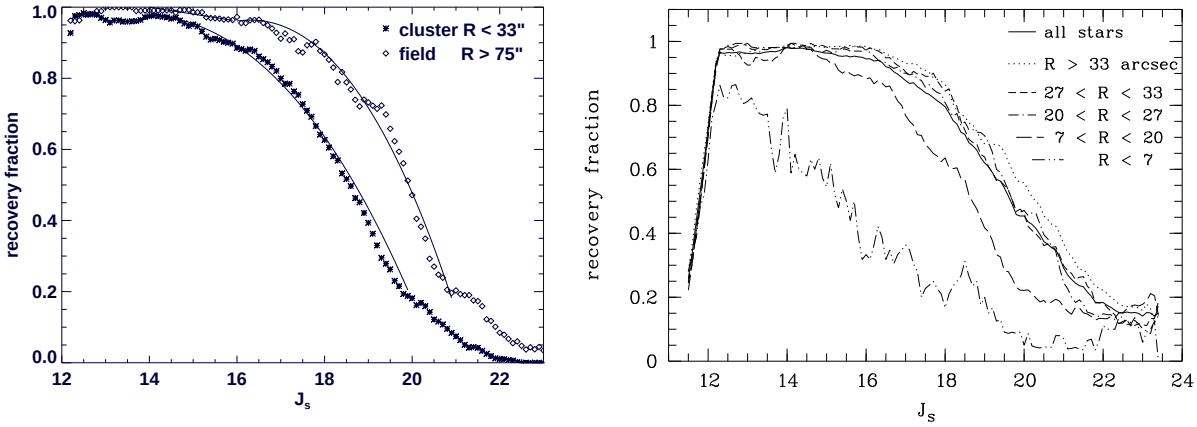

Figure 7.2: Recovery fractions from artificial star tests.
The recovery rates are shown for the cluster center and field including the polynomial fits used in the field star fraction and mass function incompleteness correction (left). The radial variation in the completeness due to varying stellar density is compared for the different annuli (right) for which the MF is calculated. Variations are significant only in the innermost annulus ($7'' < R < 20''$). The huge loss of stars in the innermost $7''$ reflects the saturation and crowding problems in the cluster core.

covered by the cluster center stars, however, the incompleteness is entirely determined by the J-band limit. Thus, only J-band incompleteness is taken into account in the mass function derivation. The correction factor f_J for each magnitude is obtained from the polynomial fit. The measured number of field stars is corrected by the factor derived for each annulus studied, and the adjusted number of field stars is then randomly removed from the cluster CMD.

As mentioned in the introduction (Sec. 2.4.2) the cluster extent is debated, with estimates ranging up to $2\farcm5$ (Nürnberger & Petr-Gotzens 2002), such that the area covered by the ISAAC data may overestimate the field star contamination. As the low-mass halo surrounding HD 97950 is mainly composed of faint, low-mass stars, the bright central cluster population should not be severely affected[1].

Fig. 7.3 shows the effects of field subtraction on the central cluster population, and also indicates the 50% completeness limit for this radial selection, down to which mass function slopes will be derived.

In the following sections, the different approaches used to derive the mass function in HD 97950 will be described in detail. Results for all MF derivations will be summarised in Tab. 7.2. Sample individual pre-main sequence and main sequence MFs are shown at the end of the description sections in Figs. 7.5 to 7.7 to allow direct comparison. The combined mass functions of this selection will be fitted in Figs. 7.8 to 7.10. The main sequence extension fainter than $J_s > 15.5$ mag, corresponding to the 1 Myr MS turn-on at $4\,M_\odot$, is excluded from the fit. In the combined MF this part is solely contributed by PMS stars.

7.3.3 Simple star counts

In the simplest model, the luminosity of a star reflects its evolutionary stage and mass. This ignores all processes changing the luminosity and thus magnitude of a star individually and independently of its evolutionary stage. The isochrone can then be applied directly to each given stellar magnitude to transform the brightness distribution into a mass function (as e.g., in the case of the Arches cluster, where the narrow main sequence supported this procedure). As this is the most frequently used

[1]Ideally, a separated field should be used to estimate the background population. One off-field was observed at a distance of $\sim 30'$ from the cluster center, but unfortunately turned out to contain an entirely different stellar population dominated by older giant stars. The strong spatial variations in the stellar population along the Carina arm complicate the determination of the field star contribution in any particular region.

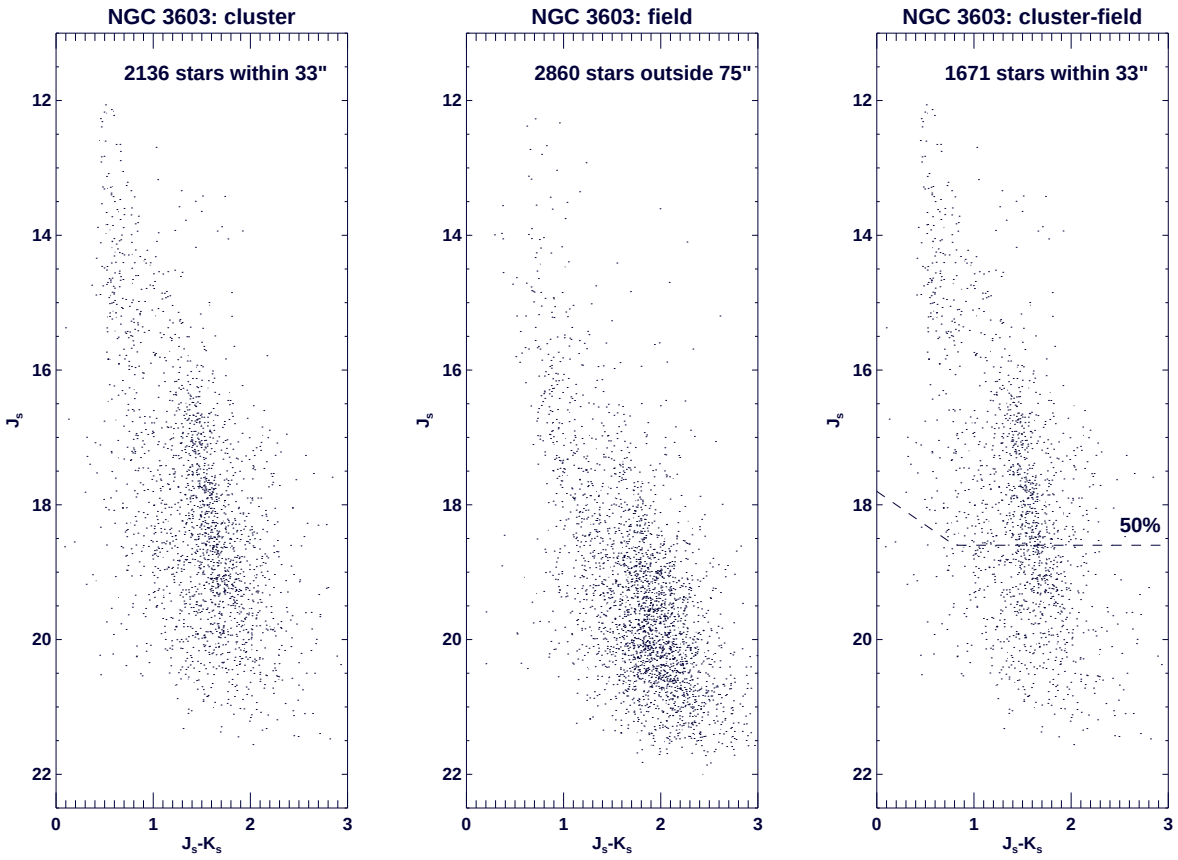

Figure 7.3: Colour-magnitude diagram of the inner 33″ of HD 97950.
The unsubtracted cluster population is shown in the left panel, the observed field star population (not yet scaled to the same area) in the middle, and the subtracted cluster population used for mass function derivations in the left panel. The 50% completeness limit down to which mass functions are fitted is indicated as a dashed line. Note that the magnitude corresponding to 50% completeness varies with radial distance from the cluster center.

method to derive mass functions, we include it here as the simplest approach. Field data are not always available, and field contribution can indeed be negligible in the dense cluster regions, such that field star contamination has rarely been taken into account in MF derivations of the HD 97950 cluster (except for the study of the cluster center by Eisenhauer et al. 1998). In order to show the effects of field contamination (which indeed turn out to have only a minor effect on the resultant MF slope), MFs are calculated with and without field subtraction.

7.3.4 Individual dereddening

As discussed in Sec. 6.4, the individual objects in NGC 3603 show varying extinction, either due to variations in the distribution of molecular material in the foreground, or due to individual reddening from remnant circumstellar envelopes. Therefore, objects have been slided along the reddening vector in the colour-magnitude diagram until an intersection with the corresponding isochrone is reached, and the mass of the star is determined from the intersection point. The extinction applied to the isochrone itself is not relevant in this case, as only the length of the dereddening path (i.e., the relative shift in the CMD) depends on the location of the isochrone, but not the desired intersection point. For the MF derivations below, isochrones matching the average foreground extinction of the MS and PMS populations were used, and stars blueward and redward of the isochrone have been shifted accordingly.

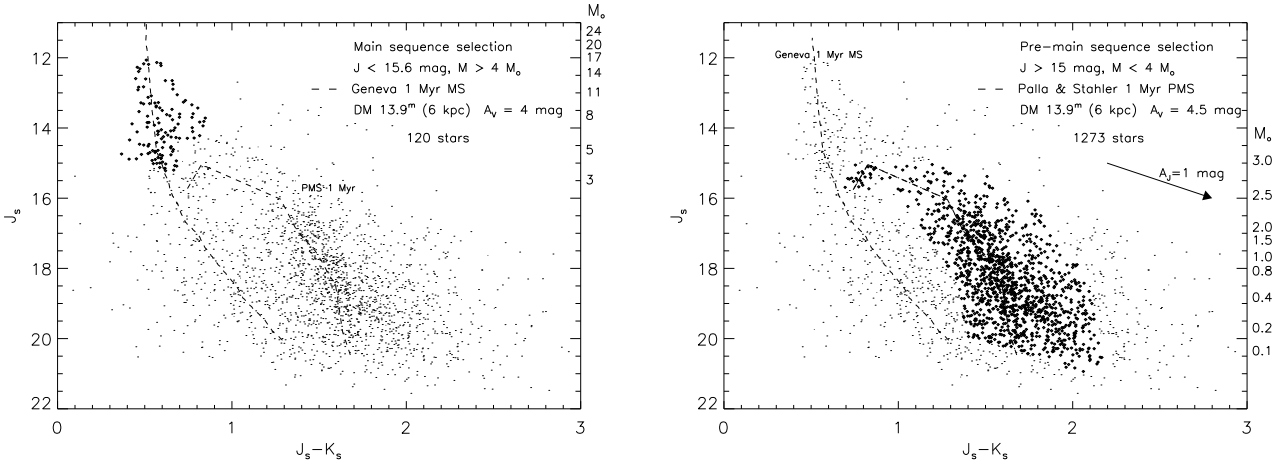

Figure 7.4: Selection of stars around the average MS (left) and PMS (right) isochrone.
Stars up to 0.25 mag bluewards of the PMS and MS isochrones are included, and redwards by 0.35 mag in the case of MS stars and 0.5 mag in the case of PMS stars. The selected stars represent a typical sample used for the MF derivation (after field subtraction).

The blue and red limits in the distance from the isochrone was determined by eye from the stellar distribution in the $J_s, J_s - K_s$ plane. As the main sequence is not affected by field star contamination, all stars around the MS have been included in the MF, with a colour selection of -0.25 mag bluewards and +0.35 mag redwards of the MS isochrone. The bulk of the PMS population, where reddening is more severe, can be included selecting colours -0.25 mag bluewards and +0.5 mag redwards of the PMS isochrone. This rejects the reddest objects, which might be affected by infrared excesses. The selection of stars contributing to the mass function is shown in Fig. 7.4.

Note that most of the stars are found in a very narrow range around the PMS, in an envelope of only -0.1/+0.15 mag. This selection does not alter the slope of the PMS MF alone, but in comparison with the MS MF too few stars are found in the transition region, such that MS and PMS do not line up. Therefore, the wider PMS selection was used, where MS and PMS line up very well.

In all following MF derivations, field subtraction and individual dereddening are taken into account.

7.3.5 Binary rejection

Although the comparison with the higher resolved HST/PC data is very suggestive, and all measures have been taken to exclude a systematic offset of the binary sequence due to problems in the photometry, one test run was made where the visible binary sequence was rejected. If binary stars are not subject to a mass bias from a different formation process as single stars, the resultant "single" mass function should represent the underlying stellar population of the star cluster in a statistical sense. Note, however, that the vertical distribution of PMS stars in the CMD does not allow such a selection. Even if the same photometric offset is included in the case of PMS stars, as is to be expected from the binary sequence extending all the way into the transition region, such an offset is invisible in the vertical PMS feature. As a consequence, the corresponding PMS stars cannot be rejected, and only the MS and the transition region (down to $2.5\,M_\odot$) are affected by binary rejection.

7.3.6 Binary correction - MS and transition region

As a first step, the visible binary candidate sequence above the main sequence and the transition population was adjusted. The J_s-band magnitude of the selected stars was increased by 0.75 mag as

Table 7.1: Fraction of stars on binary candidate sequence. Only main sequence stars are selected.

J_s mag	N_{binary}	N_{single}	$N_{binary}/(N_{single}+N_{binary})$
12 - 13 mag	9	19	0.32
13 - 14 mag	12	38	0.24
14 - 14.8 mag	15	42	0.27
all	36	99	0.28

displayed in Fig. 6.9, and an additional companion star with equal colour and magnitude was included. This procedure only takes care of equal mass binaries (as observed on the binary sequence), as for all other mass ratios no prediction can be made. The adjustment is applied after field subtraction, before individual dereddening and MF calculation. This way, the bias from individual dereddening of equal-mass binaries due to the larger brightness and thus higher mass is avoided. The resultant pairs of "single" stars are treated in exactly the same way as the rest of the population.

7.3.7 Binary correction - statistical PMS correction

Nevertheless, the problem of the merging of binaries into the PMS population remains. The fraction of stars observed on the MS sequence is approximately 30% of the total number of stars in the upper part of the diagram. When intervals of 1 mag width are studied, no trend is observed (Tab. 7.1) towards fainter stars. Thus, to correct for the equal-mass binary contribution on the PMS a constant binary fraction of 30% has been assumed. If no strange selection mechanism suppresses the formation of binaries on the PMS, these stars are burried in the PMS distribution. In order to correct for the bias imposed on the derived MF, 30% of the PMS stars have been selected randomly, shifted down by +0.75 mag and an additional companion was added, as in the case of the MS binary sequence. If the equal-mass binary fraction is the same for each mass bin, as suggested from the MS and transition region, this procedure should correct for the overestimate of individual masses due to brighter magnitudes of the binaries.

7.4 Discussion of the resultant mass functions

All resultant MF slopes are summarised in Tab. 7.2 and sample MFs are shown in Figs. 7.5 to 7.10 on the following pages. As the pre-main sequence is heavily affected by incompleteness in the entire cluster area analysed, the fit is derived for the incompleteness corrected PMS MF for completeness fractions larger than 50%. At the high-mass end of the main sequence MF, saturation losses thin out the CMD. Due to the combination of different exposures taken under varying conditions, the saturation limit is not a sharp point, but extends over a range of ~ 1 mag in J_s. Unfortunately, the detector non-linearity of the ISAAC array increases rapidly close to the saturation limit, such that the fluxes of saturated objects cannot be recovered. The approximate fraction of stars lost due to saturation in the upper mass bin, $M < 20\,M_\odot$, is $\sim 50\%$. The high-mass end of the MF has been corrected accordingly, and is included in the MF fit (otherwise, the upper end of the MF is essentially not fitable). The derived individual slopes of the MS alone are meant to give an idea on the effects of the different corrections introduced, and should not be taken at face value. The large fitting errors reflect the obvious inherent uncertainties. The PMS track naturally covers a large range in colour over a narrow mass range in the transition region where the PMS bends towards the main sequence. The colours on the transition region range from $J-K = 0.7$ mag to $J-K = 1.3$ mag with masses between 2.5 and $4\,M_\odot$. Only four model points are available for the transition region, such that the

mass transformation had to rely on interpolation between theoretically predicted colour, magnitude and thus mass values. This may well be the cause for the enhancement of stars seen in each MF in the mass bin centered on $2\,M_{\odot}$, and the subsequent decrease in the number of stars in the following mass bin centered on $3.2\,M_{\odot}$. However, the combined MS/PMS mass function is less affected by the two subsequent bins at PMS/MS transition masses, such that the continuous mass function yields a more reliable fit.

After the effort undertaken to correct for the discussed effects, the derived mass function slopes show remarkably small scatter. A few general tendencies are observed. First of all, the slope of the PMS MF is very stable with values ranging only from $\Gamma = -0.61$ to -0.85, with a scatter smaller than the formal fitting error of ~ 0.25. The main sequence MF is more severely affected by binary correction as the PMS MF. This is expected as the upper mass bins are emptied without substitution from higher mass bins, as is the case for intermediate and low mass stars. As the upper end of the MF is also heavily affected by saturation, the loss in stars and resultant steepening of the MF can be a consequence of saturating the *binary* sequence. A final conclusion on the main sequence MF is hard to draw from this data set alone, as the upper end of the MF needs to be filled with unsaturated, well-resolved data.

The slope of the combined mass function is not very affected by this scatter, but shows remarkable constancy with values ranging from -0.84 to -0.99 with a formal fitting error of 0.1. The use of an older main sequence of 2 or 3 Myr does not change the combined MF fit significantly (see Tab. 7.2).

The most complete derivation of the mass function in the central cluster area of HD 97950 including all corrections discussed in the previous sections is displayed in Fig. 7.10. The slope of the mass function including field subtraction, individual dereddening and binary correction is $\Gamma = -0.89 \pm 0.08$.

A slope $\Gamma = -0.77$ down to $M > 1 M_{\odot}$ was derived by Eisenhauer et al. (1998) from high-resolution ADONIS data in the innermost $13''$ of the cluster center, in reasonable agreement with our estimate. These authors did not account for binaries, and interpreted the observed scatter in the PMS/MS transition as an age spread in the range 0.3 to 1 Myr. Accordingly, a mean age of 0.5 Myr was used to derive masses of PMS stars. As shown in Fig. 6.6, this interpretation is consistent with the data as long as the photometric accuracy does not allow to resolve the equal-mass binary offset. A younger age and thus evolutionary state results in assigning lower masses to the stars. Comparably, binarity results in assigning stars with a given brightness to have a (well-defined) lower mass. As the 0.3 Myr isochrone coincides well with the binary sequence, the masses on the PMS derived for the transition stars at least are comparable. On the other hand, the effect of possible companions on the MF is not taken into account in the case of an age spread. Statistically adding companions at a constant fraction in all magnitude bins should, however, not alter the MF slope. Thus using a younger isochrone for the transformation of magnitudes into masses is capable to result in a comparable slope as the binary correction procedure.

A severe difference between both data sets remains, limiting the above comparison. Mass segregation in the cluster, in the sense that massive stars may be found predominantly in the cluster center as observed in the case of the Arches cluster, would cause the MF slope to steepen with increasing radius. As the ISAAC data are limited to $R > 7''$ due to saturation, while the ADONIS data only extend out to $R < 13''$, a steeper MF would be expected from ISAAC as from the central ADONIS data in the presence of mass segregation. The comparison is complicated by the different procedures used. When the MF is calculated with mere field subtraction, without dereddening and binary correction for a 1 Myr isochrone, the slope becomes $\Gamma = -0.86$, slightly, but not significantly steeper than the ADONIS slope. No significant change can be found between the ADONIS core MF and the ISAAC MF outside the core. This agreement is even more surprising as the core is known to be mass segregated from HST/WFPC2 data (Grebel et al., in prep.).

One possible interpretation of this correspondence - assuming it is real - is that the slope in a cluster area covering $7 < R < 33''$ is still dominated by the central massive stellar population. The radial variation in the mass function, studied in the next section, may reveal the dominant stellar

Table 7.2: Mass Function derivations for HD 97950.

PMS fit	MS fit	PMS + MS fit	description
$\Gamma = -0.78 \pm 0.32$	$\Gamma = -0.75 \pm 0.20$	$\Gamma = -0.91 \pm 0.10$	star counts (no field subtraction, no dereddening)
$\Gamma = -0.72 \pm 0.33$	$\Gamma = -0.72 \pm 0.25$	$\Gamma = -0.86 \pm 0.11$	star counts (with field subtraction, no deredding)
$\Gamma = -0.85 \pm 0.30$	$\Gamma = -0.56 \pm 0.20$	$\Gamma = -0.91 \pm 0.10$	with dereddening, no field subtraction
$\Gamma = -0.73 \pm 0.32$	$\Gamma = -0.57 \pm 0.20$	$\Gamma = -0.84 \pm 0.10$	with dereddening and field subtraction
$\Gamma = -0.73 \pm 0.33$	$\Gamma = -0.91 \pm 0.12$	$\Gamma = -0.99 \pm 0.10$	binary candidates rejected
$\Gamma = -0.73 \pm 0.33$	$\Gamma = -0.95 \pm 0.22$	$\Gamma = -0.96 \pm 0.09$	visible binary sequence corrected (MS and transition)
$\Gamma = -0.67 \pm 0.26$	$\Gamma = -0.84 \pm 0.13$	$\Gamma = -0.89 \pm 0.08$	visible binary seq. and statistical PMS correction 30%
$\Gamma = -0.61 \pm 0.21$	$\Gamma = -1.03 \pm 0.23$	$\Gamma = -0.91 \pm 0.08$	2 Myr MS, all corrections
$\Gamma = -0.64 \pm 0.22$	$\Gamma = -0.75 \pm 0.10$	$\Gamma = -0.84 \pm 0.09$	3 Myr MS, all corrections (fit $< 15\,M_\odot$)

Table 7.3: Radial variation of the mass function.

annulus	PMS + MS fit	remark
$7'' < R < 20''$	$\Gamma = -0.89 \pm 0.15$	MS + PMS fit
$20'' < R < 27''$	$\Gamma = -1.08 \pm 0.15$	MS + PMS fit
$27'' < R < 33''$	$\Gamma = -0.84 \pm 0.27$	PMS fit only
$33'' < R < 46''$	$\Gamma = -0.95 \pm 0.22$	PMS fit only
$46'' < R < 65''$	$\Gamma = -0.92 \pm 0.32$	PMS fit only

contribution at a given radius.

7.5 Radial variation in the mass function of HD 97950

Radial mass functions have been derived including field subtraction, individual dereddening and correction for binaries on the MS as well as on the PMS as described above. Three annuli covering equal areas have been selected, each covering 1/3 of the area enclosed within $7'' < R < 33''$. The radial selections correspond to $7'' < R < 20''$, $20'' < R < 27''$, and $27'' < R < 33''$ (cf. Fig. 6.2). The mass functions for these annuli are shown in Figs. 7.11 and 7.12.

As the resultant distributions are more irregular and limited by smaller number counts in each annulus, the PMS and MS MFs have not been fitted individually. Fig. 7.11 clearly displays the features of mass segregration as observed in the Arches cluster as well. While the low-mass (PMS) distribution decreases in number as the density decreases with larger radial distance, the shape in each annulus shows a close resemblance. The high-mass (MS) end on the other hand becomes more and more depleted with increasing radius. In the last radial bin, still within $33''$ of the cluster center and thus far within the estimated total cluster extent of $\sim 150''$ given by Nürnberger & Petr-Gotzens (2002), practically no massive stars remain. The total number of objects with $J_s < 15.5$ mag, the MS turn-on point at $4\,M_\odot$, in the outermost annulus is 4. From the extension of the main sequence to fainter magnitudes and masses, assumed to be young field stars in the surrounding NGC 3603 region, these stars can easily be young stars formed within NGC 3603 close to the cluster, falling onto the same main sequence, but need not be true members of HD 97950. The lowest panel in Fig. 7.11 is suggestive in this respect.

In stark contrast to the strong outwards variation in the main sequence population, the pre-main sequence distribution of stars remains similar throughout all annuli. The truncation at very low masses in the first and second annulus is most probably due to crowding losses of faint stars, as indicated by the incompleteness correction. As the lowest mass bins are incomplete by more than 90% (!), a

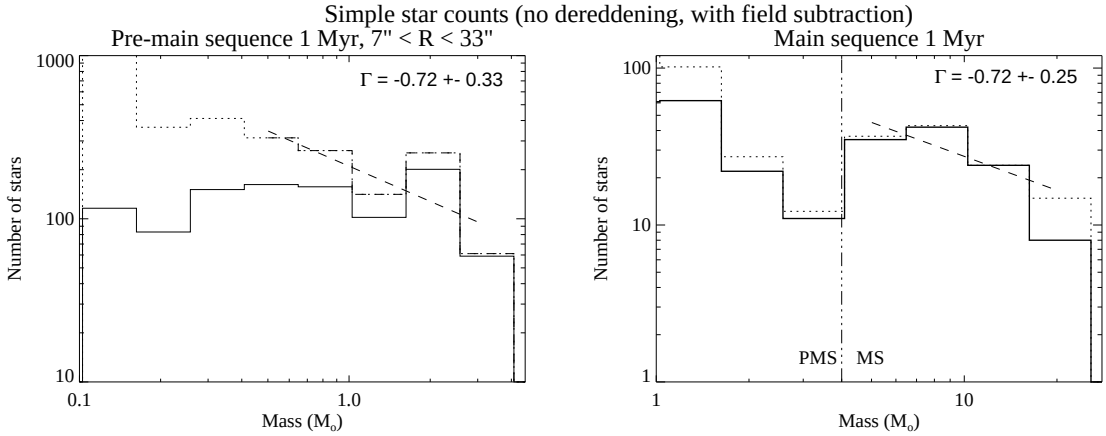

Figure 7.5: PMS and MS mass distributions of HD 97950 calculated from simple star counts.
The measured J-band magnitude of each star has been transformed directly into a stellar mass using the MS or PMS 1 Myr isochrone displayed in Fig. 7.4, with a distance modulus of 13.9 mag and constant foreground extinction of $A_V = 4.5$ mag (PMS) and $A_V = 4$ mag (MS) applied. Field stars are subtracted, but no individual dereddening is performed.

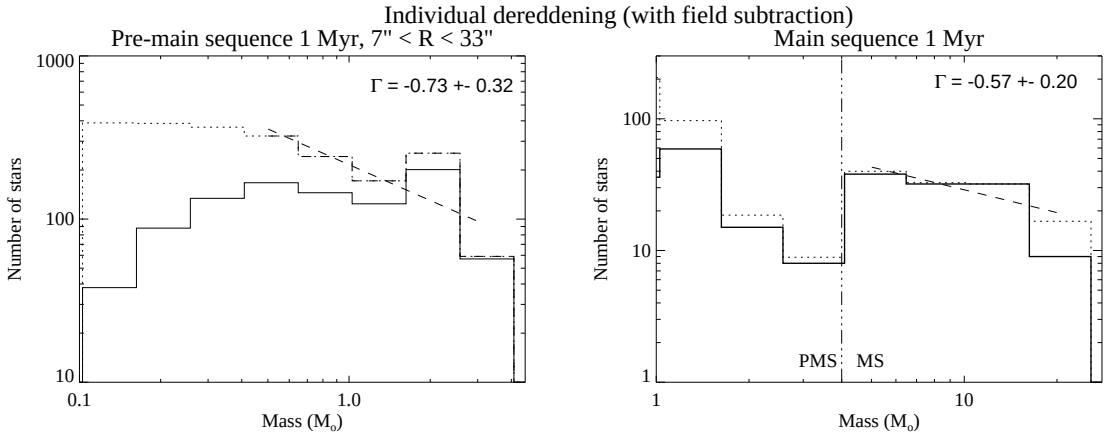

Figure 7.6: PMS and MS mass distributions as derived from individual dereddening.
Field star subtraction has been performed prior to dereddening. Individual stellar masses are determined by shifting each star in the J_s, $J_s - K_s$-plane along the reddening vector onto the PMS or MS isochrone. This procedure assumes that photometric scatter is caused by varying extinction. Cluster stars were selected in addition to the radial selection ($7'' < R < 33''$) in envelopes around the main sequence
(-0.25 mag bluewards, +0.35 mag redwards) and the pre-main sequence isochrone (-0.25 mag bluewards, +0.50 mag redwards).

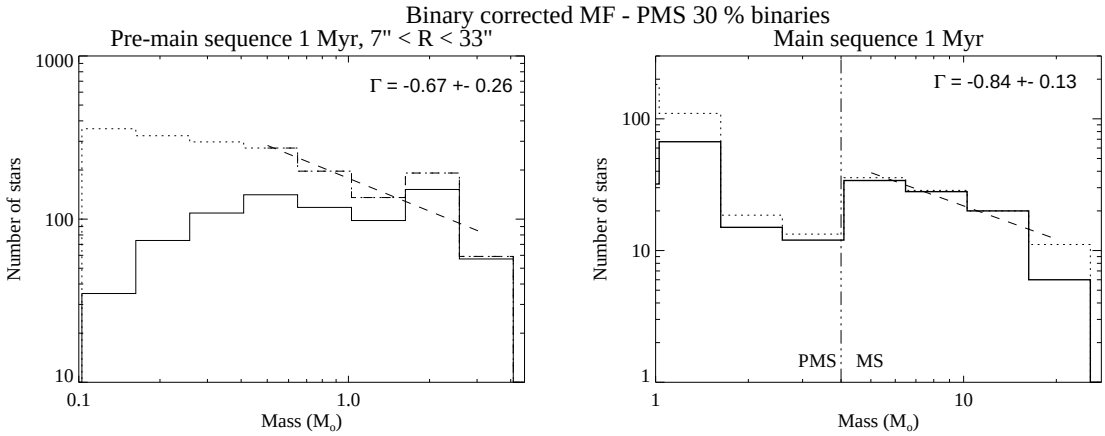

Figure 7.7: PMS and MS mass distributions derived including binary correction.
Field subtraction and individual dereddening were performed. Stars on the binary candidate sequence were shifted down by $\Delta J_s = +0.75$ mag, and 30% of the PMS stars selected randomly were treated in the same way. In both cases, one equal-mass companion was included in the colour-magnitude distribution.
Note that the upper mass bins may loose stars due to incomplete binary correction for stars brighter than the saturation limit ($J_s \sim 12$ mag).

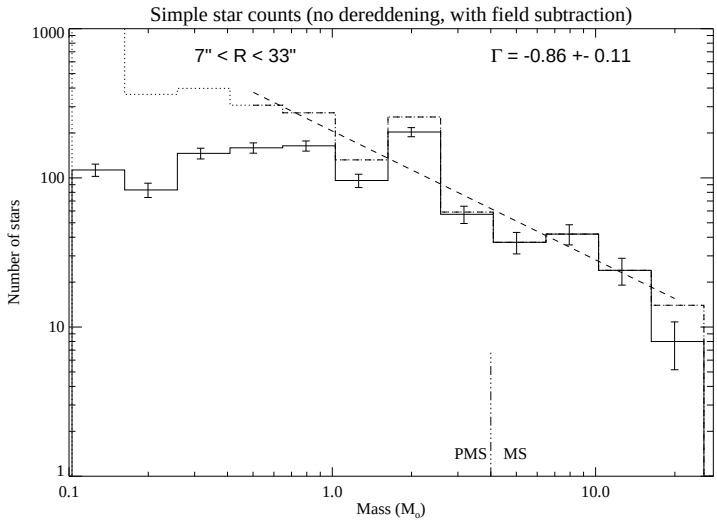

Figure 7.8: Combined PMS and MS mass function of HD 97950 calculated from simple star counts.
Mass function of HD 97950 combined from PMS and MS contributions displayed in Fig. 7.5.
Field subtraction is included, but no dereddening. Star counts in each magnitude interval are used to derive the MF.

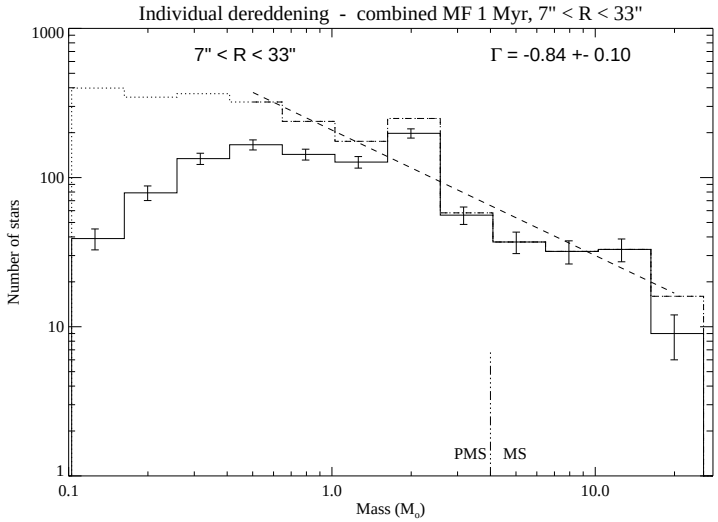

Figure 7.9: Combined PMS and MS mass function as derived from individual dereddening.
Mass function of HD 97950 combined from the PMS and MS contributions displayed in Fig. 7.6.
Field subtraction and individual dereddening are included.

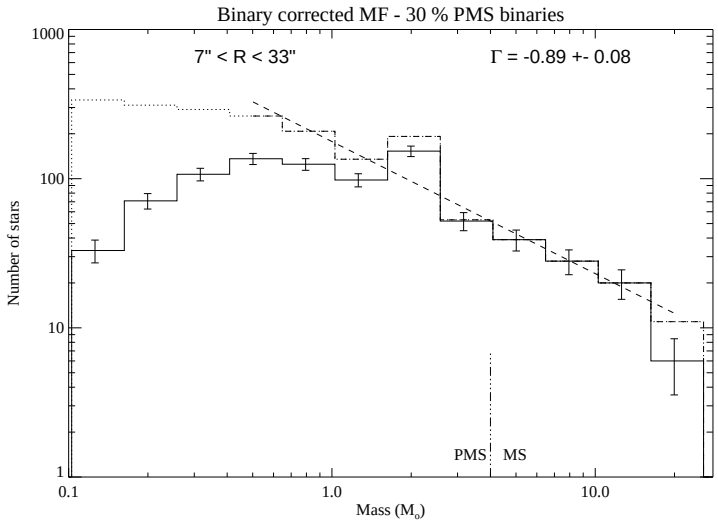

Figure 7.10: Combined PMS and MS mass function derived including binary correction.
Mass function of HD 97950 combined from PMS and MS contributions displayed in Fig. 7.7.
In addition to field subtraction and individual dereddening, the MF is corrected for stars on the binary (candidate) sequence assumed to be equal-mass binaries, and PMS stars have been corrected statistically for a binary contribution of 30% as derived from the observed binary candidate sequence.

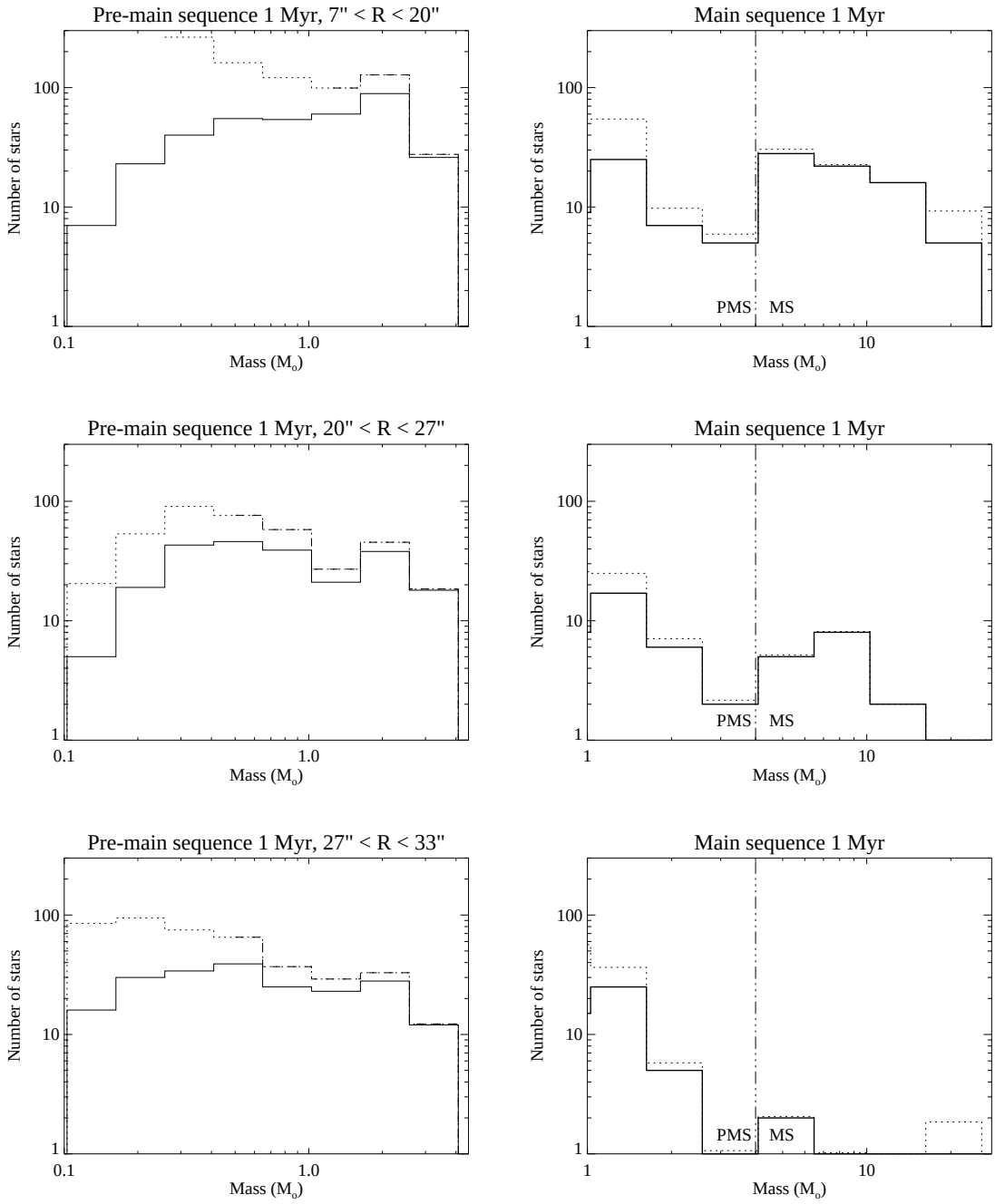

Figure 7.11: Radial variation in the PMS and MS parts of the MF.
Three consecutive annuli filling the cluster area used for the total MF derivation above are selected with equal areas, such that number counts are comparable directly. While the decrease on the PMS reflects the decrease in stellar density when moving radially outwards, the depletion of main sequence, high-mass stars in the outer annulus suggests that the massive stars are concentrated towards the cluster center, implying mass segregation at the high-mass end. The low-mass end of the PMS is heavily affected by crowding incompleteness, such that this conclusion cannot be reversed for PMS stars. Fits are purposefully excluded due to the low number statistics and the irregular MF shapes observed in each annulus.

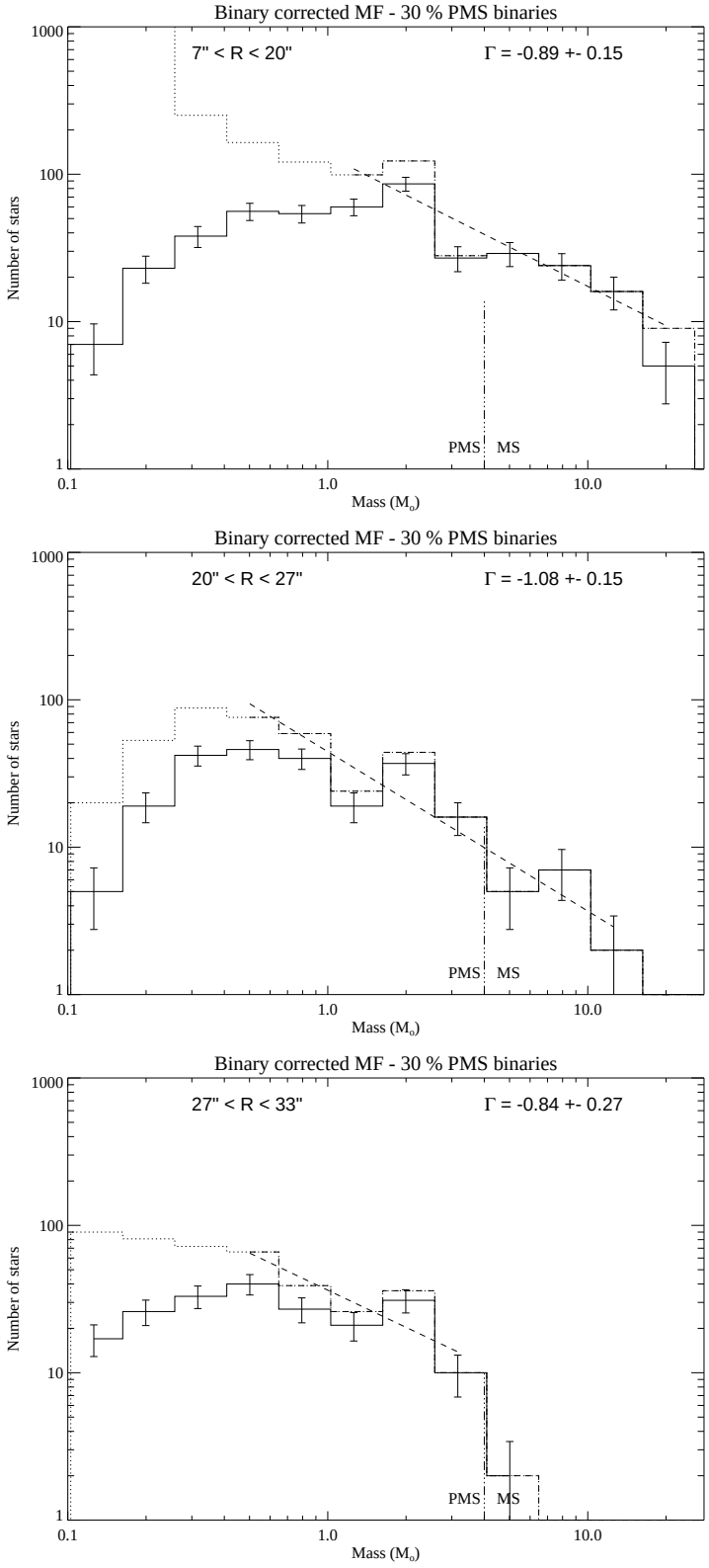

Figure 7.12: Radial variation in the combined mass function.
In the combined MF a reasonable fit could be performed in the two inner annuli up to $16\,M_{\odot}$, while in the outermost annulus only the PMS contributes significantly to the stellar population, such that the fit proceeds only from 0.4 to $4\,M_{\odot}$. Despite the observed decrease in the number of high-mass stars in the outer annuli, no clear steepening in the MF in the form of a steeper slope Γ reflects the depletion of high-mass stars at large radii.

final conclusion on a possible change in the low-mass population can only be drawn for stars more massive than $1\,M_\odot$, where the completeness fraction is more than 50% in all annuli. No tremendous change is observed in the 3 mass bins above this threshold. The 50% limit progresses down to $0.4\,M_\odot$ in the two outer annuli, where no strong variation in the MF is observed between both these annuli. Even when the analysis is extended to radii of $65''$, well outside the distinct cluster center, the field subtracted MF displays the same slope in the PMS regime (see Tab. 7.3). The relative fraction of stars detected down to the lowest mass included in the Palla & Stahler models, $0.1\,M_\odot$, increases noticably in the outermost annulus. A truncation in the mass function of HD 97950 at the low-mass end is not observed. The incompleteness simulation supports this interpretation. Although incompleteness estimates also indicate that no prominent cut-off in low-mass stars is seen in the cluster center itself, a final conclusion as to the lowest mass population below $0.4\,M_\odot$, where the center MF decreases strongly due to crowding losses, needs to await deep, higher resolution observations resolving the low-mass population in the cluster center.

The combined PMS/MS mass functions for each annulus are shown in Fig. 7.12. The slopes of the innermost two annuli agree well within the error. Despite the comparable slope, the truncation and depletion of high-mass stars yields strong evidence for mass segregation in HD 97950. This indicates that the slope alone is not adequate to describe mass segregation processes. In the outermost bin, only stars below $4\,M_\odot$, i.e. pre-main sequence stars, remain present. This picture appears familiar from the Arches cluster. A mass segregated core (as known from the HST analysis mentioned above) and an extended distribution of intermediate- and low-mass stars displaying a relatively normal, only slightly flattened mass function. To study the effects of mass segregation further, cumulative functions will be derived, and dynamical timescales will be estimated for HD 97950.

7.6 Mass segregation in HD 97950 and dynamical timescales

As the slope of the mass function does not vary significantly with radial distance from the cluster center, this measure cannot be used to draw conclusions on mass segregation in HD 97950. Due to the saturation limit at $\sim 20\,M_\odot$, the derived intermediate- and low-mass MF is dominated by the pre-main sequence population. From the mass functions, there is strong evidence that the PMS population covering a mass range of $0.4 < M < 4\,M_\odot$ from the 50% completeness limit to the PMS/MS transition is not segregated. There is no indication of a flattening of the MF at the low-mass end towards the cluster center. Nevertheless, the truncation of high-mass main sequence stars beyond a radius of $27''$ is a clear indication of mass segregation in the *massive* population. Such a behaviour can be expected for primordial mass segregation assuming that high-mass stars form predominantly in the densest cluster region, and may thus have resided close to the cluster center throughout their lifetime. Even if not formed immediately within a radius of $27''$, the migration time will be shortened if the bulk of the massive stars formed close to the center of the potential well.

Although in a cluster as young as ~ 1 Myr a location of massive stars in the cluster center is very suggestive of primordial segregation, Bonnell & Davies (1998) derive a similar stellar distribution from dynamical cluster evolution. For their richest cluster with 1500 stars randomly drawn from a combined Salpeter and Kroupa et al. (1990) MF truncated at $m_{low} = 0.1\,M_\odot$, and a standard number density profile, $n \sim r^{-2}$, 90% of the massive stars migrate into the innermost 0.5 half-mass radii within 10 crossing times, no matter whether the massive stars were originally randomly distributed in the cluster potential or concentrated near the half-mass radius. Independently of the exact segregation timescale, these models thus also yield strong evidence that initial conditions are lost fast. For a detailed comparison between the behaviour observed in HD 97950 and the simulations, allowing possible conclusions on the nature of the mass segregation observed, an estimate on the dynamical timescales in the cluster will be necessary. As we lack not only the measurements of the massive population above $20\,M_\odot$, known from the Arches cluster to contribute significantly to the potential, but also the crucial core of the cluster inside $r_{core} < 7''$, such an estimate requires additional

information from other data of the central and high-mass stellar population.

Before moving on to assemble all the pieces of evidence known from different studies in order to obtain estimates on the dynamical timescales of the starburst cluster, two other means will be investigated to derive more quantitative conclusions on the mass segregation in HD 97950. First, cumulative functions will be created from the mass distribution to avoid the binning dependence inherent to the mass functions, as already introduced in the case of the Arches cluster in Sec. 5.2.4. Secondly, the number ratio of high-mass to low-mass stars is analysed in dependence of the radius.

7.6.1 Cumulative Functions

Cumulative functions are created as described in Sec. 5.2.4. The field-subtracted, colour-selected distribution of stars used to derive the mass functions in the previous section enters the cumulative functions. The assigned masses are the same as in the MFs, derived from individual dereddening. The only difference to the mass distributions in the MFs is that the artificially added companion stars for binary correction are not counted as stars in the CF. These "stars" have not been observed as individual sources, and the correction is - in particular on the PMS - purely statistical. As the only indication for binaries is given by the binary candidate sequence observed in the higher mass population, only equal-mass binaries can be taken into account. Systems with smaller mass ratios cannot be distinguished from single stars. If the binary stars are not biased to a certain mass range, which is not expected from any cluster formation scenario, the mass distribution in binary stars is the same as in single objects. Adding companion stars thus adds to the total mass, but not to the statistical properties of the distribution. The correction for binary masses, however, is crucial, as $\sim 30\%$ of the individual masses are overestimated if the correction is not performed. Thus, the CFs are created from all stars selected as cluster members in the CMD after field-subtraction, with masses corrected for the derived binary fraction of 30%.

The resultant cumulative functions of the central cluster population as well as the radial variations in the CFs are shown in Fig. 7.13. Theoretical CFs corresponding to a single exponent power-law MF are underlaid for exponents of $-0.3 > \Gamma > -1.3$. For the main cluster area, $7'' < R < 33''$, the main sequence stars in the mass range $4 < M < 12\,M_\odot$ follow closely the $\Gamma = -0.7$ line. The irregular shape at higher masses is partially due to random sampling of the upper MF as well as saturation losses for $M > 15\,M_\odot$. Between 3 and $4\,M_\odot$, the irregularity arises in the ambiguity of stellar locations in the CMD and thus masses in the PMS/MS transition region. Independent of the exact transition mass, the pre-main sequence distribution favours a flatter value of $\Gamma \sim -0.5$. In the cluster center ($R < 20''$), the CF tangents the $\Gamma = -0.3$ curve for $M < 2\,M_\odot$, while at larger radii the CF falls towards steeper values of Γ as expected from mass segregation. On the PMS, however, this effect is weak, and the general shape of the CF remains remarkably constant over the entire radial range studied. This is particularly pronounced in Fig. 7.14, where the PMS region below $3\,M_\odot$ can hardly be distinguished in all annuli except for the flatter CF in the cluster center. The situation at the high-mass end is very different. For stars with masses $M > 2\,M_\odot$, the CF bends towards steeper values of $\Gamma \sim -0.7$ to -0.9. The innermost annulus again shows a flatter distribution represented by $\Gamma = -0.5$, increasing outwards. At larger radii, the high-mass end becomes increasingly depleted, evidenced in a steep decline of the CF towards higher masses. However, the most striking feature in the main sequence population is the sharp truncation of the CF at $\sim 2.5\,M_\odot$ for radii $R > 27''$. This cut-off corresponds to the absence of main sequence stars in the mass functions (cf. Fig. 7.12). Beyond $33''$, the irregular CF shape and increase in the scaled frequency of high-mass stars, obvious in Fig. 7.14, marks the onset of field contamination, as at large radii statistics of cluster stars become poorer and realistic field subtraction more difficult than in the dense cluster center where cluster members dominate.

Physically, the sharp truncation in massive stars at larger radii means that massive stars are highly segregated towards the cluster center. In contrast, low-mass stars do show only very weak evidence for mass segregation in the form of a slightly flatter mass distribution in the cluster center. The general

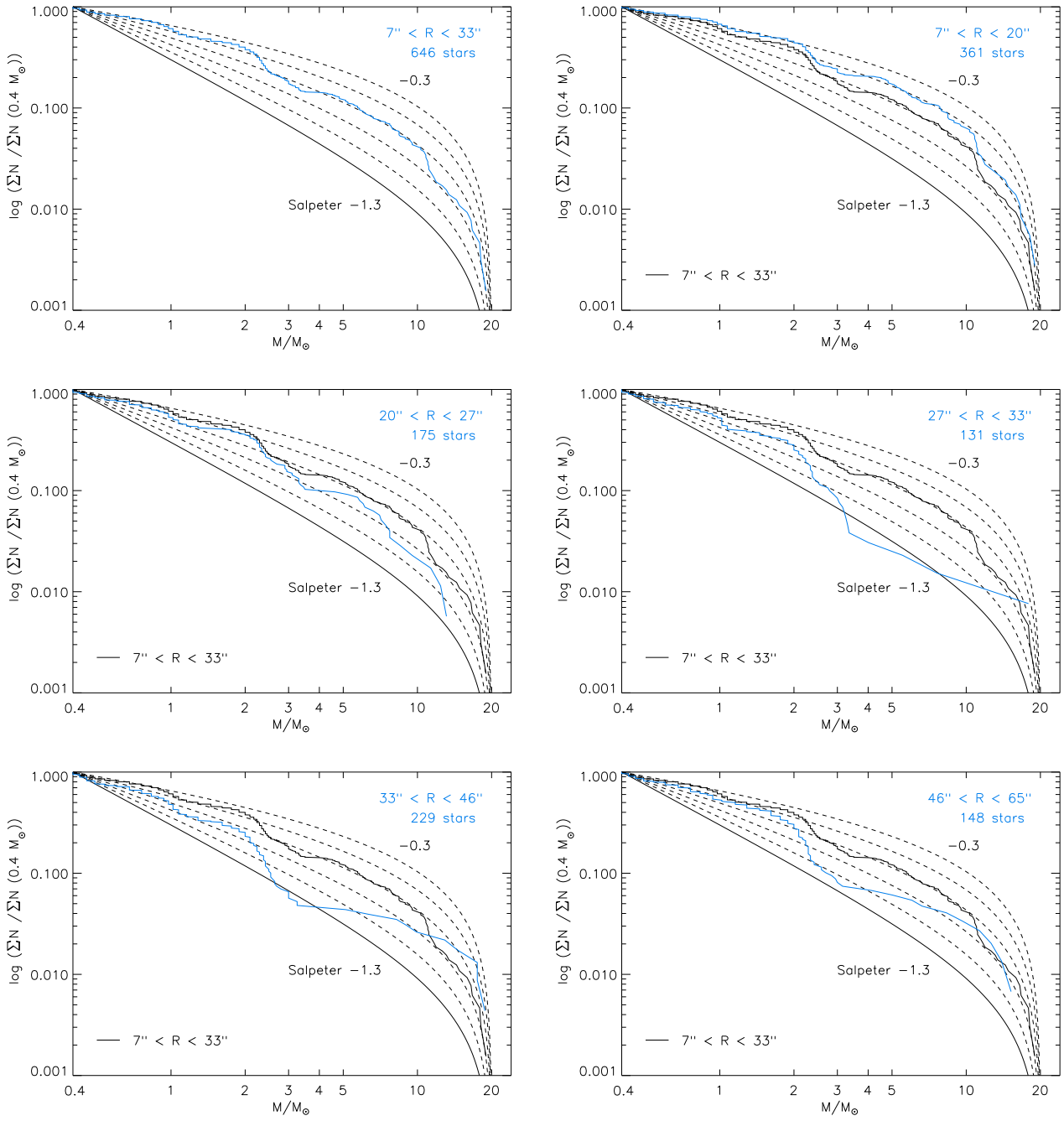

Figure 7.13: Cumulative mass distributions of HD 97950.
The CF for the cluster selection $7'' < R < 33''$ is shown in the upper left panel. Theoretical mass distributions are overlaid (dashed lines) with slopes of $-0.3 > \Gamma > -1.3$ in steps of 0.2, the latter corresponding to the Salpeter slope (solid line). All CFs are normalised to unity at $M = 0.4\,M_{\odot}$, and the absolute number of stars entering each CF is given in the upper right corner. The radial CFs are displayed in the subsequent panels, with annuli indicated in the upper right corner. In each radial CF, the cluster CF from the first panel is also shown for comparison. The two outer annuli extending to $65''$ indicate that the pre-main sequence population ($M < 4\,M_{\odot}$) is not truncated even at large radii, while the main sequence population is strongly concentrated towards the cluster center.

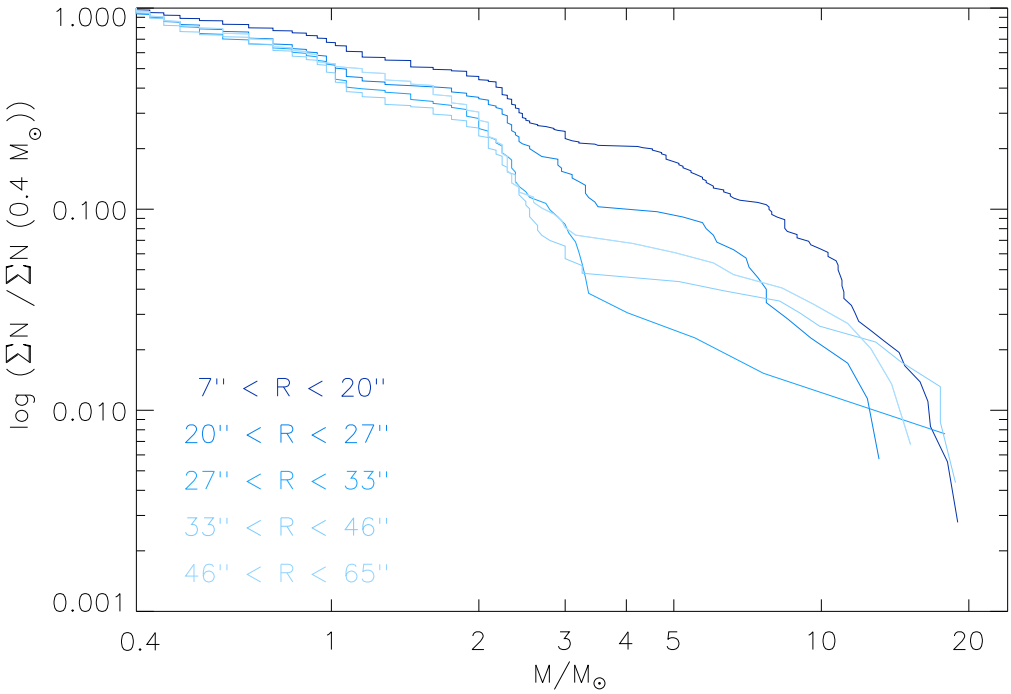

Figure 7.14: Radial cumulative mass distributions of HD 97950.
This comparison between radial CFs of all annuli shows - in contrast to the binning-limited MF - a clear trend towards decreasing values of Γ with increasing radius in the inner three annuli. Beyond $33''$, the increase at the high-mass end is most probably due to incomplete field subtraction. On the low-mass end, however, the mass distribution correponds very well to the cluster pre-main sequence distribution. Indeed, between all 5 annuli, no deviation in the distribution can be detected below $3\,M_{\odot}$ except for a slight flattening in the cluster center (top curve). At masses above $3\,M_{\odot}$, a strong decrease in the relative fraction of high-mass stars is observed, confirming the mass segregation observed in the MFs.

shape, however, remains constant out to radii where almost no main sequence stars remain. This supports the finding of Nürnberger & Petr-Gotzens (2002) of a cluster extent of $R \sim 150''$ beyond the edges of our field of view. This pre-main sequence population can be interpreted as an extended halo of low-mass stars comparable to the halos observed on different spatial scales around the Trapezium in the Orion NGC 2024 cluster (Hillenbrand 1997), and R 136 in the LMC (Moffat et al. 1994).

As in the case of the Arches cluster, there is again an important lesson to learn from these cumulative distributions. Namely, binning effects influence the mass functions significantly, and the assumption of a single exponent power-law distribution is over-simplified. While the MF concept is useful as a tool to compare results from different data sets and regions, yielding a single characteristic value, the assumptions entering such analyses have to be carefully reviewed before conclusions on "universality" or "deviation" from a certain mass distribution are drawn.

7.6.2 Fraction of high- to low-mass stars

The fraction of high-mass main sequence stars to low-mass pre-main sequence stars, $f(high/low) = n(>4\,M_{\odot})/n(<4\,M_{\odot})$, is derived in dependence of distance from the cluster center. The mass derivations for each separate annulus (cf. Fig. 7.14) are used including individual field-star and incompleteness corrections for each radial selection. In addition, the cluster population within $7'' < R < 33''$, yielding better statistics than the outer annuli, is split into $5''$ bins at a step of $2\farcs5$ to allow a more complete radial coverage. The MS/PMS transition mass, $M = 4\,M_{\odot}$, as the natural mass

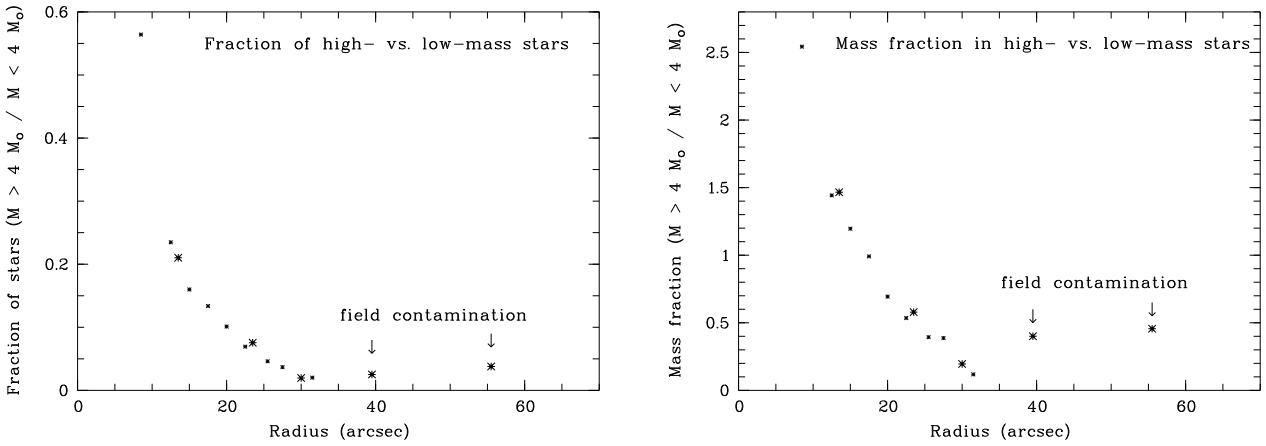

Figure 7.15: Fraction of high- to low-mass stars vs. radius.
The diagram shows the radial change in the number ratio of stars with $M \geq 4\,M_\odot$ to stars with $M < 4\,M_\odot$ (left). Large symbols are derived for the five radial annuli used to study MF variations including individual incompleteness corrections for each annulus, while small symbols are fractions derived from average incompleteness within $7'' < R < 33''$. The MS/PMS transition is chosen as mass limit between the high- and the low-mass population, as these two populations are known to be physically different, such that the ratio simultaneously reveals the radial change in the number of MS vs. PMS stars. The strong decrease in the fraction of high-mass stars reflects the segregation of massive stars towards the cluster center. The right panel shows the radial variation in the mass fraction for the same criteria.

separation in the stellar population of HD 97950 is chosen to distinguish high- and low mass stars. Consequently, the fraction of high- to low-mass stars also reflects the fraction of MS to PMS stars.

A strong decrease in the fraction of massive vs. low-mass stars is seen in Fig. 7.15. While 56 % of the stars in the cluster center, $7'' < R < 10''$, have masses above $4\,M_\odot$, this fraction drops to 10 % already at a radius of $20''$. At a radius of $33''$, the contribution of massive stars is below 2 %. Beyond this radius, field contamination at the bright end slightly skews the ratios again towards higher values. The steep decrease reflects the high-density concentration of massive stars in the cluster center, while at larger radii, $R > 20''$, the cluster is dominated by the extended low-mass population.

An even steeper drop is observed in the *mass fraction* of high- vs. low-mass stars (right panel in Fig. 7.15). While the total mass in high-mass stars exceeds the low-mass contribution by a factor of 2.5 close to the cluster center, meaning that high-mass stars contribute 72 % to the total mass, the ratio of the mass in high- over low-mass stars drops to 0.1 at $R = 33''$, such that high-mass stars contribute only ~ 10 % of the total mass at large radii.

As can be seen in Fig. 7.15, these variations in the number and mass fractions with radius are a very efficient tool to quantify mass segregation effects.

7.6.3 Dynamical Timescales

The dynamical timescale for HD 97950 can be estimated as described in Sec. 5.1.5 for the Arches cluster. Using eq. 5.1 requires estimates of the total mass of the cluster (or, more precisely, the mass confined within the half-mass radius), the number of stars in the cluster, and the half-mass radius. Given the ISAAC data alone, we face a severe limitation when deriving integrated cluster properties due to the lack of data in the cluster center population within $R < 7''$, which is very close to the cluster's core radius of $7\farcs35$ derived by Grebel et al. (in prep). This means that the half-mass radius, r_{hm}, as well as the total mass confined within r_{hm} cannot be deduced from the ISAAC data. As the HST/WFPC2 data are currently the highest resolution data available, yielding a most complete census of the central population, the half-mass radius of $6\farcs3$ derived in Grebel et al. is adopted. At a distance of 6 kpc, this corresponds to a half-mass radius of 0.18 pc. In order to estimate the mass lost

in the cluster center, the mass function within the core radius derived by Grebel et al. is extrapolated down to $0.1\,M_\odot$. The MF inside the cluster core is mainly flat, except for a steeper decline at the high-mass end beyond $M > 50\,M_\odot$. The number of stars in each mass bin is multiplied with the mass of the bin center, assumed to be the average mass in each bin. This procedure overestimates the mass slightly, as the number of stars decreases from low to high masses within each bin. The flat slope observed in the cluster center, however, indicates that the gradient is small. This procedure allows to obtain a crude estimate of the mass confined within the cluster center, sufficient for our purpose to obtain an order-of-magnitude estimate of the relaxation time. A total mass of $M \sim 2500\,M_\odot$ is included in this mass function in the 50% completeness range with $M > 5\,M_\odot$. This number reveals the strong central concentration of the starburst cluster, as the total mass found in the ISAAC data out to a radius of $65''$ or 9 core radii totals to $\sim 2200\,M_\odot$ down to $M > 0.4\,M_\odot$, the ISAAC 50% completeness limit, and only $\sim 1000\,M_\odot$ down to $M > 5\,M_\odot$. The strong concentration of stellar mass, and thus high density, in the cluster center explains the small half-mass radius, lying according to the HST data even within the core radius of 0.22 pc ($d = 6$ kpc). The flat core MF with a slope of $\Gamma = -0.31 \pm 0.11$ in the mass range $5 < M < 50\,M_\odot$ is extrapolated down to $0.1\,M_\odot$, as no indication for a low-mass cut-off is observed in either data set. Due to the very flat slope, this extrapolation adds only $\sim 400\,M_\odot$, yielding a total core mass of $\sim 3000\,M_\odot$.

The ISAAC MF is extrapolated to the low mass end, and the upper mass bin lost to saturation, where exact brightnesses and masses of the stars cannot be derived, is also estimated by linear extrapolation. The mass derived from magnitudes for individual stars in the field-subtracted MFs out to $65''$ sums up to $2300\,M_\odot$. Of these, $1600\,M_\odot$ are found in the inner $33''$. Accounting for incompleteness and binaries as in the MF derivation adds $\sim 340\,M_\odot$ within $7'' < R < 33''$. Extrapolating the observed MF with a slope of $\Gamma = -0.9 \pm 0.1$ to $M = 0.1\,M_\odot$ yields a low-mass contribution of $\sim 1200\,M_\odot$ within $7'' < R < 33''$. This adds up to a total of $\sim 3140\,M_\odot$. In the outer annuli, $33'' < R < 65''$, where the population with respect to binaries is not known in such detail, the MF with $\Gamma = -0.92 \pm 0.1$ is corrected for incompleteness and extrapolated to $0.1\,M_\odot$ yielding $\sim 270\,M_\odot$ in addition to $725\,M_\odot$ measured for individual stars, summing up to $\sim 1000\,M_\odot$. Taken together, the inner and outer mass estimates yield a total mass of $\sim 4140\,M_\odot$.

These estimates combined with the central $7''$ yield a total cluster mass for HD 97950 of $\sim 7000\,M_\odot$. Although the half-mass radius may be slightly larger than estimated from the HST data due to the contribution of the very extended halo of intermediate- and low-mass stars, a remarkable $3000\,M_\odot$ of the stellar mass in the starburst are found in the cluster core. As the core mass is very close to the estimated half mass of the cluster, the core radius of ~ 0.2 pc will be used below to estimate the relaxation time, along with a confined mass of $\sim 3500\,M_\odot$, half the mass determined for the starburst cluster. The characteristic (median) mass in the extrapolated core MF denotes to $1\,M_\odot$, which is in agreement with the value derived by Grebel et al. The number of stars contained within 0.2 pc in the extrapolated MF is only 475, reflecting the strong bias to massive stars in the flat core MF.

Inserting all the numbers, $M = 3500\,M_\odot$ and $m_* = 1\,M_\odot$, $r_{hm} = 0.2$ pc, and $N = 475$ stars, into eq. 5.1 yields a relaxation time of 2.1 Myr, in good agreement with the value derived in Grebel et al. using a slightly different method yielding a total cluster mass of $5000\,M_\odot$ and a value of $N = 5000$. Note that the most relevant parameter in the relaxation time estimate is the half-mass radius. If the total cluster mass is underestimated as a consequence of missing stars in the halo or oversubtracting field stars, which may be the case in this analysis due to the lack of a field estimate at large radii, the half-mass radius will be underestimated. A factor of two larger half-mass radius already yields $t_{rh} \sim 6$ Myr. The dependence on r_{hm} with the 3/2 power supercedes the moderate square-root dependence on the confined mass and the weak influence of the natural logarithm of N. But even with a larger half-mass radius, the relaxation time will hardly be in excess of 10 Myr, such that the evaporation time of the cluster, $t_{evap} \sim 136\,t_{rh}$ is on the order of 1 Gyr at most, and below 300 Myr for $t_{rh} = 2.1$ Myr.

The short relaxation and evaporation timescales of the dense starburst indicate that HD 97950 will

not survive long enough to turn into a globular cluster. Clearly, the cluster is not able to sustain its population over a Hubble time, as achieved by the bound potentials of globular clusters. In this sense, HD 97950 belongs indeed to the population of "open clusters", as it is in the process of dissolution. In comparison to Arches, however, the NGC 3603 region offers a huge advantage for cluster survival. The Galactic tidal forces are negligible at a GC distance of $\sim$ 8 kpc, and will thus not accelerate disruption. Thus, despite the comparable relaxation time derived from internal cluster dynamics, HD 97950 is likely to survive for the estimated evaporation timescale of a few 100 Myr.

If the above statement and estimates are true, the rare occurence of objects comparable in mass and density to HD 97950 indicates that a special environment providing sufficient gas and dust densities is nevertheless required to form starburst clusters such as HD 97950 and Arches.

Chapter 8

From Orion to R 136 - a structural comparison

After having analysed both compact Milky Way starburst clusters in detail, the assembled properties shall be put into the context of massive star forming regions. For this purpose, two well-studied regions at different ends of the mass scale of young, massive star clusters are chosen for a detailed comparison. First, NGC 3603 is compared to the massive 30 Doradus region in the LMC, which exhibits several characteristics in common with NGC 3603. With a total mass of $2 \cdot 10^4\,M_\odot$, the central cluster R 136 in 30 Dor is at the upper mass end of local young star clusters, and at the same time at the low-mass end of Milky Way globular clusters. At the "low-mass" end, the nearby Orion nebula region is chosen as one of the best-studied star forming regions for comparison with NGC 3603 and Arches. While a comparison of 30 Dor and Orion with NGC 3603 is straight-forward, the Arches cluster exhibits drastically different characteristics, complicating the comparison. The differences between the Arches cluster born in the special Galactic Center environment and the other star forming regions will be discussed.

A summary of the basic parameters derived for Arches and HD 97950, as well as literature values for R 136 and Orion is given in Tab. 8.1. Properties of the Antennae starburst clusters and Milky Way globular clusters are included for comparison.

8.1 NGC 3603 and 30 Doradus

8.1.1 A morphological comparison

The NGC 3603 region and its central starburst cluster HD 97950 are frequently compared to the 30 Doradus star-forming complex in the Large Magellanic Cloud, hosting the "super star cluster" R 136. In a detailed comparison between NGC 3603 and R 136, Moffat et al. (1994) entitle NGC 3603 the "Galactic Clone of R136 at the Core of 30 Doradus, but without the Massive Surrounding Cluster Halo". There are, indeed, striking similarities between both regions, which shall be investigated further in the context of the new mass function determinations.

Both clusters are with an age of 1-2 Myr equally young, and contain a massive O-star population in their centers. The main difference between HD 97950 and R 136 is the total mass in stars, with $2 \times 10^4\,M_\odot$ in R 136 (Hunter et al. 1995) a factor of 2-3 larger than the total mass of $7000\,M_\odot$ derived earlier for HD 97950. With the given stellar mass content, R 136 was very productive in forming high-mass stars. As opposed to the three O3-type stars identified by Drissen et al. (1995), Massey & Hunter (1998) classify 65 stars spectroscopically with types earlier than B0, of which 40 stars are of type O3, 4 are WN6 stars, 6 are in the O3/WN6 transition phase to Wolf-Rayet stars, and one O3-O3 binary is found. This adds up to 52 early O stars compared to only 3 such stars identified in HD 97950

Table 8.1: Comparison of young, massive clusters. Basic parameters of the clusters discussed below are collected (see text for details), and the starburst clusters in the merging Antennae galaxies, as well as Milky Way globular clusters are included for comparison.

cluster	M_{total} $M_\odot$	extent pc	r_{core} pc	ρ_{core} $M_\odot\,\mathrm{pc}^{-3}$	age Myr	MF slope Γ	ref
Arches	10^4	1 (?)	0.2	$3 \cdot 10^5$	$2-3$	-0.9 ± 0.15	3, 4
HD 97950	$7 \cdot 10^3$	5	0.2	10^5	$1-3$	-0.9 ± 0.1	4
R 136	$2 \cdot 10^4$	4.7	0.02	$5 \cdot 10^4$	$1-5$	-1.3 ± 0.1	1
Orion	10^3	3	0.2	$4 \cdot 10^4$	$0.3-1$	-1.2 ± 0.1	2
Antennae starbursts	$10^4 - 10^6$	$1-10$	?	10^3	$1-20$	?	5
Milky Way GCs	10^4 - few 10^5	few pc	≈ 1	$10^2 - 10^6$	10 Gyr	-1.3	various

1 - Massey & Hunter (1998); 2 - Hillenbrand & Hartmann (1998); 3 - Figer et al. (1999); 4 - this work; 5 - Whitmore et al. (1999). Average Milky Way globular cluster parameters compiled from various sources.

by Drissen et al. (1995). In the 65 brightest stars with types B0 and earlier spectroscopically analysed by Massey & Hunter, a strong bias to O3 stars is observed. A comparably large number of O3 stars is not known in any other local star-forming region. Clearly, a much larger initial gas mass was required to form such an impressive agglomeration of the most massive stars known. This concentration of O3 stars supports high-mass star formation models requiring enhanced densities and distinct physical processes for the formation of high-mass stars, supporting primordial segregation.

In the case of HD 97950, these most massive stars are concentrated in the cluster center as expected from primordial mass segregation. The situation in R 136, however, is very different. While in HD 97950 more than 90% of the early O-star population ($M > 25\,M_\odot$) is confined to the innermost 0.5 pc, only 50% of the most massive stars are found within 0.6 pc in R 136, while the remainder is spread out to radii as large as 4 pc (Massey & Hunter 1998). Surrounding the core population, a gap between 0.6 and 2.5 pc is found, where only few high-mass stars are observed. Hunter et al. (1995) interprete this as an indication for dynamical segregation in the cluster center, in consistency with cluster evolution models. The existence of massive stars out to large radii, where migration times are longer than in the dense cluster center, strongly suggests that high-mass stars also form in regions with lower density, in contradiction to evidence derived from Orion and NGC 3603 (see below), where no indication of an extended halo containing *massive* stars is found. This leaves us with the open question whether a low metallicity environment as in the LMC allows the formation of high-mass stars at lower initial gas densities well outside the center of the potential well, while the solar metallicity suggested for NGC 3603 requires higher gas densities to form the highest mass stars. One alternative to a metallicity dependence is that the individual molecular cloud cores collapsing into stars in 30 Doradus were more massive and dense than in NGC 3603, as may be expected for a significantly more massive cloud.

Comparable to the morphology observed in HD 97950, R 136 displays a distinct dense cluster core surrounded by a stellar halo. While the spatial extent of the denser cluster center containing the high-mass population in R 136 with a radius of 4.7 pc (Hunter et al. 1995) agrees well with the cluster radius of 4.4 pc derived for HD 97950 by Nürnberger & Petr-Gotzens (2002), the low-mass halo around R 136 is detectable out to a distance of 130 pc from the cluster center, where it merges smoothly into the field population (Moffat et al. 1994). For this extended halo to form and exhibit such a uniform density profile, a large and presumably very massive, extended molecular cloud is required. In contrast to the vast stellar halo, the core radius of R 136 is estimated as small as 0.02 pc from the brightness

surface profile (Hunter et al. 1995), a factor of 10 smaller than the core radius derived for HD 97950 from the density profile (Grebel et al., in prep.). As the core in R 136 could not yet be resolved due to the large distance to the LMC, it can only be speculated that the larger total mass is responsible for a faster relaxation process and the condensed core. Hunter et al. (1995) argue that the dynamical relaxation process is completed in R 136 in the innermost 0.4 pc, with the relaxation timescale for high-mass stars being much smaller than the cluster age within this radius. This situation resembles the derivations for HD 97950 (and Orion, Hillenbrand & Hartmann 1998, see below) in the respect that a short dynamical relaxation time prohibits to distinguish primordial and dynamical segregation. In the extended halo surrounding R 136, however, the relaxation timescale is much larger due to the lower density and larger distance from the cluster center, such that stars formed in the outer regions of the cluster are not significantly segregated, but still found essentially at their birth positions. This implies that even the formation of the highest mass stars is *not* confined to the densest cluster region. The original extent and mass already suggested from the large low-mass halo surrounding R 136 might have facilitated the fragmentation of clumps with an initial mass and density sufficient to form O3 stars, while the moderate size of clouds in the Milky Way may prohibit such a scenario. In a moderate cloud such as NGC 3603, the formation of massive stars may indeed be confined to the dense cluster center.

The central 4.7 pc of R 136 exhibit a normal mass function with a slope of $\Gamma = -1.3 \pm 0.1$ in the mass range $2.8 < M < 120\,M_\odot$. The massive end, $20 < M < 120\,M_\odot$, of this MF is obtained from spectroscopy of the high-mass population (Massey & Hunter 1998). In the MF derivation, the $120\,M_\odot$ upper mass limit is imposed from the truncation of stellar evolution models. From luminosity and - where available - spectroscopy of the brightest, highest-mass stars, Massey & Hunter derive initial masses of up to $150\,M_\odot$. Given the total mass of the cluster, this is in agreement with an untruncated normal mass function up to the highest masses.

Hunter (1996) studies the radial variation in the MF slope in the mass range $2.8 < M < 15\,M_\odot$ in four annuli with $0.11 < R < 1.1$ pc. From inner to outer annuli, values of -1.0 ± 0.4, -0.7 ± 0.4, -1.1 ± 0.3 and -1.1 ± 0.2[1], respectively, are derived, showing no variation with radius within the uncertainties. The same behaviour was derived in the case of HD 97950. If the small core radius of 0.02 pc derived by the same authors is correct, these data sets only resolve the cluster beyond 5 core radii. Mass segregation is observed in HD 97950 only inside the core radius of 0.2 pc. Even if the estimate for the core radius of R 136 is wrong by a factor of ten, a larger core would only barely be resolved even with the HST/WFPC2 data analysed in Hunter et al. (1995). The extrapolated core density of R 136 is a factor of 3 higher than in HD 97950 (Moffat et al. 1994), and the integrated spectrum suggests a large number of O- and WR-type stars to be missed in the core of R 136 (Massey & Hunter 1998). A mass segregated core can thus not be ruled out in R 136. The mass function slope of $\Gamma = -1.0 \pm 0.2$ ($2.8 < M < 15\,M_\odot$) observed in the outer annuli agrees extremely well with the slope of $\Gamma = -0.9 \pm 0.1$ ($0.4 < M < 20\,M_\odot$), both subject to the same saturation limitation at the massive end.

Although the spatial distribution of high-mass stars differs drastically from the morphology observed in HD 97950, the slope of the mass function is almost identical. As already discussed in context of the radial variation and mass segregation in HD 97950, this adds to the warning that the slope of the MF alone is not sufficient to understand mass segregation and in particular the star formation history in a certain region, and care has to be taken when different star-forming environments are compared using these simplified numbers only.

8.1.2 The nature of the massive stars

From a detailed analysis of the spectra, strong indication is given that the stars classified as WN6 Wolf-Rayet stars are in fact not evolved objects, but still in their hydrogen burning phase. The

[1] cf. Massey & Hunter (1998) for corrections in the values given in Hunter (1996)

observed emission lines are interpreted by Massey & Hunter (1998) as well as by Drissen et al. (1995) as arising from a strong stellar wind. It is particularly intriguing that these stars are a factor of ten more luminous than expected for WN6 stars. This leads the above authors to suggest masses in excess of 120 $M_\odot$, the mass of an O3 star, implying that stars earlier than type O3 are found in both clusters.

8.1.3 Age spread

In the low-mass population of R 136, an age spread is observed. A main sequence as well as a pre-main sequence population of stars with masses $M < 5\,M_\odot$ coexists in the cluster, suggesting ages of 1-5 Myr for the low-mass stars. After the ignition of the high-mass stars 1-2 Myr ago, the formation of low-mass stars is terminated. This scenario supports cluster formation models suggesting the high-mass stars to form last. Although such an age spread is not readily detected in the CMD of HD 97950, the main sequence population is observed to extent beyond the 1 Myr PMS turn-off (cf. Fig. 6.4). This population is assumed to be the young population affiliated with NGC 3603 outside of the central cluster, and thus was ignored in the analysis. These stars may well belong to the low-mass halo around HD 97950, depicting a star formation history comparable to R 136. In contrast to R 136, however, the existence of PMS stars with ages younger than the high-mass population cannot be excluded before the spread observed in the PMS/MS transition region is fully understood.

If the scatter on the PMS is explained by the existence of a pronounced binary population as suggested from comparison with stellar evolution models, no PMS age spread is required to understand the observed colour-magnitude distribution in HD 97950. In this case, low-mass star formation might have halted with the ignition of the highest mass stars. Such a scenario is particularly likely if the massive stars with WR properties are main sequence stars in their hydrogen core burning phase, and thus younger than evolved WR stars. An age for this highest-mass population of 1 Myr would be in very good agreement with the age of the MS/PMS transition suggested from evolutionary models. An age spread in the starburst cluster HD 97950 is thus not very likely. The surrounding NGC 3603 region, however, clearly displays star formation events of various ages.

8.2 Arches, NGC 3603 and Orion

One of the best studied star-forming regions in the Milky Way is the Orion molecular cloud (M 42). At a distance of only 450 pc, the Orion nebula is sufficiently close to resolve the embedded population down to the substellar regime (Muench et al. 2002). The extended molecular cloud hosts the young Orion nuclear cluster (ONC) containing stars with ages between 0.3 and 1 Myr in its center. The Trapezium system, a dense cluster of massive stars, forms the core of the ONC. It is particularly interesting for the comparison with NGC 3603 and Arches that the ONC was the first young cluster where mass segregation was observed (Hillenbrand 1997).

The ONC contains $\sim 2000\,M_\odot$ within a radius of 2 pc. In the same radius, the analysis in the preceeding chapter yields a total mass of $7000\,M_\odot$ in HD 97950, when the MF is extrapolated to $0.1\,M_\odot$. The core radius derived from King model fitting is in both clusters 0.2 pc (Hillenbrand & Hartmann 1998, Grebel et al., in prep.). The central *stellar* density inside the core is also very comparable, with $\rho_c = 1.7{\cdot}10^4$ stars/pc^3 in the Trapezium core and $\rho_c = 1.4{\cdot}10^4$ stars/pc^3 in HD 97950. There is, however, one significant difference between both clusters - the central *mass* density is with $\rho_c = 3/4\pi\ 3000\,M_\odot/(0.2\mathrm{pc})^3 \sim 10^5\,M_\odot/\mathrm{pc}^3$ from the parameters derived above for HD 97950 about one order of magnitude higher than the $2 \cdot 10^4\,M_\odot/\mathrm{pc}^3$ in the Trapezium. Given the large number of at least 40 O-stars in HD 97950 (Drissen et al. 1995), versus a mere ~ 10 OB stars in the ONC, the difference in mass density is not surprising. HD 97950 contains the entire mass found in the ONC *only* within its core.

Nevertheless, there are a number of similarities between both clusters suggesting a comparison. Hillenbrand & Hartmann (1998, HH98) performed a detailed dynamical analysis of the ONC and

its core, the Trapezium, and the mass segregation first studied by Hillenbrand (1997). From the central stellar density, the number of stars in the core, the mean density and the measured velocity dispersion of 2.5 km/s, HH98 derive a relaxation time of 6.5 Myr, slightly longer but comparable to t_{rh} in HD 97950. This timescale is longer than the maximum age of ~ 1 Myr, suggesting that some amount of primordial segregation had to be present. The same authors also note that if only the massive core with $\sim 400\,M_\odot$ is taken into account, the higher mean mass and stellar density causes a decrease to $t_{rh} \sim 0.6$ Myr, comparable to the age of the young cluster population. This means that in the Trapezium, too, observational evidence for primordial segregation is weak, as the massive stars may have migrated to the cluster center within the lifetime of the cluster.

Hillenbrand & Hartmann argue, however, that the estimate of the relaxation time from a mean density and characteristic mass in a smooth potential as given in Binney & Tremaine (1987) may be oversimplified. As the outer ONC population is younger than one crossing time of the cluster, and the massive stars show a very strong central concentration, these authors conclude that some amount of primordial segregation in the Trapezium is very likely, implying that the massive stars indeed require a certain gas and/or stellar density to form. This supports formation scenarios with enhanced accretion rates such as the models by Behrend & Maeder (2001) and Bonnell et al. (2001), requiring high densities of molecular material for high-mass stars to form. Bonnell & Davies (1998) perform detailed N-body simulations of ONC-type clusters, and find that the mean mass in the core as well as the ratio of high- to low-mass stars can only be recovered if the massive stars are initially placed close to the core. As the mass confined within the core radius of HD 97950 is even larger, and the masses of the stars are much more extreme than in the case of the ONC, some amount of primordial segregation is expected in HD 97950 as well from these models.

Even if a clear answer on the nature of the mass segregation observed cannot be given, the behaviour of the segregated stars is surprisingly similar. HH98 derive cumulative functions with radius for several mass bins. These CFs show a different shape for massive stars with $M > 5\,M_\odot$, while the three mass bins between 0.3 and $5\,M_\odot$ investigated all show a remarkably identical behaviour. In the cluster core ($R < 0.5$ pc), however, all four mass intervalls follow each other closely, indicating strong segregation in the core, producing a bias to massive stars with respect to the low-mass population. The similarity over the wide range in masses suggests a flat MF exclusively in the core of the ONC.

This behaviour is very similar to the radial variations in the MF and CF observed in HD 97950 as well as in Arches. Both starburst clusters show a strong concentration of stars towards the cluster core, while the low-mass population in different annuli decreases essentially with the density profile, not displaying segregation effects. Consequently, the flat MF slope observed in both starbursts dominates the cluster center, while at radii larger than the core radius the MF rapidly turns towards a standard MF. At larger radii, mass segregation in the ONC is observed down to $1 - 2\,M_\odot$, but not below these masses. This is very comparable to HD 97950, where the cumulative functions of the PMS population up to masses of $\sim 3\,M_\odot$ are indistinguishable at different annuli, while for larger masses strong changes are observed.

The mass function in the Trapezium system has been investigated by Muench et al. (2002). A slope of $\Gamma = -1.2 \pm 0.2$ is found for $M > 0.6\,M_\odot$, including source reddening and field correction. In HD 97950, $\Gamma = -0.9 \pm 0.1$ is determined from the ISAAC data. Although these slopes barely agree within the errors, the low fitting uncertainties probably underestimate the true slope uncertainty, as no photometric or age and distance uncertainties are taken into account. Thus, there may be a weak indication of a flattened mass distribution in HD 97950, while the MF in the Trapezium follows a standard Salpeter law.

Given the slight difference in the mass function slopes in these different clusters as well as the small radial changes in the MF slope, it becomes clear that the slope alone is not sufficient as a tool to study mass segregation. The truncation of the MF at the high-mass end also needs to be taken into account. On the other hand, cumulative distributions provide a better handle on variations in the underlying mass distribution, allowing to distinguish the variation in the shape of the distribution

without dependence on binning and the power-law assumption implicit in the determination of the (power-law) slope Γ.

In conclusion, the radial variation in the mass distribution observed in HD 97950 and the Trapezium is comparable despite the fact that the starburst cluster hosts 40 massive O-stars as opposed to only 3 O-stars in the Trapezium system. Note that this scaling is very similar to the scaling in the number of O3 stars between R 136 and HD 97950. Over the three mass scales covered by these clusters, a remarkable similarity is observed in the morphology of the cluster centers.

A similar radial variation is also observed in the Galactic Center Arches cluster. This cluster, too, displays a core heavily biased to high masses, reflected in a flat core MF as seen in the core MF of HD 97950 derived from HST data (Grebel et al., in prep.). Beyond the core radius of 0.2 pc, again comparable to the core radii in both HD 97050 and the Trapezium, the MF slope steepens rapidly to standard values. However, a sharp truncation in the mass function is observed below $10\,M_{\odot}$, indicating - in stark contrast to the low-mass halo observed around the other clusters - a strong lack in low-mass stars.

Despite the severely mass segregated core, the mass function obtained for a sample covering the densest cluster regions within a radius of ~ 1 pc in both Arches and HD 97950 displays a relatively normal slope of $\Gamma = -0.9 \pm 0.1$. Although this value is significantly flatter than the Salpeter slope of $\Gamma = -1.35$, it is only slightly flattened with respect to the average slope of $\Gamma = -1.1 \pm 0.3$ observed in young star-forming regions in the Milky Way by Massey et al. (1995a). Although the flattening observed in the integrated cluster MF is weak, the agreement between the two slopes derived is remarkable given the entirely different procedures used to transform magnitudes into masses. The Arches MF was derived after correcting for the general increase in reddening observed with distance from the Arches cluster center, but without accounting for field stars due to the small field of view just covering the cluster center itself. The MF in HD 97950 included field subtraction obtained from the edges of the large combined ISAAC mosaic, and the colour scatter in the CMD suggested strong extinction variations, such that individual dereddening was applied before magnitudes were transformed into masses. In addition, the main contribution to the stellar population in HD 97950 comes from pre-main sequence stars with masses below $4\,M_{\odot}$, such that PMS and MS had to be combined to yield the integrated MF, while in the slightly older Arches cluster no PMS contribution is observed down to the 75% completeness limit of $\sim 2.5\,M_{\odot}$. As a consequence of the larger distance and significantly increased extinction along the line of sight to the Galactic Center as compared to the Carina spiral arm, both MFs cover a distinct mass range. In Arches, the mass range probed with NAOS/CONICA covers $2.5 < M < 65\,M_{\odot}$, while the low extinction in HD 97950 allows to penetrate down to $0.4\,M_{\odot}$, but saturation limits the upper MF to $M < 20\,M_{\odot}$. Furthermore, the Arches MF can only be fitted with a single power law down to $10\,M_{\odot}$, beyond which the MF drastically flattens, such that the overlap region between both derived MF slopes covers essentially one logarithmic mass bin. Despite these differences, the slopes observed in both clusters agree extremely well. Although in the case of starburst clusters in the Milky Way we are limited two a very small survey, the agreement between these two slopes indicates a slightly flattened mass function in the central regions of Milky Way starburst clusters.

Can we extent this conclusion to the *initial* mass function in the starburst clusters?
In order to understand the nature of the mass segregation, both clusters were compared with cluster formation models. These models suggest very short relaxation timescales for compact, massive clusters, and in particular migration times to the cluster center of only a few crossing times for the high-mass stars. In the same short timescale, low-mass stars will be ejected from the cluster center during the relaxation process, forming a low-mass halo around the central cluster core. This picture fits the observed morphology in both starburst clusters. However, if high-mass stars can only form in the region with the strongest gravitational potential accumulating the largest amount of molecular material at the highest density, while low-mass stars form throughout the gas concentration condensing into the cluster, such a morphology would also naturally arise from the primordial formation loci of

stars with low and high masses. Consequently, the integrated mass function over the entire cluster field represents the *initial* mass distribution most closely. Due to our limited field of view and the handicap imposed at the low-mass end by the increasing extinction with distance from both cluster centers, a "complete" MF is hard to deduce. Given these obstacles, a final word on the *initial* mass function cannot be said. The very young cluster age of only 1-2 Myr along with the prominent concentration of stars towards the cluster center in both objects is in any case very suggestive of an enhanced formation of massive stars in the cluster cores due to primordial mass segregation.

There is another interesting aspect not as evident in this scenario. If a certain density is required to form the high-mass stars observed predominantly in the cluster center, i.e. with masses above $\sim 10\,M_{\odot}$, implying that enhanced accretion as suggested by Behrend & Maeder (2001) and Bonnell et al. (2001) and possibly stellar interactions as suggested by Bonnell et al. (1998) are required to form stars above a certain mass threshold, the presence of a statistically relevant sample of O- and early B-type stars may be sufficient to flatten the MF. While the outer annuli are dominated by the intermediate- and low-mass population formed in the standard gravitational collapse and subsequent disk-accretion model (Adams, Lada, & Shu 1987), this population should display the normal MF produced as a consequence of the fragmentation process involved. Such a scenario can be depicted in a toy model where a sphere of enhanced density is inserted into the center of a molecular clump, which is just at the verge of fragmentation. Subsequently, the outer parts of the cloud will collapse into individual stars without feeling the central density peak. In the center of the cloud, however, the enhanced density allows processes such as competitive and enhanced accretion, and stellar collisions to form a high-mass core. In reality, the core will not be a distinct entity, but the cloud will show a steep density gradient towards the core.

The density profile for a singular isothermal sphere undergoing cloud collapse follows $\rho \sim r^{-2}$ (see, e.g., Adams, Lada, & Shu 1987 for a discussion). Massive cloud cores in the Orion region display a slightly flatter profile with $\rho \sim r^{-1.6}$, with a tendency that more massive cores have steeper profiles than low-mass cores (Caselli & Myers 1995), indicating an increase in the central density with increasing proto-cluster clump mass. There is at least one example of a molecular cloud at the verge of cluster formation displaying characteristics as suggested in the above scenario. Cesaroni et al. (2003) study the young proto-cluster in the G24.78+0.08 molecular cloud, where massive young stellar objects are just condensed in the dense cloud core. The extent of the proto-stellar cluster is with 1 pc radius comparable to the extent of the dense cluster centers of Arches and HD 97950. The dense core, where the massive YSOs are found, has a linear size of only 0.2 pc. Such a native state will naturally evolve into a segregated cluster with a core-halo morphology exactly as observed in HD 97950, and, on a higher mass scale, also in Arches.

8.3 Stellar mass distributions on four scales

The comparison between R 136, HD 97950, Arches and Orion spans a range in total stellar masses from $2 \cdot 10^4\,M_{\odot}$ via a few 1000 to $\sim 1000\,M_{\odot}$. Over this range in masses, the morphology of these star clusters with comparably young ages between 0.3 to 2 Myr is remarkably similar. Except for Arches, all clusters exhibit a compact, mass segregated core surrounded by an extended halo of low- to intermediate-mass stars. The Arches cluster also displays a highly mass segregated core, but the surrounding halo is dominated by stars with mass in excess of $10\,M_{\odot}$. The mass segregation is - except inside the core - not evidenced in a flat mass function, but in the truncation of the high-mass end of the MF. The cut-off mass of the MF decreases with increasing distance from the cluster center.

The dynamical timescales in all four clusters are comparable to the cluster age, with the dynamical timescale in the core being even shorter. This suggests that the cluster core is dynamically segregated. The absence of a large number of massive stars at larger radii (as compared to the core), where migration timescales are longer, in HD 97950 and Arches suggests that a significant amount of primordial segregation was also present. A similar conclusion is drawn by Hillenbrand & Hartmann (1998) for

the Orion nuclear cluster.

Two main conclusions can be drawn from this comparison. First of all, while the mass function slope is consistent in all regions given the inherent uncertainties, with a slight tendency of a flattened MF in the starburst clusters Arches and HD 97950, the truncation in the MF can be drastically different. While no low-mass cut-off is observed in HD 97950, R 136 and Orion, the MF in Arches flattens below $10\,M_{\odot}$, indicating a lack of low- and intermediate-mass stars. The high-mass end of the mass function, however, increases in all discussed star-forming regions with a power-law consistent with the dependence of the highest stellar mass on the total mass of the cluster as found by Larson (1982). While random sampling of the high-mass tail may steepen the MF slightly towards the highest mass bin, no evicence for a high-mass cut-off depending on the star-forming environment is observed.

Radial variations in the MF also display no significant change in the MF slope except inside the core radius, while the high-mass end is more and more depleted with increasing radius. Thus, the mass function slope alone, widely used to compare star forming regions as well as variations within individual sites of star formation, does not satisfactorily depict the stellar mass distribution, in particular with respect to mass segregation. Secondly, the estimates of the dynamical timescales in all of the discussed star clusters are small close to the cluster center. While primordial mass segregation is a likely requirement to form stars in excess of $M > 20\,M_{\odot}$, some amount of dynamical segregation has probably condensed the stellar population in the cluster center even further.

From the comparison presented above, the dominant environmental influence is observed in the form of a truncated low-mass MF in the Arches cluster. In the extreme conditions in the Galactic Center region, tidal forces may either strip off the low-mass population very rapidly, or some selective mechanism prohibits the formation of low-mass stars in a dense environment. In the latter case, the lack of low-mass stars has to be taken into account in stellar population synthesis models of galactic nuclei. The slope of the mass function in the different fitted mass ranges, however, is once more observed to be remarkably invariant.

Chapter 9

Summary and Outlook

The two young, massive and compact starburst clusters Arches and NGC 3603 have been analysed with respect to the stellar mass distribution and radial variations of the mass function. Mass segregation observed in both cluster cores is discussed and compared with the well-studied Orion and 30 Doradus regions, as well as with star- and cluster formation models.

In the course of the Arches analysis, the available adaptive optics data sets from the Gemini/Hokupa'a and VLT/NAOS-CONICA AO systems are technically analysed and compared in detail to HST/NICMOS2 observations. This study allowed a deep understanding of the advantages and limitations of AO data, undispensable for the scientific interpretation. The comparison with HST reveals the capabilities given by recently developed AO systems, while at the same time the limitations and complications due to the complexity of the AO technique are shown.

The distance of 8 kpc and foreground extinction of $A_V \sim 30$ mag towards the Galactic Center region were the limiting factor in all studies of the Arches cluster. The most stringent constraint when resolving the stellar population arising from the large distance and compactness of Arches is the high stellar density in the cluster center causing severe crowding effects. As a consequence, even the high spatial resolution of $0\farcs18$ of the Gemini and HST data resolved the bright central population only down to 20 mag in K or $\sim 10\,M_\odot$ in the dense center of the Arches cluster. The near-diffraction limited resolution of 69 mas in the NAOS/CONICA observations allowed to resolve the cluster center population down to $K = 21$ mag or masses below $3\,M_\odot$. In addition to the larger photometric depth and lower mass limit, with these high-resolution data the bright, dense cluster center population is resolved for the first time.

The central cluster of NGC 3603 was observed with VLT/ISAAC under excellent seeing conditions delivering seeing-limited, high-resolution images with a resolution of less than $0\farcs4$. These data allow to penetrate as close as $7''$ into the cluster center. The deep ISAAC photometry covered a dynamic range of $11.4 < K < 20$ mag corresponding to a mass range of $0.4 < M < 20\,M_\odot$ at a distance of 6 kpc and foreground extinction of $A_V = 4.5$ mag. VLT/ISAAC L-band data supplemented the JHK photometry and served as tracers for disk fractions in the NGC 3603 central cluster HD 97950 and its immediate vicinity. In addition, narrow-band Hα HST/WFPC2 data were analysed with respect to enhanced Hα emission indicative of accretion processes and circumstellar material.

From the near-infrared colour-magnitude diagrams, present-day mass functions of both clusters were derived, and the variation of the mass function slope with distance form the cluster center was studied. Mass segregation effects were revealed from these mass functions as well as from cumulative distributions. Cumulative functions were shown to be particularly well suited to detect segregation effects, while the slope of the mass function, Γ, is insufficient as an indicator for mass segregation.

In the following sections, the results of these studies are summarised. An overview of the main findings in the technical analysis of the AO data is given in Sec. 9.1. The scientific interpretation of both the Arches and NGC 3603 data, as well as implications for star formation in starburst clusters, is summarised in Sec. 9.2.

9.1 Technical analysis of AO data in a crowded stellar field

Adaptive optics data allow near-diffraction limited observations, thus exploiting the light-collecting power and diffraction-limited resolution of large telescopes such as the Gemini and VLT 8m mirrors.

The adaptive optics correction is a complex physical process that results in images not as straight forward to understand and interprete as seeing-limited photometry. Due to the partial correction achievable with standard AO systems, the diffraction-limited core is accompanied by an extended seeing-limited halo. The flux in this halo depends on the quality of the AO correction, i.e. the Strehl ratio. It is shown in the technical analysis that in the low-Strehl (5%) case of the Hokupa'a data, this seeing halo severely hinders the detection of faint neighbours near bright sources. This means that in a crowded stellar field a large fraction of the low-mass population is lost. Moreover, these seeing-halos impose a strongly varying background to the image, complicating the extraction of exact photometry, causing a large scatter in the resultant colour-magnitude distribution. The comparison with HST/NICMOS data shows that the photometric uncertainty significantly increases with increasing stellar density towards the cluster center. In comparison to HST/NICMOS, only 50% of the stars detected at the diffraction-limited resolution of $0\farcs18$ (H-band) of the HST 2.4 m mirror are resolved with Gemini/Hokupa'a given the same spatial resolution. The loss of faint stars is a consequence of the enhanced background due to the imperfect AO correction. As a consequence, the luminosity function is incomplete at the faint end, thus not exhibiting the sharp cut-off expected at the detection limit, but a smooth turn-over at significantly brighter magnitudes. Thus, care has to be taken when interpreting luminosity functions derived from low-Strehl AO data.

The moderate-Strehl (20%) NAOS/CONICA data, on the other hand, show remarkably small intrinsic scatter in the main sequence of the Arches cluster. The NACO resolution of 82 mas in both H and K exceeds the resolution of the NICMOS2 camera by a factor of 2.2 in H and 2.5 in K. The photometric depth is limited by the high infrared sky background from the Earth's atmosphere in ground-based observations, such that a factor of 4 longer integration time is required with NACO as compared to HST to achieve the same photometric depth in H. In K, where the sensitivity of the NACO system is optimised, deeper photometry can be obtained within a factor of 2 longer integration time with respect to NICMOS2, yielding a detection limit exceeding the NICMOS photometry by 1 mag. The NACO data resolve faint companions more efficiently than NICMOS due to the higher spatial resolution of the 8m mirror, which yields a more complete census of the stars in particular in the cluster center. The NACO observations comprise the most completely resolved census of stars in the Arches cluster center along with the deepest photometry.

In summary, adaptive optics observations are a very powerful tool to extend ground-based observations to the diffraction-limited resolution of 8m class telescopes by circumventing the turbulence broadening imposed by the Earth's atmosphere in seeing-limited observations. At the same time, the light collecting power of large telescopes is exploited more efficiently by concentrating the flux into a narrow peak. Even moderate Strehl ratios below 20% yield excellent photometry and spatial resolution from the ground. The remaining limitation is given by the complex, spatially varying PSF shape, complicating the analysis in particular in low-Strehl observations, and the unpredictable nature of the atmospheric turbulence and thus AO performance.

9.2 Scientific Results

9.2.1 Colour-magnitude and Colour-colour diagrams

The analysis of the Arches cluster field revealed a strong radial increase in extinction with distance from the cluster center corresponding to $\Delta A_V = 10$ mag from 0.2 to 0.8 pc radius. A cavity of constant, low extinction is observed in the inner 0.2 pc of the cluster center, indicating the expulsion of remnant material by the massive O-star winds or/and photoevaporation. A similar, albeit lower increase in

extinction of $\Delta A_V \sim 4$ mag is observed in the center of HD 97950 when moving radially outwards from 0.2 to 1 pc, beyond which extinction variations become very irregular due to the influence of nebular emission from the HII region. This extinction variation turned out to be non-negligible in the mass function derivation of both clusters and had thus to be corrected.

In the case of the Arches cluster, a linear fit of the colour variation vs. radius allowed to describe the extinction variation. The colours and magnitudes of the stars were then corrected according to their radial distance from the cluster center. Additional scatter in the CMD was consistent with the photometric uncertainty in the data, suggesting that individual reddening and infrared excesses are negligible for the mass function derivation in this case. After correction for the trend in extinction, the colour-magnitude diagram of the Arches cluster exhibits a very confined main sequence population, that merges into the bulge background population beyond $K \sim 16$ mag. The bulge background imposed a severe limitation to the analysis below $10\,M_\odot$ as no field data were available. At magnitudes slightly brighter than $K = 16$ mag, shortly before the bulge population becomes the dominant feature in the CMD, the Arches population thins out. Although the observed gap is weak, this gap may indicate the main sequence turn-on point of the young cluster.

In contrast to the confined Arches main sequence, the colour-magnitude and colour-colour diagrams of HD 97950 display a wide variety of features. A pronounced pre-main sequence population dominates the CMD, followed by a horizontal transition region at the hydrogen-burning turn-on point. The main sequence/pre-main sequence transition covers a range of 2.5 to $4\,M_\odot$ according to 1 Myr pre-main sequence evolutionary models. A distinct population offset of ~ 0.7 mag above the transition region and the main sequence is interpreted as a binary (candidate) sequence. On optical HST/WFPC2 image, 20% of the binary candidates are resolved into individual stars, consistent with the wide end ($a > 360$ AU) of the binary separation distribution as observed in nearby star-forming regions, supporting the binary hypothesis. This identification explains the wide scatter in magnitude observed in the PMS/MS transition, which was interpreted as a possible age spread in HD 97950 before. With this identification, no evidence for an age spread in the starburst cluster is found.

The pre-main sequence as well as the main sequence both exhibit a large scatter in $J - K$ colour. This scatter is most likely caused by individual reddening, as also indicated by strong reddening features in the colour-colour diagram. In particular on the main sequence, a bend towards bluer colours and thus lower extinction is observed when progressing from fainter to brighter magnitudes. This reflects the decrease in extinction towards the cluster center, where most of the brightest stars reside. As the spatial variation of the extinction is much more irregular, this trend could not be fitted in a simple manner as in the Arches cluster. In particular, spatial variations and intrinsic reddening cannot be distinguished easily. To account for these effects, individual dereddening of each star to the locus of the isochrone was applied in the mass function derivation.

$JHKL$ colour-colour diagrams allowed to derive disk fractions from L-band excess ratios. A slight radial increase in the disk fraction from 20% close to the cluster center to 33% and 41% in subsequent annuli is observed with increasing distance from the cluster center. This trend is expected from photoevaporation of circumstellar material by the strong UV radiation field from the central O-stars. The uncertainties are, however, large due to the low number of excess stars detected in L. Independent of the observed trend, the derived total excess fraction of 27% in the central $33''$ is very low for a 1 Myr young population. For comparison, the Trapezium population with comparable age displays a disk fraction as high as 80%. Disk fractions between 50 and 80% are also found in other young star forming regions. This yields strong evidence for disk depletion in starburst clusters. If disk survival has a shorter timescale in starbursts than in less compact and massive star-forming regions such as the Orion region, the formation of plantes may also be quenched. Then, if the formation of compact clusters proceeded in a similar fashion throughout the age of the Universe, implying that the massive globular clusters also formed in this mode of star formation, it is not surprising that planets are not detected in globular clusters.

In addition to the L-band excess objects found, several stars are identified as Hα emission sources

from narrow-band HST data. These sources, surprisingly confined to the inner 20″ of the cluster center, are most likely Herbig Ae/Be stars when found in the PMS/MS transition stage, and classical T Tauri stars when located redwards of the pre-main sequence in the CMD. While the correlation of 50% of the Hα sources with L-band excess stars supports the disk hypothesis for both enhanced emission characteristics, the anti-correlation between Hα emission and binary candidates underpins the binary identification. This is consistent with observations and theories suggesting the disks around binary stars to be less stable due to tidal disruption than the disks around single objects. The close proximity of Hα emission stars to the cluster center suggests that either *massive* disks are capable to survive photo-evaporation by the internse UV radiation field originating from the ≥ 40 O-stars for the 1 Myr lifetime of the cluster, or that these stars have migrated into the cluster center only recently, and therefore still harbour circumstellar material.

9.3 Mass Functions and Mass Segregation

Mass functions are derived for Arches and the central NGC 3603 cluster HD 97950 via isochrone fitting to the colour-magnitude distribution. The distances of 8 kpc to Arches and 6 kpc to NGC 3603 as well as a foreground extinction of 27 mag and 4.5 mag (pre-main sequence), respectively, were applied to the isochrones to allow transformation of magnitudes into stellar masses. In the case of the Arches cluster, a 2 Myr isochrone of the Geneva set of models was most consistent with the data. For HD 97950, two sets of models were required. The 1 Myr pre-main sequence isochrone from Palla & Stahler (1999) was used in combination with the 1 Myr Geneva isochrone to derive individual masses. The foreground extinction of the main sequence had to be estimated 0.5 mag lower than the average observed on the pre-main sequence in order to fit the data. Individual dereddening to the isochrone locus was applied in the case of HD 97950. The observed binary (candidate) sequence was treated in different ways to probe the effect of binarity on the resultant mass function. The correction does not alter the MF significantly.

The integrated mass function slope found in both starburst clusters is $\Gamma = -0.9 \pm 0.1$ in the innermost 0.8 pc of the cluster center. This result is surprising given the entirely different approaches in the analysis of both star clusters. While the obscuration and faintness of the Arches population allowed to derive the MF only down to $\sim 2\,M_\odot$ at most, and the fit yielding the slope covers a mass range of $10 < M < 65\,M_\odot$ due to the flattening of the MF observed below $10\,M_\odot$ and the unknown field contribution, the MF in HD 97950 is derived for $0.4 < M < 20\,M_\odot$, beyond which bright stars are saturated. In the case of HD 97950, individual dereddening, field subtraction and binary correction are applied, while the Arches population was corrected only for the trend in extinction over the field with the assumption that the observed residual scatter can entirely be accounted for by photometric scatter due to the crowded Arches field. Furthermore, at the high-mass end of the Arches population field contamination was assumed to be negligible as suggested by the stellar population at large radii. Despite these different procedures and the different mass coverage of both MFs, the resultant slopes are identical. Although a chance coincidence cannot be excluded in the presence of only two objects, this may indicate a slight flattening in the starburst cluster MF with respect to the Salpeter or average Milky Way mass functions.

Note that from the entire NACO field, a slope of $\Gamma = -1.1 \pm 0.1$ is derived, covering radii out to 1 pc. This result most probably indicates the onset of field contamination at large radii rather than a standard MF, as field stars were not subtracted in the analysis of the Arches population.

The radial analysis of the mass function shows that only the immediate cluster core, in both clusters confined to a core radius of ~ 0.2 pc, displays a flatter mass function slope. In the case of the Arches cluster, a slope of $\Gamma = -0.7 \pm 0.1$ is derived. In subsequent equal-area annuli the slope increases to -0.82 ± 0.13 and -1.1 ± 0.26, indicating that only the densest core region is biased to high-mass stars.

The core of HD 97950 suffers from heavy saturation in the ISAAC data, such that the core was

excluded from this analysis. Grebel et al. (in prep.) derive a MF slope as flat as $\Gamma = -0.3 \pm 0.15$ in the core of HD 97950. The slopes derived form the ISAAC data in this work in equal-area annuli outside the core radius of 0.2 pc are -0.89 ± 0.15, -1.08 ± 0.15, and -0.84 ± 0.27. Except for some scatter, no trend is observed with increasing distance from the cluster center.

The flatter MF slope in the core regions of both starburst clusters is a strong indication for mass segregation. This is not the only evidence found for segregation processes. The MF in HD 97950, despite displaying a relatively constant slope, is increasingly depleted in high-mass stars, reflecting the concentration of the highest mass stars to the cluster core. This interpretation is confirmed from cumulative mass distributions for both clusters, displaying a steeper increase from high to low masses in the cluster center due to the larger number of massive stars detected in the core. While the cumulative function of the Arches cluster follows closely the distribution expected for a single power-law, the pre-main sequence and main sequence CFs in HD 97950 are clearly distinct. The PMS CF is flat with a sharp turn-over towards the MS population, and displays the same shape out to the largest annulus at a distance of 2 pc from the cluster center. The main sequence CF follows the distribution for a slightly steeper power-law than the PMS, and becomes heavily depleted with increasing radius, as already suggested from the mass functions. Thus, a strong halo-core morphology is found in HD 97950.

Unfortunately, the low-mass end cannot be studied in the Arches cluster due to the lack of field data, prohibiting a direct comparison. The flattening of the MF observed for masses $M < 10\,M_{\odot}$ is, however, a strong indication of a depleted low-mass population. Consequently, a halo of low-mass stars would only be expected in the case of violent relaxation, and would rapidly be lost into the high density stellar background of the Galactic Center population. The analysis of comparably resolved field data is capable to reveal such an overdensity of low-mass stars in the immediate vicinity of the Arches cluster, and will thus be very interesting in this respect.

From extrapolation of the mass functions, the dynamical timescales were estimated for both clusters. The relaxation time is with ~ 2 Myr in both Arches and HD 97950 similar to the cluster age. This means that primordial and dynamical segregation cannot be distinguished from this estimate alone. In particular, the relaxation time is not constant over the entire cluster volume, as assumed in the simple approach used to derive the dynamical timescales. The timescale for dynamical relaxation increases with increasing distance from the cluster center due to the decreasing stellar density. As essentially no high-mass stars are found at large radii, the most probable formation scenario for the high-mass stars suggests that some amount of primordial mass segregation was present, confining the high-mass stars to the center of the cluster. The original population of newly formed stars was concentrated further into the cluster core due to dynamical evolution. A similar scenario is suggested for the Orion nuclear cluster and R 136 in 30 Doradus. Furthermore, the morphological comparison shows strong similarities between all three objects, depicting a highly concentrated and massive core (the Trapezium in the case of Orion) surrounded by an extended low-mass stellar halo. Apart from minor differences, the final integrated mass distribution appears to be similar irrespective of metallicity and core density, but the high-mass cut-off is scaled with the total mass of the molecular clump out of which the cluster formed, and thus with the emergent cluster mass.

Despite these indications of a "universal" IMF in different environments when only the MF slope is considered, the Arches cluster, located in the most extreme local star-forming environment, displays an entirely different picture. Although the integrated MF displays a normal slope outside the cluster core, the truncation below $10\,M_{\odot}$ deviates drastically from the other star-forming regions discussed, where no low-mass cut-off is observed. If confirmed, such a truncated MF has severe implications in the understanding of distant stellar populations in galactic nuclei and, in particular, starburst galaxies. The massive clusters observed in tidal interaction regions of merging galaxies experience strong tidal shear forces, comparable to the tidal shear exerted on the Arches cluster by the Galactic Center. The MF - and presumably also the IMF - may differ drastically from the standard Salpeter power-law, such that stellar population synthesis models applying a standard MF can be severely biased. For instance,

a truncated MF is deduced indirectly for the young, massive clusters in the starburst galaxy M 82 (Rieke et al. 1993, Smith & Gallagher 2001). The resolved stellar population of the Arches cluster provides the first direct evidence for such a behaviour, and thus a possible template for extragalactic starbursts. Clearly, further work on the stellar population in the Arches cluster will be illuminating in this respect.

In summary, both the Arches and central NGC 3603 starburst clusters studied display a mass function slope of $\Gamma = -0.9$, with a heavily mass segregated core, beyond which the MF is slightly flatter, but close to, the average slope of $\Gamma = -1.1$ found in the Milky Way by Massey et al. (1995a). A distinct core-halo structure is observed in HD 97950 similar to other sites of massive star formation, indicating that the Carina spiral arm is a typical star-forming environment. No evidence for a low-mass cut-off is found in HD 97950. The Arches cluster, on the other hand, shows strong indication of a truncated mass function below $10\,M_{\odot}$. This result has to be confirmed by observations of the field star population. The different behaviour observed in both starburst clusters yields strong evidence that an extreme environment such as the Galactic Center region can result in a truncated MF in a massive starburst cluster, while the central density and total mass of the cluster itself do not lead to a truncated MF. In particular, this implies that the formation of low-mass stars is not quenched as a consequence of high-mass star formation. Nevertheless, the process of low-mass star formation may be interrupted with hydrogen ignition in the high-mass stars.

For a deeper understanding in particular of the dynamical evolution of starburst clusters such as the Arches and central NGC 3603 cluster, a detailed spectroscopic and proper motion study is required. In addition, spectral classification allows the direct determination of stellar masses independent of model isochrones. Even if available for only a fraction of the intermediate- and low-mass populations in these clusters, a more detailed understanding of the mass distributions will be possible from deep infrared spectroscopic studies.

As nature tends to do whatever it can to make the life of a scientist more interesting, it is very likely that all the discussed phenomena mix wildly to produce the final result we observe. The puzzle we are faced with is to disentangle the bits and pieces and understand each process individually. As far as the prossibility of disentangling each peace of evidence is concerned, I am convinced that nature finds a way to avoid the completing of the puzzle, may it be for the sake of the astronomer not to be bored.

Acknowledgement

Although a thesis has to be a finished entity in the end, the science presented will never really be finished, as nature - fortunately - provides us with a never-ending sequence of mysteries. Similarly, although one has to sign in the end that the work presented is entirely the author's own, a thesis would never be possible without the aid of many helpful hands.

First of all, I would like to thank Eva Grebel, Wolfgang Brandner and Hans-Walter Rix for offering and supporting such a fascinating thesis topic. Many special thanks to Eva Grebel and Wolfgang Brandner for an infinite number of stimulating scientific discussions. Specials thanks also to Hans-Walter Rix for continuous support and encouragement - it is rare to find a person who - despite all directoral obligations - is exactly always there when needed.

In addition to the strong support I found at MPIA, parts of this work were carried out during a half-year stay at the European Southern Observatory. I wish to thank ESO, in particular Wolfgang Brandner and Bruno Leibundgut, for supporting this important experience, where I had the chance to widen my horizon with respect to the obstacles of bringing a complex instrument such as NAOS/CONICA into operations.

As for the contents of this work, many thanks to Wolfgang Brandner for providing me with a wealth of challenging data. Although tackeling them was not always easy, and it took a while to understand all their obstacles, the outcome is - at least to my personal feeling - very rewarding. Many thanks also to Don Figer, who kindly contributed the HST/NICMOS data, without which the technical analysis and understanding of the AO data would not have been possible. Special thanks to Eva Grebel for contributing the Hα data, and to Bernhard Brandl for providing the L-band data, which significantly enriched the analysis of the fascinating NGC 3603 region.

Clearly, understanding in particular the AO data, would never have been possible without the scientific experience and guidance of experienced people such as Wolfgang Brandner. So, many, many thanks for all his encouragement and infinite patience in uncounted scientific discussions - as well as in life. Thank you, also for being there as a friend and a shoulder to lean on when life became harder than expected.

As a scientific thesis is always to some extend a technical challenge and would not be possible without technical support, I wish to thank Ulli Hiller and Walter Rauh for their fast response to computer problems and for keeping the system running. Special thanks also to Rainer Lenzen and Markus Hartung and the entire NACO team for all the hassels they've gone through.

My thanks to Wolfgang Brandner, Eckhard Sutorius, Rainer Köhler, Immo Appenzeller and Hans-Walter Rix for carefully reading the manuscript and providing me with very helpful comments, and for accompanying me with care and consideration - and lots of patience - through the final, stressful phases of a PhD thesis.

As for environmental influences during the work, thanks to the friendly colleagues at MPIA for the nice working environment, and to Immo Appenzeller and the people at the Landessternwarte for providing a wonderful living environment. The Königstuhl has become a very dear home to me, which I will miss very, very much, and I sincerely hope that some of the contacts may last.

There are many great people you meet along the way to numerous to be mentioned, who contribute by sharing their experience and knowledge, as well as their friendliness and motivation. My special thanks to all of them.

Although the people one meets in the course of the work are important for the scientific outcome, a thesis is also a large part of the life that is shared by the friends that - despite all the thesis grumpiness they have to face - stay friends until the end. As I know it was not always easy for them, I also wish to thank them here.

My deep thanks to Eckhard Sutorius for the very long way we have been going together, and for everything we have shared and still share. Thank you for the wonderful time in Heidelberg, which - without exaggeration - was the best time in my life. Thanks also for all your support and encouragement, for your friendship and love.

Things do not always go the way we would like them to. For the long way we have been going together a very private word may be allowed here. There will always be a dragon's tear in a dolphin's eye..... and I know that, finding a Dragon as a friend, means having a friend for life. Thanks for simply being there.

Many thanks also to all the friends that accompanied me on the way -
Clemens & Sabine, Anna & Felix Schmitz, Sven Archibald Hubertus Müller, Eva Manthey, Steffi Wiemann, Nuria "more muffins!!!" Huelamo, Herve Bouy, Irina Kretz & Stefan Noll, Bernd Lang & Martina Kleinheinrich, Angela and Maren Hempel, Elena Puga, and numerous others for many joyful moments between hard thesis work. Many thanks also to Maunzer for the quiet moments in the storm. To my exceptional friend Inge Hipp, thank you for always being there, sharing your wisdom. I sincerely hope that many of the friendships that lasted through or evolved during the thesis will last over space and time.

My thanks and love to my parents for their day- and night-time support, never ending encouragement and - more than anything else - for simply being there. More than many people in the world I know that this is not self-evident, and I will never take it for granted. Thank you so much!

Last not least, thank you very, very much Rai Weiss, David Shoemaker, Paul Schechter and Phil Myers for your encouragement on my way back to leaf-counting!

Euch allen vielen lieben Dank!

Bibliography

Adams, F. C., Lada, C. J., Shu, F. H. 1987, ApJ, 312, 788

Adams, F. C., Shu, F. H., Lada, C. J. 1988, ApJ, 326, 865

Artymowicz, Lubow 1994, ApJ, 421, 651

Baier, G., Ladebeck, R., Weigelt, G. 1985, A&A, 151, 61

Balick, B., Boeshaar, G. O., Gull, T. R. 1980, ApJ, 242, 584

Baraffe, I., Chabrier, G., Allard, F., Hauschildt, P. H. 2002, A&A, 382, 563

Behrend, R., Maeder, A. 2001, A&A, 373, 190

Binney, J., Tremaine, S. 1987, Galactic Dynamics, Princeton University Press, 514

Blum, R. D., Schaerer, D., Pasquali, A., et al. 2001, AJ, 122, 1875

Bonnell, I. A., Davies, M. B. 1998, MNRAS, 295, 691

Bonnell, I. A., Bate. M. R., Zinnecker, H. 1998, MNRAS, 298, 93

Bonnell, I. A., Clarke, C. J., Bate, M. R., Pringle, J. E. 2001, MNRAS, 324, 573

Brandl, B., Brandner, W., Eisenhauer, F., Moffat, A. F. J., Palla, F., Zinnecker, H. 1999, A&AL, 352, 69

Brandner, W., Chu, Y.-H., Eisenhauer, F., Grebel, E. K., Points, S. D. 1997, ApJL, 489, 153

Brandner, W., Grebel, E. K., Barbá, R. H., et al. 2001, AJ, 122, 858 (B00)

Brandner, W., Grebel, E. K., Chu, Y., Dottori, H., Brandl, B., Richling, S. , Yorke, H. W., Points, S. D., Zinnecker, H. 2000, AJ, 119, 292

Carr, J. S., Sellgren, K., Balachandran, S. C. 2000, ApJ, 530, 307

Caselli, P., Myers, P. C. 1995, ApJ, 446, 665

Charlot, S., Bruzual, A. G. 1991, ApJ, 367, 126

Cesaroni, R., Codella, C., Furuya, R. S., Testi, L. 2003, A&A, 401, 227

Cohen, M., Kuhi, L. V. 1979, ApJS, 41, 743

Conti, P. 1999, PASP, 111, 251

Cotera, A. S., Erickson, E. F., Colgan, S. W. J., Simpson. J. P., Allen, D. A., Burton, M. G., 1996, ApJ, 461, 750

Cotera, A. S., Simpson, J. P., Erickson, E. F., et al. 2000, ApJS, 129, 123

Crowther, P. A., Dessart, L., Hillier, D. J., Abbott, J. B., Fullerton, A. W. 2002, A&A, 392, 653

Crowther, P. A., Smith, L. J., Hillier, D. J., Schmutz, W. 1995, A&A, 293, 427

Devillard, N. 1997, The messenger No 87

Diolaiti, E., Bedinelli, O., Bonaccini, D. Close, L., Currie, D., Parmeggiani, G., 2000, A&AS, 147, 335

Dolphin, A. 2000, PASP, 112, 1397

Drissen, L., Moffat, A. F. J., Walborn, N. R., Shara, M. M. 1995, AJ, 110, 2235

Duquennoy, A., Mayor, M. 1991, A&A, 248, 485

Dutra, C. M., Bica, E. 2000, A&A, 359, 347

Dutra, C. M., Bica, E. 2001, A&A, 376, 434

Eisenhauer, F., Quirrenbach, A., Zinnecker, H., et al. 1998, ApJ, 498, 278

Elmegreen, B. 1999, ApJ, 515, 323

Elmegreen, B. 2001, in ASP Conf. Ser., Vol. 249, The Central kpc of Starbursts and AGN, eds. J. H. Knapen, J. E. Beckman, I. Shlosman, and T. J. Mahoney, in press

Figer, D. F., Kim, S. S., Morris, M., et al. 1999, ApJ, 525, 750 (F99)

Figer, D. F., Najarro, F., Gilmore, Diane, et al. 2002, ApJ, 581, 258

Finkenzeller, U., Mundt, R. 1985, A&AS, 55, 109

Flicker, R. C., Rigaut, F. J. 2002, PASP, 114, 1006

Frogel, J. A., Persson, S. E., Aaronson, M 1977, ApJ, 213, 723

Frogel, J. A., Whitford, A. E. 1987, ApJ, 320, 199

Frogel, J. A., Tiede, G. P., Kuchinski, L. E. 1999, AJ, 117, 2296

Fruchter, A. S., Hook, R.N. 2002, PASP, 114, 144

Goss, W. M., Radhakrishnan, V. 1969, ApL, 4, 199

Grabelsky, D. A., Cohen, R. S., Bronfman, L., Thaddeus, P. 1987, ApJ, 315, 122

Grabelsky, D. A., Cohen, R. S., Bronfman, L., Thaddeus, P. 1988, ApJ, 331, 181

Graves, J. E., Northcott, M. J., Roddier, F. J., et al. 2000, SPIE, 4007, 126

Grebel, E. K., Roberts, W. J., Will, J. M., de Boer, K. S. 1993, SSRv, 66, 65

Grebel, E. K., Brandner, W., Roberts, W. J. 1996, A&A, 311, 470

Grebel, E. K., Chu, Y.-H. 2000, AJ, 119, 787

Haisch, K. E. Jr., Lada, E. A., Lada, C. J. 2001, ApJL, 553, 153

Hillenbrand, L. A., Strom, S. E., Vrba, F. J., Keene, J. 1992, ApJ, 397, 613

Hillenbrand, L. A. 1997, AJ, 113, 1733

Hillenbrand, L. A., Hartmann, L. W. 1998, ApJ, 492, 540

Hodapp, K.-W., Hora, J. L., Hall, D. N. B., et al. 1996, New Astronomy, 1, 177

Hofmann, K.-H., Weigelt, G. 1986, A&AL, 167, 15

Hofmann, K.-H., Seggewiss, W., Weigelt, G. 1995, A&A, 300, 403

Howarth, I. D., Prinja, R. K. 1989, ApJS, 96, 527

Hunter, D. A., Shaya, E. J., Holtzman, J. A., Light, R. M., et al. 1995, ApJ, 448, 179

Hunter, D. A., O'Neil, E. J. Jr., Lynds, R., et al. 1996, ApJL, 459, 27

Johnstone, D., Hollenbach, D., Bally, J. 1998, ApJ, 499, 758

Kähler, H. 1999, A&A, 346, 67

Köhler, R. 2001, AJ, 122, 3325

Kennicutt, R. C., Jr. 1984, ApJ, 287, 116

Kenyon, S. J., Whitney, B. A., Gomez, M., Hartmann, L. 1993, ApJ, 414, 773

Kim, S. S., Morris, M., Lee, H. M. 1999, ApJ, 525, 228

Kim, S. S., Figer, D. F., Lee, H. M., Morris, M. 2000, ApJ, 545, 301

Krabbe, A., Genzel, R., Drapatz, S., Rotaciuc, V. 1991, ApJL, 382, 19

Krabbe, A., Genzel, R., Eckart, A., et al. 1995, ApJL, 447, 95

Kroupa, P. 2001, MNRAS, 322, 231

Kroupa, P., Tout, C. A., Gilmore, G. 1990, MNRAS, 244, 76

Lada, C. J., Lada, E. A. 2002, A&A Ann. Rev., 2002, in press, astro-ph/0301540

Lada, C. J., Adams, F. C., 1992, ApJ, 393, 278

Lang, C. C., Goss, W. M., Morris, M. 2001, AJ, 121, 2681

Larson, R. B. 1982, MNRAS, 200, 159

Lejeune, T., Schaerer, D. 2001, A&A, 366, 538

Massey, P., Lang, C. C., DeGioia-Eastwood, K., Garmany, C. D. 1995b, ApJ, 438, 188

Massey, P., Johnson, K. E., DeGioia-Eastwood, K. 1995a, ApJ, 454, 151

Massey, P., Hunter, D. A. 1998, ApJ, 493, 180

McNamara, D. H., Madsen, J. B., Barnes, J., Ericksen, B. F. 2000, PASP, V112, Issue 768, 202

Melnick, J., Tapia, M., Terlevich, R. 1989, A&A, 213, 89

Miller, G. E., Scalo, J. M. 1979, ApJS, 41, 513

Moffat, A. F. J. 1983, A&A, 124, 273

Moffat, A. F. J., Niemela, V. S. 1984, ApJ, 284, 631

Moffat, A. F. J., Drissen, L., Shara, M. M. 1994, ApJ, 436, 183

Moffat, A. F. J., Corcoran, M. F., Stevens, I. R., et al. 2002, ApJ, 573, 191

Morris, M. 1993, ApJ, 408, 496

Mücke, A. 2002, ESO Workshop on the Origin of Stars and Plantes: The VLT View, ed. J. Alves, M. McCaughres (Heidelberg: Springer), on CDrom

Muench, A. A., Lada, E. A., Lada, C. J., Alves, J. 2002, ApJ, 573, 366

Nagata, T., Woodward, C.E., Shure, M., Kobayashi, N. 1995, AJ, 109, 1676

Nürnberger, D. E. A., Bronfman, L., Yorke, H. W., Zinnecker, H. 2002, A&A, 394, 253

Nürnberger, D. E. A., Petr-Gotzens, M. G. 2002, A&A, 382, 537

Nürnberger, D. E. A., Stanke, T. 2003, A&A, in press

O'Dell, C. R., Wen, Z., Hu, X. 1993, ApJ, 410, 696

Osterloh, M., Beckwith S. V. W. 1995, ApJ, 439, 288

Ott, T., Eckart, A., Genzel, R. 1999, ApJ, 523, 248

Palla, F., Stahler, F. W. 1999, ApJ, 525, 772

Papaloizou, Pringle 1977, MNRAS, 181, 441

Parker, N. D. 1991, MNRAS ,251, 63

Persi, P., Tapia, M., Roth, M., Ferrari-Toniolo, M. 1985, A&A, 144, 275

Petr, M. G., Coude Du Foresto, V., Beckwith, S. V. W., Richichi, A., McCaughrean, M. J. 1998, ApJ, 500, 825

Portegies Zwart, S. F., Makino, J., McMillan, S. L. W., Hut, P. 1999, A&A, 348, 117

Portegies Zwart, S. F., Makino, J., McMillan, S. L. W., Hut, P. 2001, ApJL, 546, 101

Portegies Zwart, S. F., Makino, J., McMillan, S. L. W., Hut, P. 2002, ApJ, 565, 265

de Pree, C. G., Nysewander, Melissa C., Goss, W. M. 1999, AJ, 117, 2902

Prosser, C. F., Stauffer, J. R., Hartmann, L., et al. 1994, ApJ, 421, 517

Ramirez, S. V., Sellgren, K., Carr, J. S., et al. 2000, ApJ, 537, 205

Rich, R. 1988, AJ, 95, 828

Rieke, G. H., Lebofsky, M. J. 1985, ApJ, 288, 618

Rieke, G. H., Loken, K., Rieke, M. J., Tamblyn, P. 1993, ApJ, 412, 99

Roddier, F. (ed.) 1999, *Adaptive Optics in Astronomy*, Cambridge University Press, Cambridge, UK

Sagar, R., Munari, U., de Boer, K. S. 2001, MNRAS, 327, 23

Salpeter, E. E. 1955, ApJ, 121, 161

Scalo, J. M. 1986, in *Fundamentals of Cosmic Physics*, 11, 1

Scalo, J. M. 1998, in ASP Conf. Ser., Vol. 142, *The stellar initial mass function*, 201

Schaerer, D., Meynet, G., Maeder, A., Schaller, G. 1993, A&AS, 98, 523

Schaller, G., Schaerer, D., Meynet, G., Maeder, A. 1992, A&AS, 96, 269

Serabyn, E., Shupe, D., Figer, D.F. 1998, Natur, 394, 448

Sher, D. 1965, 1965, JRASC, 59, 67

Smith, L. J., Maeder, A. 1989, A&A, 211, 71

Smith, L. J, Gallagher, J. S. III 2001, MNRAS, 326, 1027

Stetson, P. B. 1987, PASP, 99, 191

Stetson, P. B. 1990, PASP, 102, 932

Stolte, A., Grebel, E. K., Brandner, W., Figer, D. F. 2002, A&A, 394, 459

Subramaniam, A., Sagar, R., Bhatt, H. C. 1993, A&A, 273, 100

Tapia, M., Bohigas, J., Pérez, B., Roth, M., Ruiz, Ma. T. 2001, RMxAA, 37, 39

Terndrup, D. M., Frogel, J. A., Whitford, A. E. 1990, ApJ, 357, 453

Terndrup, D. M., Frogel, J. A., Whitford, A. E. 1991, ApJ, 378, 742

Timmermann, R., Genzel, R., Poglitsch, A., Lutz, D., Madden, S.C., Nikola, T., Geis, N., Townes, C.H. 1996, ApJ, 466, 242

Tody, D. 1993, in ASP Conf. Ser., Vol. 52, Astronomical Data Analysis Software and Systems II, eds. R. J. Hanisch, R. J. V. Brissenden, J. Barnes, 173

Tokovinin, A. A. 2001, *Adaptive Optics Tutorial*, URL: www.ctio.noao.edu/ atokovin/tutorial

Walborn, N. R. 1973, ApJL, 182, 21

Whitmore, B. C., Zhang, Q., Leitherer, C. et al. 1999, AJ, 118, 1551

Yi, S., Demarque, P., Kim, Y.-C., et al. 2001, ApJS, 136, 417

Yorke, H. W., Krügel, E. 1977, A&A, 54, 183

Yusef-Zadeh, F., Morris, M., Chance, D. 1984, Natur, 310, 557